Università degli Studi di Cagliari

Università degli Studi di Sassari

DOTTORATO DI RICERCA

In Science e Tecnologie Chimiche

Ciclo XXXVI

UniCa-UniSS

# Functionalization of Food Packaging with Active Antimicrobial Agent

CHIM/01 Chimica Analitica

Presentata da: Giulio Casula

Coordinatore Dottorato: Prof.ssa Carla Cannas

Tutor: Prof.ssa Antonella Rossi

Esame finale anno accademico 2023-2024

Ministero dell'Università e della Ricerca
REGIONE AUTONOMA DELLA SARDEGNA
ETH zürich
FSC Fondo per lo Sviluppo e la Coesione

# Contents

# Abstract

The development of new antimicrobial food-packaging that exhibits antimicrobial activity, is crucial for extending the shelf-life of fresh food products. Surface functionalization is a useful strategy for imparting antimicrobial properties to commercially available food-grade polymers used in packaging material. This work of thesis presents an analytical approach for investigating the surface functionalization of food-grade polyvinylchloride (PVC) using various surface-sensitive techniques such as X-ray photoelectron spectroscopy (XPS), angle-resolved XPS (ARXPS), atomic force microscopy (AFM), scanning electron microscopy (SEM) and attenuated total reflection-Fourier transform infrared spectroscopy (ATR-FTIR).

The following is a brief description of the experimental setup for functionalizing the PVC surface with two potential antimicrobial agents Polyhexamethylene guanidine (PHMG) and 4-(10,15,20-triphenilporphyrin-5-yl)-aniline (TPPA). Firstly, the food-grade PVC samples were functionalized with (3-mercaptopropyl) trimethoxy-silane (MPTMS). Then, 3-(aminopropyl)-triethoxysilane (APTES) and glutaraldehyde were anchored to the surface. The functionalized samples were named M-PVC, A-PVC and G-PVC, according to the literature. The presence of the glutaraldehyde on the surface allowed PHMG and TPPA to be grafted through a reaction between the carbonyl groups of glutaraldehyde and the amino groups present in both PHMG and TPPA.

The characterization of the surface and the interpretation of the XPS / ARXPS results were challenging due to the presence of carbon atoms in both the substrate (PVC) and the organic functionalization layers.  To solve this problem, a new idea was proposed to use freshly cleaved gold as a carbon-free substrate. This substrate is also ideally flat as it is required by ARXPS measurements. The same functionalization process as on PVC was possible due the great affinity between thiols presents in the MPTMS and gold. This analytical approach allowed estimating the curve fitting parameters for resolving the C 1s spectra. The individual signals in the overlapping C1s spectra could be assigned to the different functional groups of the functionalization layer.  Applying these results to the curve fitting of C 1s spectra of functionalized layers on PVC allowed for the distinguishing of the substrate from the components ascribed to the functionalization layer. The composition of the functionalized layers obtained on PVC was found to be in agreement with the results obtained on gold samples.

The ARXPS results revealed the distribution of the elements in the functionalized layer. The thickness of the functionalization layer was estimated to be 1.4 (0.3) nm and 1.2 (0.4) nm for the

step M-PVC and A-PVC respectively, after taking into account the contamination. For G-PVC and P-PVC, the layer thickness was estimated to be greater than 6 nm because the signals from the substrate were not detected. This suggests the formation of a more complex layer, although more measurements are needed to understand the functionalization mechanism.

ATR-FTIR was exploited as a rapid technique for characterizing the PVC before and after the functionalization process. The successful functionalization was confirmed by the presence of specific vibrational bands of the molecules used, such as the asymmetric stretching of the Si-O-Si at 1082 $cm^{-1}$ due to the presence of MPTMS and APTES, and the C=N stretching band (1630 $cm^{-1}$). The presence of PHMG was confirmed by the presence of an intense band attributed to the C=N bond of the of the PHMG's iminium groups. After the last step of functionalization with PHMG, the bands of the previous steps were not detected, suggesting the possible formation of a multilayer structure.

In addition, AFM and SEM were exploited to study the change in the topography and morphology of PVC after functionalization. AFM showed an increase in roughness while SEM indicated the formation of a thick layer of PHMG after the last functionalization step, possibly due to a polymerization reaction that can occur between PHMG molecules.

It has been shown that P-PVC has good antimicrobial properties against *S.Aureus* and *E.Coli,* as well as on typical Sardinian food samples like culurgiones (fresh pasta) and carasau bread. Based on these promising achievements from in-vitro and food samples studies, P-PVC has the potential to be used as an antimicrobial packaging material for food. However, further investigation is required, particularly regarding the final steps of functionalization, the homogeneity of the functionalized layers and the reaction mechanism.

# Chapter 1.

This chapter presents a brief overview of the role of antimicrobial food-packaging in extending food shelf-life and the scope of this work.

## Introduction to the Analytical Problem and Motivation of the Work

Food-packaging play a central role in the food manufacturing process, being a key component in ensuring the preservation of the quality of food products during storage, transportation and end-user applications[1–3]. Its importance resides in preserving both fresh and processed food items from external elements such as contaminants, spoilage bacteria, mechanical loads, and physical harm [4–8]. Furthermore, the growing request in the consumers of less processed food products, that have commonly an inferior shelf-life, compromise the food safety [9–11]. Since the food spoilage and corruption from food-borne pathogens is one of the most common causes of food degradation, the interest of the food-packaging industry is directed toward the development of innovative materials that can preserve the food quality and prolong the shelf-life [12]. The shelf-life is defined as "*the duration, under specified storage conditions, within which food retains desired sensory, chemical, physical, and biological characteristics, hence is the time during which the food remains safe and complies with any label declaration*" [13].

To address the prolonged freshness of food, conventional practices involve the direct addition of preservatives to food; however, this approach has raised concerns due to its tendency towards overuse and its implications for human health[9].

An alternative approach is represented by active packaging. Active packaging does not only fulfil the conventional role of a physical protective barrier from external environment, but it is also designed to actively contribute to the preservation of the food quality [4,14]. In the active packaging, the package, the product and the environment work together to prolong the shelf-life, enhancing the safety, and not altering the sensory attributes, thus ensuring the overall quality of products [15–17].

The antimicrobial packaging (AM) is recognized as the most promising version of active packaging systems. AM are materials in which an active antimicrobial substance is incorporated or immobilized onto the material surface. They can be divided into two categories: migrating systems, where the active antimicrobial substance can migrate from the material to the food product, and non-migrating systems where the inhibition of the bacterial growth occurs at the food product surface without the release of the antimicrobial agent [11]. These systems can be obtained by the surface modification of a polymer or a packaging material to immobilize the active substance onto its surface. The surface functionalization of a polymer can be achieved by the reaction of specific functional groups of the material with the functionalizer molecule, by the formation of e.g. amide, ester, ether and thioether groups [18–20]. An advantage of surface immobilization of the antimicrobial active agent is to preserve the bulk properties of the material, instead of incorporating it into the polymeric matrix, and in addition, less amount of active agent is required for achieving a good antimicrobial efficiency [21]. The study and understanding of the functionalization process is important to obtain an antimicrobial food-packaging suitable for commercial applications and, for this purpose, the development of an analytical strategy for controlling and understanding the surface functionalization of a complex matrix such as polymeric materials is crucial.

## 1.1 Scope of the thesis

This thesis aims to the optimization of the surface functionalization of food-grade polyvinyl chloride (PVC) for obtaining an antimicrobial food-packaging by grafting an active antimicrobial agent onto the polymer surface. PVC is still considered one of the best materials in food-packaging since it does not alter the taste of the packaged food, it is light, cost-efficient, transparent and it has good mechanical properties and acts as a barrier against oxygen and water. Last but not least in medical applications is still used because it can easily be sterilized by irradiation [22]. More recently researches devoted they efforts to explore innovative bio-plastics because of the environmental concerns but so far, more work is needed to achieve the same performances and versatility of PVC and to ensure the reduction of possible risks associated to the transfer of allergens from bio-based packaging for food contact [23]. Polyhexametilenguanidine (PHMG) is studied in this work to achieve the surface functionalization of the polymer in four sequential steps: first grafting of 3-(mercaptopropyl)trimethoxysilane (MPTMS) onto the food-grade PVC by the formation of a thioether bond between the sulfur atom present in the MPTMS. Due to the presence of Si-O groups on top of the first functionalization layer, (3-aminopropyl) triethoxysilane (APTES) can be attached to the polymer surface in a second step, and the amino group of APTES can react with the carbonyl group of the glutaraldehyde to form a third functionalization layer onto the polymer surface. Finally, PHMG has been covalently bonded to the polymer surface, conferring to the food-grade PVC antimicrobial properties.

This work also aims to develop an analytical strategy for characterizing the surface of the functionalized PVC by exploiting surface-sensitive techniques such as X-ray photoelectron spectroscopy (XPS), angle-resolved XPS (ARXPS), Fourier-transform infrared spectroscopy (FT-IR), attenuated total reflectance spectroscopy (ATR) Fourier-transform infrared spectroscopy, atomic force microscopy (AFM), scanning electron microscopy (SEM), contact angle measurements. Moreover, the antimicrobial activity of the functionalized polymer was tested, and the preliminary results of these tests will be discussed. Contact angle and AFM measurements were carried out in order to obtain information about the hydrophobicity and surface roughness of the modified polymer since these parameters play an important role in bacterial adhesion to the polymer surface [24].

## 1.2 Outline of the thesis

This work is organized into 9 chapters: The first chapter provides a brief introduction to the importance of developing and characterizing new materials for extending the food products shelf-life. The second chapter gives a theoretical background on surface functionalization with organic compounds and their role in the polymer functionalization, and more detailed information on the antimicrobial polymers available on the market. Chapter 3 describes all the techniques exploited for the characterization of the food-grade PVC before and after the surface functionalization, followed by the fourth chapter, in which the functionalization protocol is described in detail. In the fifth chapter, the development of the analytical strategy for characterizing the first two steps of functionalization with MPTMS and APTES is discussed, followed by chapter six, in which the analytical protocol developed on fresh-cleaved gold samples is applied for characterizing the food-grade PVC surface. Furthermore, the results obtained by exploiting AFM and SEM will be discussed. In Chapter 7, the characterization of functionalized food PVC by exploiting ATR FT-IR spectroscopy on the P-PVC samples is explored. Finally, in chapter 8 the antimicrobial activity preliminary results of the functionalized PVC will be presented. In chapter 9 a comprehensive conclusion on this work is drawn and the outlook will be presented.

# References

[1] "J.H. Han, D. Patel, J.E. Kim, S.C. Min, Retardation of Listeria Monocytogenes Growth in Mozzarella Cheese Using Antimicrobial Sachets Containing Rosemary Oil and Thyme Oil, Journal of Food Science 79 (2014) E2272–E2278. https://doi.org/10.1111/1750-3841.12659.

[2] A. Ambaw, T. Fadiji, U.L. Opara, Thermo-Mechanical Analysis in the Fresh Fruit Cold Chain: A Review on Recent Advances, Foods 10 (2021) 1357. https://doi.org/10.3390/foods10061357.

[3] J. Brockgreitens, A. Abbas, Responsive Food Packaging: Recent Progress and Technological Prospects, Comprehensive Reviews in Food Science and Food Safety 15 (2016) 3–15. https://doi.org/10.1111/1541-4337.12174.

[4] T. Fadiji, T.M. Berry, C.J. Coetzee, U.L. Opara, Mechanical design and performance testing of corrugated paperboard packaging for the postharvest handling of horticultural produce, Biosystems Engineering 171 (2018) 220–244. https://doi.org/10.1016/j.biosystemseng.2018.05.004.

[5] K.K. Samanta, S. Basak, S.K. Chattopadhyay, Potentials of Fibrous and Nonfibrous Materials in Biodegradable Packaging, in: S.S. Muthu (Ed.), Environmental Footprints of Packaging, Springer, Singapore, 2016: pp. 75–113. https://doi.org/10.1007/978-981-287-913-4_4.

[6] S. Mangaraj, A. Yadav, L.M. Bal, S.K. Dash, N.K. Mahanti, Application of Biodegradable Polymers in Food Packaging Industry: A Comprehensive Review, J Package Technol Res 3 (2019) 77–96. https://doi.org/10.1007/s41783-018-0049-y.

[7] D. Restuccia, U.G. Spizzirri, O.I. Parisi, G. Cirillo, M. Curcio, F. Iemma, F. Puoci, G. Vinci, N. Picci, New EU regulation aspects and global market of active and intelligent packaging for food industry applications, Food Control 21 (2010) 1425–1435. https://doi.org/10.1016/j.foodcont.2010.04.028.

[8] K. Marsh, B. Bugusu, Food Packaging—Roles, Materials, and Environmental Issues, Journal of Food Science 72 (2007) R39–R55. https://doi.org/10.1111/j.1750-3841.2007.00301.x.

[9] J. Ju, C. Wang, Y. Qiao, D. Li, W. Li, Effects of Tea Polyphenol Combined with Nisin on the Quality of Weever (Lateolabrax japonicus) in the Initial Stage of Fresh-Frozen or Chilled Storage State, Journal of Aquatic Food Product Technology 26 (2017) 543–552. https://doi.org/10.1080/10498850.2016.1233472.

[10] S.A. Sofi, J. Singh, S. Rafiq, U. Ashraf, B.N. Dar, G.A. Nayik, A Comprehensive Review on Antimicrobial Packaging and its Use in Food Packaging, Current Nutrition & Food Science 14 (n.d.) 305–312.

[11] P. Suppakul, J. Miltz, K. Sonneveld, S. w. Bigger, Active Packaging Technologies with an Emphasis on Antimicrobial Packaging and its Applications, Journal of Food Science 68 (2003) 408–420. https://doi.org/10.1111/j.1365-2621.2003.tb05687.x.

[12] S.H. Kamarudin, M. Rayung, F. Abu, S. Ahmad, F. Fadil, A.A. Karim, M.N. Norizan, N. Sarifuddin, M.S.Z. Mat Desa, M.S. Mohd Basri, H. Samsudin, L.C. Abdullah, A Review on Antimicrobial Packaging from Biodegradable Polymer Composites, Polymers (Basel) 14 (2022) 174. https://doi.org/10.3390/polym14010174.

[13] L. Manzocco, S. Calligaris, M.C. Nicoli, 9 - Methods for food shelf life determination and prediction, in: E.A. Decker (Ed.), Oxidation in Foods and Beverages and Antioxidant Applications, Woodhead Publishing, 2010: pp. 196–222. https://doi.org/10.1533/9780857090447.1.196.

[14] R.W. Anwar, Sugiarto, E. Warsiki, The comparison of antimicrobial packaging properties with different applications incorporation method of active material, IOP Conf. Ser.: Earth Environ. Sci. 141 (2018) 012002. https://doi.org/10.1088/1755-1315/141/1/012002.

[15] V.A. Jideani, K. Vogt, Antimicrobial Packaging for Extending the Shelf Life of Bread—A Review, Critical Reviews in Food Science and Nutrition 56 (2016) 1313–1324. https://doi.org/10.1080/10408398.2013.768198.

[16] Ph.D Student, Department of Food and Nutrition, Punjab Agricultural University Ludhiana, Punjab, P. Prasad, A. Kochhar, Active Packaging in Food Industry: A Review, IOSRJESTFT 8 (2014) 01–07. https://doi.org/10.9790/2402-08530107.

[17] S. Quintavalla, L. Vicini, Antimicrobial food packaging in meat industry, Meat Science 62 (2002) 373–380. https://doi.org/10.1016/S0309-1740(02)00121-3.

[18] J.M. Goddard, J.H. Hotchkiss, Polymer surface modification for the attachment of bioactive compounds, Progress in Polymer Science 32 (2007) 698–725. https://doi.org/10.1016/j.progpolymsci.2007.04.002.

[19] T. Kameda, M. Ono, G. Grause, T. Mizoguchi, T. Yoshioka, Antibacterial effect of thiocyanate substituted poly(vinyl chloride), J Polym Res 18 (2011) 945–947. https://doi.org/10.1007/s10965-010-9492-3.

[20] P. Farkaš, S. Bystrický, Chemical conjugation of biomacromolecules: A mini-review, Chem. Pap. 64 (2010) 683–695. https://doi.org/10.2478/s11696-010-0057-z.

[21] L.J. Bastarrachea, D.E. Wong, M.J. Roman, Z. Lin, J.M. Goddard, Active Packaging Coatings, Coatings 5 (2015) 771–791. https://doi.org/10.3390/coatings5040771.

[22] R.B. Pearson, PVC as a food packaging material, Food Chemistry 8 (1982) 85–96. https://doi.org/10.1016/0308-8146(82)90004-8.

[23] A. Cavazza, M. Mattarozzi, A. Franzoni, M. Careri, A spotlight on analytical prospects in food allergens: From emerging allergens and novel foods to bioplastics and plant-based sustainable food contact materials, Food Chemistry 388 (2022) 132951. https://doi.org/10.1016/j.foodchem.2022.132951.

[24] I. Georgakopoulos-Soares, E.L. Papazoglou, P. Karmiris-Obratański, N.E. Karkalos, A.P. Markopoulos, Surface antibacterial properties enhanced through engineered textures and surface roughness: A review, Colloids and Surfaces B: Biointerfaces 231 (2023) 113584. https://doi.org/10.1016/j.colsurfb.2023.113584."

# Chapter 2. State of the art

In the first part of this chapter, polymers used in the packaging industries are introduced together with the comparison with biopolymers and their properties.

In the second part emphasis on surface modification approaches and related studies is provided. In the last part of this chapter the attention is focused on factors influencing adhesion and biofilm formation.

## 2.1Polymers in the food-packaging industries

The main role of food-packaging is to guarantee the quality of a food product to the final customer during transportation, storage and retailing phase, minimizing the costs [1]. For this purpose, a wide range of materials have been exploited including ceramics, paper, metals, and plastics. Plastics material represent the most used material in the food-packaging industry due to their versatility, lightweight, ease of processing and cost-efficiency [2]. In fact, 30% of the total production of polymer industry is represented by polymers for food-packaging applications [3].

Food-packaging polymers can be divided into two main categories: petroleum-based polymers and biopolymers. Among these two categories, petroleum-based polymers are the most ones, despite the environmental concerns toward their disposal and recyclability. In food-packaging the most used ones are polyethylene terephthalate (PET), high-density and low-density polyethylene (HDPE and LDPE) and polyvinyl chloride (PVC) because of their large availability, low cost, and because of their mechanical properties as tensile and tear strength, ability as gas barriers [4–6]. PVC is recognized for its high strength, transparency and excellent oil barrier [7]. Although PVC possesses many beneficial properties, it can be easily degraded at high temperatures and decomposes with the release of hydrogen chloride (HCl). Because of this instability, PVC for food-packaging is mixed with a large number of plasticizers to reduce the thermal degradation. Furthermore, the addition of these plasticizers improves the elasticity and the stretch properties of the polymeric film allowing its application as food-packaging.

Biopolymers are polymers that are constituted entirely or partially by renewable resources [8]. The interest towards these materials is growing due to all the benefits associated to their development such as the preservation of resources and the reduction of the carbon footprint. Furthermore, biopolymers represent a new alternative to the petroleum-based polymers that can reduce the petroleum dependence [9]. Despite all the advantages on the environmental perspective, biopolymers represent only the 0.5% of the 400 million of tons of plastic produced annually [10] because of the scarce mechanical properties associated with the biopolymers [11]. Polysaccharides (cellulose, pectin, chitosan) lipids, proteins (casein, collagen etc.) and microbial polymers (polylactic acid, polyhydroxyalkanoates etc.) are some examples of the biopolymers reported in the literature [12–15]. Some concerns are also connected to the release of allergens when there is a contact of bio-polymers surfaces and foods [16].

## 2.2 Surface functionalization of polymeric substrates

The surface functionalization of polymeric substrates is one of the most promising methods for the modification of food-packaging materials with antimicrobial properties. In the literature numerous examples are given on how to incorporate an active antimicrobial compound onto the polymer surface:

- Surface immobilization through non-covalent interactions that rely on electrostatic interactions between the polymer surface that possess a certain net charge that can attract the specific active molecule, such as an enzyme [17].
- Surface immobilization through covalent interactions: in this case the active molecule is grafted onto the polymer surface by covalent bond.
- Layer-by-layer assembly in which the functionalization consists in the alternate deposition of polyelectrolytes with opposite charge [18]. To achieve this functionalization the polymer surface can be activated through UV radiation or plasma [19,20], that allow the polymer to have a net charge, or the polyelectrolytes can be attached to the surface covalently. The polyelectrolytes used in the layer-by-layer assembly are proteins, polysaccharides, or synthetic polymers.
- Photografting can be exploited for surface functionalization of the polymeric substrate as well as for incorporating active agents in the polymer matrix. In photografting the surface modification is achieved by exposition of the polymer to UV radiation in the range comprised between 315-400 nm, in the presence of a photoinitiator [21,22]. The exposure to the UV light generates free radical on the polymer surface that can consequently react with the photoinitiators such as benzophenone [23], anthraquinone [24] thioxantone [24] allowing their attachment onto the polymer surface [25].

Surface immobilization with covalent interaction represent a promising method for the development of antimicrobial food-packaging, although the polymer surface is generally inert. Because its intrinsic inertly (low reactivity), the polymer surface can be modified with different methods such as corona discharge, UV light irradiation or plasma treatment. On the other hand, some polymers such as PVC, PET or chitosan have specific functional groups that allow the formation of covalent bonds with the target active molecule. One of the main benefits of the covalent immobilization of the active molecule onto the polymer surface is that the active molecule cannot migrate towards the surface of the food product, avoiding the compromission of the food product characteristics.

One way to achieve the surface immobilization of the active antimicrobial molecules is also the modification of the surface polymer by SAMs, with a bottom-up approach in which the polymer surface is modified with silanes, thus allowing the attachments of specific functional groups without compromising the polymer mechanical properties [26].

## 2.3 Antimicrobial active agents

Active agents can be classified according to their origin (synthetic or natural-based), how they operate (antioxidant, oxygen scavenger, antimicrobial agents etc) or its structure (organic, inorganic, metals, enzymes, antibiotics etc) [11].

A group of most studied active agents with antimicrobial properties are metallic nanoparticles such as silver and copper [27] nanoparticles and oxide nanoparticles (ZnO, $TiO_2$, CuO)[28,29]. Packaging with these types of antimicrobial agents have been studied widely in the literature, but their application in the market is still restricted in Europe due concerns regarding their long-term impact on environment and human health [30], but the interest towards the development of food-packaging functionalized with metallic or oxide nanoparticles is expected to grow. The mechanism by which they exert their antimicrobial activity is not fully understood, even though in the literature many studies have been published [31,32].

Another example of antimicrobial agent widely studied is represented by animal-derived and plant-derived antimicrobial agents. Some characteristics examples of animal-derived include proteins such as lactoferrin[33], or enzyme such as lysozyme[34]. On the other hand, essential oils or extracts are the most common plant based antimicrobial agents [35].

Another category of antimicrobial agents involves the use of quaternary ammonium salts (QAs) and polyhexametilenguanidine (PHMG). Their activity relies on their capacity to anchor the cytoplasmatic membrane of the bacteria and lead to the lysis of the cell. Moreover, PHMG has shown good antifungal and antiviral activity[36]; thanks to its high-water solubility it can be exploited as hospital sanitizers and in the production of medical-grade antimicrobial polymers [26] and antimicrobial fabrics [37].

## 2.4 Antimicrobial polymers

In the literature many examples of antimicrobial polymers have been reported for applications in food-packaging or for medical applications. Some inherently antimicrobial polymers such as chitosan have widely been studied in the last decades. Chitosan is known for its antimicrobial activity and many authors studied its properties and the possibility to exploit as antimicrobial food-packaging in combination with other polymers that present better mechanical properties [38–40]. Table 1 summarize some examples of antimicrobial polymer classes present in the literature:

*Table 1 Examples of antimicrobial polymer classes present in in the literature functionalized with different antimicrobial agents*

| Polymer | Antimicrobial agent | Targeted organism | Reference |
|---|---|---|---|
| Polyvinilchloride (PVC) | PHMG | *S. aureus* | [26] |
| | Orange essential oil | *E. coli and S. aureus* | [41] |
| | Quaternarium ammonium salt | *P. aeruginosa, S. aureus, A. baumannii* and *B. subtilis.* | [42] |
| Polyvinyl alcohol (PVA) | Vanilline and chitosan | *E. coli, S. aureus* | [43] |
| | PHMG | *E. coli, S. aureus* | [44] |
| Low-density polyethylene (LDPE) | ZnO | *E. coli* | [45] |
| | Silver nanoparticles | *E. coli, S. aureus, E. faecalis* and *S. enterica* | [46] |
| | Thymol | *E. coli* and *Salmonella* | [47] |
| Polylactic acid | Ag-Cu | *L. monocytogenes* | [48] |

| | | | |
|---|---|---|---|
| (PLA) | nanoparticles and cinnamon essential oil | | |
| | ZnO and chitosan | *E. coli* | [49] |
| PET | Chitosan and QAs | *E. coli, S. aureus* | [40] |

Many examples reported in the literature exploit different methodology for functionalizing the polymeric substrate; one of the most used is the incorporation of the antimicrobial compounds in the matrix, while less examples of surface functionalization have been reported. The incorporation of the antimicrobial molecule into the matrix is the simplest way to add antimicrobial properties to the polymer, but this may compromise the mechanical properties and may lead to the release of antimicrobial compound. Regarding these aspects, Ahmed et alii [48] reported an example of antimicrobial composite that consist of a polylactic acid substrate (PLA) mixed with polyethylene glycol (PEG) as copolymer, in which cinnamon and essential oil and Ag-Cu nanoparticles were added by compression-molding method. The antimicrobial properties of this composite were demonstrated to last 150 days and were correlated to the release of $Ag^+$ and $Cu^{2+}$ ions from the polymer matrix. Furthermore, cinnamon essential oils, which is mainly constituted by cinnamaldehyde, can inhibit the enzymatic activity of the bacterial colonies. The loss of antimicrobial activity of the polymer was attributed also to the evaporation of the active compound of the cinnamon essential oil that has been widely reported in literature [50,51].

In the case of surface covalent functionalization, migration of the antimicrobial compound is not expected. Examples of covalent attachment are reported for PVC, PLA and PVA samples. Villanueva et alii reported two examples of surface functionalization of medical-grade PVC with PHMG [26] and QAs [42] by previous modification the surface with 3-(mercaptopropyl)-trimethoxysilane and aminopropyltriethoxysilane to confer to the polymer surface the functional groups necessary for the grafting of the active molecules. In both cases, the stability of the functionalization was demonstrated, and it has been reported that both PHMG and QAs were not released from the surface, thus leading to a higher durability of the antimicrobial effect. Moreover, the biofilm formation test has been carried out and the anchoring of the antimicrobial agent onto the surface prevent the formation of a biofilm, hence the polymer showed low bacterial attachment.

These antimicrobial polymers were mainly characterized using ATR-FTIR spectroscopy. This technique allows for understanding the functional groups in the analysed samples by taking advantage of the shorter analysis time with respect to other techniques. Moreover, ATR-FTIR can help ascertain the antimicrobial effect of these polymers, as residuals of dead bacteria can be found on the polymeric samples, giving characteristic vibrational bands. While there are examples of ATR-FTIR spectra obtained on antimicrobial materials in the literature [52–54], there are not many examples of packaging analysed before and after being used as food-packaging or for contaminated samples. One example is a chitosan-chestnut polymer used for storing filled fresh pasta [53]; ATR-FTIR was used to evaluate changes in the spectra due to antibacterial effects against *E. coli*. As presented and discussed in Chapter 8, the characteristic vibrational band of bacterial strain can overlap with the vibrational band of the food samples, as fatty acids and carbohydrates can be found in both bacteria and food samples. [55,56]

## 2.5 Roughness and hydrophobicity influence on bacterial adhesion

Bacterial surface colonization first involves bacteria adhesion to the surface, leading to the growth of colonies and biofilms [57]. The adhesion process onto a surface depends on different aspects, starting with the type of bacteria that can be divided in Gram-positive (e.g. *S. aureus*) or Gram-negative (e.g. *E. coli*) based on the structural properties of the bacterial wall, with Gram-negative more negatively charged due to the presence of polysaccharides and a thinner membrane, and Gram-positive bacteria with a more rigid cellular membrane [57]. Moreover, the adhesion can be assisted by extracellular appendages such as flagella and pili, which play a role in the initial attachment of bacteria to a surface. [58] Bacterial cell surfaces generally carry a net negative charge under most physiological conditions [59]. On the other hand, the bacterial cell surface is dynamic since it responds to environmental changes through the adsorption of ions and macromolecules. Moreover, pH may allow the association or dissociation of the charged groups. These surface charges may promote bacterial adhesion, which can further support bacterial growth [59,60].

The bacterial adhesion is also influenced by the surface properties such as roughness and the hydrophobicity of the material surface. Many examples of how surface roughness may influence the bacterial adhesion are reported in the literature [61–64]. Generally, a higher surface roughness in the range of submicrometer and micrometer scale promotes the bacterial adhesion [61–64]. Choi et al.[65] reported the results obtained on a PMMA film with different roughness values of 0.1 μm and 5 μm, the bacterial adhesion of *Pseudomonas fluorescens* increased with the surface roughness. In the same work, the influence of the surface wettability in the bacterial adhesion by comparing two materials with the same roughness but different surface hydrophobicity. Cyclic olefinic copolymer (COC), the most hydrophobic material tested, showed a more favourable surface to the bacterial adhesion of the *P. fluorescens.* Hydrophobicity is typically linked to an increase of the bacterial adhesion onto these surface; this is due to the lipid moiety of the lipopolysaccharide present in the outer membrane of the bacterial cells [65–67], hence surfaces with a contact angle greater than 90 ° typically have a higher probability of favouring a biofilm formation.

In [61], a range of both hydrophilic and hydrophobic surfaces were presented, and the role of hydrophobic surfaces in promoting bacterial adhesion was discussed. These surfaces exhibited a higher adhesion force between the bacteria and the surface, and may reduce the velocity of the bacteria during collision, thereby promoting the adhesion process [68]. On the other hand, superhydrophobic surfaces (contact angle >150°) demonstrated good antimicrobial activities. Several examples in the literature showed a reduction in *P. aeruginosa* adhesion force on superhydrophobic surfaces [69,70]. This decrease in bacterial adhesion was attributed to the trapped air, which prevents the adhesion mechanism, thereby conferring them good antibacterial activity [71].

## References

[1] "R. Coles, D. McDowell, M.J. Kirwan, Food Packaging Technology, CRC Press, 2003.

[2] J. Luna, A. Vílchez, Chapter Seven - Polymer Nanocomposites for Food Packaging, in: R. Busquets (Ed.), Emerging Nanotechnologies in Food Science, Elsevier, Boston, 2017: pp. 119–147. https://doi.org/10.1016/B978-0-323-42980-1.00007-8.

[3] Resource1.pdf, (n.d.). https://www.worldpackaging.org/Uploads/2018-04/Resource1.pdf (accessed January 18, 2024).

[4] V. Siracusa, P. Rocculi, S. Romani, M.D. Rosa, Biodegradable polymers for food packaging: a review, Trends in Food Science & Technology 19 (2008) 634–643. https://doi.org/10.1016/j.tifs.2008.07.003.

[5] T. Huang, Y. Qian, J. Wei, C. Zhou, Polymeric Antimicrobial Food Packaging and Its Applications, Polymers 11 (2019) 560. https://doi.org/10.3390/polym11030560.

[6] K. Marsh, B. Bugusu, Food Packaging—Roles, Materials, and Environmental Issues, Journal of Food Science 72 (2007) R39–R55. https://doi.org/10.1111/j.1750-3841.2007.00301.x.

[7] Food Packaging, (n.d.). https://onlinelibrary.wiley.com/doi/epdf/10.1002/9781118846315.ch11 (accessed January 18, 2024).

[8] R.P. Babu, K. O'Connor, R. Seeram, Current progress on bio-based polymers and their future trends, Prog Biomater 2 (2013) 8. https://doi.org/10.1186/2194-0517-2-8.

[9] O. Wolf, M. Crank, M. Patel, F. Marscheider-Weidemann, J. Schleich, B. Hüsing, G. Angerer, Tehno-Economic Feasibility of Large-Scale Production of Bio-Based Polymers in Europe, Fraunhofer ISI (2005).

[10] EUBIO_Admin, Market, European Bioplastics e.V. (n.d.). https://www.european-bioplastics.org/market/ (accessed January 18, 2024).

[11] A. Duda-Chodak, T. Tarko, K. Petka-Poniatowska, Antimicrobial Compounds in Food Packaging, International Journal of Molecular Sciences 24 (2023) 2457. https://doi.org/10.3390/ijms24032457.

[12] M. Mujtaba, J. Lipponen, M. Ojanen, S. Puttonen, H. Vaittinen, Trends and challenges in the development of bio-based barrier coating materials for paper/cardboard food packaging; a review, Science of The Total Environment 851 (2022) 158328. https://doi.org/10.1016/j.scitotenv.2022.158328.

[13] J. Wang, M. Euring, K. Ostendorf, K. Zhang, Biobased materials for food packaging, Journal of Bioresources and Bioproducts 7 (2022) 1–13. https://doi.org/10.1016/j.jobab.2021.11.004.

[14] F. Baghi, A. Gharsallaoui, E. Dumas, S. Ghnimi, Advancements in Biodegradable Active Films for Food Packaging: Effects of Nano/Microcapsule Incorporation, Foods 11 (2022) 760. https://doi.org/10.3390/foods11050760.

[15] T. Huq, A. Khan, D. Brown, N. Dhayagude, Z. He, Y. Ni, Sources, production and commercial applications of fungal chitosan: A review, Journal of Bioresources and Bioproducts 7 (2022) 85–98. https://doi.org/10.1016/j.jobab.2022.01.002.

[16] A. Cavazza, M. Mattarozzi, A. Franzoni, M. Careri, A spotlight on analytical prospects in food allergens: From emerging allergens and novel foods to bioplastics and plant-based sustainable food contact materials, Food Chemistry 388 (2022) 132951. https://doi.org/10.1016/j.foodchem.2022.132951.

[17] M. Sardar, R. Agarwal, A. Kumar, M.N. Gupta, Noncovalent immobilization of enzymes on an enteric polymer Eudragit S-100, Enzyme and Microbial Technology 20 (1997) 361–367. https://doi.org/10.1016/S0141-0229(96)00152-4.

[18] G. Decher, Fuzzy Nanoassemblies: Toward Layered Polymeric Multicomposites, Science 277 (1997) 1232–1237.

[19] B.D. Ratner, Surface modification of polymers: chemical, biological and surface analytical challenges, Biosensors and Bioelectronics 10 (1995) 797–804. https://doi.org/10.1016/0956-5663(95)99218-A.

[20] C.-M. Chan, T.-M. Ko, H. Hiraoka, Polymer surface modification by plasmas and photons, Surface Science Reports 24 (1996) 1–54. https://doi.org/10.1016/0167-5729(96)80003-3.

[21] Radical Chain Polymerization, in: Principles of Polymerization, John Wiley & Sons, Ltd, 2004: pp. 198–349. https://doi.org/10.1002/047147875X.ch3.

[22] J. Fouassier, X. Allonas, J. Lalevée, C. Dietlin, Photoinitiators for Free Radical Polymerization Reactions, in: Photochemistry and Photophysics of Polymer Materials, 2010: pp. 351–419. https://doi.org/10.1002/9780470594179.ch10.

[23] S.G. Dunkirk, S.L. Gregg, L.W. Duran, J.D. Monfils, J.E. Haapala, J.A. Marcy, D.L. Clapper, R.A. Amos, P.E. Guire, Photochemical coatings for the prevention of bacterial colonization, J Biomater Appl 6 (1991) 131–156. https://doi.org/10.1177/088532829100600203.

[24] C. Carlini, L. Angiolini, Polymers as free radical photoinitiators, in: Synthesis and Photosynthesis, Springer, Berlin, Heidelberg, 1995: pp. 127–214. https://doi.org/10.1007/3-540-58908-2_4.

[25] B.D. Ratner, A.S. Hoffman, S.L. McArthur, 1.4.2 - Physicochemical Surface Modification of Materials Used in Medicine, in: W.R. Wagner, S.E. Sakiyama-Elbert, G. Zhang, M.J. Yaszemski (Eds.), Biomaterials Science (Fourth Edition), Academic Press, 2020: pp. 487–505. https://doi.org/10.1016/B978-0-12-816137-1.00033-7.

[26] M.E. Villanueva, J.A. González, E. Rodríguez-Castellón, S. Teves, G.J. Copello, Antimicrobial surface functionalization of PVC by a guanidine based antimicrobial polymer, Materials Science and Engineering: C 67 (2016) 214–220. https://doi.org/10.1016/j.msec.2016.05.052.

[27] E. Sánchez-López, D. Gomes, G. Esteruelas, L. Bonilla, A.L. Lopez-Machado, R. Galindo, A. Cano, M. Espina, M. Ettcheto, A. Camins, A.M. Silva, A. Durazzo, A. Santini, M.L. Garcia, E.B. Souto, Metal-Based Nanoparticles as Antimicrobial Agents: An Overview, Nanomaterials (Basel) 10 (2020) 292. https://doi.org/10.3390/nano10020292.

[28] V.T. Nguyen, V.T. Vu, T.H. Nguyen, T.A. Nguyen, V.K. Tran, P. Nguyen-Tri, Antibacterial Activity of TiO2- and ZnO-Decorated with Silver Nanoparticles, Journal of Composites Science 3 (2019) 61. https://doi.org/10.3390/jcs3020061.

[29] N. Cioffi, N. Ditaranto, L. Torsi, L. Sabbatini, Approaches to Synthesis and Characterization of Spherical and Anisotropic Copper Nanomaterials, in: Nanotechnologies for the Life Sciences, John Wiley & Sons, Ltd, 2010. https://doi.org/10.1002/9783527610419.ntls0123.

[30] S.H. Kamarudin, M. Rayung, F. Abu, S. Ahmad, F. Fadil, A.A. Karim, M.N. Norizan, N. Sarifuddin, M.S.Z. Mat Desa, M.S. Mohd Basri, H. Samsudin, L.C. Abdullah, A Review on Antimicrobial Packaging from Biodegradable Polymer Composites, Polymers (Basel) 14 (2022) 174. https://doi.org/10.3390/polym14010174.

[31] A. Sirelkhatim, S. Mahmud, A. Seeni, N.H.M. Kaus, L.C. Ann, S.K.M. Bakhori, H. Hasan, D. Mohamad, Review on Zinc Oxide Nanoparticles: Antibacterial Activity and Toxicity Mechanism, Nano-Micro Lett. 7 (2015) 219–242. https://doi.org/10.1007/s40820-015-0040-x.

[32] M.J. Hajipour, K.M. Fromm, A. Akbar Ashkarran, D. Jimenez de Aberasturi, I.R. de Larramendi, T. Rojo, V. Serpooshan, W.J. Parak, M. Mahmoudi, Antibacterial properties of nanoparticles, Trends in Biotechnology 30 (2012) 499–511. https://doi.org/10.1016/j.tibtech.2012.06.004.

[33] B. Niaz, F. Saeed, A. Ahmed, M. Imran, A.A. Maan, M.K.I. Khan, T. Tufail, F.M. Anjum, S. Hussain, H.A.R. Suleria, Lactoferrin (LF): a natural antimicrobial protein, International Journal of Food Properties 22 (2019) 1626–1641. https://doi.org/10.1080/10942912.2019.1666137.

[34] N. Nawaz, S. Wen, F. Wang, S. Nawaz, J. Raza, M. Iftikhar, M. Usman, Lysozyme and Its Application as Antibacterial Agent in Food Industry, Molecules 27 (2022) 6305. https://doi.org/10.3390/molecules27196305.

[35] M.K. Swamy, M.S. Akhtar, U.R. Sinniah, Antimicrobial Properties of Plant Essential Oils against Human Pathogens and Their Mode of Action: An Updated Review, Evid Based Complement Alternat Med 2016 (2016) 3012462. https://doi.org/10.1155/2016/3012462.

[36] O. Kukharenko, J.-F. Bardeau, I. Zaets, L. Ovcharenko, O. Tarasyuk, S. Porhyn, I. Mischenko, A. Vovk, S. Rogalsky, N. Kozyrovska, Promising low cost antimicrobial composite material based on bacterial cellulose and polyhexamethylene guanidine hydrochloride, European Polymer Journal 60 (2014) 247–254. https://doi.org/10.1016/j.eurpolymj.2014.09.014.

[37] T.N. Yudanova, I.F. Skokova, L.I. Gavrikova, L.S. Gal'braikh, Fabrication of textile materials with a combined biological effect, Fibre Chem 31 (1999) 90–94. https://doi.org/10.1007/BF02358629.

[38] H. Haghighi, S.K. Leugoue, F. Pfeifer, H.W. Siesler, F. Licciardello, P. Fava, A. Pulvirenti, Development of antimicrobial films based on chitosan-polyvinyl alcohol blend enriched with ethyl lauroyl arginate (LAE) for food packaging applications, Food Hydrocolloids 100 (2020) 105419. https://doi.org/10.1016/j.foodhyd.2019.105419.

[39] K. Odjo, Q.A. Al-Maqtari, H. Yu, Y. Xie, Y. Guo, M. Li, Y. Du, K. Liu, Y. Chen, W. Yao, Preparation and characterization of chitosan-based antimicrobial films containing encapsulated lemon essential oil by ionic gelation and cranberry juice, Food Chemistry 397 (2022) 133781. https://doi.org/10.1016/j.foodchem.2022.133781.

[40] T. Min, Z. Zhu, X. Sun, Z. Yuan, J. Zha, Y. Wen, Highly efficient antifogging and antibacterial food packaging film fabricated by novel quaternary ammonium chitosan composite, Food Chem 308 (2020) 125682. https://doi.org/10.1016/j.foodchem.2019.125682.

[41] A. Kumar Sinha, H.K. Narang, S. Bhattacharya, Evaluation of Bending Strength of Abaca Reinforced Polymer Composites, Materials Today: Proceedings 5 (2018) 7284–7288. https://doi.org/10.1016/j.matpr.2017.11.396.

[42] M.E. Villanueva, A. Salinas, J.A. González, S. Teves, G.J. Copello, Dual antibacterial effect of immobilized quaternary ammonium and aliphatic groups on PVC, New J. Chem. 39 (2015) 9200–9206. https://doi.org/10.1039/C5NJ01766A.

[43] S.S. Narasagoudr, V.G. Hegde, V.N. Vanjeri, R.B. Chougale, S.P. Masti, Ethyl vanillin incorporated chitosan/poly(vinyl alcohol) active films for food packaging applications, Carbohydrate Polymers 236 (2020) 116049. https://doi.org/10.1016/j.carbpol.2020.116049.

[44] E. Olewnik-Kruszkowska, M. Gierszewska, E. Jakubowska, I. Tarach, V. Sedlarik, M. Pummerova, Antibacterial Films Based on PVA and PVA-Chitosan Modified with Poly(Hexamethylene Guanidine), Polymers (Basel) 11 (2019) 2093. https://doi.org/10.3390/polym11122093.

[45] M.R. de Andrade, T.B.R. Nery, T.I. de Santana E Santana, I.L. Leal, L.A.P. Rodrigues, J.H. de Oliveira Reis, J.I. Druzian, B.A.S. Machado, Effect of Cellulose Nanocrystals from Different Lignocellulosic Residues to Chitosan/Glycerol Films, Polymers (Basel) 11 (2019) 658. https://doi.org/10.3390/polym11040658.

[46] M. Yu, R. Huang, C. He, Q. Wu, X. Zhao, Hybrid Composites from Wheat Straw, Inorganic Filler, and Recycled Polypropylene: Morphology and Mechanical and Thermal Expansion Performance, International Journal of Polymer Science 2016 (2016) e2520670. https://doi.org/10.1155/2016/2520670.

[47] M. Krepker, R. Shemesh, Y. Danin Poleg, Y. Kashi, A. Vaxman, E. Segal, Active food packaging films with synergistic antimicrobial activity, Food Control 76 (2017) 117–126. https://doi.org/10.1016/j.foodcont.2017.01.014.

[48] J. Ahmed, Y.A. Arfat, A. Bher, M. Mulla, H. Jacob, R. Auras, Active Chicken Meat Packaging Based on Polylactide Films and Bimetallic Ag-Cu Nanoparticles and Essential Oil, J Food Sci 83 (2018) 1299–1310. https://doi.org/10.1111/1750-3841.14121.

[49] J. Andrade-Del Olmo, L. Pérez-Álvarez, L. Ruiz-Rubio, J.L. Vilas-Vilela, Antibacterial chitosan electrostatic/covalent coating onto biodegradable poly (l-lactic acid), Food Hydrocolloids 105 (2020) 105835. https://doi.org/10.1016/j.foodhyd.2020.105835.

[50] P. Hili, C.S. Evans, R.G. Veness, Antimicrobial action of essential oils: the effect of dimethylsulphoxide on the activity of cinnamon oil, Lett Appl Microbiol 24 (1997) 269–275. https://doi.org/10.1046/j.1472-765x.1997.00073.x.

[51] F. Kong, Y.F. Hu, Biomolecule immobilization techniques for bioactive paper fabrication, Anal Bioanal Chem 403 (2012) 7–13. https://doi.org/10.1007/s00216-012-5821-1.

[52] D. Naumann, D. Helm, H. Labischinski, Microbiological characterizations by FT-IR spectroscopy, Nature 351 (1991) 81–82. https://doi.org/10.1038/351081a0.

[53] K. Kõrge, M. Bajić, B. Likozar, U. Novak, Active chitosan–chestnut extract films used for packaging and storage of fresh pasta, International Journal of Food Science & Technology 55 (2020) 3043–3052. https://doi.org/10.1111/ijfs.14569.

[54] F. Faghihzadeh, N.M. Anaya, L.A. Schifman, V. Oyanedel-Craver, Fourier transform infrared spectroscopy to assess molecular-level changes in microorganisms exposed to nanoparticles, Nanotechnol. Environ. Eng. 1 (2016) 1. https://doi.org/10.1007/s41204-016-0001-8.

[55] A. Durazzo, J. Kiefer, M. Lucarini, E. Camilli, S. Marconi, P. Gabrielli, A. Aguzzi, L. Gambelli, S. Lisciani, L. Marletta, Qualitative Analysis of Traditional Italian Dishes: FTIR Approach, Sustainability 10 (2018) 4112. https://doi.org/10.3390/su10114112.

[56] M. Lucarini, A. Durazzo, J. Sánchez del Pulgar, P. Gabrielli, G. Lombardi-Boccia, Determination of fatty acid content in meat and meat products: The FTIR-ATR approach, Food Chemistry 267 (2018) 223–230. https://doi.org/10.1016/j.foodchem.2017.11.042.

[57] I. Georgakopoulos-Soares, E.L. Papazoglou, P. Karmiris-Obratański, N.E. Karkalos, A.P. Markopoulos, Surface antibacterial properties enhanced through engineered textures and surface roughness: A review, Colloids and Surfaces B: Biointerfaces 231 (2023) 113584. https://doi.org/10.1016/j.colsurfb.2023.113584.

[58] C. Berne, A. Ducret, G.G. Hardy, Y.V. Brun, Adhesins Involved in Attachment to Abiotic Surfaces by Gram-Negative Bacteria, in: Microbial Biofilms, John Wiley & Sons, Ltd, 2015: pp. 163–199. https://doi.org/10.1128/9781555817466.ch9.

[59] A.T. Poortinga, R. Bos, W. Norde, H.J. Busscher, Electric double layer interactions in bacterial adhesion to surfaces, Surface Science Reports 47 (2002) 1–32. https://doi.org/10.1016/S0167-5729(02)00032-8.

[60] J. Sjollema, S.A.J. Zaat, V. Fontaine, M. Ramstedt, R. Luginbuehl, K. Thevissen, J. Li, H.C. van der Mei, H.J. Busscher, In vitro methods for the evaluation of antimicrobial surface designs, Acta Biomaterialia 70 (2018) 12–24. https://doi.org/10.1016/j.actbio.2018.02.001.

[61] K. Yang, J. Shi, L. Wang, Y. Chen, C. Liang, L. Yang, L.-N. Wang, Bacterial anti-adhesion surface design: Surface patterning, roughness and wettability: A review, Journal of Materials Science & Technology 99 (2022) 82–100. https://doi.org/10.1016/j.jmst.2021.05.028.

[62] A. Lu, Y. Gao, T. Jin, X. Luo, Q. Zeng, Z. Shang, Effects of surface roughness and texture on the bacterial adhesion on the bearing surface of bio-ceramic joint implants: An in vitro study, Ceramics International 46 (2020) 6550–6559. https://doi.org/10.1016/j.ceramint.2019.11.139.

[63] O. Seddiki, C. Harnagea, L. Levesque, D. Mantovani, F. Rosei, Evidence of antibacterial activity on titanium surfaces through nanotextures, Applied Surface Science 308 (2014) 275–284. https://doi.org/10.1016/j.apsusc.2014.04.155.

[64] T. Wassmann, S. Kreis, M. Behr, R. Buergers, The influence of surface texture and wettability on initial bacterial adhesion on titanium and zirconium oxide dental implants, Int J Implant Dent 3 (2017) 32. https://doi.org/10.1186/s40729-017-0093-3.

[65] S.Y. Choi, O. Habimana, P. Flood, E.G. Reynaud, B.J. Rodriguez, N. Zhang, E. Casey, M.D. Gilchrist, Material- and feature-dependent effects on cell adhesion to micro injection moulded medical polymers, Colloids and Surfaces B: Biointerfaces 145 (2016) 46–54. https://doi.org/10.1016/j.colsurfb.2016.04.032.

[66] M. Katsikogianni, Y.F. Missirlis, Concise review of mechanisms of bacterial adhesion to biomaterials and of techniques used in estimating bacteria-material interactions, Eur Cell Mater 8 (2004) 37–57. https://doi.org/10.22203/ecm.v008a05.

[67] E. Vanhaecke, J.P. Remon, M. Moors, F. Raes, D. De Rudder, A. Van Peteghem, Kinetics of Pseudomonas aeruginosa adhesion to 304 and 316-L stainless steel: role of cell surface hydrophobicity, Applied and Environmental Microbiology 56 (1990) 788–795. https://doi.org/10.1128/aem.56.3.788-795.1990.

[68] M. Qi, X. Gong, B. Wu, G. Zhang, Landing Dynamics of Swimming Bacteria on a Polymeric Surface: Effect of Surface Properties, Langmuir 33 (2017) 3525–3533. https://doi.org/10.1021/acs.langmuir.7b00439.

[69] O. Bazaka, K. Bazaka, V.K. Truong, I. Levchenko, M.V. Jacob, Y. Estrin, R. Lapovok, B. Chichkov, E. Fadeeva, P. Kingshott, R.J. Crawford, E.P. Ivanova, Effect of titanium surface topography on plasma deposition of antibacterial polymer coatings, Applied Surface Science 521 (2020) 146375. https://doi.org/10.1016/j.apsusc.2020.146375.

[70] Q. Pan, Y. Cao, W. Xue, D. Zhu, W. Liu, Picosecond Laser-Textured Stainless Steel Superhydrophobic Surface with an Antibacterial Adhesion Property, Langmuir 35 (2019) 11414–11421. https://doi.org/10.1021/acs.langmuir.9b01333.

[71] J. Lin, X. Cai, Z. Liu, N. Liu, M. Xie, B. Zhou, H. Wang, Z. Guo, Anti-liquid-Interfering and Bacterially Antiadhesive Strategy for Highly Stretchable and Ultrasensitive Strain Sensors Based on Cassie-Baxter Wetting State, Advanced Functional Materials 30 (2020) 2000398. https://doi.org/10.1002/adfm.202000398."

# Chapter 3 Characterization Techniques

This chapter briefly describes the principle of the techniques exploited in this thesis. First the surface characterization techniques will be presented: X-ray photoelectron spectroscopy (XPS) and Angle-resolved XPS, attenuated total reflection Fourier transform infrared spectroscopy (ATR FT-IR spectroscopy) and atomic force microscopy (AFM). A paragraph will briefly treat the water contact angle measurements and another one will be dedicated to scanning electron microscopy.

Then the bulk characterization techniques: Fourier transform infrared spectroscopy (FT-IR), nuclear magnetic resonance (NMR), and ultraviolet – visible spectroscopy (UV-Vis), will be outlined since they were used for the characterization of the products synthesized in this work.

Chapter 8 presents the microbiological tests and the procedures used in this thesis.

The detailed measurement procedures are provided in the experimental part of the individual chapters.

## 3.1 X-ray Photoelectron Spectroscopy (XPS) and Angle-Resolved XPS (ARXPS)

### 3.1.1 Basic principles

X-ray photoelectron spectroscopy (XPS) is a surface-sensitive analytical technique since the detected photoelectron are coming from few nanometres of a solid under investigation, usually less than 10nm for the kinetic energies used in laboratory experiments. It allows the identification of the elements, except hydrogen and helium; it is used for investigating the chemical environments of the elements (speciation) and it can provide the quantitative composition of the outer layer of the material. XPS is based on the photoelectric effect [1–4], which involves the ejection of an electron from a core level when interacts with an X-ray photon: This occurs when the energy of the photon ($h\nu$) has a frequency, n, which is larger than the threshold frequency of the electron in the atom. Atoms contain electrons that have quantized energies, resulting in the emission of electrons with unique kinetic energy values for each atom. When an X-ray photon with appropriate energy ($h\nu$) is absorbed by an electron, it is emitted from its energy level. In an XPS experiment, the kinetic energy (KE) of the photoemitted electrons is measured by the analyser spectrometer, which produces a spectrum of electron intensity (number of electrons at a given energy) as a function of energy.

The kinetic energy of the photoelectrons is dependent on the energy of the X-ray source ($h\nu$) and it is not an intrinsic material property. Therefore, XPS spectra report the signal intensity versus the binding energy of the photoelectrons. The binding energy of a photoemitted electron (BE), as per the definition provided by ISO 18115-1:2013, represents the energy required to remove an electron from a specific electronic level to the Fermi level of a solid or to the vacuum level of a free atom or molecule. This parameter depends on the emitting atom and its chemical state. The relation between kinetic energy (KE) and binding energy (BE) for a conductive sample in electrical contact with the spectrometer is:

$$BE^F = E_f - E_i = h\nu - KE - \phi_{spect.} \qquad 3.1$$

Where $BE^F$ is the binding energy relative to the Fermi level of the sample, Ef and Ei are the final energy and the initial energy state of the atom before and after the photoemission, respectively, $h\nu$ is the photon energy, and $\phi_{spect.}$ is the spectrometer work function, that is experimentally determined during the calibration of the spectrometer; since $h\nu$ and $\phi_{spect}$ are known, KE is measured, $BE^F$ can be easily calculated.

The Fermi level of a conductive grounded sample is aligned according to the diagram shown in Figure 3.1. The kinetic energy of the photoelectrons leaving the sample ($KE_1$) is:

$$KE_1 = h\nu - BE^F - \phi_s \qquad 3.2$$

where $\phi_s$ represents the sample work function. The kinetic energy of the photoelectrons reaching the detector, thus the quantity measured by the instrument ($KE_2$) is:

$$KE_2 = h\nu - BE^F - \phi_s - (\phi_{spect} - \phi_s) = h\nu - BE^F - \phi_{spect} \qquad 3.3$$

and it is independent on the work function of the sample. Thus, for conductive samples it is possible to establish an absolute BE scale that is independent on the properties of the sample itself.

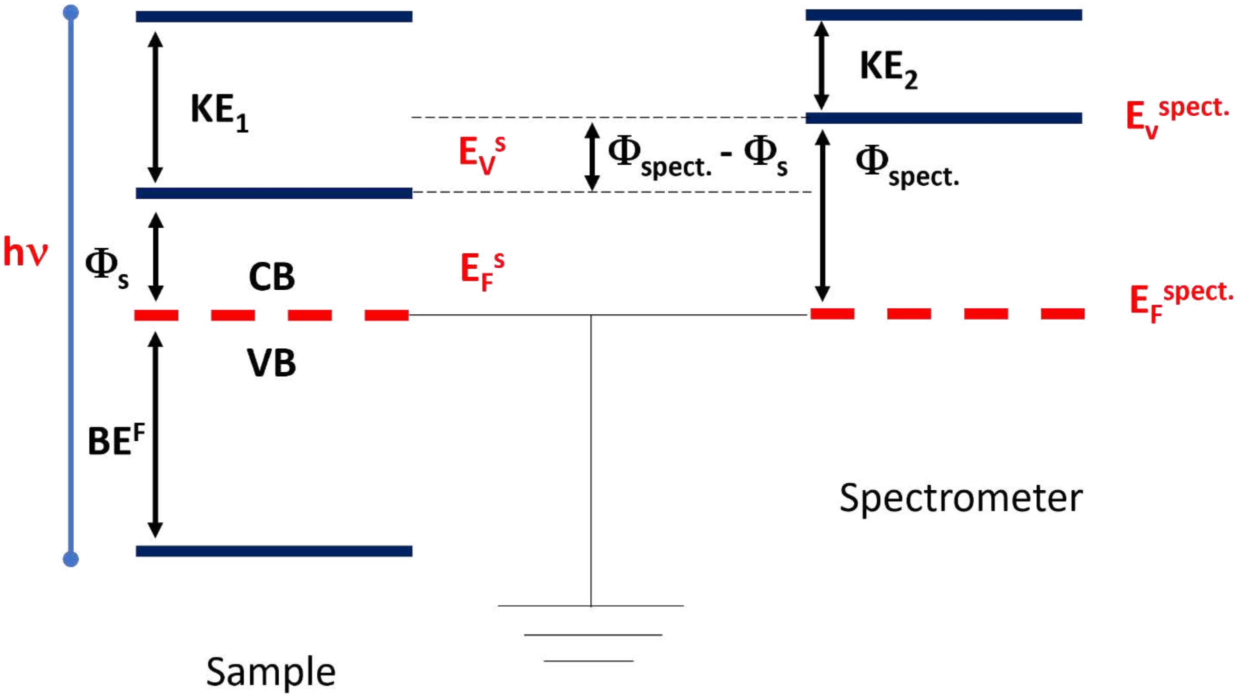

*Figure 3.1: Diagram of the energy levels in conductive samples during an XPS experiment. hν: radiation energy; KE$_1$: kinetic energy of the photoemitted electron; KE$_2$: kinetic energy of the detected electron; VB: valence band; CB: conduction band; $E_F^s$: sample Fermi level; $E_F^{spect}$: spectrometer Fermi level; $E_V^s$: sample vacuum level; $E_V^{spect}$: spectrometer vacuum level; $\phi_s$: sample work function; $\phi_{spect}$ : spectrometer work function. This picture it has been adapted from [4]*

On the contrary, in the case of an insulator, the Fermi level of the sample and of the spectrometer are not aligned and a neutralization is necessary for compensating the sample charging. The neutralization is accomplished using a low energy electron source combined with low energy ions, usually argon ions. The kinetic energy measured by the spectrometer in the case of insulating samples is $KE=h\nu-BE^F-\phi_s+E_e$, where $E_e$ is the effective energy of the flooding electrons relative to the instrument Fermi level. [3] For insulators, even if $E_e$ is known, the binding energy cannot be absolutely determined if the sample work function is not known.

Figure 3.2 schematizes the electron photoemission process that is possible if the energy of the incident photon is greater than the BE of the electron.

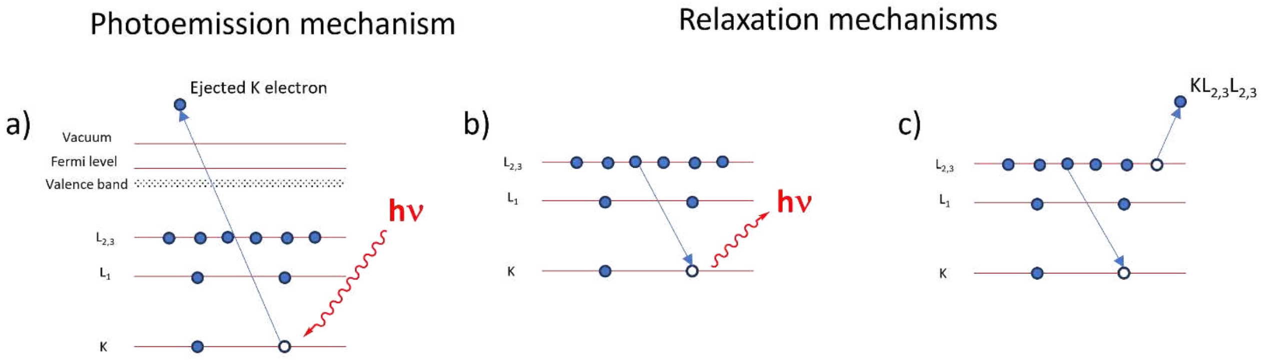

*Figure 3.2 Scheme of the photoemission process (a); scheme of the relaxation process following the photoemission of the electron (a,b): a) X-Ray fluorescence, b) Auger secondary electron emission. Picture adapted from [2]*

The photoemission of the electron generates a vacancy (Figure 3.2a). This excited ionized state will relax by filling the hole with an electron from a higher energy level. Two competitive mechanisms can occur: X-ray fluorescence emission or emission of an Auger secondary electron (Figure 3.2b-3.2c). The Auger emission is the dominant relaxation process for element with low atomic number, increasing the atomic number X-ray fluorescence becomes the most probable relaxation mechanism.

Upon X-ray fluorescence, no emission of electrons occurs. Thus, X-ray fluorescence does not contribute to the XP spectra. As far as the Auger emission, a secondary electron is emitted with a kinetic energy equal to the difference between the energy levels involved in the transition. Auger electrons are detected in a X-ray photoelectron spectrum and contribute with various signals to the spectrum, providing the so-called X-ray induced Auger electron spectra (XAES).

The XPS peak intensity, $I_{A_{q,m}}$, (peak area in cps*eV) is correlated to the volume density of atoms of the $i^{th}$ species through a fundamental equation (3.4). This equation takes into account several factors such as the element A that emitted the electrons from an orbital q, excited by a radiation m, geometrical factors like the analysed area and the solid angle of acceptance of the analyser, instrumental factors as the X-ray flux on the sample at the characteristic energy and matrix factors like the photoionization cross-section, $\sigma_{Aq,m}$, (in barns) [7] the asymmetry factor also known as Reilman factor [5], and the inelastic mean free path ($\lambda_{Aq,m}$) [6]. The equation can be written as follows:

$$I_{A_{q,m}} = \frac{g_{Aq,m} \cdot \sigma_{Aq,m} \cdot C_A \rho_m \Lambda_{Aq,m} \cdot \left[1 - e^{-\frac{t}{\Lambda_{Aq,m}}}\right] e^{-\frac{l_C}{\Lambda_{Aq,m}}}}{M_A} \qquad 3.4$$

This under the assumptions that the sample is homogeneous, smooth on an atomic scale, amorphous or polycrystalline to avoid diffraction effects. $\sigma$ values depend also on the X-ray source, but minor differences can be observed for the two most common sources exploited in laboratory (Al K$\alpha$ and Mg K$\alpha$).

XPS sampling depth varies with the kinetic energy of the electrons, and it is determined by the attenuation length ($\Lambda$). According to ISO 18115-1:2023, the effective attenuation length is defined as a "*parameter which, when introduced in place of the inelastic mean free path into an expression derived for AES and XPS on the assumption that elastic scattering effects are negligible for a given quantitative application, corrects that expression for elastic scattering effects*". The inelastic mean free path, IMFP (l), is defined as the "*average distance that an electron with a given energy travels between successive inelastic collisions*" [7]. The same International Standard further provides the definition of emission angle $\theta$ as "*angle between the trajectory of a particle or photon as it leaves a surface (3.2), and the local or average surface normal"*; The formula, which correlates the attenuation length to the effective attenuation length or inelastic mean free path, is:

$$\Lambda = \lambda cos\theta \qquad 3.5$$

As reported in note 2 of ISO 18115: 2023 entry number 12.45 "For emission angles of up to about 60° (with respect to the surface normal), it is often satisfactory to use a single value of this parameter".

Equation 3.6 describes the intensity of the photoelectron signal measured as a function of the depth z assuming that only inelastic scattering is contributing to electron attenuation:

$$I_z = I_0 e^{\frac{-z}{\lambda cos\theta}} \qquad 3.6$$

$I_0$ is defined as the peak intensity originated from the depth z while $\lambda$ is the inelastic mean free path and $\theta$ is the emission. The sampling depth is estimated to be given by: d=3$\lambda$cos$\theta$.

In 1979 Seah and Dench proposed a semi- empirical approach to calculate the IMFP [6] and proposed the following equation:

$$\lambda = \left(\frac{A}{KE^2}\right) + B\sqrt{KE} \quad 3.7$$

In this equation A and B represents two empirical parameters that depends on the type of material, while KE is the kinetic energy. Table 3.1 shows the values for A and B:

*Table 3.2 Tables of the A and B value for equation 3.7*

| | A | B |
|---|---|---|
| Element | 143 | 0.054 |
| Organic compounds | 31 | 0.087 |
| Inorganic compounds | 641 | 0.096 |

More recently Tanuma Powell and Penn proposed predictive formula for estimating the IMFP in a solid which is considered the most reliable since parameters like the density of the material (g/cm$^3$), the number of valence electrons and the energy band gap are taken into account [8–10]. The use of this approach is limited by the fact that sometimes the sample surface has not a defined stoichiometry and thus Seah and Dench semi-empirical approach is preferred. In this work the semi-empirical approach is applied.

XPS information are obtained within the sampling depth, which is defined as the specimen thickness, measured normal to the surface, from which a specified percentage (~ 95%) of the detected signal originates[7].

### 3.1.2 Spectral interpretation

*The survey spectrum*

XPS is used to determine the elemental composition of a sample surface and assess the absence of contaminants. This is achieved by identifying the signals present in the survey spectrum, also known as the wide spectrum, recorded between 0 and 1250 eV when the X-ray source is MgK$\alpha$, or up to 1400 eV when the source is AlK$\alpha$. Peak identification is performed by comparing the experimental binding energy with the reference tables and /or using an electronic database [11,12]. The survey spectrum consists of photoelectron and Auger signals. The height of the photoelectron signals depends on the element's concentration and, within other parameters, on the photoionization cross section [7] as described above. However, it should be noticed that the aforementioned statement is only partially true when dealing with a sample containing more than one element.

### *High-resolution spectra*

High-resolution spectra, also known as narrow-scan or detailed spectra, are acquired for the elements of interest detected in the survey spectrum. The high-resolution spectra can provide information on the chemical state of the elements present on the sample surface; peak areas are used for the quantification. Often these spectra contain more than one photoelectron signal and if the energy resolution adopted in the experimental is not high enough, they are multicomponent in character. Separation of the overlapping signal is usually done by curve-fitting.

### *Curve -fitting of high-resolution spectrum*

Data processing starts from the visual inspection of the high-resolution spectra: the presence of signals with more than one maximum and the presence of shoulders or asymmetry together with a full width at half maximum wider than 15% of the width determined on reference (pure) compounds is considered an indication of the presence of multiple photoelectron signals [14,15]. The first step of the curve fitting procedure consists in using model functions that generates a synthetic signal with the aim of simulating the experimental photoelectron signal. The model functions are derived from the signals obtained analysing reference standard elements and/or compounds using the same experimental settings used for the analysis of the real sample. Typical model curves are symmetric mixed Gaussian /Lorentzian that can be used for the fit of C1s signals originated from polymers. Graphitic materials show C1s signals with an asymmetry is detected towards high binding energy values. In this case, one can use a Voigt function, which is a convolution of a Gaussian and a Lorentzian function to which an exponential tail function is added. Other line shapes available in CasaXPS are asymmetric Lorentzian (LA) ad finite Lorentzian (LF). A very useful comparison of the various line shapes including Doniach-Sunich (DS) most used in the past is provided in [15].

The curve fitting procedure provide information on the line shape of the signal, its width (FWHM height) and on the binding energy values of the various components together with the peak areas. The binding energy of the photoelectrons are characteristic for the element and for the orbital. The measurement of the binding energy value allows in the most common situation the element identification. Depending on the nature of the chemical bonds in which the atom is involved, the binding energy of the electrons may vary. This results in a shift of the photoelectron signal, which is known as chemical shift. Therefore, more information on the surface chemistry of a sample can be obtained. Considering the initial state effects i.e. changes in core potential due to local environment alterations and the final state effects (e.g. relaxation following the photoemission) the chemical shift, ΔBE, can be expressed as:

$$\Delta BE = \Delta V + \Delta \phi - \Delta R \quad 3.8$$

In this equation ΔV represents the change in the ground state core potential, ΔR is the change in relaxation energy, Δϕ indicates the change of the reference potential. Relaxation energy ($\Delta R$) contribution originates from intra-atomic and extra-atomic relaxations. Intra-atomic relaxation refers to the rearrangement of the outer shell electrons with smaller BE than the photoemitted electron, while contribution of inner shell electron rearrangement is negligible. The nature of extra-atomic relaxation varies with the material analysed. In conducting samples like metals, valence band electrons screen the core hole as they move between atoms. In ionic solids like alkali halides, electrons undergo polarization due to the core hole's presence, constrained by their limited mobility among atoms [4].

Peaks originating from orbitals with l > 0 (p, d, f orbitals) result in a doublet due to spin-orbit coupling. This splitting results from the interaction between spin angular momentum (s = ± ½) and orbital angular momentum (l). The relative intensity of these peaks depends on their respective degeneracies, with their area ratio corresponding to the ratio of their multiplicity. The binding energy difference between the doublet components is determined by the spin-orbit coupling constant $J_{nl}$, which depends on the expectation value $<1/r^3>$ of the orbital involved, where r is the average radius [16].

Electronic rearrangement effects following the photoemission process give rise to shake-up and shake-off satellites. In the case of shake-up satellites, a valence electron is excited to a higher energy level because of the energy relaxation of the core-hole level. Conversely, shake-off satellites occur when photoionization is succeeded by the excitation of an electron.

XPS not only offers qualitative insights into the surface's chemical composition but also serves as a quantitative technique.

The quantitative analysis by XPS relies on the peak areas under the assumption that only elastically scattered photoelectrons contributed to the signal. It is thus necessary to remove or to take into account the inelastically scattered electrons, which contribute to the background. Different background subtraction models are available in commercial software: a very useful summary is provided in [17], which gives a comprehensive overview on this topic. In the present thesis various background subtraction models were considered and the application of U3-Tougaard iterative resulted to be the most suited for processing the carbon and the oxygen photoelectron spectra [18].

Quantitative analysis to calculate the surface composition started with the experimental areas corrected for relative sensitivity factors that take into account the Scofield photoionization cross-section [19], the angular asymmetry factor of the photoemission from each atom [19], and the electron inelastic mean free path (IMFP, in nm) of the emitted electrons in the matrix M calculated according to Seah and Dench [6], using the following equation:

$$X_A = \frac{\frac{I_A}{S_A}}{\sum_{i=1}^{n} \frac{I_n}{S_n}}$$

Where XA is the atomic fraction of the species A, IA the intensity (area) of the photoelectron signal and SA is the relative sensitivity factor.

Furthermore, XPS allows the estimation of layer thickness, making it highly valuable for investigating thin films. Various methods, including angle-resolved analysis (ARXPS), depth profiling, and the three-layers model, exist for estimating both the thickness and composition of thin films.

*The spectrometer*

The XPS spectrometer [3] is composed of an X-ray source, a sample stage, a lens system, an analyser, and a detector, all housed in an ultra-high vacuum environment. The most commonly used X-ray sources in XPS spectrometers include Al Kα (1486.6 eV) and Mg Kα (1253.6 eV). The analyser discriminates ejected electrons based on their kinetic energy (KE), and the detector counts the number of emitted photoelectrons at a specific KE. Two essential accessories are the electron flood source, utilized for charge compensation in insulating samples when employing a monochromatic source, and the ion source (typically $Ar^+$ ion), employed for removing contaminants from sample surfaces, such as organic contamination layers, through sputtering. This source can also perform sputtering depth-profile analysis.

*Angle-resolved X-ray photoelectron spectroscopy (ARXPS)*

Angle-resolved XPS [2,3], also known as angle-dependent XPS or ADXPS, is a method enabling the determination of thin film thickness and identification of in-depth homogeneity or non-homogeneity in the uppermost layers of samples. ARXPS offers several advantages, with the two most significant being:

- Non-destructive analysis: The rate of damage is typically sufficiently slow, allowing the acquisition of chemical state information from the outermost surface more easily than depth profiling methods involving sputtering.
- Good absolute depth resolution.

A limitation is that the thickness of the analysed layers cannot exceed two or three times the attenuation length (approx. 4-6 nm), as a substrate signal is necessary to estimate film thickness. For thicker layers, the substrate peak is often too small for accurate measurement. The intensity of the photoelectron signal, measured as a function of depth (d), is described by the equation:

$$I = I_0 e^{-d/\lambda cos\theta} \quad 3.9$$

Where $I_0$ is the peak intensity originating from depth d, $\theta$ is the emission angle and $\lambda$ is the inelastic mean free path of the photoelectron. Taking into account a thin layer (thickness d) of material A on a substrate B and integrating equation 3.9 between 0 and d the following equation is obtained:

$$I_A = I_A^{\infty} \left[\left(1 - e^{-\frac{d}{(\lambda_{A,A} cos\theta)}}\right)\right] \quad 3.10$$

Where $I_A$ is the measured intensity of the photoelectron signal from element A in a specific chemical state and from a specific transition. $I_A^{\infty}$ is the intensity of the photoelectron signal from element A in a specific chemical state and from a specific transition from a thick layer of material A. $\lambda_{A,A}$ is the inelastic mean free-path for a photoelectron emitted in a layer A for electrons emitted from A. $\theta$ is the emission angle.

The signal from B arriving at the B-A interface is $I_B^{\infty}$, assuming that layer B is thick compared to $\lambda_{B,B}$, this signal is attenuated by passing through the layer A:

$$I_B = I_B^{\infty} \left[\left(1 - e^{-\frac{d}{\lambda_{B,A} cos\theta}}\right)\right] \quad 3.11$$

Where $\lambda_{B,A}$ represents the IMFP of the electrons emitted from B and passing through A. The intensity ratio indicated by R is given by:

$$R = \frac{I_A}{I_B} = R_\infty \frac{\left[\left(1-e^{-\frac{d}{(\lambda_{A,A}cos\theta)}}\right)\right]}{\left[\left(1-e^{-\frac{d}{\lambda_{B,A}cos\theta}}\right)\right]} \quad 3.12$$

$R_\infty$ is the ratio between $I_A^\infty$ e $I_B^\infty$ and can be calculated considering the atom number density (atoms per unit volume) and the IMFP of the two materials. The atom number density $\sigma$ is given by ratio of the density D of the material, and the formula weight F. $R_\infty$ is given by:

$$R_\infty = \frac{\sigma_{B,A}\lambda_{B,A}}{\sigma_{B,B}\lambda_{B,B}} = \left(\frac{D_A F_B}{D_B F_A}\right)\left(\frac{\lambda_{B,A}}{\lambda_{A,A}}\right) \quad 3.13$$

Assuming $I_{A,A} = I_{B,A} = I_A$ equation 3.14 can be rearranged, and taking the natural logarithm allows for the calculation of the equivalent thickness of an overlayer (d) using Hill equation [20]:

$$d = \lambda cos\theta \; ln\left(1 + \frac{R}{R_\infty}\right) \quad 3.14$$

This approach can be applied to data recorded at one angle, assuming the attenuation of the substrate from a discrete overlayer. A more rigorous approach to obtain the thickness of an overlayer is to perform an ARXPS experiment at different emission angles and plot ln $(1+R/R_\infty)$ versus $1/cos\theta$: a straight line is obtained, and its slope is equal to $d/\lambda_A$.

It is crucial to emphasize that the methods presented for thickness estimation by ARXPS are applicable only under the assumption that $\lambda_{A,A} = \lambda_{B,A} = \lambda_A$ meaning that the difference in the binding energy of signals from the substrate and the film is negligible.

Elastic scattering affects ARXPS measurements: at emission angles higher than 60 degrees more intensity from the substrate than expected is observed (often exceeding 50%). This effect can be mitigated considering the emission angles $\theta<63°$ [21]. At small emission angles, near the surface normal, less intensity from the substrate is observed than expected. This effect is small typically 5-10%, depending on the material, and is minimized at about $\theta=45°$.

*Roughness effects*

Samples analysed by XPS should be ideally flat: this means that the structure sizes should be in the range of (or below) the attenuation length of the measured photoelectrons i.e. the surface roughness values should be in the order of few Å. In this work the XPS spectra were acquired on food-grade PVC and for comparison also on gold surfaces having measured in this case a roughness, Rq value, lower than 0.4 nm. These samples were obtained through a template – stripping method [22]. In her Ph.D. thesis Passiu has presented the XPS results obtained on gold surfaces with surface roughness, going from ultraflat (Rq < 0.4 nm) to measured roughness higher than 1 nm [23].

This topic was object of various investigations: Gunter et al. [24] reported that thickness of an overlayer on a rough substrate can be determined without taking the roughness into account if the spectra are collected at an emission angle of between 35° and 45°, sometimes called the roughness magic angle [25].

In the case of rough surfaces, the peak intensity of the overlayer is higher than it would be for atomically flat surfaces; at high emission angles, when the technique becomes more surface sensitive, lower intensities are collected for the overlayer signals of rough surface than those for flat ones.

XPS intensities, neglecting roughness effects results in an average estimated error less than 10% in the determined thickness [26].

*Advantages and Disadvantages of XPS analysis of Polymers*

X-ray photoelectron spectroscopy can be successfully utilized for determining the surface composition of polymer materials. It not only identifies the elements present on the surface, but it also provides information on the chemical state of the carbon and oxygen in various functional groups. This identification is performed using reference materials, even if it has to be emphasised that not always pure polymers are commercially available. The technique is particularly effective for homogeneous samples, and it can be used in angular resolved mode to track stratification processes in multicomponent systems.

However, there are some disadvantages to this technique, such as the requirement of ultra-high vacuum, the sample's sensitivity to degradation due to X-ray and electron interaction, and the need for an ideally flat surface. To minimize changes in the polymer analysis, it is necessary to reduce the acquisition time and find a compromise between measuring time and signal-to-noise ratio.

## 3.2 Attenuated total reflection – Fourier transform infrared spectroscopy

Attenuated total reflection Fourier Transform infrared (ATR-FTIR) spectroscopy has emerged as a versatile and powerful analytical technique in characterizing the surface of a wide range of materials using electromagnetic radiation in the infrared region. The technique is based on the phenomenon of total internal reflection analysis, which was first discovered by Isaac Newton in the 17th century. However, it was only in the 1960s that Fahrenfort [1961] and Harrick [1967] described the ATR technique and applied this phenomenon for obtaining absorption spectra.

This analytical technique combines the principle of Fourier Transform infrared spectroscopy (FTIR) and attenuated total reflection (ATR) to investigate the molecular composition of the samples. The infrared radiation propagates in the total internal reflection element (ATR crystal) and undergoes total reflection at the interface between the denser medium (ATR crystal) and the rarer one (the sample under investigation). The two media have different refractive indexes and at the interface an electromagnetic wave decays exponentially and penetrates into the rarer medium. This wave is known as “evanescent wave”. More in detail, when an infrared radiation (ranging from 7800 and 350 $cm^{-1}$ in the case of a ceramic source) passes through the crystal and interacts with the sample, it undergoes multiple internal reflection, thus enhancing the sensitivity and enabling the detection of even trace amount of analyte. ATR-FTIR allows the investigation of a large range of materials that cannot be easily studied by means of FT-IR spectroscopy due to their opacity. Moreover, this technique is useful in this work since it is exploited for characterising food-grade polyvinyl chloride (PVC) before and after functionalization with nanometre thick layers. This is a molecular spectroscopy that operates in air and can provide useful information, complementary to those obtained by XPS, on the molecular structure of the sample. The penetration depth can be estimated using Harrick’s equation [27]:

$$d_p = \frac{1}{\gamma} = \frac{\lambda_1}{2\pi n_1 \sqrt{sin^2\varphi - n_{21}^2}}$$

where $\lambda_1$ is the wavelength (in the denser medium), while $n_{21}$ is the ratio between the refractive index of the rarer medium (PVC in this work) and the refractive index of the denser phase ($n_{1,diamond}$ = 2.4)($n_{21} = \frac{n_2}{n_1} = 2.4/1.46$) [28].

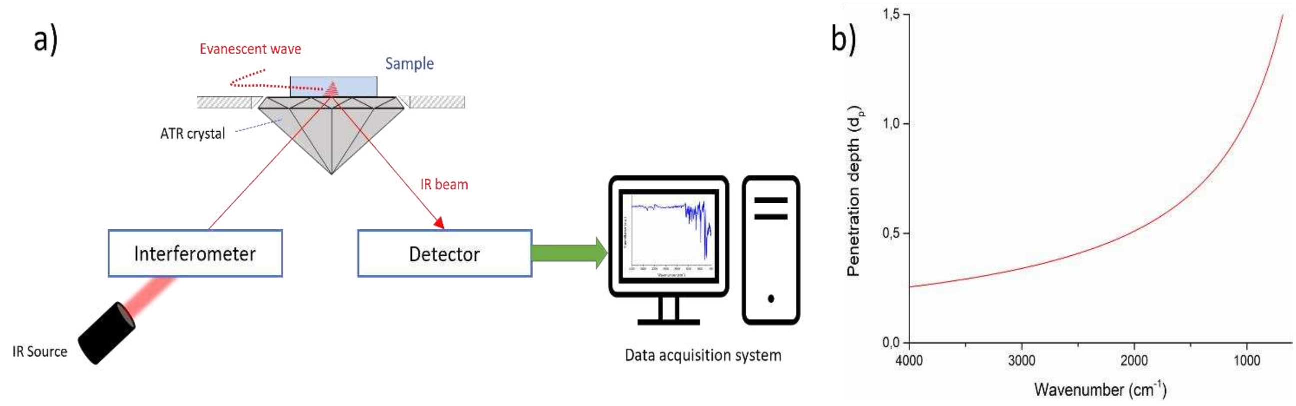

*Figure 3.3 a) Schematic representation of the ATR-FTIR Spectrometer Figure adapted from [29] . b) Penetration depth (nm) in function of the wavenumber (cm-1)*

The scheme of an ATR-FTIR spectrometer is shown in Figure 3.3. It includes an infrared radiation source, an ATR crystal and a detector. The infrared source emits radiation in the infrared range frequencies, and the type of source depends on the instrument used; the most common sources are the ceramic ones, which emit in the range from 7800 to 350 $cm^{-1}$. Typically, the analysed region in ATR-FTIR spectroscopy is 4000-400 $cm^{-1}$. The most common ATR crystal is a diamond one and serves as the interface between the sample and the infrared beam, while the detector measures the intensity of the reflected infrared radiation. ATR-FTIR spectroscopy results are reported as a plot of transmittance (T%) versus wavenumber ($cm^{-1}$) and involves scanning the infrared spectrum over a predefined range of frequencies while monitoring the intensity of the reflected light expressed in terms of transmittance.

Peak identification consists of assigning specific absorption bands in the spectrum to corresponding molecular vibration of specific functional groups present in the samples. The absorption frequencies are determined by the specific vibrational modes of the molecular bonds. By comparing the experimental spectra of a sample with the spectra of known compounds reported in the literature it can be possible to assign the bands based on similarities in band position and shape. Spectral interpretation by peak identification is not straightforward, since the band position and intensities are affected by different factors such as bond strength, bond length, molecular symmetry and samples complexity, moreover spectral overlap can be observed.

## 3.3 Atomic Force Microscopy (AFM)

Atomic Force Microscopy (AFM) was first introduced in 1985 by Binnig, Quate and Gerber [30] as a scanning-probe technique. It is used to map the surface topography of a sample with sub-nanometric resolution, and to measure surface properties like adhesion and friction. The AFM works by using a sharp tip, which is attached to the free end of a cantilever, which is brought into proximity of the sample surface. Piezoelectric elements allow scanning over the surface. The cantilever deflects due to the forces acting between the tip and the sample. On the back of the cantilever there is a small reflectance device, and it reflects a laser beam that is detected by a four-quadrant photodiode allowing distinguishing within normal and lateral deflections and the measurement of the deflection. In figure 3.4 a schematic representation of the AFM is shown.

AFM can operate in different modes; the two most common ones are the contact mode and the tapping mode. The tapping mode is useful when analysing soft samples, such as polymeric films, because of the short contact time and reduced lateral forces that reduce the damage of the tip and the sample. In this mode, the tip oscillates close to its resonance frequency, and lightly taps the surface while scanning. The resonance frequency, f, depends on its stiffness, k, and on the effective mass, $m_{eff}$, and it is given by the formula:

$$f = \frac{1}{2\pi} \cdot \sqrt{\frac{k}{m_{eff}}} \qquad 3.15$$

k is a constant and depends on the mechanical properties of the material (Young's module) and on geometry. The calibration of the cantilever and the tip is needed for accurate measurements [31]. The oscillation amplitude of the cantilever is kept constant by adjusting the distance between the tip and the sample surface during the scan. This variation in height is measured to obtain topographical information, as the force influences the oscillation amplitude of the cantilever.

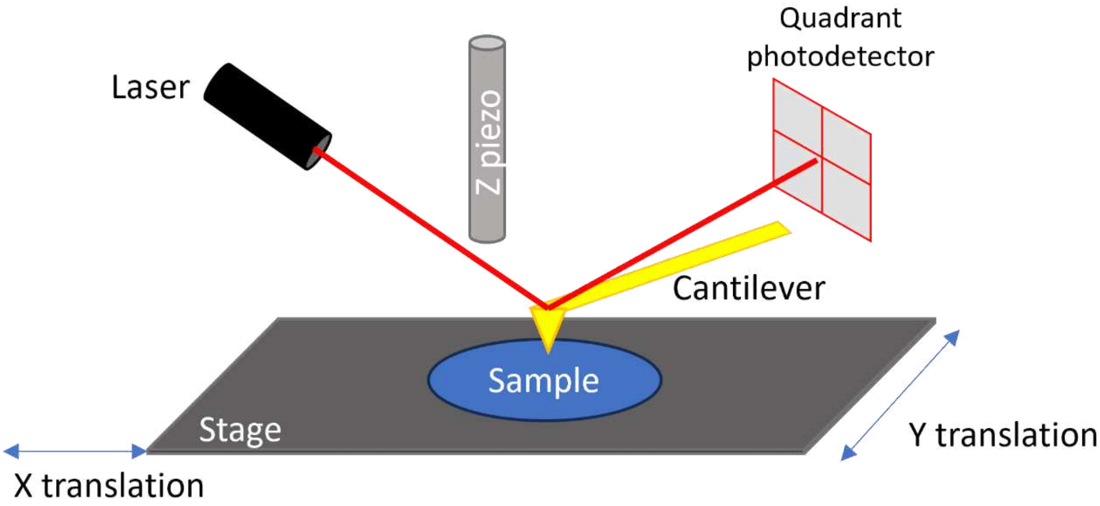

*Figure 3.4 AFM general scheme*

AFM offers the advantage of operating in ambient air and does not require vacuum conditions or special sample preparation. It can analyse both insulating and conductive samples- and its capability to map the phase of oscillation relative to the driving signal provides valuable information about the adhesion and sample stiffness variation across the scanned area. Unlike many microscopic techniques, AFM measurements are not limited by diffraction, allowing a sub-nanometre resolution in the vertical direction. However, the lateral resolution is constrained by the tip size, which is typically a few nanometres.

It should be noted that the AFM technique has some limitations, such as long acquisition times and limited scan areas (15µm). Additionally, some artifacts may be detected in the final images due to the

The finite size of the tip, its deterioration and of the possibility of picking up contamination from the sample surface (e.g. dust). Despite these drawbacks, AFM is widely used in the literature for the acquisition of surface information on polymeric surface, mainly it is exploited for calculate the roughness of the samples [32]. It can also be used to monitor the surface roughness of the samples after their functionalization.

Different approaches to estimate the roughness of the samples can be exploited. The mean roughness ($R_a$) can be calculated by the following equation:

$$R_a = \frac{1}{N}\sum_{n=1}^{N}(|z_n - \bar{z}|)^i \qquad 3.\ 16$$

Where $R_a$ is the mean roughness, N is the number of analysed points, $z_n$ is the height value of the n point and $\bar{z}$ is the average height value.

Another approach to estimating the surface roughness is to consider the Fourier transform of roughness profile. In AFM the term "wavelength" refers to the characteristic size or spatial frequency depending on the specific application of the analysed sample, for example it can refer to the periodicity of roughness features such as scratches or grains. This approach considers the characteristic size or spatial frequency the wavelength of the is useful because considers the specific effects of roughness in field such as biology or tribology that are typically wavelength-dependent. One method to calculate the roughness by considering Fourier transform in the calculation is to apply the "power spectral density function" that apply the "*Fast Fourier transform"* as follows:

$$W_1(K_x) = \frac{2\pi}{NMh} \sum_{j=0}^{M-1} \left|\hat{P}_j(K_x)\right|^2$$

Where $P_j(K_x)$ is the Fourier coefficient of the *j*-th row. By applying this equation using Gwydion software a graph showing $W_1$ versus $K_x$ is obtained, by fitting the experimental curve obtained with a Gaussian curve the value σ and T can be calculated. σ represents the root mean square deviation of the heights and T denotes the autocorrelation length that represents a characteristic length scale over which the heights in the AFM image are correlated with each other.

## 3.4 SEM

Scanning electron microscopy (SEM) is a technique that relies on the interaction between a focused electron beam and the sample under investigation. When a sample is bombarded with high-energy electrons a wide range of interaction occurs, among these interactions the low-energy secondary electrons (SE) produced by inelastic scattering of primary electrons and elastically backscattered primary electrons (BSE) are typically detected in SEM. The SE are electrons of the incident beam that undergoes through inelastic scattering in the sample, or electrons emitted from the sample atoms, while the BSE are electrons of the incident beam which have been elastically scattered by the sample. Figure 3.5 shows the schematic representation of a SEM.

Since SE electrons are electrons inelastically scattered or emitted from the sample after the interaction between the sample and the incident beam, they have a lower energy with respect of the BSE. Consequently, only the SE emitted from the top few nanometres can escape from the sample surface and reach the detector, facilitating the acquisition of surface morphology and topographical information.

BSE on the other hand is originated from elastic scattering events, therefore their energy is the same of the incident beam, which is comprised between 1 and 40 keV. The BSE have higher energies and can carry information about the bulk composition. Moreover, BSE are influenced by the atomic number of the atoms of the sample constituents, henceforth higher the atomic number the higher the intensity of BSE.

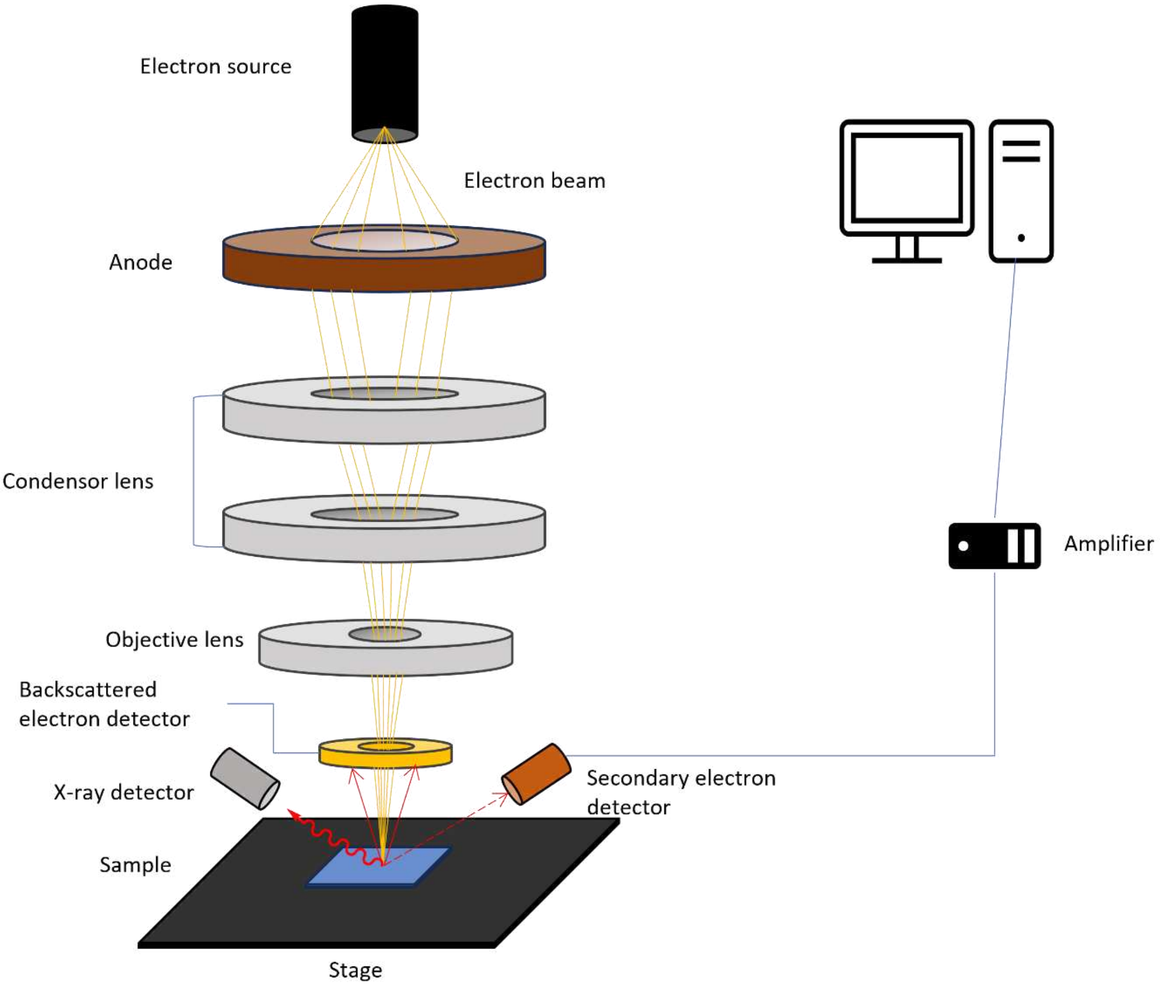

*Figure 3.5 Schematic representation of a Scanning Electron Spectroscopy (SEM)*

High vacuum environment is necessary for performing SEM measurements, this allows the electron beam to travel without collision. A focused electron beam is scanned across the analysed surface of the sample to obtain the SEM images. The analysed sample must be conductive and electrically grounded to avoid charging effects. Non-conductive sample can be analysed if previously covered by a thin metallic layer, thus allowing the acquisition of images of non-conductive samples such as polymers. Moreover, water containing samples cannot be analysed by SEM without a previous pre-treatment consisting of drying procedures or cryogenic freezing. An alternative is to use an environmental SEM (eSEM) that allows characterizing these two types of samples without any pre-treatment procedure of the surface. eSEM consists of a high vacuum environment in the beam column area, while a higher vacuum is kept in the sample proximity, these conditions allow the characterization of non-conductive sample, even in humid conditions. A SEM image consists of pixels in the grey scale: each pixel corresponds to an analysis point. The brighter is the pixel, the more electrons are emitted from that spot.

In this work images of food-grade PVC in the as received state, and following its surface functionalization, were acquired by means of SEM.

## 3.5 Static contact-angle measurements

Surface energy, denoted as $\gamma$, describes the work that is needed to increase the surface area of a fluid by an unit area, and it is represented as energy per unit area[33]. A drop of about 9 µl is placed on an ideally flat surface, in a state of thermodynamic equilibrium, the contact angle $\theta$ is measured as the tangent between the solid sample and the drop and it is described by Young's equation [34].

$$cos\theta = \frac{\gamma_{SG}-\gamma_{SL}}{\gamma_{LG}} \qquad 3.17$$

This angle is influenced by the interfacial tension $\gamma$ between the liquid and the solid, a higher tension leads to a greatest angle. Contact - angle measurements were carried out in water for measuring the static contact-angle in this work, it provides information about the wettability of the surface, indicating if the sample surface is hydrophobic or hydrophilic. If the surface is hydrophilic the droplet spreads over the sample area ($\theta < 90°$), on a hydrophobic surface the drop forms an angle $\theta > 90°$

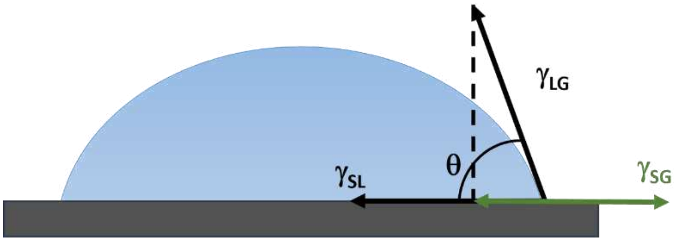

*Figure 3.6 Surface tensions between the solid and the liquid ($\gamma_{SL}$), the liquid and the gas ($\gamma_{LG}$), and the solid and gas phases ($\gamma_{SG}$), influence the contact angle measurements adapted from*

The hydrophobicity may be related to the formation of biofilms of bacteria onto the surface polymer [35]. It has been shown has a more hydrophobic surface reduce the attachment of gram-positive bacteria in the case of medical-grade PVC [36].

The static contact-angle measurement is the average of 6 independent measurements. In the case of a smooth and homogeneous surface a standard deviation of 1° is expected.

# References

[1] "J.F. Watts, J. Wolstenholme, An Introduction to Surface Analysis by XPS and AES, John Wiley & Sons, 2019.

[2] J. Matthew, Surface analysis by Auger and x-ray photoelectron spectroscopy. D. Briggs and J. T. Grant (eds). IMPublications, Chichester, UK and SurfaceSpectra, Manchester, UK, 2003. 900 pp., ISBN 1-901019-04-7, 900 pp, Surface and Interface Analysis 36 (2004) 1647–1647. https://doi.org/10.1002/sia.2005.

[3] F.A. Stevie, C.L. Donley, Introduction to x-ray photoelectron spectroscopy, Journal of Vacuum Science & Technology A: Vacuum, Surfaces, and Films 38 (2020) 063204. https://doi.org/10.1116/6.0000412.

[4] Surface Analysis – The Principal Techniques | Wiley Online Books, (n.d.). https://onlinelibrary.wiley.com/doi/book/10.1002/9780470721582 (accessed January 3, 2024).

[5] R.F. Reilman, A. Msezane, S.T. Manson, Relative intensities in photoelectron spectroscopy of atoms and molecules, Journal of Electron Spectroscopy and Related Phenomena 8 (1976) 389–394. https://doi.org/10.1016/0368-2048(76)80025-4.

[6] M.P. Seah, W.A. Dench, Quantitative electron spectroscopy of surfaces: A standard data base for electron inelastic mean free paths in solids, Surface and Interface Analysis 1 (1979) 2–11. https://doi.org/10.1002/sia.740010103.

[7] ISO 18115-1:2023(en), Surface chemical analysis — Vocabulary — Part 1: General terms and terms used in spectroscopy, (n.d.). https://www.iso.org/obp/ui/en/#iso:std:iso:18115:-1:ed-3:v1:en (accessed April 4, 2024).

[8] S. Tanuma, C.J. Powell, D.R. Penn, Calculations of electorn inelastic mean free paths. II. Data for 27 elements over the 50–2000 eV range, Surface and Interface Analysis 17 (1991) 911–926. https://doi.org/10.1002/sia.740171304.

[9] S. Tanuma, C.J. Powell, D.R. Penn, Calculation of electron inelastic mean free paths (IMFPs) VII. Reliability of the TPP-2M IMFP predictive equation, Surface and Interface Analysis 35 (2003) 268–275. https://doi.org/10.1002/sia.1526.

[10] C.J. Powell, A. Jablonski, S. Tanuma, D.R. Penn, Effects of elastic and inelastic electron scattering on quantitative surface analyses by AES and XPS, Journal of Electron Spectroscopy and Related Phenomena 68 (1994) 605–616. https://doi.org/10.1016/0368-2048(94)80023-5.

[11] J.F. Moulder, J. Chastain, eds., Handbook of X-ray photoelectron spectroscopy: a reference book of standard spectra for identification and interpretation of XPS data, Update, Perkin-Elmer Corporation, Eden Prairie, Minn, 1992.

[12] C. Powell, X-ray Photoelectron Spectroscopy Database XPS,Version 4.1, NIST Standard Reference Database 20, (1989). https://doi.org/10.18434/T4T88K.

[13] C. Ye, W. Liu, Y. Chen, L. Yu, Room-temperature ionic liquids: a novel versatile lubricant, Chem. Commun. (2001) 2244–2245. https://doi.org/10.1039/B106935G.

[14] G.H. Major, N. Fairley, P.M.A. Sherwood, M.R. Linford, J. Terry, V. Fernandez, K. Artyushkova, Practical guide for curve fitting in x-ray photoelectron spectroscopy, Journal of Vacuum Science & Technology A 38 (2020) 061203. https://doi.org/10.1116/6.0000377.

[15] T.R. Gengenbach, G.H. Major, M.R. Linford, C.D. Easton, Practical guides for x-ray photoelectron spectroscopy (XPS): Interpreting the carbon 1s spectrum, Journal of Vacuum Science & Technology A 39 (2021) 013204. https://doi.org/10.1116/6.0000682.

[16] Grant J.T., AES: Basic Principles, Spectral Features and Quantitative Analysis, in: Surface Analysis by Auger and X-Ray Photoelectron Spectroscopy, IMPublication, (IM Publications and Surface Spectra Limited, Chichester and Manchester, UK, n.d.: pp. 57–88.

[17] M.H. Engelhard, D.R. Baer, A. Herrera-Gomez, P.M.A. Sherwood, Introductory guide to backgrounds in XPS spectra and their impact on determining peak intensities, Journal of Vacuum Science & Technology A: Vacuum, Surfaces, and Films 38 (2020) 063203. https://doi.org/10.1116/6.0000359.

[18] G. Casula, M. Fantauzzi, B. Elsener, A. Rossi, Surface modification of food-grade PVC monitored by angle-resolved XPS, Vacuum (2024) 113010. https://doi.org/10.1016/j.vacuum.2024.113010.

[19] J.H. Scofield, Hartree-Slater subshell photoionization cross-sections at 1254 and 1487 eV, Journal of Electron Spectroscopy and Related Phenomena 8 (1976) 129–137. https://doi.org/10.1016/0368-2048(76)80015-1.

[20] J.M. Hill, D.G. Royce, C.S. Fadley, L.F. Wagner, F.J. Grunthaner, Properties of oxidized silicon as determined by angular-dependent X-ray photoelectron spectroscopy, Chemical Physics Letters 44 (1976) 225–231. https://doi.org/10.1016/0009-2614(76)80496-4.

[21] P.J. Cumpson, M.P. Seah, Elastic Scattering Corrections in AES and XPS. II. Estimating Attenuation Lengths and Conditions Required for their Valid Use in Overlayer/Substrate Experiments, Surface and Interface Analysis 25 (1997) 430–446. https://doi.org/10.1002/(SICI)1096-9918(199706)25:6<430::AID-SIA254>3.0.CO;2-7.

[22] M. Hegner, P. Wagner, G. Semenza, Ultralarge atomically flat template-stripped Au surfaces for scanning probe microscopy, Surface Science 291 (1993) 39–46. https://doi.org/10.1016/0039-6028(93)91474-4.

[23] C. Passiu, XPS and DFT Investigation of the Au-S Interface, Doctoral Thesis, ETH Zurich, 2019. https://doi.org/10.3929/ethz-b-000335671.

[24] P.L.J. Gunter, O.L.J. Gijzeman, J.W. Niemantsverdriet, Surface roughness effects in quantitative XPS: magic angle for determining overlayer thickness, Applied Surface Science 115 (1997) 342–346. https://doi.org/10.1016/S0169-4332(97)00007-X.

[25] W.S.M. Werner, Magic angle for surface roughness for intensity ratios in AES/XPS, Surface and Interface Analysis 23 (1995) 696–704. https://doi.org/10.1002/sia.740231008.

[26] P.J. Cumpson, Surface Analysis by Auger and X-Ray Photoelectron Spectroscopy, in: Surface Analysis by Auger and X-Ray Photoelectron Spectroscopy, IM Publications and Surface Spectra Limited, Chichester and Manchester, UK, 2003, n.d.: p. 651.

[27] N.J. Harrick, K.H. Beckmann, Internal Reflection Spectroscopy, in: P.F. Kane, G.B. Larrabee (Eds.), Characterization of Solid Surfaces, Springer US, Boston, MA, 1974: pp. 215–245. https://doi.org/10.1007/978-1-4613-4490-2_11.

[28] Callister, W.D., Materials Science and Engineering: An Introduction., 7th Edition, New York, New York, 2007.

[29] Attenuated Total Reflectance ATR-FTIR Spectroscopy Principles, Specac Ltd (2021). https://specac.com/theory-articles/introduction-to-atr-ftir-spectroscopy-part-1-the-basics/ (accessed March 3, 2024).

[30] G. Binnig, C.F. Quate, Ch. Gerber, Atomic Force Microscope, Phys. Rev. Lett. 56 (1986) 930–933. https://doi.org/10.1103/PhysRevLett.56.930.

[31] K. (Kirill) Feldman, Scanning force microscopy of organic thin films, (2000). https://doi.org/10.6100/IR542440.

[32] V. Bellitto, Atomic Force Microscopy: Imaging, Measuring and Manipulating Surfaces at the Atomic Scale, BoD – Books on Demand, 2012.

[33] K.-Y. Law, H. Zhao, Contact Angle Measurements and Surface Characterization Techniques, in: K.-Y. Law, H. Zhao (Eds.), Surface Wetting: Characterization, Contact Angle, and Fundamentals, Springer International Publishing, Cham, 2016: pp. 7–34. https://doi.org/10.1007/978-3-319-25214-8_2.

[34] B. Widom, Capillarity and Wetting Phenomena: Drops, Bubbles, Pearls, Waves, Physics Today 57 (2004) 66–67. https://doi.org/10.1063/1.1878340.

[35] J. Chandra, J.D. Patel, J. Li, G. Zhou, P.K. Mukherjee, T.S. McCormick, J.M. Anderson, M.A. Ghannoum, Modification of Surface Properties of Biomaterials Influences the Ability of Candida albicans To Form Biofilms, Appl Environ Microbiol 71 (2005) 8795–8801. https://doi.org/10.1128/AEM.71.12.8795-8801.2005.

[36] A. Yousefi Rad, H. Ayhan, Ü. Kisa, E. Pişkin, Adhesion of different bacterial strains to low-temperature plasma treated biomedical PVC catheter surfaces, Journal of Biomaterials Science, Polymer Edition 9 (1998) 915–929. https://doi.org/10.1163/156856298X00244."

# Chapter 4 Surface functionalization of food-grade PVC with antimicrobial active agents

In this chapter, I present an overview of the protocol used for the surface functionalization of food-grade PVC with two antimicrobial compounds, polyhexamethylenguanidine (PHMG) and 4-(10,15,20triphenylporphyrin-5-yl) aniline (TPPA). The synthesis of TPPA was carried out at the D-CHAB of the ETH in Zürich, under the supervision of Professor Yamakoshi and Dr. Çelic.

The LC-MS measurements were performed at the ETH in Zürich by the MoBiAS MS service, while the NMR spectra were acquired by using the NMR Service is located in HCI D314 at the ETH in Zürich.

## 4.1 Introduction

Polyvinyl chloride (PVC) is one of the most used polymers in the food industry. Moreover, PVC surfaces can be easily modified: thanks to the presence of the C-Cl bond, PVC is particularly suitable for functionalization through nucleophilic substitution reactions. The concentration of the functionalizing solution, solvents, and substrate composition, such as the presence of plasticizers and stabilizers, might play a central role in the surface modification of a polymer.

In the literature, PVC surface modification has been reported by Villanueva et. Alii [1,2]. Villanueva proposes a protocol for functionalizing medical-grade PVC with polyhexamethylenguanidine (PHMG), an antimicrobial guanidine-based polymer. The proposed procedure involves surface modification in four different steps. Firstly the grafting of the (3-mercaptopropyl)-trimethoxysilane (MPTMS) is done, followed by the anchoring of the 3-(aminopropyl)-triethoxysilane (APTES) via silanols group reaction. The APTES amino group can further react with glutaraldehyde, allowing the immobilization of this compound. Finally, due to the presence of carbonylic groups on the polymer surface, the immobilization of PHMG has been achieved through the formation of iminium bond.

The following paragraphs describe the optimization of the functionalization process of food-grade PVC with PHMG, based on the results previously reported in [2]. The primary emphasis will be on the role of the solvents used in each step and the time of exposure to the solution.

Moreover, a novel protocol for grafting a porphyrin-based compound onto food-grade PVC samples of will be presented. Porphyrins are known for their antimicrobial properties related to their ability to catalyse peroxidase and oxidase reactions, making them a potential antimicrobial agent for developing antimicrobial food-packaging [3].

## 4.2 Experimental

### 4.2.1 Materials

Food-grade PVC samples were purchased from *VWR* (Italy) and cut into square pieces of 1 cm$^2$. There was no detailed information about the type and quantity of plasticizers and stabilizers. (3-mercaptopropyl) trimethoxy-silane (MPTMS) and 96% ethanol were also from *VWR* (Italy). MPTMS is soluble in acetone and ethanol, but insoluble in water. 3-(aminopropyl)-triethoxysilane (APTES) was purchased from *Sigma Aldrich*, and is soluble in ethanol. Glutaraldehyde 25% aqueous solution was purchased from *Sigma Aldrich*. The solutions for the functionalization process were made up using a phosphate buffer pH 7.5 solution obtained from dihydrogen phosphate anhydrous purchased from *Fluka (USA)* (>99.0%). 1,6 Hexamethylendiamine (>99.5%) and guanidine hydrochloride (purity grade>99.5%) exploited for the polyhexamethylenguanidine (PHMG) synthesis were produced by *Acros organics (Belgium).* Finally, the 4-nitrobenzaldehyde (98%), benzaldehyde (≥ 99%), and pyrrole (reagent grade 98%) were purchased from *Sigma Aldrich*.

### 4.2.2 Nuclear magnetic resonance spectroscopy (NMR)

NMR spectroscopy was exploited for confirming the structure of the porphyrins reported in (§4.3) by acquiring the $^1$H-NMR spectra. An AV III 400 MHz Ascend NMR spectrometer was used. A spectral width of 20 Hz was carefully selected to detect the negative chemical shifts characteristic of porphyrins. This narrow spectral width ensured precision in capturing subtle chemical variations within the molecules. Additionally, employing 32 scans during the acquisition process further enhanced the signal-to-noise ratio. The measurement were performed in deuterated chloroform $CDCl_3$, and the spectra were processed by MestReNova software Version 14.3.3-33362.

### *4.2.3 M-PVC*

Food-grade PVC samples were cut into 1 cm$^2$ squares and washed by immersing the samples in ethanol 96% v/v solution for an hour. Then, the washed samples were dipped into a 10% MPTMS solution in 96% v/v ethanol for another hour and washed again in ethanol for another hour. When exposed to the MPTMS solution, the PVC samples reacted with the thiol group of the MPTMS via a nucleophilic substitution, which allowed the grafting of MPTMS chains onto the surface of the polymer. The reaction scheme is illustrated in Figure 4.1:

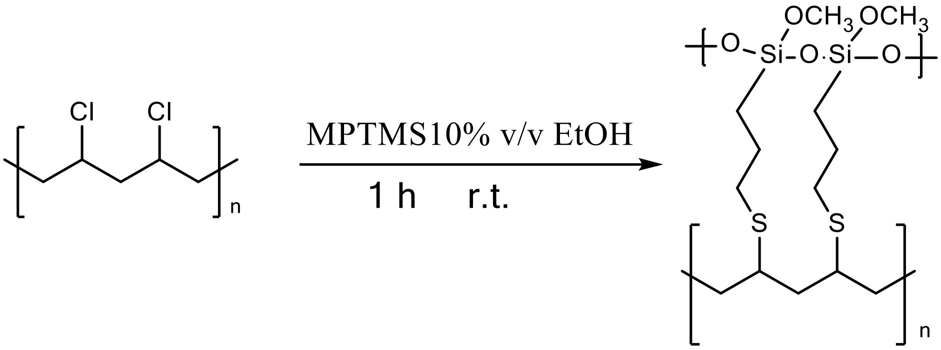

*Figure 4.1 Reaction scheme of PVC functionalized with MPTMS*

It was observed in the literature that the surface of PVC was modified using acetone. However, ethanol was preferred in this work as acetone is known to cause swelling of the polymer. Moreover, while a 5% v/v solution was used in previous studies, it was found that a 10% v/v solution in ethanol yielded better results, as reported in [4].

### 4.2.4 A-PVC

The M-PVC samples were dipped into a 7.52 mM (3-Aminopropyl)triethoxysilane (APTES) prepared in an ethanol 96% v/v and ammonia 20% v/v solution with a 7:2 ratio for one hour. After this procedure, the sample was rinsed in the solution (Ethanol and ammonia) for one hour to eliminate the non-reacted residual.

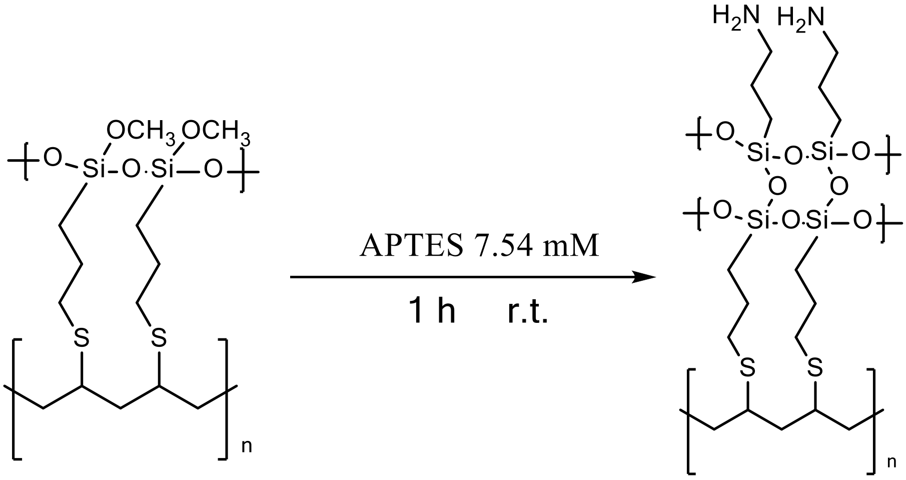

*Figure 4.2 Reaction scheme of M-PVC with APTES*

Different APTES solutions with concentrations of 3.5 mM and 7.54 mM were tested to find the best conditions for anchoring APTES to the M-PVC surface. The solution with a concentration of 7.54 mM was chosen because it successfully grafted APTES onto the M-PVC surfaces. This was confirmed by the bands at 1650 cm$^{-1}$ typical of the N-H bending, and at 1100 cm$^{-1}$ typical of the Si-

O-Si asymmetric stretching, observed in the FT-IR spectra (Figure 4.3), both of which are assigned to APTES [5,6]. In the literature, an exposure time of 18 hours is reported for achieving functionalization with APTES. However, for this work, an exposure time of one hour was selected to avoid the formation of a multilayer onto the surface, as shorter exposure time ranging from 30 minutes to one hour are suggested for different substrates such as gold or $SiO_2$ [7].

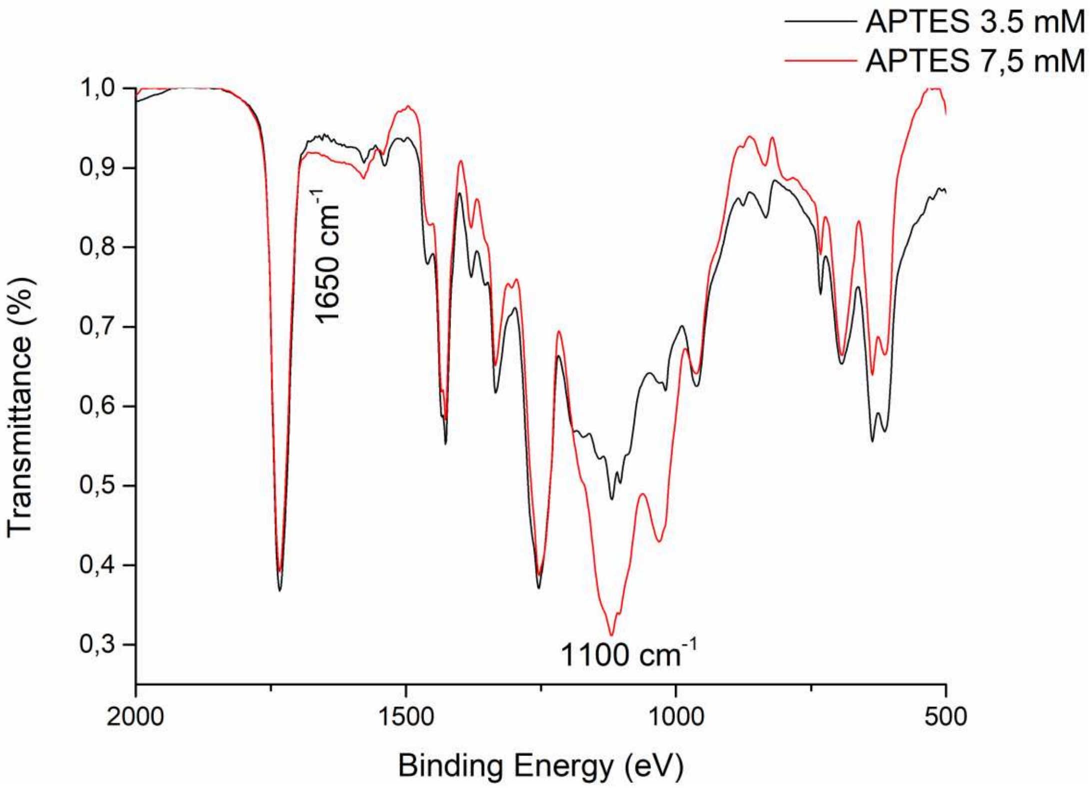

*Figure 4.3 FT-IR Spectra acquired on A-PVC obtained after immersion in 3.5 mM APTES solution (black) and 7.5 mM APTES solution (red)*

In Chapter 7, I will discuss the assignment of the other bands.

### *4.2.5 G-PVC*

G-PVC samples were prepared by dipping A-PVC samples in a 1% phosphate buffer (pH=7.5) glutaraldehyde solution for one hour at room temperature. The functionalized samples were washed with the buffer solution to eliminate the unreacted glutaraldehyde residuals.

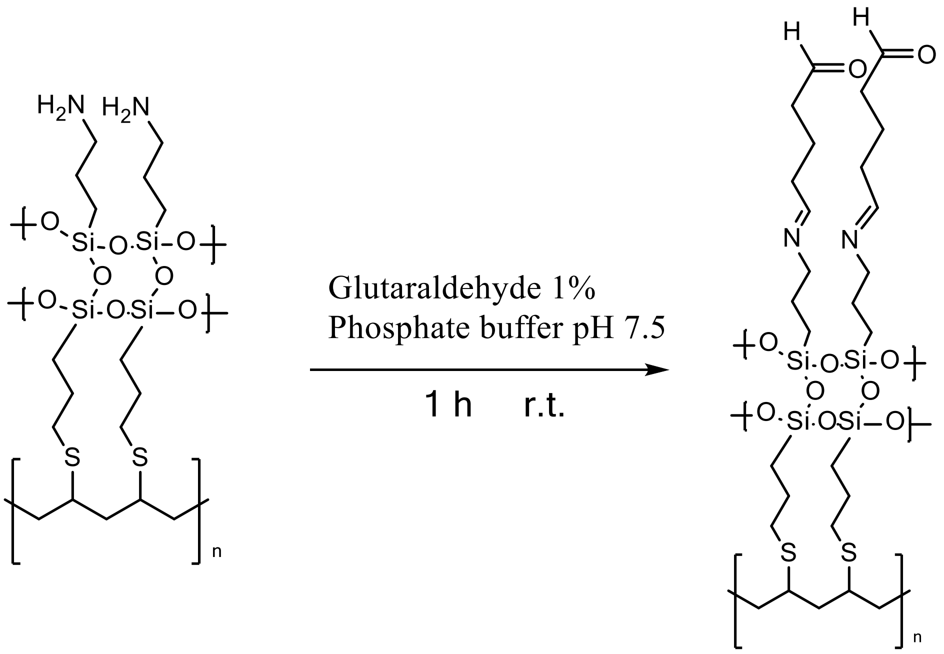

*Figure 4.4 Reaction scheme of A-PVC with glutaraldehyde*

To prepare G-PVC samples, the A-PVC samples were dipped in a phosphate buffer solution (1 % v/v, pH 7.5) for one hour at room temperature. After functionalization with glutaraldehyde, the samples were immersed in phosphate buffer solution (pH= 7.5) to remove any excess of non-reacted glutaraldehyde.

### 4.2.6 P-PVC

Polyhexamethylene guanidine (PHMG) was synthesized using a well-established procedure mentioned in the literature [8]. According to this reaction equimolar quantities of hexamethylenediamine and guanidine hydrochloride were placed in a two-necked flask and heated with an oil bath at 80 °C with a magnetic stirring. Both starting reagents melted entirely at this temperature, and then the temperature was raised to 100 °C and kept for one hour. This polymerization reaction led to the formation of PHMG and ammonia as a side product that was neutralized by bubbling into an HCl 1M aqueous solution. After the first hour at 100 °C, the temperature was increased by 20 °C until it reached 180 °C, and then kept constant for another hour. The reaction scheme between hexamethylenediamine and guanidine hydrochloride is reported in Figure 4.5:

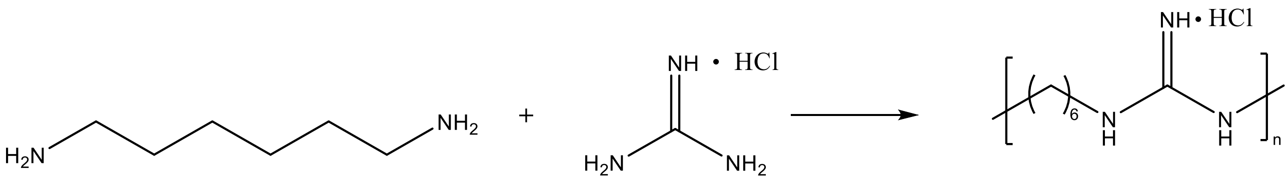

*Figure 4.5 Synthesis of polyhexamethyleneguanidine (PHMG)*

After cooling in the air, the product appeared as a viscous liquid that solidified at room temperature. The vitreous solid contained in the flask was then solubilized in a saturated NaCl aqueous solution and heated until to boiling point. The precipitation of PHMG chloride salt was observed when the solution began boiling. The suspension was then filtered and the solid was collected in a glass petri dish. The petri dish was left overnight at 130 °C to obtain the dried product.

The dried product was characterized by FT-IR spectroscopy to observe the characteristics band of the PHMG. An aqueous solution of PHMG (10 % w/w) was prepared in distilled water and used as solution for the last functionalization step. G-PVC samples were exposed to the 10% w/w aqueous solution of PHMG to prepare P-PVC samples. The carbonylic group of glutaraldehyde reacts with the nitrogen of the PHMG by forming an immine bond as shown in Figure 4.6.

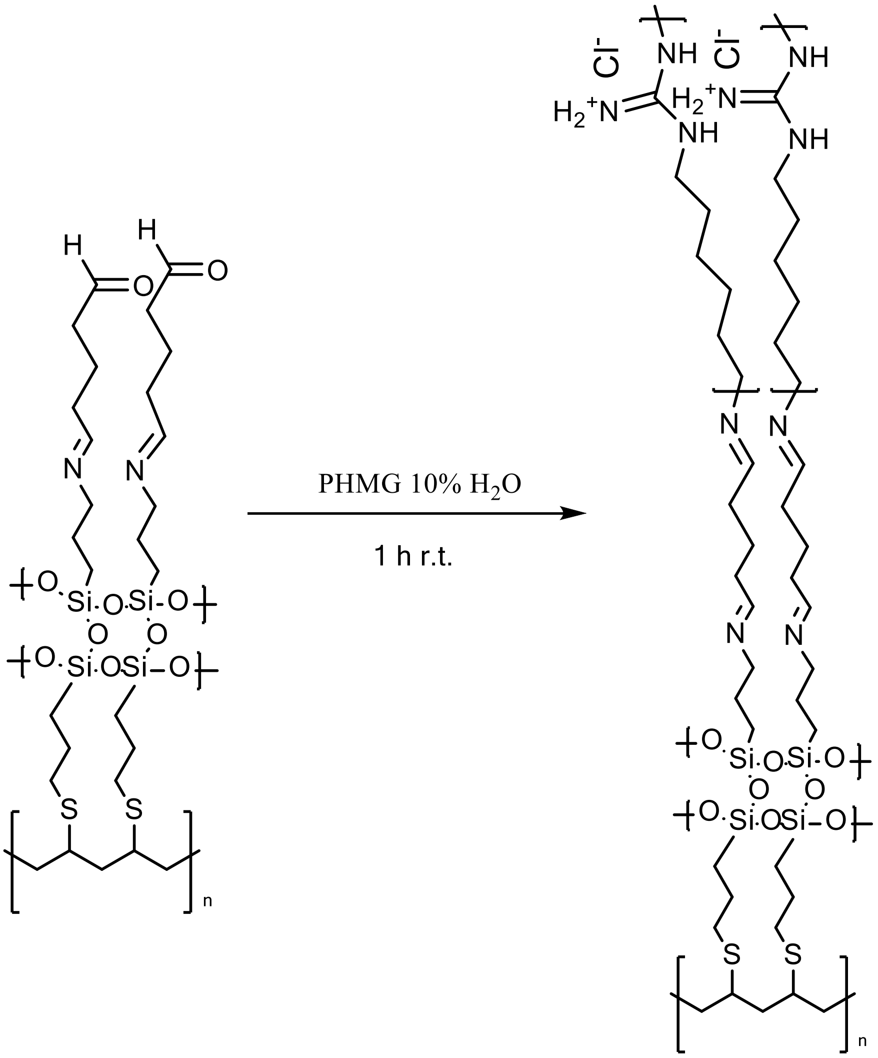

Figure 4.6 Reaction scheme of G-PVC with PHMG

The grafting of PHMG onto the polymer surface leads to a change visible to the naked eye. In fact, the surface looked opal, and it did not present the same flexibility and elasticity as the starting material.

## 4.3 Functionalization of food-grade PVC with porphyrins

### 4.3.1 Synthesis of 4-(10,15,20-triphenilporphyrin-5-yl)-aniline

Porphyrins represent a antimicrobial active agent that can be natural or synthetic[3]. Their antimicrobial properties are attributed to their ability to catalyse peroxidase and oxidase reaction[3]. Moreover, their light-dependent antimicrobial activity has been demonstrated, thus allowing porphyrins to be a promising candidate for developing active food-packaging[9,10].

In this work the 4-(10,15,20 triphenylporphyrin-5-yl)-aniline (TPPA) was synthesized by following the procedure reported in the literature [11]. TPPA was obtained firstly by synthesizing 5-(4-nitrophenyl)-10,15,20-triphenylporphyrin (Figure 4.7) by the reaction between 4-

nitrobenzaldehyde (1 g; 5.0 mmol; 1 eq), benzaldehyde (1.58 ml; 15.1 mmol; 3 eq) and pyrrole (1.39 ml; 20.1 mmol; 4eq) that were dissolved in 500 ml of dichloromethane in a round bottom flask at room temperature, and the flask was purged with $N_2$. The mixture was stirred in these conditions for 15 minutes until complete solubilization of the three reagents; after 15 minutes, boron trifluoride diethyl etherate ($BF_3OEt_2$; 0.25 ml; 2 mmol; 0.4 eq) was added as Lewis acid catalyst that activates the carbonyl group of the 4-nitrobenzaldehyde and benzaldehyde making them more susceptible to nucleophilic attack from pyrrole. The mixture was stirred at room temperature for one hour under nitrogen. After one hour, 2,3-Dichloro-5,6-dicyano-1,4-benzoquinone (DDQ; 3.4 g; 15.1 mmol) was added to the mixture as an oxidizing reagent that allowed the cyclization of the reagents to form porphyrin ring and ensuring proper reaction conditions. The mixture was stirred under nitrogen and protected from light for one hour since DDQ is photosensitive. Column chromatography in dichloromethane (DCM) gave three different fractions; the second fraction was the desired product (334 mg; yield = 10%). The solvent was dried under reduced pressure.

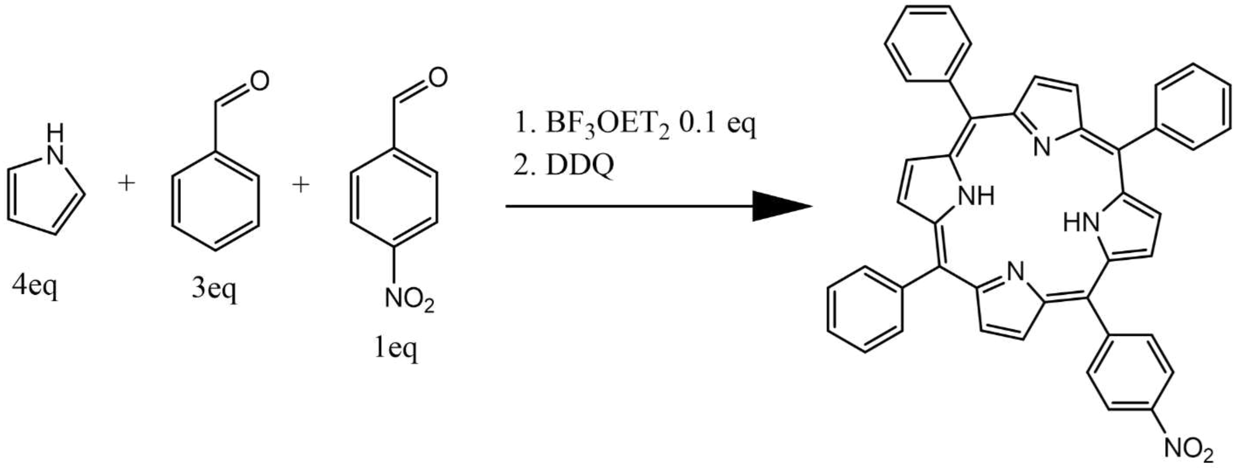

*Figure 4.77 Synthesis scheme of 5-(4-nitrophenyl)-10,15,20-triphenylporphyrin*

The desired product structure was confirmed by $^1H$ NMR performed in $CDCl_3$. The following signals were detected: $\delta$: 8.88 ppm (m, 6H, $\beta$-pyrrole); 8.74 ppm (d, 2H, $\beta$-pyrrole); 8.62 ppm (d, 2H, ortho-4-nitrophenyl); 8.39 ppm (d, 2H, meta-4-nitrophenyl); 8.23 ppm (d, 6H, ortho-triphenyl); 7.78 ppm (m, 10H, meta/para-triphenyl); -2.73 ppm (s, 2H, NH pyrrole). The LC-MS analysis further confirm the compound structure, a $M^+$ of 660 g/mol characteristic of $C_{44}H_{30}N_5O_2$ was found. The NMR spectra are shown in figure 4.8.

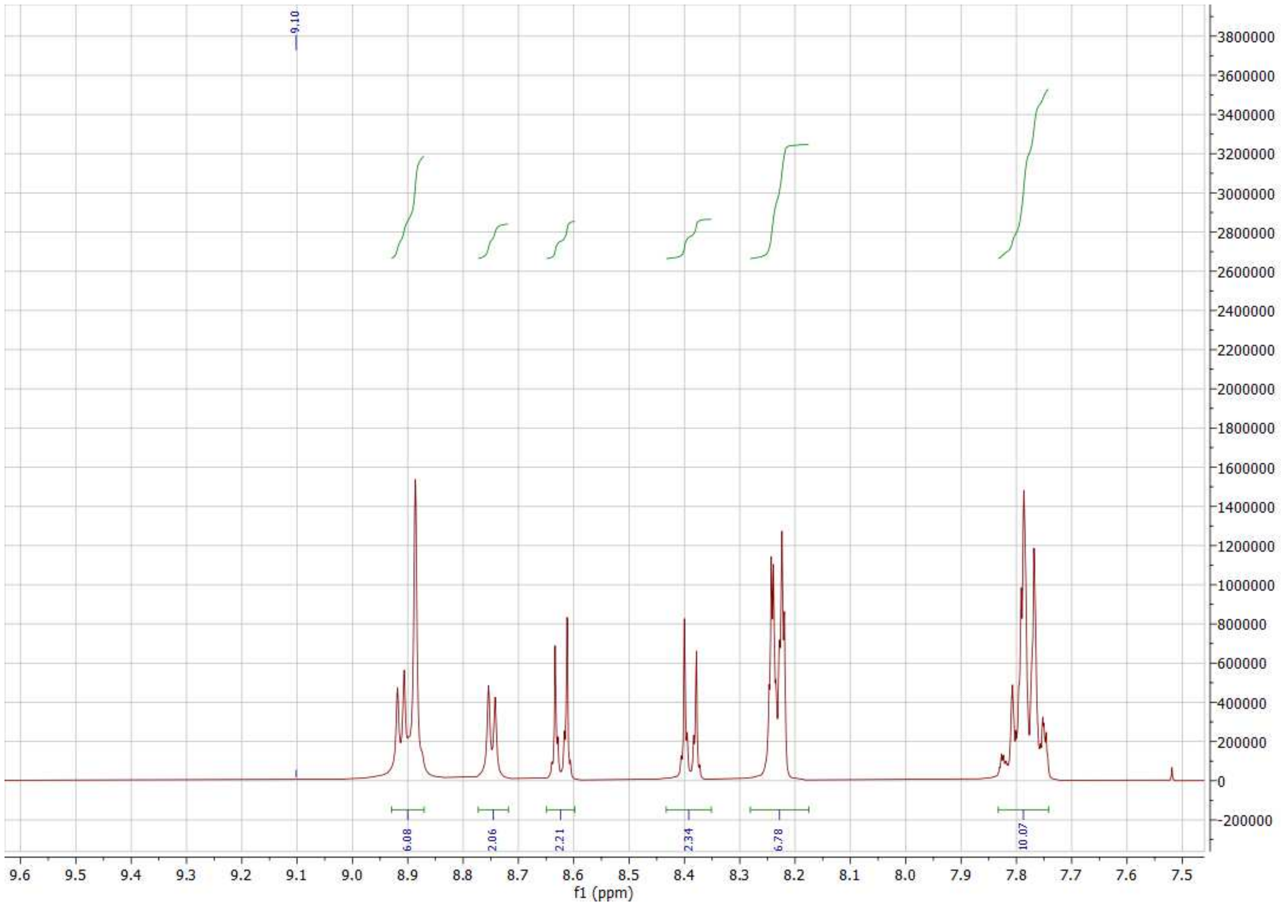

*Figure 4.8 NMR spectrum of the was obtained firstly by synthesizing the 5-(4-nitrophenyl)-10,15,20-triphenylporphyrin*

The 5-(4-nitrophenyl)-10,15,20-triphenylporphyrin was used for synthesizing the TPPA by reducing it to an amino group, a nitro group with tin chloride 334 mg (0.5 mmol, 1eq) of 5-(4-nitrophenyl)-10,15,20-triphenylporphyrin was transferred into a round bottom flask. and 30 mL of concentrate hydrochloric acid was added. Consequently, tin chloride ($SnCl_2$, 571.2 mg, 2.5 mmol, 5 eq) was added and the mixture was stirred for one hour at 65 °C. The reaction was quenched with distilled water, and ammonia (25% v/v) was added to the reaction flask until pH = 8 was achieved; this step is necessary to convert the protonated porphyrin that appears green in solution to the unprotonated porphyrin that appears purple. Following the addition of ammonia, the solution turned deep purple. The aqueous phase was extracted with DCM in a separation funnel. Subsequently, the organic phase was collected and dried with magnesium sulphate. The dried organic phase was concentrated under pressure and purified by column chromatography (DCM/silica gel); two fractions were detected. The first can be ascribed to the starting material, and the second can be ascribed to the desired product, TPPA. The solvent was dried under reduced pressure (TPPA: 284 mg; yield = 89%), and $^1$H NMR in $CDCl_3$ confirmed the product structure. The following signals were detected: $\delta$: 8.98 ppm (d, 2H, $\beta$-pyrrole); 8.90 ppm (m, 6H, $\beta$-pyrrole); 8.26

ppm (m, 6H, ortho-triphenyl); 7.99 ppm (d, 2H, ortho-4-aminophenyl); 7.79 ppm (m, 9H, meta/para-triphenyl); 7.02 ppm (d, 2H, meta-4-aminophenyl); 3.91 ppm (s, 2H, amino); -2.66 ppm (s, 2H, NH pyrrole). The LC-MS analysis further confirmed the compound structure, a peak at $M^+$ of 630 g/mol characteristic of $C_{44}H_{30}N_5H_2$ was found. The NMR spectra are shown in Figure 4.9.

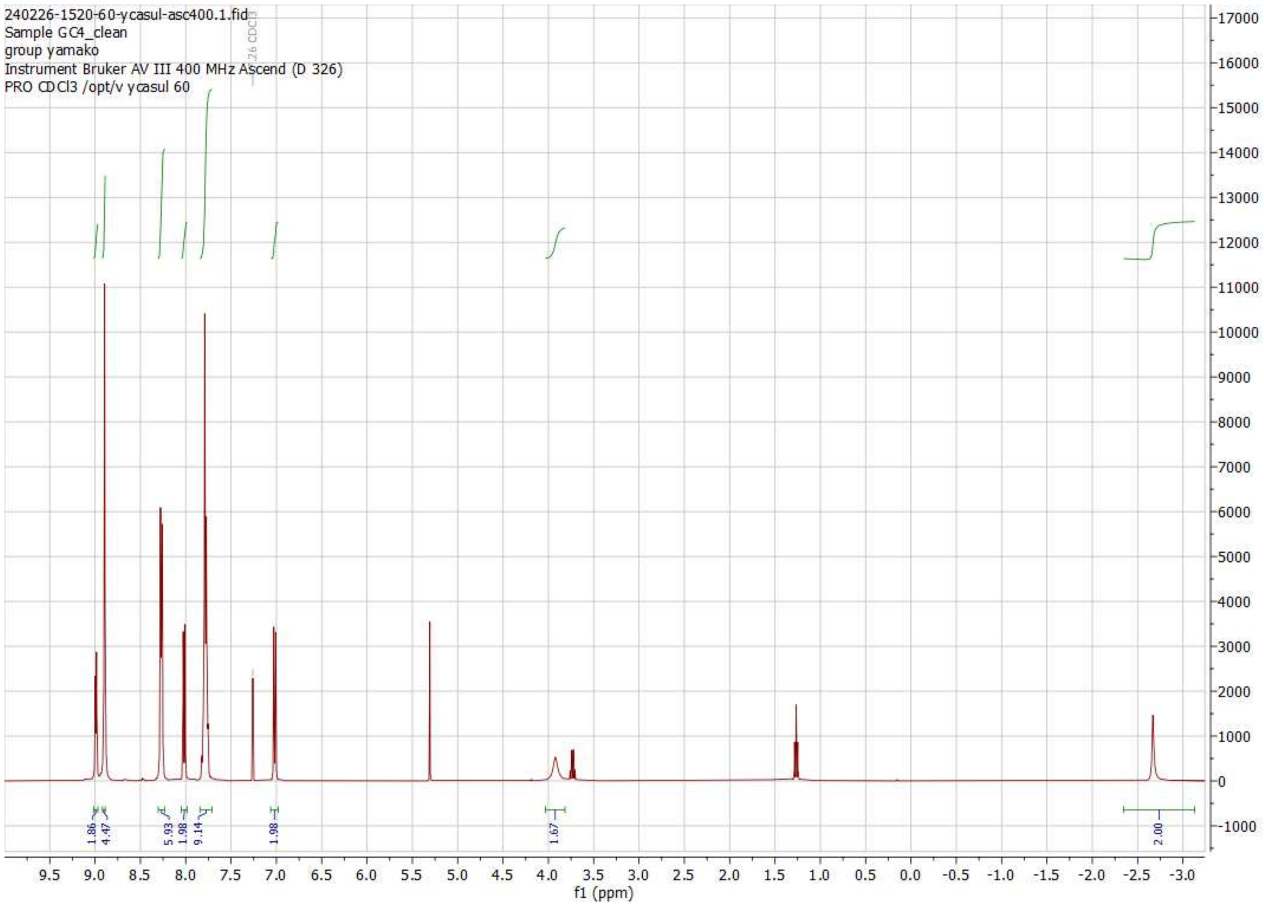

*Figure 4.8 NMR spectrum of 4-(10,15,20 triphenylporphyrin-5-yl)-aniline*

The reaction scheme is reported in Figure 4.10.

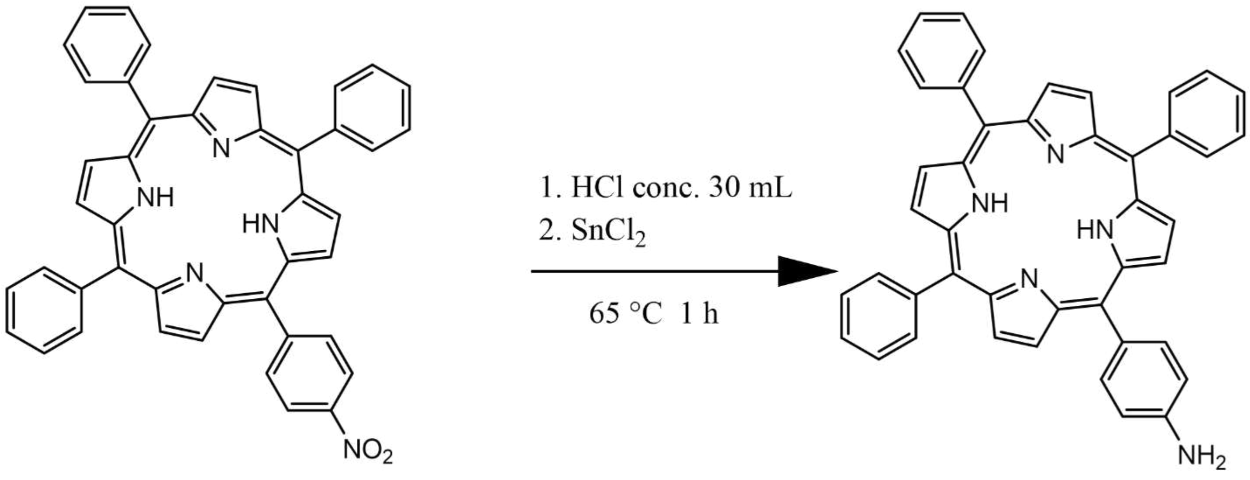

*Figure 4.9 Synthesis scheme of 4-(10,15,20-triphenilporphirin-5-yl) amine*

TPPA was soluble in DCM and partially soluble in ethanol. To perform the surface functionalization of food-grade PVC, a 1 mM solution of TPPA in ethanol was prepared.

### *4.3.2 TPPA-PVC*

To functionalize the surface of food-grade PVC, a 1 mM solution of TPPA in ethanol was prepared. The effect of the immersion time on the reaction between the amino groups of TPPA and the carbonyl group of glutaraldehyde in G-PVC was investigated to obtain the best functionalizing conditions. The success of the functionalization was ascertained by exciting with a UV lamp (λ = 366 nm) the PVC samples exposed to TPPA for 1h, 3h and 12 h. After one hour of immersion time, the functionalized PVC appeared fluorescent. The reaction scheme of G-PVC with TPPA solution is shown in Figure 4.10.

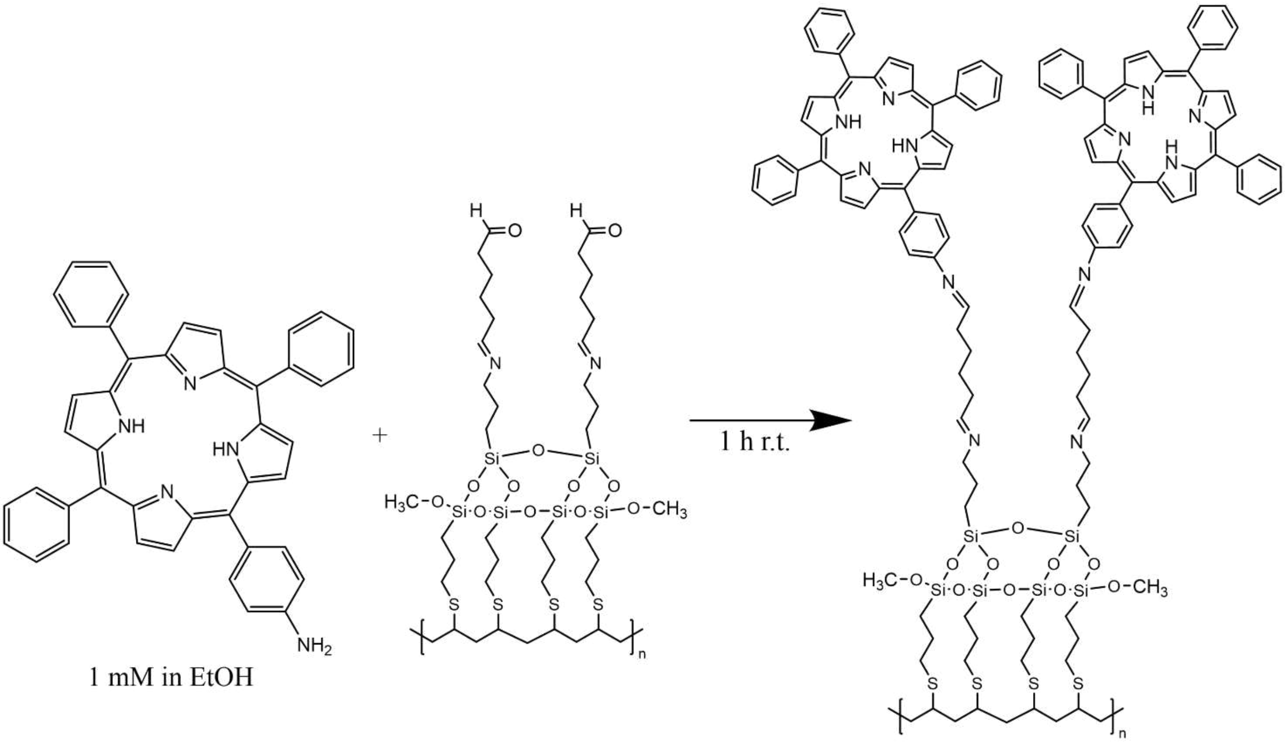

*Figure 4.10 Reaction scheme of G-PVC with TPPA*

After 12 h of immersion, small purple particles due to the precipitation of TPPA were observed. Henceforth, to remove the non-reacted TPPA from the surface sample, functionalized PVC was immersed in ethanol for two hours in an ultrasonic bath; the solvent was replaced every 15 minutes until the washing solution was clear. The ethanol used for this procedure turns light purple in the presence of TPPA. ATR-FTIR was used to confirm the grafting of the compound onto the sample surface, suggesting that only after 12 hours the functionalization with TPPA occurs (section 7.3).

*References*

[1] "M.E. Villanueva, A. Salinas, J.A. González, S. Teves, G.J. Copello, Dual antibacterial effect of immobilized quaternary ammonium and aliphatic groups on PVC, New J. Chem. 39 (2015) 9200–9206. https://doi.org/10.1039/C5NJ01766A.

[2] M.E. Villanueva, J.A. González, E. Rodríguez-Castellón, S. Teves, G.J. Copello, Antimicrobial surface functionalization of PVC by a guanidine based antimicrobial polymer, Materials Science and Engineering: C 67 (2016) 214–220. https://doi.org/10.1016/j.msec.2016.05.052.

[3] I. Stojiljkovic, B.D. Evavold, V. Kumar, Antimicrobial properties of porphyrins, Expert Opinion on Investigational Drugs 10 (2001) 309–320. https://doi.org/10.1517/13543784.10.2.309.

[4] G. Casula, M. Fantauzzi, B. Elsener, A. Rossi, Surface modification of food-grade PVC monitored by angle-resolved XPS, Vacuum (2024) 113010. https://doi.org/10.1016/j.vacuum.2024.113010.

[5] A. Boldeiu, K. Mihaela, A. Radoi, M. Danila, M. Simion, F. Craciunoiu, R. Pascu, I. Mihalache, T. Ignat, Microstructures and growth characteristics of polyelectrolytes on silicon using layer-by-layer assembly, Central European Journal of Chemistry 11 (2012) 205–214. https://doi.org/10.2478/s11532-012-0152-9.

[6] E. Lecoq, D. Duday, S. Bulou, G. Frache, F. Hilt, R. Maurau, P. Choquet, Plasma Polymerization of APTES to Elaborate Nitrogen Containing Organosilicon Thin Films: Influence of Process Parameters and Discussion About the Growing Mechanisms, Plasma Processes and Polymers 10 (2013) 250–261. https://doi.org/10.1002/ppap.201200108.

[7] M. Zhu, M.Z. Lerum, W. Chen, How To Prepare Reproducible, Homogeneous, and Hydrolytically Stable Aminosilane-Derived Layers on Silica, Langmuir 28 (2012) 416–423. https://doi.org/10.1021/la203638g.

[8] E. Olewnik-Kruszkowska, M. Gierszewska, E. Jakubowska, I. Tarach, V. Sedlarik, M. Pummerova, Antibacterial Films Based on PVA and PVA-Chitosan Modified with Poly(Hexamethylene Guanidine), Polymers (Basel) 11 (2019) 2093. https://doi.org/10.3390/polym11122093.

[9] A. Altmann, M. Eden, G. Hüttmann, C. Schell, R. Rahmanzadeh, Porphyrin-based sensor films for monitoring food spoilage, Food Packaging and Shelf Life 38 (2023) 101105. https://doi.org/10.1016/j.fpsl.2023.101105.

[10] H. Yan, X. Lin, N. Duan, I.M. Khan, Z. Wang, S. Wu, Gelatin–carboxymethyl cellulose film incorporated porphyrin metal–organic frameworks with photodynamic/photothermal synergistic antibacterial activities for pork packaging application, Journal of Food Engineering 353 (2023) 111556. https://doi.org/10.1016/j.jfoodeng.2023.111556.

[11] G.-P. Yan, D. Bischa, S.E. Bottle, Synthesis and properties of novel porphyrin spin probes containing isoindoline nitroxides, Free Radic Biol Med 43 (2007) 111–116. https://doi.org/10.1016/j.freeradbiomed.2007.03.032."

# Chapter 5 A model system - characterization of silanes on freshly cleaved gold samples

This chapter provides an analytical strategy that uses X-ray photoelectron spectroscopy to determine the composition and thickness of silane overlayer on freshly cleaved gold surfaces. The strategy is discussed in detail, starting with a brief introduction about the current state of surface functionalization of gold with silane. This is followed by the presentation of experimental details of XPS measurement, and finally, the results and discussion.

It is worth noting that the results discussed in this chapter have been recently published [1].

## 5.1 Introduction

The surface functionalization of a material allows for tailor-made properties distinct from those typical of the bulk, thus opening new possibilities for scientific and technological applications. One method for surface modification involves the creation of self-assembled monolayers (SAMs), which can be described as arrangements of molecules adsorbed onto a solid surface, capable of spontaneously aggregating from the solution or gas phase [2,3]. SAMs exhibit remarkable versatility and can modify different materials, including metals and polymers. Due to their adaptability SAMs are employed across various disciplines, from UV-lithography [4] to the development of antimicrobial polymers [5,6]. Traditionally, gold is used as a substrate for growing thin layers, such as SAMs, on its surface using organic thiols. Organosulfur compounds like thiols, disulfides, and sulfides can interact with a gold substrate through spontaneous adsorption, whether from the liquid or vapor phase, forming SAMs [7].

The formation of self-assembled monolayers (SAMs) via substrate immersion in a diluted ethanolic solution of thiols is time-dependent, typically requiring 12-18 hours to develop well-organized SAMs [7]. Short immersion times may result in weaker interactions, such as dithiolate formation, between the thiol sulphur atoms and the gold surface [8–10]. Additionally, thiols can undergo reactions in ambient conditions, particularly in the presence of water, leading to the formation of disulfides that may be physisorbed onto the substrate [11].

(3-mercaptopropyl)trimethoxysilane (MPTMS) is widely utilized in surface modification of gold surfaces due to its thiol groups [12,13]. This functionalization leads to the formation of a layer in which the Si-$OCH_3$ groups are external and available to anchor further molecules such as (3-aminopropyl)triethoxysilane (APTES)

APTES is another commonly used molecule for functionalizing silicon-based substrates, thanks to the presence of the Si-OEt group. Yang et al. reported an example of an APTES monolayer on gold, where the gold electrode surface was initially modified with potassium hydroxide (KOH) to create a hydroxyl-activated gold surface. This facilitated subsequent anchoring of the APTES monolayer through the reaction of surface -OH groups with Si-OEt groups [14].

MPTMS and APTES can be combined to create a multi-layered system via the reaction of their Si-O groups. This reaction has been suggested for polymer functionalization [5,6], serving as an intermediate step in surface functionalization of medical-grade PVC to impart antimicrobial properties. No XPS surface characterization was documented for MPTMS-APTES layers.

Since XPS is a surface-sensitive technique that allows obtaining detailed compositional information for layers with thicknesses ranging from 0.5 nm to 10 nm [15], depending on the kinetic energy of the photoemitted electrons and the photoelectron inelastic mean free path ($\lambda$, IMFP) in [16,17], material properties and the emission angle (§ 3.1.1) surface functionalization can be monitored exploiting this technique. However, in the case of PVC functionalization with MPTMS and APTES, the curve fitting of C 1s XPS signals is challenging, as carbon is present both in the polymeric substrate and in the functionalizing molecules. To identify the C 1s signal components belonging to the functionalization layer and to distinguish them from those of the polymer substrate, the functionalization with MPTMS and APTES of a substrate that does not contain carbon can be carried out. Thus, the curve fitting parameters and the binding energy values of the signals ascribed to the functionalizing molecules can be obtained. Since MPTMS has a -SH group, a freshly cleaved gold sample with low roughness (< 0.3 nm) was chosen in this work as a model carbon-free substrate for both obtaining the curve fitting parameters of the signals ascribed to the functionalizing molecules and for validating the results obtained on functionalized PVC.

Numerous examples of gold surface functionalization with thiols exist in the literature [2,18,19] for various applications, although gold surface functionalization with MPTMS is reported without XPS analysis [20]. On the other hand, Penna et al. [21] provided XPS results for MPTMS reacted with a glass surface, while Graf et al. [22] utilized XPS to investigate APTES monolayers on a silicon surface, proposing potential molecular arrangements based on their findings. Despite the abundant literature on surface modification involving MPTMS or APTES analyzed by XPS, no publications have reported the comprehensive use of XPS and ARXPS for characterizing MPTMS overlayers on gold further grafted with APTES. Angle-resolved XPS (ARXPS) is particularly effective for analysing thin layers like self-assembled monolayers (SAMs) [23], enabling determination of layer distribution and thickness through various approaches [24,25].

This chapter investigates the overlayer formed by MPTMS on gold, subsequently grafted with APTES, utilizing XPS and ARXPS to elucidate the spatial arrangement and calculate the overlayer thickness and composition of the functionalization layer on gold surfaces. In paragraph 5.3, the subsequent functionalization steps, consisting of the grafting of glutaraldehyde and PHMG are presented. Moreover, XPS and ARXPS characterization of this model system enables the determination of curve-fitting parameters for the C 1s signal and other functional groups within the functionalization layer. This is critical for developing an analytical strategy and is a valuable reference for researchers engaged in XPS characterization of more intricate systems, such as polymers functionalized using the same protocol. Additionally, ARXPS will be employed to investigate the spatial distribution of different functional groups and the overlayer thickness [24,26], potentially elucidating three-dimensional arrangements of the functionalization layer and the formation of three-dimensional cross-linking of silanes, as proposed in [27] based on FTIR investigation.

## 5.2 Experimental

### 5.2.1 Materials

(3-mercaptopropyl) trimethoxysilane (MPTMS) and 96% ethanol were purchased from VWR (Italy). MPTMS was soluble in ethanol but not in water, while (3-aminopropyl) triethoxysilane (APTES) was purchased from sigma Aldrich, APTES was soluble in ethanol.

To prepare the gold samples, the method described by Passiu et al. [28], was followed, which involved depositing 80 nm-thick gold films on silicon wafers through electron-beam evaporation. The silicon wafers were cleaned using a piranha solution, and template stripping was performed immediately before analysis to minimize ambient exposure. The roughness (Ra) of the gold samples was determined to be 0.3 nm.

### 5.2.2 Surface functionalization of gold samples with MPTMS and APTES

To functionalize freshly cleaved gold samples with MPTMS and APTES, using the same conditions applied on PVC samples and presented in Chapter 4 were used. The reaction scheme of MPTMS and APTES is illustrated in Figure 5.1.

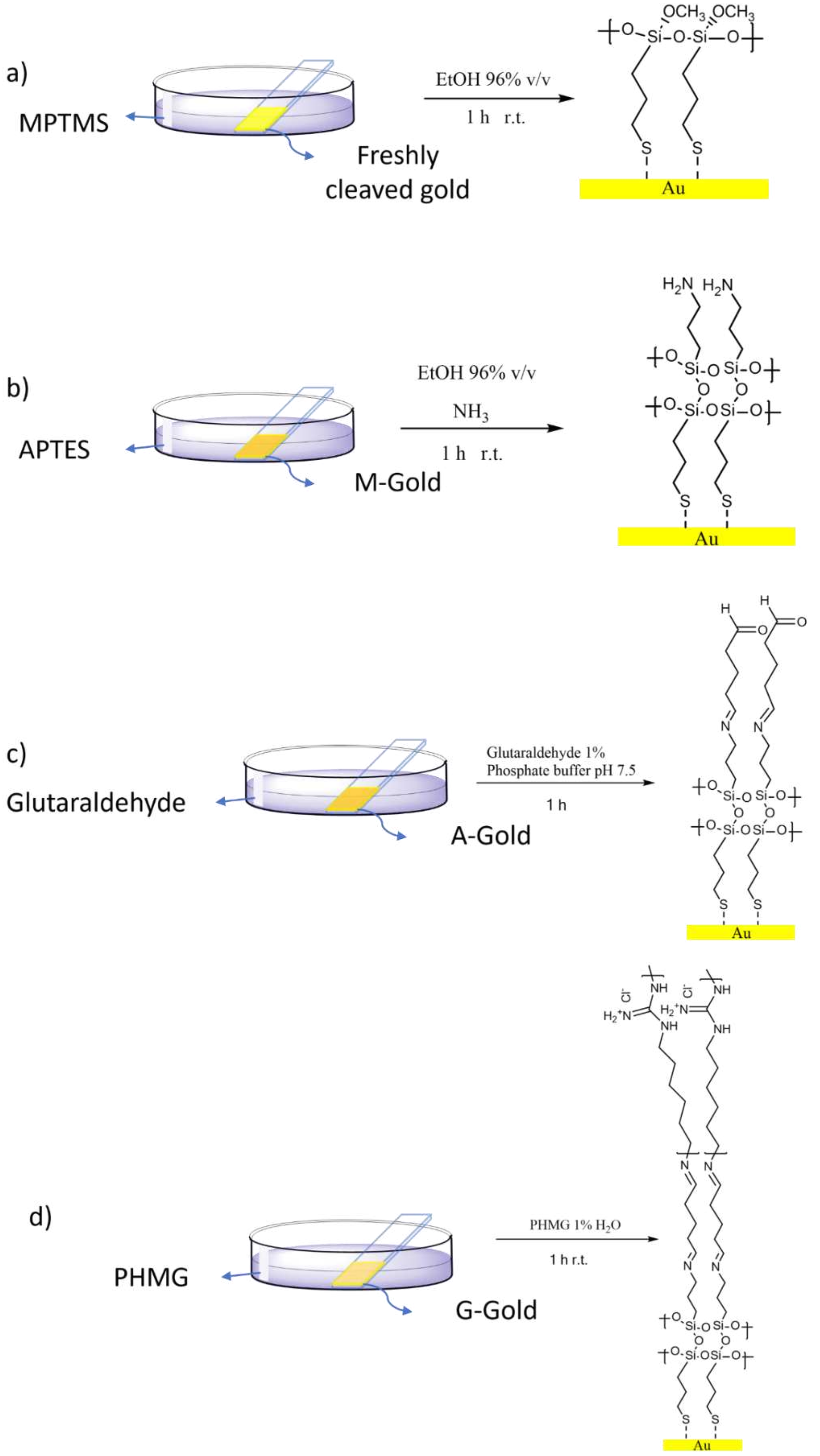

*Figure 5.8 Reaction scheme of MPTMS (a), APTES (b), Glutaraldehyde (c) and PHMG (d) on freshly cleaved gold surface*

The freshly cleaved gold samples were immersed for one hour in ethanol at 96% v/v, and subsequently, they were immersed in 10% MPTMS in ethanol for the first step of functionalization.

After the functionalization, the samples were again immersed in ethanol for one hour to remove non-reacted MPTMS residuals from the surface; no visible changes were observed. The samples functionalized with MPTMS are named M-gold. The M-gold samples were then immersed in a 7.5 mM solution of APTES solubilized in a mixture of ethanol 96% v/v and ammonia 20% v/v at a ratio of 7:2. As shown in Figure 5.1b the outward-facing silanes groups of MPTMS on M-gold samples should react with the silane's groups of the APTES, thus allows grafting APTES onto the M-gold surface. After this functionalization step, the samples were named A-gold and were immersed for one hour in ethanol solution to remove non-reacted APTES residuals. M-gold and A-gold were dried with argon flux before being transferred to the x-ray spectrometer.

A-gold samples are immersed in a 1% glutaraldehyde phosphate buffer (pH=7.5) solution for 1 h. As shown in figure 5.1c the carbonyl groups of glutaraldehyde can react with the amino groups of the APTES forming a C=N bond, allowing the grafting of glutaraldehyde onto the A-gold samples. The samples were subsequently immersed in a phosphate buffer solution to remove the non-reacted glutaraldehyde and were named G-gold.

Finally, the PHMG molecules were grafted on G-gold samples by dipping G-gold samples in a 10% PHMG aqueous solution; the terminal groups of PHMG can react with the free carbonyl groups present in G-gold samples. The samples were subsequently rinsed with distilled water to remove the non-reacted PHMG from the samples surface. The samples prepared following this procedure were named P-gold.

The samples were named using the nomenclature proposed by Villanueva et alii on PVC [5].

### 5.2.3 X-ray photoelectron spectroscopy (XPS) and Angle-resolved X-ray photoelectron spectroscopy (ARXPS)

X-ray photoelectron spectroscopy (XPS) measurements were performed using a Theta Probe spectrometer manufactured by Thermo Fisher Scientific, East Grinstead, UK. The analysis chamber was maintened at a base pressure of $1\text{x}10^{-9}$ mbar or lower throughout the experiment; monitoring the pressure allowed us to assess the stability of the samples under vacuum. To prevent sample cross-contamination, only one sample at a time was analysed at a time in the chamber. As the samples were conductive no charge neutralization was required during spectrum acquisition. The spectra were acquired using a monochromatic Al-K$\alpha_{1,2}$ source (hν = 1486.6 eV) with a nominal 400 µm spot size and a power of 100 W. The spectra were acquired in fixed analyser transmission (FAT) mode, with a pass energy of 150 eV and 200 eV for high resolution and survey spectra, respectively. The energy step size used was 0.1 eV for high-resolution spectra and 1 eV for survey spectra. Each experiment lasted for a total of 40 minutes, with the survey spectrum acquisition taking 10 minutes and the high-resolution spectra taking 30 minutes.

A periodic calibration was performed in agreement with ISO 15472:2010 to ensure the linearity of the binding energy scale. The energy resolution, assessed through the full width at half maximum (FWHM) at the peak height of Ag $3d_{5/2}$ signal at 368.20 eV, was found to be 1.27 eV. This was measured under the same conditions adopted for the acquisition of the high-resolution spectra of the freshly cleaved gold and functionalized gold samples. The binding energy scale was referenced to Au $4f_{7/2}$ at 83.97 eV. The FWHM at the peak height for Au $4f_{7/2}$ was measured and found to be 1.2 (0.1) eV. High-resolution spectra were resolved into their components after background subtraction using the iterative U3-Tougaard model [29].

The apparent composition in atomic percent (% at) was determined from peak areas of the high-resolution spectra, following the curve-fitting procedure, and corrected for relative sensitivity factors. These factors accounted for Scofield's photoionization cross-section[30], asymmetry factor[30], intensity/energy response function [31], and inelastic mean free path[32] as described in Chapter 3 – paragraph 3.1.1.

Angle-Resolved XPS (ARXPS) spectra were collected in angle-resolved lens mode using the Theta Probe spectrometer, which allowed the parallel collection of angle-resolved data without tilting the sample, thanks to a 2D detector. Photoelectrons were detected from 16 different emission angles ranging from 24.9° to 81.1°. The emission angle is defined as the angle between the direction of the photoemitted electrons and the sample surface normal. To minimize elastic scattering effects, only the spectra acquired at emission angles lower than 60° were considered [27]. These effects could affect the thickness estimation, apparent concentration, and relative depth plot calculation [33,34]. The ARXPS data were collected with the same pass energy as standard mode XPS and the angular signature was acquired under the same condition. The total acquisition time was 35 minutes. The spectra were curve fitted by CasaXPS software (version 2.3.24PR1.0 Casa Software Ltd, Teignmouth, UK) [35]. Avantage software (v4.88, Thermo Fisher Scientific, East Grinstead, UK) was used to obtain the relative depth plot. The analyses were performed on three different samples with three analysed areas selected on each sample. The binding energy values, and the atomic composition were calculated as mean values with standard deviation reported in parenthesis. In Table 5.1 the curve-fitting parameters and the Residual Standard Deviation (RSTD) calculated by Casa XPS software are reported.

*Table 5.1 Curve-fitting parameters used for processing the most intense signals of freshly cleaved gold, M-Gold and A-Gold.*

| | FWHM (eV) | Background | Line shape | Constrains | |
|---|---|---|---|---|---|
| Au 4f | 1.2 (0.1) | U 3 Tougaard | GL(50) T(5.5) | Area Au 4f$_{5/2}$ = Area Au 4f$_{7/2}$ x 0.75<br>FWHM Au 4f$_{5/2}$ = FWHM Au 4f$_{7/2}$ x 1 | 1.033 M-gold<br>1.009 A-gold |
| C 1s contamination | 1.6 (0.1) | | GL(30) | FWHM C 1s Contamination = FWHM C 1s C-Si, C-C x 1 | 0.9869 M-gold<br>0.9516 A-gold |
| C 1s C-Si, C-C | 1.6 (0.1) | | GL(30) | | |
| C 1s C-S | 1.6 (0.1) | | GL(30) | FWHM C 1s C-S = FWHM C 1s C-Si, C-C x 1<br>Area C 1s C-S=Area C-Si, C-C x 0.5 | |
| C 1s methoxide | 1.6 (0.1) | | GL(30) | FWHM C 1s methoxide = FWHM C 1s C-Si, C-C x 1 | |
| C 1s of the NH(C*O)O group | 1.6 (0.1) | | GL(30) | FWHM C 1s of the NH(C*O)O group = FWHM C 1s of C-Si, and of C-C x 1 | |
| O 1s Si-O-Si | 1.8 (0.1) | | GL(30) | | 0.9489 M-gold<br>0.9471 A-Gold |
| O 1s of the NH(CO)O* carbamate group | 1.8 (0.1) | | GL(30) | FWHM O 1s NH(CO)O* = FWHM O 1s Si-O-Si x 1 | |
| O 1s of the NH(CO*)O carbamate group | 1.8 (0.1) | | GL(30) | Area O 1s NH(CO*)O = Area O 1s NH(CO)O* x 1<br>FWHM O 1s NH(CO)O* = FWHM O1s Si-O-Si x 1 | |
| S 2p | 1.6 (0.1) | | GL(30) | Area S 2p$_{1/2}$ = Area S 2p$_{3/2}$ x 0.5<br>FWHM S 2p$_{1/2}$ = FWHM S 2p$_{3/2}$ x 1 | 0.9407 M-gold<br>0.9569 A-gold |

| | | | | | |
|---|---|---|---|---|---|
| | | | | BE $2p_{1/2}$ = BE $2p_{3/2}$ + 1.16 | |
| Si 2p | 1.5 (0.1) | | GL(30) | Area Si $2p_{1/2}$ = Area Si $2p_{3/2}$ x 0.5 | 0.9864<br>M-gold |
| | | | | FWHM Si $2p_{1/2}$ = FWHM Si $2p_{3/2}$ x 1 | 1.018<br>A-gold |
| | | | | BE $2p_{1/2}$ = BE $2p_{3/2}$ + 0.6 | |
| N 1s $-NH_2$ | 1.6 (0.1) | | GL(30) | | |
| N 1s $-NH_3^+$ | 1.6 (0.1) | | GL(30) | FWHM N 1s $-NH_3^+$ = FWHM N 1s $-NH_2$ x 1 | 0.8934<br>A-gold |
| N 1s -N*H(CO)O | 1.6 (0.1) | | GL(30) | FWHM -N*H(CO)O = FWHM N 1s $-NH_2$ x 1 | |

## 5.3 Results

### 5.3.1 XPS results on freshly cleaved gold

XPS was exploited for characterising freshly cleaved gold samples before and after the functionalization described in section 5.2.2. The survey spectrum acquired on freshly cleaved gold surfaces allowed the identification of the elements that are present in the surface sample. The survey spectrum (Figure 5.2) of fresh cleaved gold shows the presence of the signal that can be ascribed only to the gold sample, and a barely visible C 1s signal probably due to the short-time exposure to the environment.

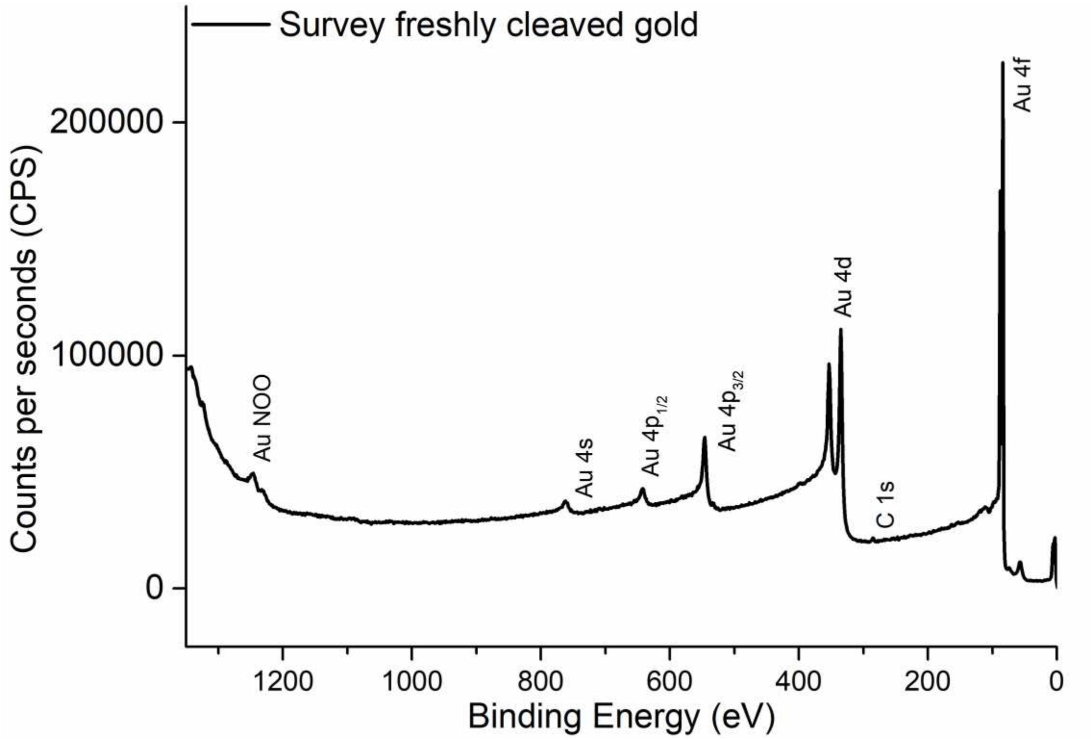

*Figure 5.2 Survey spectrum of freshly cleaved gold samples*

The Au 4f signal was curve-fitted with a doublet due to the spin-orbit coupling after background subtraction with U 3 Tougaard model (Figure 5.3). The energy separation between the $4f_{7/2}$ and $4f_{5/2}$ was 3.7 eV and the area ratio was 4:3. The full width at half-maximum height (FWHM) was 1.2 eV for both peaks. The two components were fitted with a Gaussian/Lorentzian line shape and a tail function (GL(70)T(5)) as shown in [28].

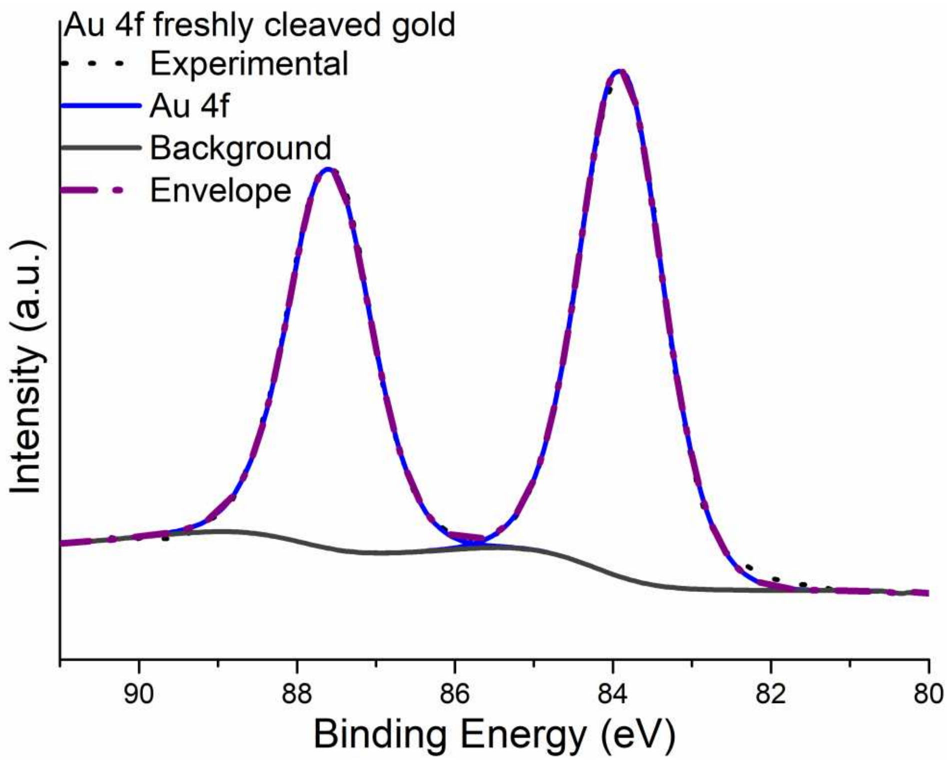

*Figure 5.3 High-resolution spectrum of Au 4f signal acquired on freshly cleaved gold samples.*

### 5.3.2 XPS and ARXPS results on M-gold

#### 5.3.2.1 XPS results

The survey spectrum of the gold samples functionalized with MPTMS (M-gold) showed the presence of the silicon, sulphur, oxygen, and carbon signals that can be ascribed to the MPTMS layer; the Au 4f signal was still detected, but its intensity was lower due to the attenuation by the organic layer. (Figure 5.4) The presence of the functionalization overlayer of MPTMS was also responsible for the change in the background shape.

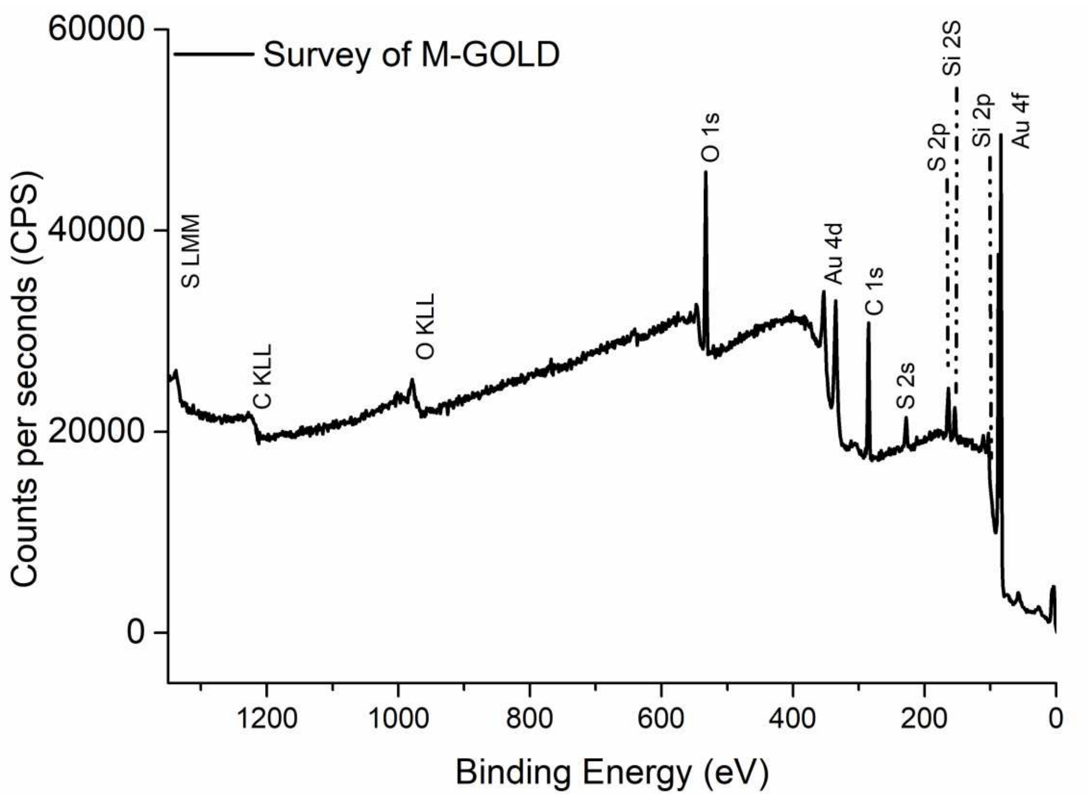

*Figure 5.4 Survey spectrum of M-gold samples.*

Examples of high-resolution spectra of the C 1s, S 2p, Si 2p, O 1s and Au 4f are shown in Figure 5.5. The spectra were acquired to investigate the chemical state of the elements and for their quantitative analysis. The binding energies of all the different components of C 1s, S 2p, O 1s and Si 2p signals revealed on the M-gold samples are given in Table 5.2 together with the atomic concentration (at%). The composition was calculated assuming the in-depth-homogeneity of the layer; gold was not included in the calculation.

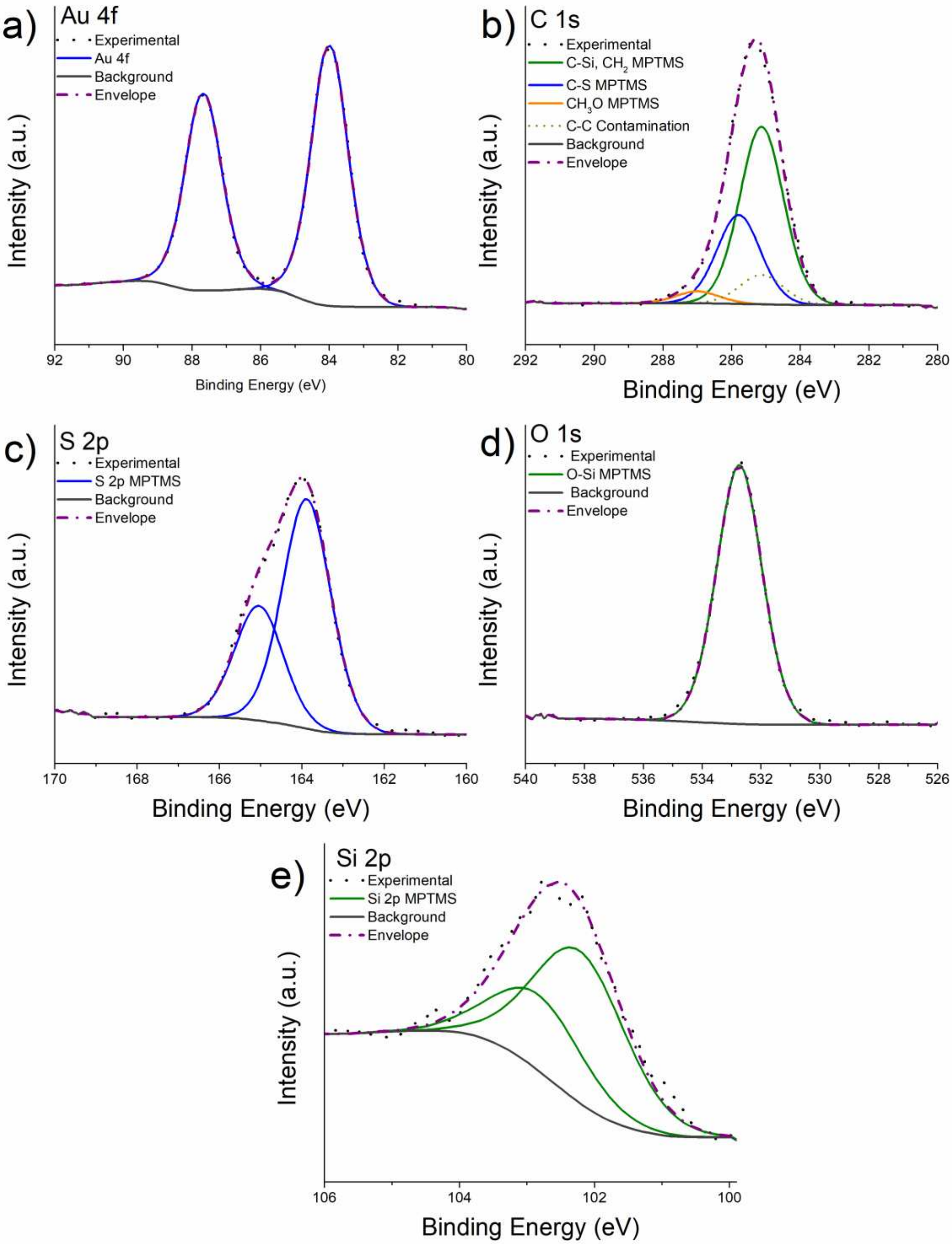

*Figure 5.5 High-resolution spectra of Au 4f (a), C 1s (b), S 2p (c), O 1s (d), and Si 2p (e) signals of the freshly cleaved gold after functionalization with MPTMS (M-gold)*

Figure 5a shows the Au 4f signal that was resolved with the same parameters used for freshly cleaved gold sample.

C 1s signal on M-gold samples (Figure 5.5b) consisted of three components ascribed to the MPTMS layer: C-Si and $CH_2$ of the MPTMS chain at 284.9 eV, one component at 285.9 eV assigned to the C-S and one attributed to the $CH_3O$ at 287.0 eV. Furthermore, a component attributed to the aliphatic component of the contamination layer at 285 eV was considered. The area ratio of the components assigned to the C-Si and $CH_2$ and of the C-S component was constrained to be 2:1 as suggested by the stoichiometry of MPTMS assuming the formation of a monolayer as shown in Figure 5.1.

The S 2p signals were fitted with a doublet due to the spin-orbit coupling with an area ratio between S $2p_{3/2}$ and S $2p_{1/2}$ was constrained to be equal to 2:1 and with an energy separation of 1.16 eV. The S $2p_{3/2}$ component was found to be at 163.7 (0.1) eV. The O 1s signal was resolved with a single component at 532.6 eV assigned to the -O-Si component of the MPTMS as reported also in [36]. The Si 2p signals (Figure 5.5e) consisted of a doublet due to the spin-orbit coupling with an energy separation of 0.6 eV between the $2p_{3/2}$ and $2p_{1/2}$ component, with an area ratio constrained to be 2:1. The binding energy of Si $2p_{3/2}$ was found to be 102.3 eV, similar binding energy have been reported for Si-O groups in [37].

*Table 5.2 Binding energies values (eV) and composition (at%) for M-Gold samples. Mean values over three independent measurements are reported; the standard deviations are given in parentheses.*

| | Binding energy (eV) | M-Gold 10% at % | Expected stoichiometry (at%) |
|---|---|---|---|
| C 1s C-Si, $CH_2$ | 284.9 (0.1) | 27 (2) | 24 |
| C 1s C-S | 285.9 (0.2) | 13 (1) | 12 |
| C 1s Methoxide ($-OCH_3$) | 287.0 (0.1) | 4 (1) | 12 |
| O 1s Si-O-Si | 532.6 (0.1) | 29 (3) | 29 |
| S 2p | 163.7 (0.1) | 13 (2) | 12 |
| Si 2p | 102.3 (0.2) | 13 (2) | 12 |

Atomic ratio of between sulphur and silicon was found to be equal to 1 : 1, thus confirming the expected stoichiometry in the case of a monolayer of MPTMS. It is important to note that the experimental at% of $Si-OCH_3$ was only 4% instead of the expected 12%; this finding can be justified considering the hydrolysis of the $OCH_3$ bonds to yield silanols, which can react with the silanols of other MPTMS molecules forming a three-dimensional cross-linking and resulting on the formation of Si-O-Si bond. Table 5.2 also shows the comparison with the expected stoichiometry.

#### 5.3.2.2 ARXPS results

High-resolution spectra in angle-resolved mode for C 1s, O 1s, Si 2p, Au 4f and S 2p (Figure 5.6) were collected on the M-gold samples at different emission angles; by increasing the emission angle the sampling depth decreases thus allowing obtaining information about the outer layer of the analysed surface.

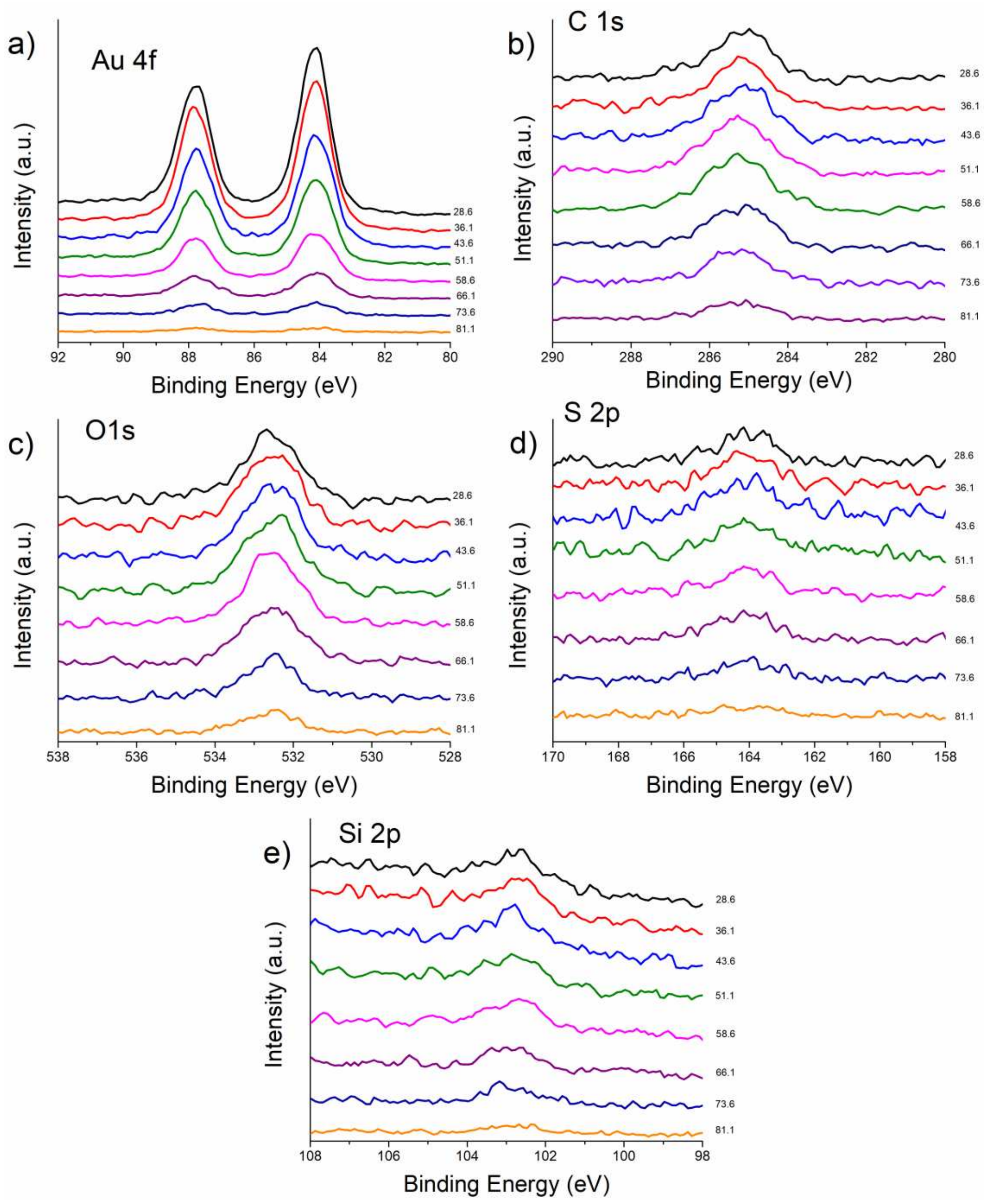

*Figure 5.6 High-resolution spectra of Au 4f (a), C 1s (b), O 1s (c), S 2p (d) and Si 2p (e) acquired in angle-resolved XPS*

The quantitative analysis allowed calculating the apparent concentration in atomic percentage at each emission angle. The apparent concentration versus emission angle plot is shown in Figure 5.7a; it can be noted that the concentration of the carbon C-Si and of O-Si increases with the emission angle, while the gold at%, ascribed to the substrate, decreases.

The in-depth distribution of the functional groups, the so-called relative depth plot (Figure 5.7b), was obtained calculating the logarithm of the area ratio of the peak at near grazing angles (58.6 degrees) to that at near normal emission angle (24.8 degrees).

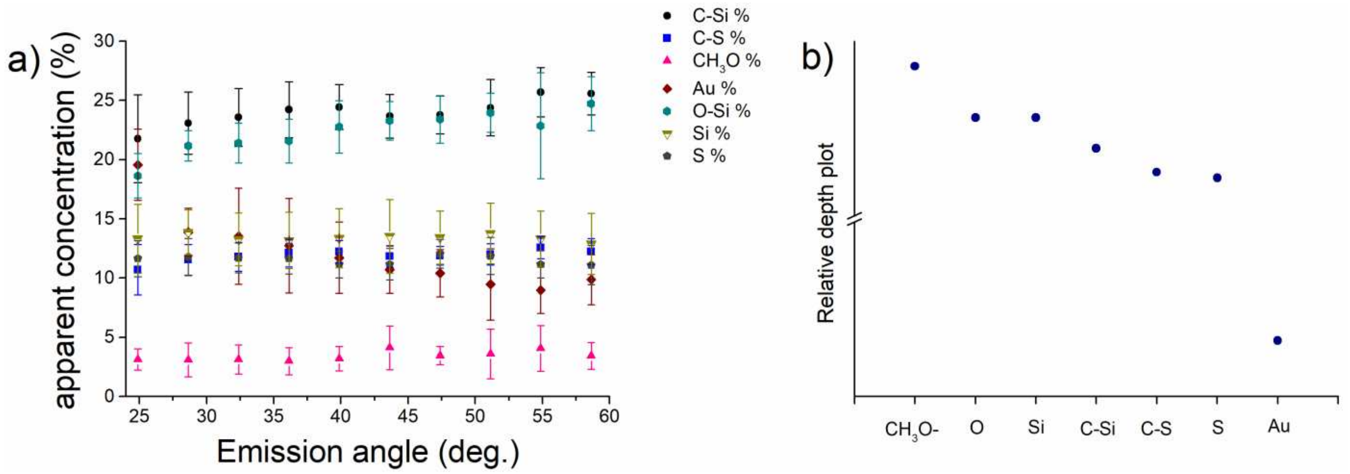

*Figure 5.7 Apparent concentration (%) versus emission angle calculated for Au, Si, S, C-Si, O-Si, $CH_3O$ and C-S (a) and relative depth plot (b) for M-gold*

The relative depth plot confirms the spatial distribution of the functional groups proposed in Figure 5.1a, suggesting that the MPTMS molecules might be adsorbed on the gold surface through sulphur atoms and the Si-O functional group are in the outer part of the layer.

### 5.3.3 XPS and ARXPS results on A-gold

#### 5.3.3.1 XPS results

Samples of A-gold were prepared following the procedure outlined in section 5.2.2. These samples were analysed using X-ray photoelectron spectroscopy. Figure 5.8 provides an example of survey spectrum. In addition to the signals revealed in the M-gold samples (Figure 5.4), the nitrogen signal was detected, indicating the presence of APTES on the sample surface. Following the grafting of APTES, the Au 4f signal was still detected but with an attenuated intensity compared to the M-gold samples.

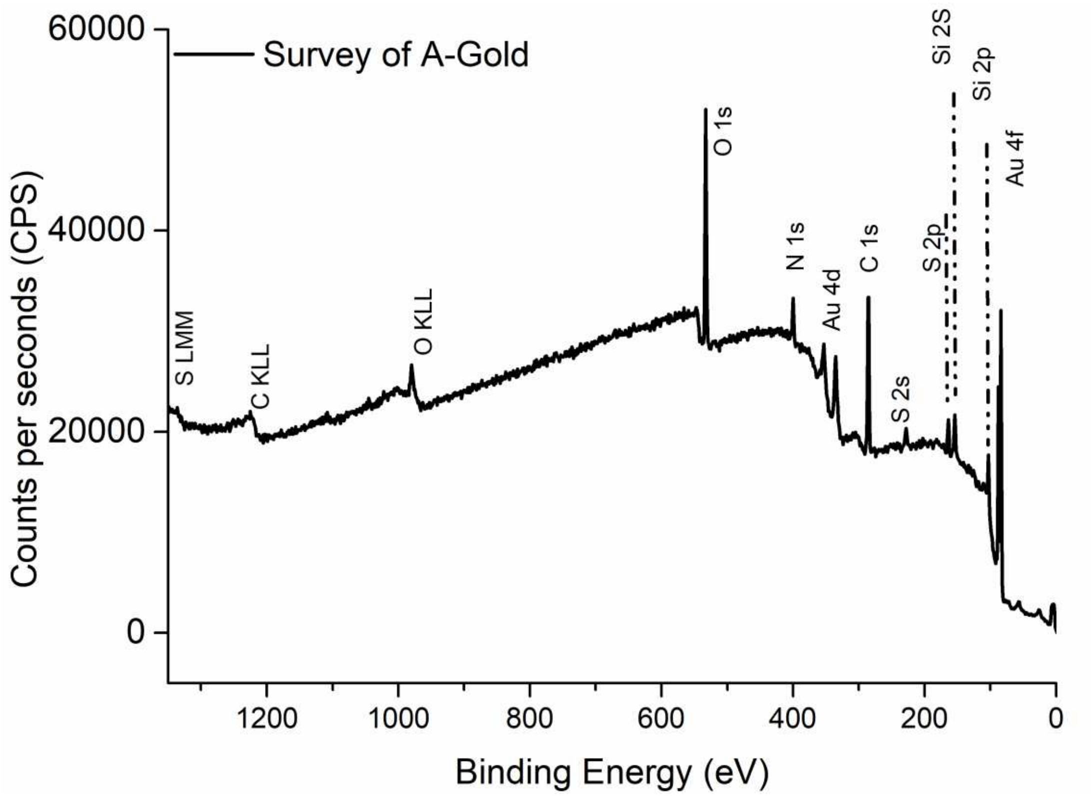

*Figure 5.8 Survey spectrum of A-gold samples*

Figure 5.9 shows the high-resolution of the most intense signals revealed in the A-gold samples: Au 4f, C 1s, N 1s, O 1s, S 2p and Si 2p. The curve fitting parameters that were used for the M-gold samples have been applied again.

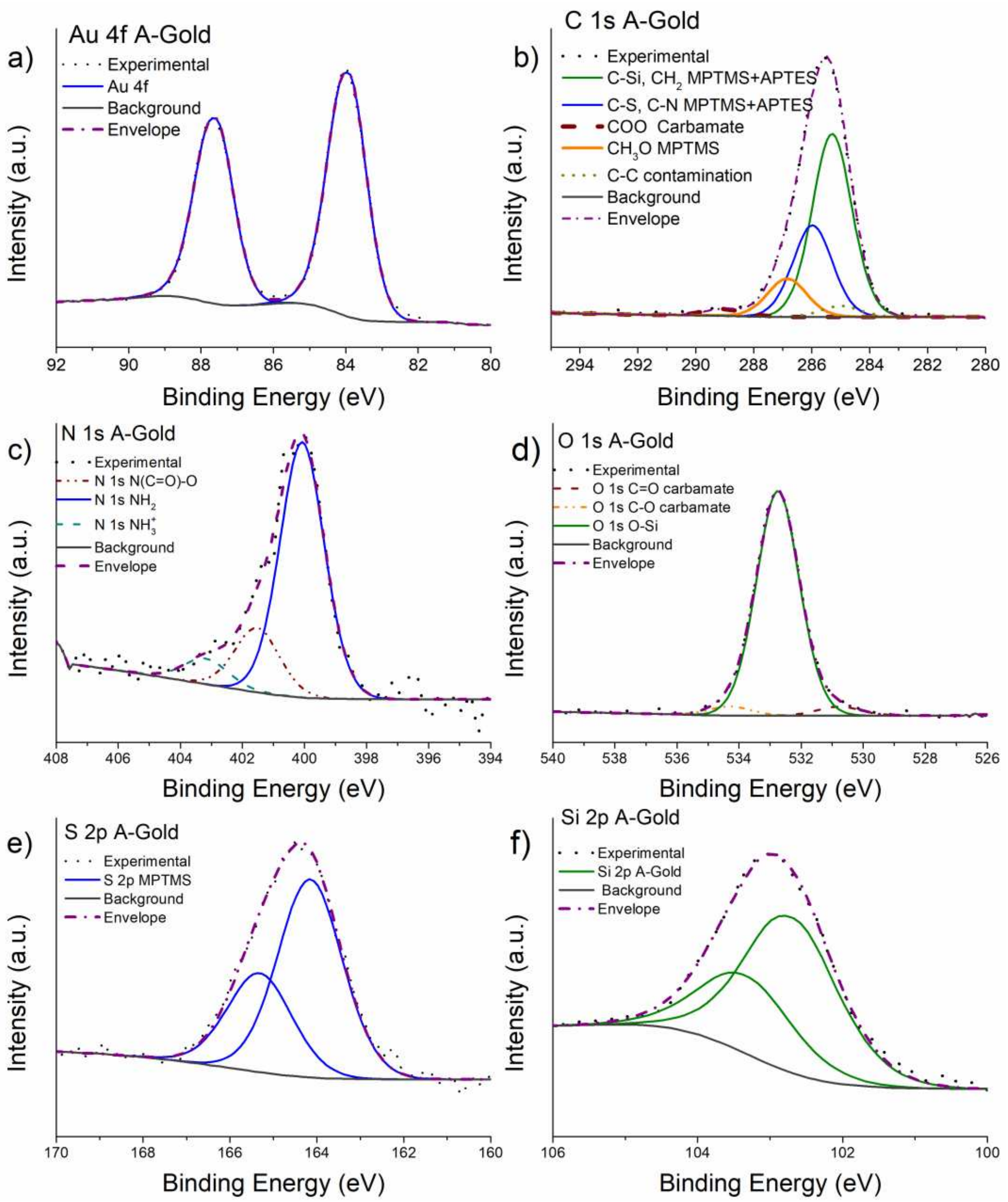

*Figure 5.9 High-resolution spectra of Au 4f (a), C 1s (b), N 1s (c), O 1s (d), S 2p (e) and Si 2p (f) acquired on A-Gold sample*

The Au 4f signal was still detected after the functionalization with MPTMS and APTES, and no difference in the line shape was observed (Figure 5.9a). High-resolution spectra of the C 1s signals were fitted with five components; four are ascribed to the MPTMS-APTES overlayer and one is attributed to the contamination layer. The component found at 285.3 eV is assigned to the C-Si and $CH_2$ of the MPTMS-APTES layer, while the component at 286 eV is ascribed to the C-S and C-N bond; their area ratio was constrained to be 2:1 as expected from the stoichiometry of the model showed in Figure 5.1. The C-Si and $CH_2$ also observed in M-gold samples were shifted by +0.4 eV in A-gold samples. The component at 289 eV of the C 1s can be ascribed to the presence of COO species probable related to the formation of carbamate by reaction of APTES amino groups with the $CO_2$.

The N 1s high resolution spectra in Figure 5.9c showed multiple components that were fitted by considering three different components at 399.8 eV, 400.8 eV, and 402.2 eV. These components were assigned to -$NH_2$, NHCOO (carbamate), and -$NH_3^+$ [22]. The presence of the NHCOO carbamate component supports the identification of the COO component in the C 1s spectra at 289 eV. The -$NH_2$ components can be ascribed to the free amino groups of the APTES chain, while the -$NH_3^+$ contribution may be associated with weak hydrogen bonds between amino groups of the APTES along with the presence of water and humidity, which can cause the formation of -$NH_3^+$.

The signal shape of the O 1s spectra suggests the presence of two additional components aside from the main component observed in the M-gold samples attributed to the O-Si groups. The binding energy associated with these two components are 534.2 eV and 531.1 eV, respectively, and are they are assigned to the C-O and C=O of the carbamate respectively; their area ratio was constrained to be 1 : 1.

The curve fitting model exploited on M-gold samples has been applied to the S 2p and Si 2p signals of the A-gold samples (Figure 5.9e and 9f). On both signals, a chemical shift of +0.4 eV in the binding energies was observed with respect to the binding energies observed on M-gold.

Table 5.3 summarized the binding energies of the most intense peaks as well as the quantitative analysis results obtained on A-gold samples. It is worth noting that also in the case of A-gold samples C 1s, the methoxide component is observed, suggesting that also after the functionalization with APTES not all the methoxide groups are hydrolysed.

*Table 5.3 Binding energies values (eV) and composition (at%) for A-Gold samples. Mean values over three independent measurements are reported; the standard deviations are given in parentheses.*

| | **Binding energy (eV)** | **A-Gold at %** | **Expected stoichiometry (at%)** |
|---|---|---|---|
| **C 1s C-Si, C-C** | 285.3 (0.1) | 27 (1) | 30 |
| **C 1s C-S** | 286.0 (0.2) | 13 (1) | 15 |
| **C 1s Methoxide** | 287.0 (0.2) | 4 (1) | - |
| **C 1s O-C=O carbamate** | 289.2 (0.2) | 1.2 (0.2) | - |
| **O 1s C=O* carbamate** | 531.1 (0.2) | 1.3 (0.5) | - |
| **O 1s Si-O-Si** | 532.7 (0.1) | 23 (2) | 23 |

| | | | |
|---|---|---|---|
| **O 1s O*-C carbamate** | 534.2 (0.1) | 1.3 (0.5) | - |
| **S 2p** | 164.1 (0.1) | 10 (2) | 10 |
| **Si 2p** | 102.7 (0.1) | 15 (1) | 15 |
| **N 1s -NH$_2$** | 399.8 (0.3) | 3 (1) | 3 |
| **N 1s NHCOO** | 400.8 (0.3) | 1.2 (0.4) | - |
| N 1s -NH$_3^+$ | 402.2 (0.3) | 0.6 (0.1) | - |

The experimental composition (at%) obtained by quantitative analysis of the XPS measurement on A-gold samples, shows a N 1s and S 2p atomic ratio equal to 1 : 2 (Table 5.3); this result may suggest that the reaction between MPTMS and APTES is not 1:1, but a reaction of one molecule of APTES every two molecules of MPTMS is most probable. This is substantiated by the atomic ratio of Si 2p and S 2p signals that is equal to 1.5 : 1; the expected stoichiometry reported in Table 5.3 is calculated considering a reaction ratio MPTMS : APTES equal to 2 : 1.

#### 5.3.3.2 ARXPS results

High-resolution ARXPS spectra were collected on A-gold samples and are presented in Figure 5.10. Figure 5.10c, shows that the N 1s signal was revealed at angles above 28.6 degrees, indicating its presence in the outermost surface layer, as predicted by the model provided in Figure 5.3.

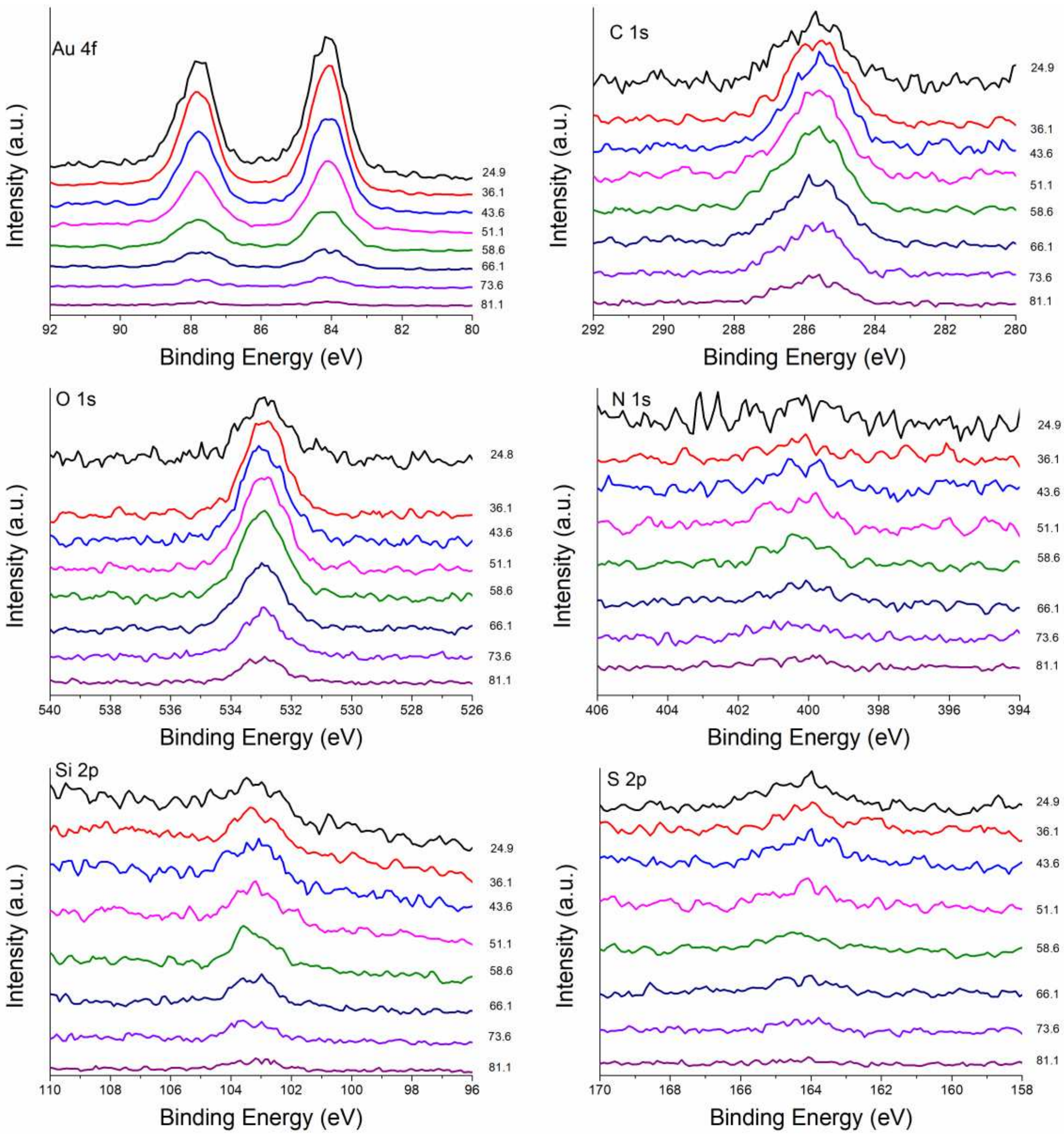

*Figure 5.10 High-resolution spectra of Au 4f (a), C 1s (b), N 1s, (c), O 1s (d), S 2p (e) and Si 2p (f) acquired in angle-resolved XPS*

Figure 5.11a shows the apparent concentration (at%) calculated at each emission angle for carbon bonded to silicon, nitrogen, sulphur, silicon, gold, and the oxygen ascribed to O-Si groups. Gold apparent concentration decreases at higher emission angles, as observed also on M-gold samples, while C-Si and nitrogen concentrations increase at higher emission angles. The relative depth plot calculated for A-gold samples is also shown in Figure 5.11b. The relative depth plot confirms the spatial distribution proposed in Figure 5.2b for the -gold samples with the nitrogen located on the outermost surface and sulphur atoms at the gold-MPTMS interface.

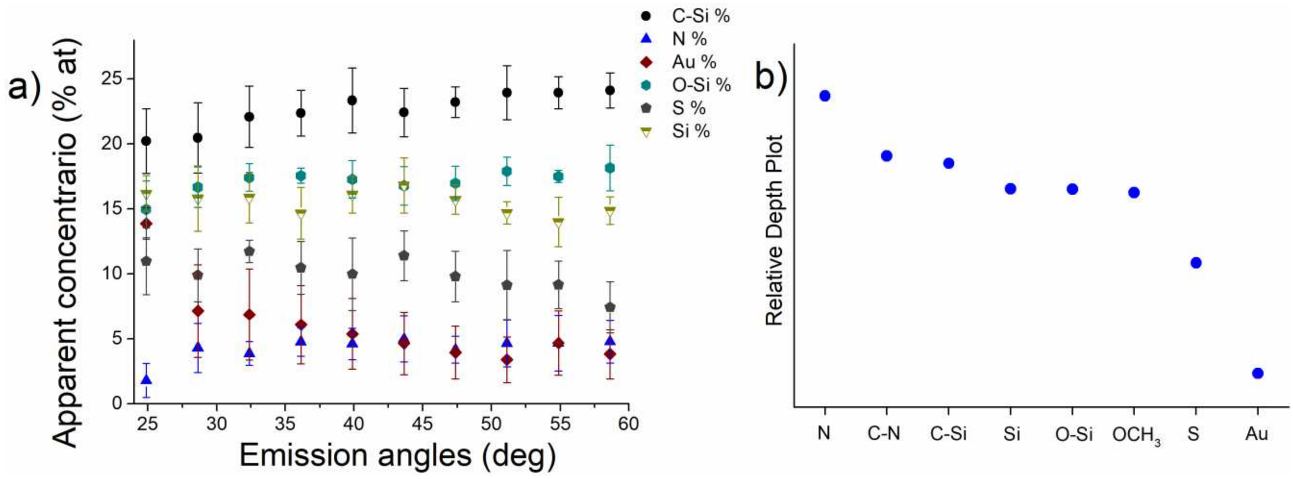

*Figure 5.11 Apparent concentration (%) versus emission angle calculated for Au, Si, S, C-Si, O-Si and N (a) and relative depth plot (b) for A-gold*

### 5.3.4 XPS and ARXPS results on G-gold

The results presented below were obtained from three samples of G-gold. The composition of the sample surface, reported in the following paragraphs, is the average of compositions obtained from three different analysed areas of three independent samples. The standard deviations are also provided in parentheses.

#### 5.3.4.1 XPS results

Figure 5.12 shows the survey spectrum of G-gold samples prepared as discussed in section 5.2.2. In the survey spectrum the signal of all the elements that were present in the A-gold samples, namely Au, C, O, N, Si and S, are still detectable.

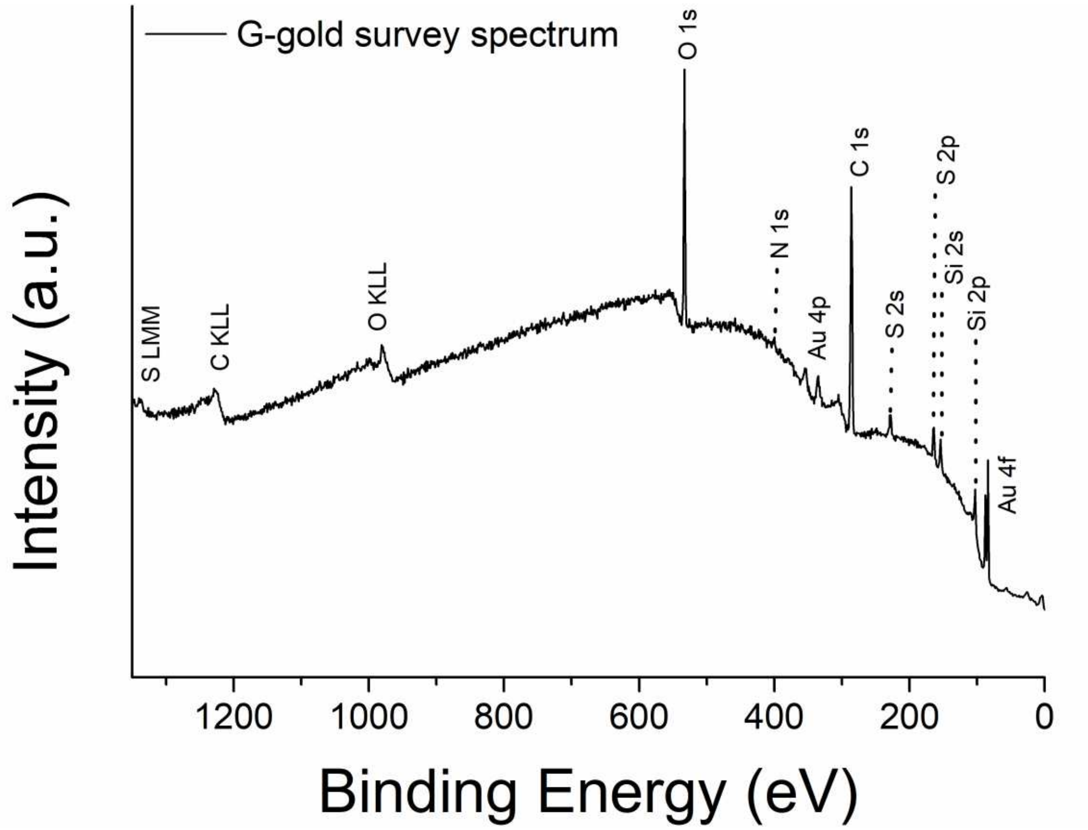

*Figure 5.12 Survey spectrum of G-gold sample*

Figure 5.13 shows the high-resolution spectra of the most intense signals revealed in G-gold: Au 4f, C 1s, N 1s, O 1s, S 2p and Si 2p, together with the X-ray induced Auger signals: C KLL, O KLL and S LMM.

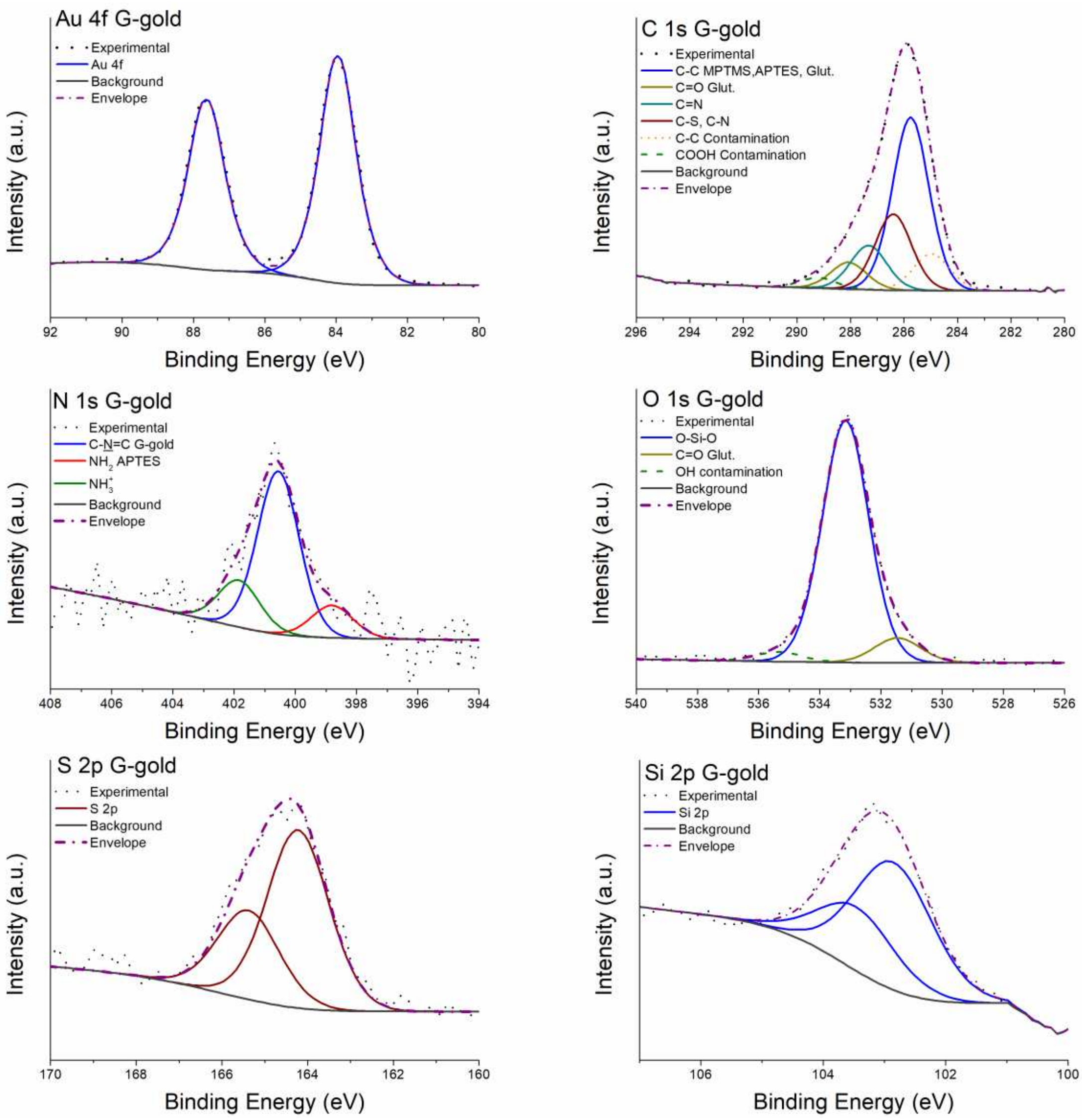

*Figure 5.13 High-resolution spectra of Au 4f (a), C 1s (b), N 1s (c), O 1s (d), S 2p (e) and Si 2p (f) acquired on G-Gold sample.*

The parameters used for curve-fitting in the G-gold sample were the same as those used for M-gold and A-gold. The glutaraldehyde layer strongly attenuated the S 2p and Si 2p signals (Figure 5.1 c). Both signals were fitted with a doublet, as shown in section 5.3.3.1 for A-gold. The C 1s signal was fitted with six components. Two of them were attributed to contamination, while the other four were ascribed to the functionalization layer. The components of the functionalization layer were detected at 285.6 eV, 286.2 eV, 287.4 eV and 288.0 eV and were assigned to C-C carbons of MPTMS, APTES and glutaraldehyde; C-S/C-N; C=N and C=O functional groups, respectively [22,38,39]. The C-C components were shifted by +0.3 eV with respect to the component C-Si/$CH_2$ found in A-gold samples. This shift might be due to the presence of many electronegative functional groups, such as C=O, Si-O, C-N, which could affect the binding energy of the C-C carbon atoms detected. The two components at 285 eV and 289.2 eV were assigned to the contamination layer.

The N 1s signal was observed to have three components, indicating the existence of different nitrogen chemical states. The most intense component was found to be at 400.6 eV, and it was attributed to the C-N=C group due to the reaction between the -$NH_2$ groups of APTES and the carbonyl groups of the glutaraldehyde (Figure 5.1 c). The other two components at 399.2 eV and 402.3 eV were ascribed to the presence of $NH_2$ and $NH_3^+$ groups, which were also observed on A-gold samples [22,38,39]. The presence of these two components suggests that the reaction between APTES and glutaraldehyde was not complete.

The O 1s signal had three components, with the most intense was found at 533.2 eV, assigned to the Si-O-Si associated to the silanes of MPTMS/APTES layer. The component at 531.5 eV was assigned to the C=O oxygen of the glutaraldehyde, while the small component at 535.1 eV was attributed to the contamination layer [38]. No area constraint was used for O 1s components, while the full width at half maximum at the peak height (FWHM) of the C=O and contamination components was imposed to be equal to the FWHM of O-Si component.

The quantitative analysis results are reported in table 5.4. The contribution of carbon from the contamination layer was not considered in the calculation.

*Table 5.4 Binding energies values (eV) and composition (at%) for G-Gold sample. Mean values over three different analysed areas of three sample are reported. The standard deviations are given in parentheses.*

| Element | BE (eV) | At% | Expected stoichiometry (at%) |
|---|---|---|---|
| **C 1s C-C MPTMS/APTES/GLUT** | 285.6 (0.2) | 30 (3) | 33 |
| **C 1s C-S/C-N** | 286.2 (0.2) | 13 (1) | 13 |
| **C=N and methoxy** | 287.4 (0.1) | 6 (3) | 4 |
| **C 1s C=O glut** | 288.0 (0.1) | 4 (2) | 3 |
| **COO contam.** | 289.2 (0.1) | 2.2 (0.4) | - |
| **N 1s $NH_2$** | 399.2 (0.2) | 1.3 (0.5) | 1 |
| **N 1s C-N=C** | 400.6 (0.1) | 2.0 (0.4) | 3 |

| | | | |
|---|---|---|---|
| **N 1s $NH_3^+$** | 402.3 (0.3) | 0.9 (0.1) | 1 |
| **O 1s O-Si** | 533.2 (0.1) | 19 (2) | 20 |
| **O 1s C=O** | 531.5 (0.1) | 3 (1) | 3 |
| **O 1s contam.** | 535.1 (0.2) | 2 (1) | - |
| **S2p** | 164.1 (0.1) | 6 (2) | 8 |
| **Si2p** | 102.9 (0.1) | 11 (2) | 13 |

The experimental atomic ratio between the components of the N 1s signals involved in the C-N=C bonds and non-reacted nitrogen of APTES was about 1.7:1, suggesting a reaction ratio APTES : glutaraldehyde of 5:3.

### 5.3.4.2 ARXPS results

Figure 5.14 shows the high-resolution spectra acquired in ARXPS for the most intense signals detected in the G-gold sample.

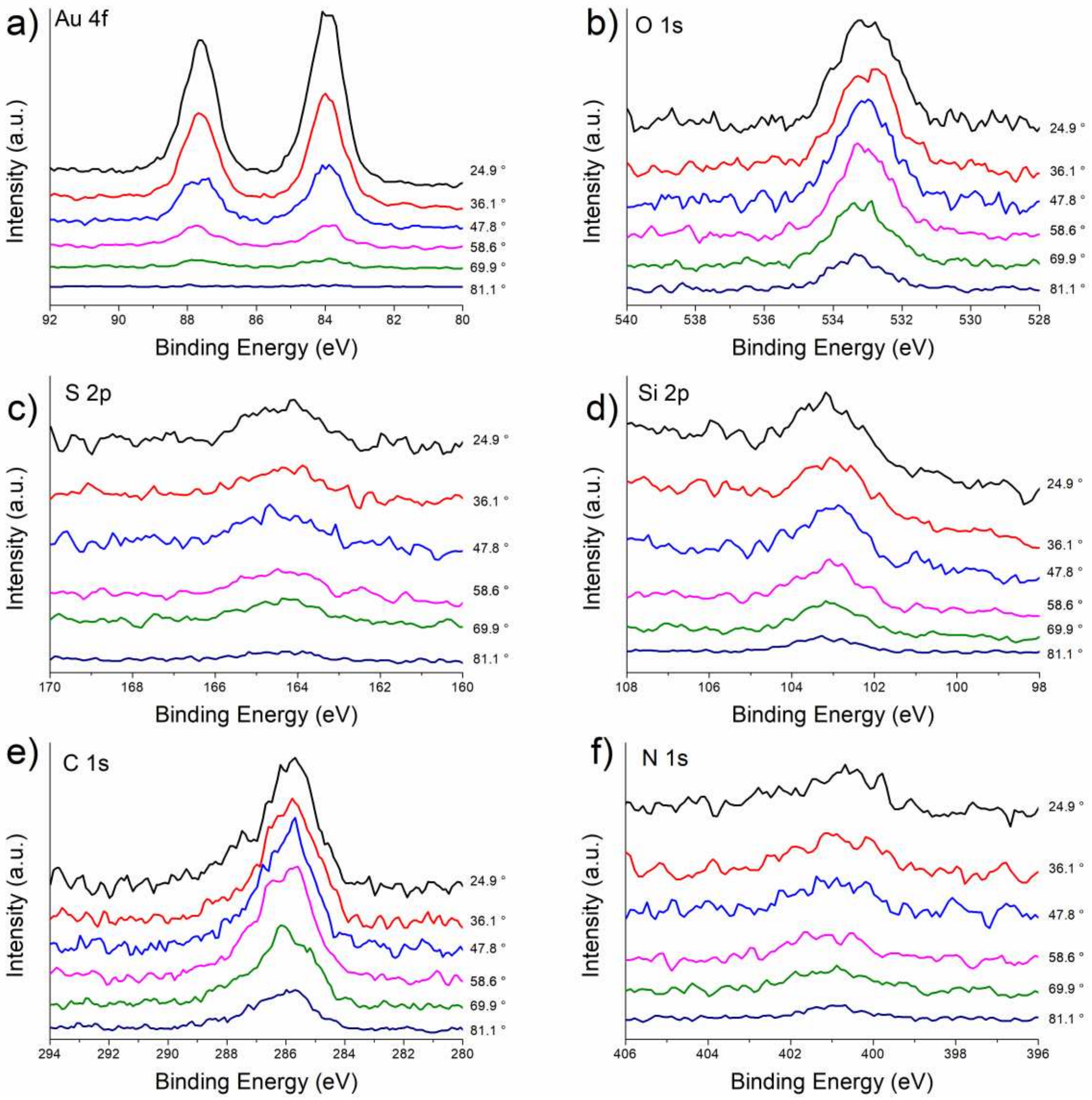

*Figure 5.14 High-resolution spectra of Au 4f (a), O 1s (b), S 2p (d), Si 2p (c), C 1s (e) and N 1s, (f) acquired in angle-resolved XPS*

Figure 5.15a shows the relationship between the apparent concentration of the characteristic functional groups of the functionalization layer and the emission angle. The concentration (at%) of Au decreases as the emission angle increases, which is expected because the gold signals come from the substrate. On the other hand, the apparent concentration of C-C increases with the emission angle, indicating that the carbon chain of the MPTMS/APTES/Glutaraldehyde (M/A/G) layer is facing the outer layer of the surface.

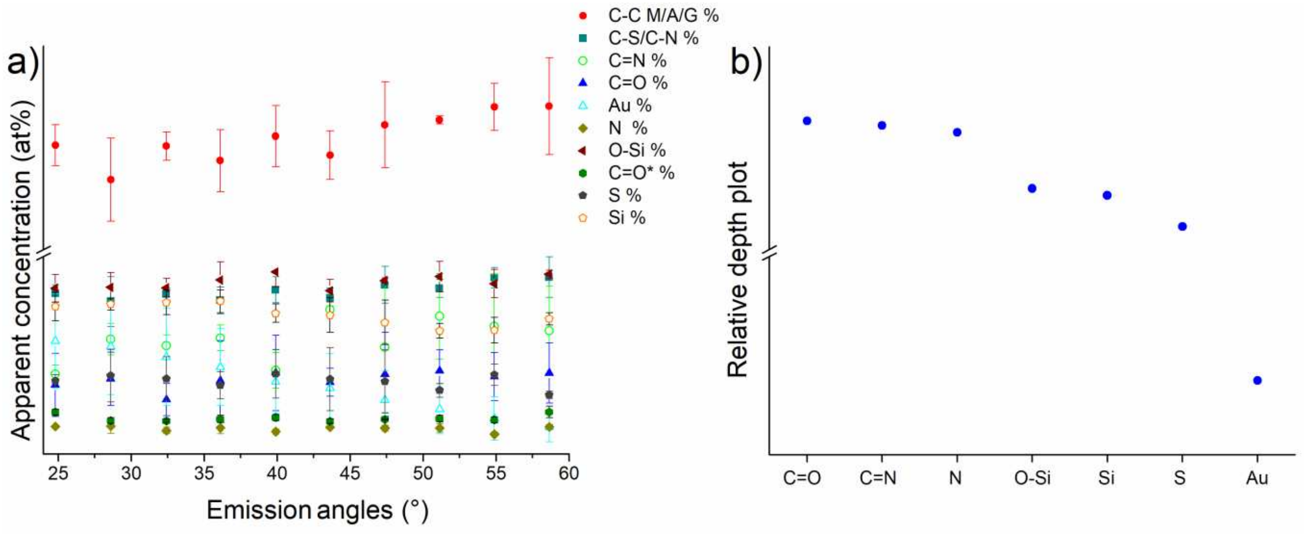

*Figure 5.15 Apparent concentration (%) versus emission angle calculated for Au, Si, S, C-C M/A/G, O-S, C=O and N (a) and relative depth plot (b) for G-gold. Mean values and standard deviation are calculated over the results obtained on three analysed areas of one sample.*

The relative depth plot reported in Figure 5.15b confirmed the spatial disposition of the functional groups with the C=O of the glutaraldehyde layer facing the outward layer and the gold atoms at the greater depth.

### 5.3.5 XPS and ARXPS results on P-gold

The following results obtained on P-gold were obtained by analysing a single sample; the concentration here reported, and the standard deviations are referred to three different analysed areas on the same sample.

#### 5.3.5.1 XPS results

In the survey spectrum (Figure 5.16), obtained from the gold sample functionalized with PHMG (P-gold), the absence of the Au 4f signal suggests the formation of a layer that is thicker than the sampling depth for the photoelectrons emitted from gold traveling through an organic layer. This layer can be estimated to be 6 nm (see Chapter 3, paragraph 3.1.1, equation 3.5). However, the Si 2p and S 2p signals are still detected but are strongly attenuated. The C 1s and N 1s signals are the most intense signals observed in the spectrum, indicating the presence of PHMG on the sample surface (Figure 5.1 d). Furthermore, signals of chlorine (Cl 2p, Cl 2s and Cl LMM) and sodium (Na 2s, Na 1s and Na KLL) are also detected. The presence of these signals can be attributed to the procedure followed for synthesizing PHMG (Chapter 4, paragraph 4.2.1.4). The vitreous PHMG was dissolved in a saturated NaCl solution and heated, then the PHMG was precipitated as a chloride salt when the solution cooled down.

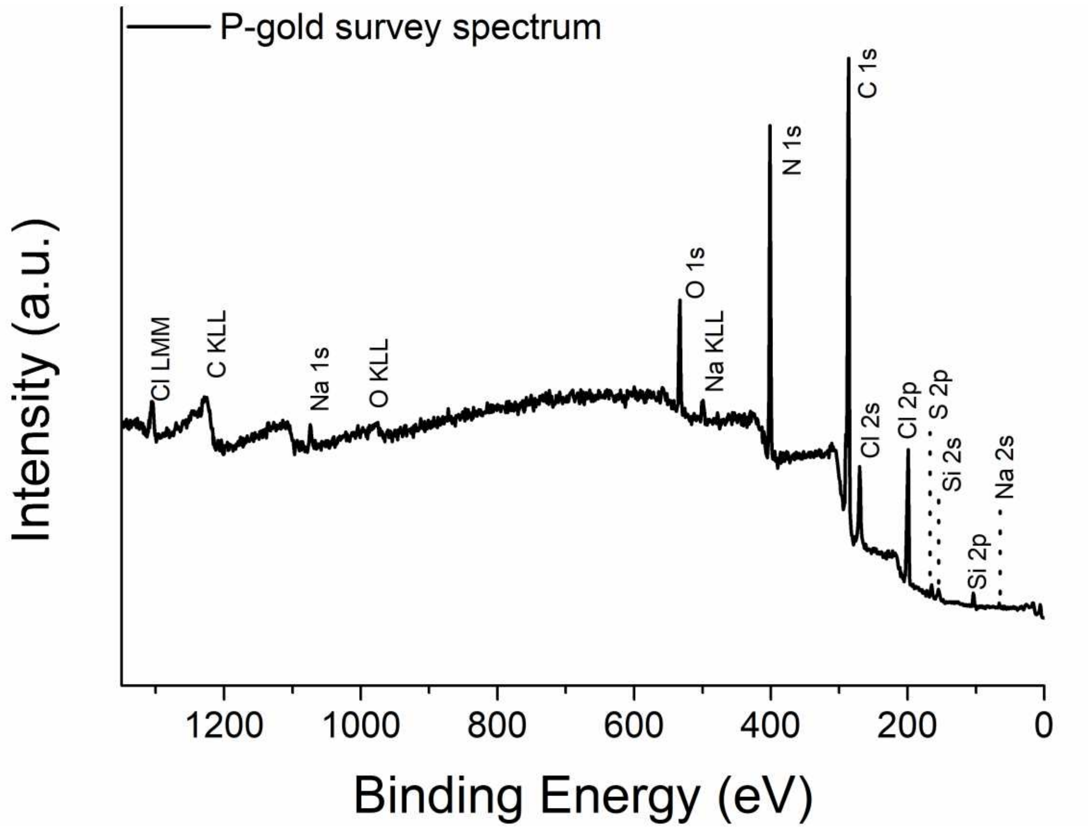

*Figure 5.16 Survey spectrum of P-gold sample*

Figure 5.17 shows the high-resolution spectra of the most intense signals ascribed to the functionalization layer.

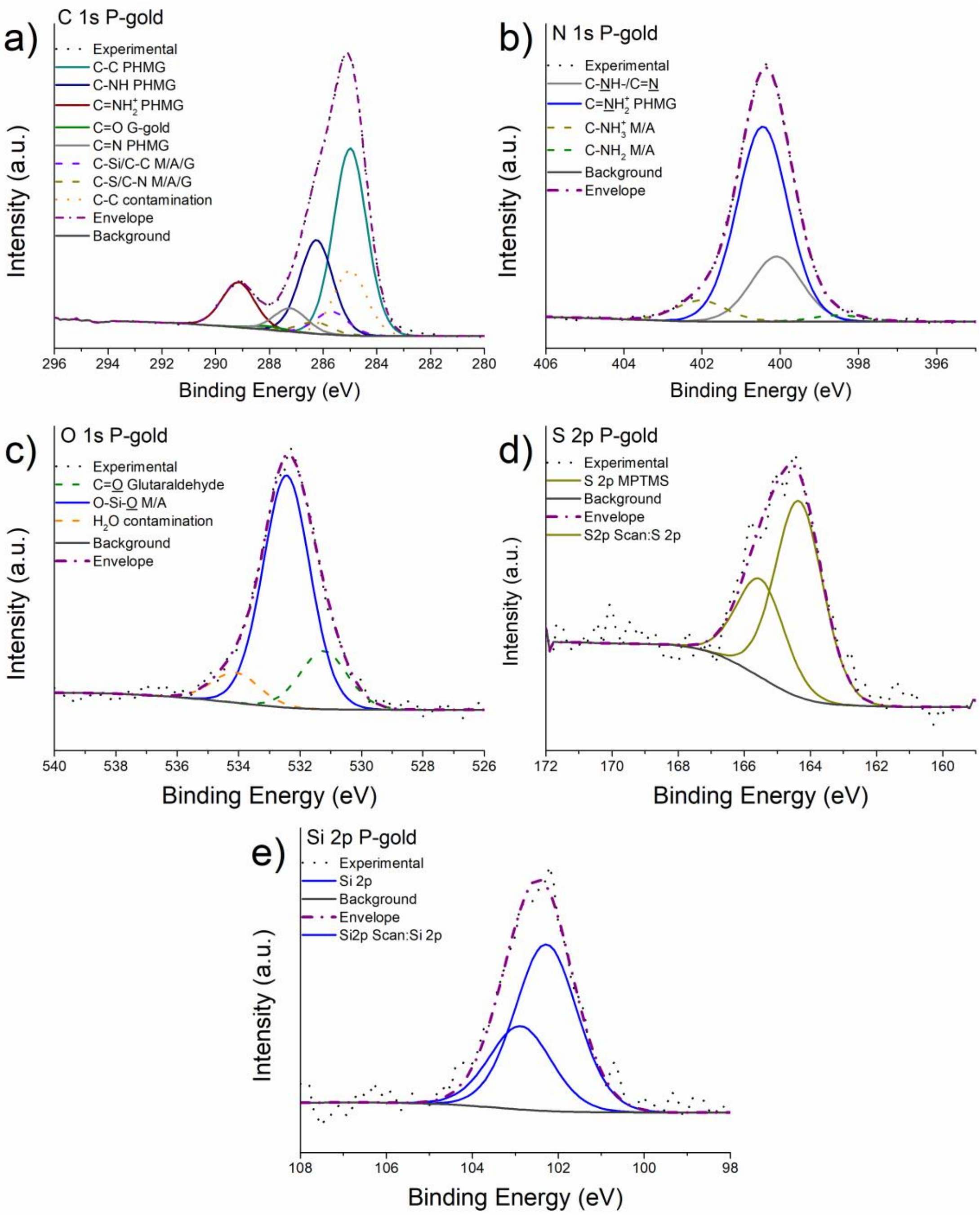

*Figure 5.17 High-resolution spectra of C 1s (a), N 1s (b), O 1s (c), S 2p (d) and Si 2p (e) acquired on P-Gold sample*

The absence of the Au 4f signal led to select the C-C component, ascribed to the PHMG layer, as internal reference of the binding energy scale; its value was set at 285 eV [40]. The C 1s signal of P-Gold sample was processed by curve fitting with four synthetic components assigned to the PHMG: three contributions due to C- Si, C-N and C-C from functionalization layers on gold substrate. Specifically, the C-C carbon chain of the PHMG was found at 285 eV, C-NH groups at 286.2 eV [22] and C=N due the reaction between glutaraldehyde and the amino groups of the PHMG and the iminium groups C=NH$_2^+$ [41,42] at 287.0 eV and 289.0 eV, respectively. The area ratio of the C-C and C-NH components was constrained to be equal to 2:1 as the PHMG molecule (Figure 3.4) has an atomic ratio of 2:1 between the aliphatic carbon atoms and the secondary amine (C-NH-) carbon atoms. Although S 2p and Si 2p signals were detected, the C 1s spectra were fitted by considering the contribution of various functional groups associated with the previous steps such as the presence of the components ascribed to the C-Si/C-C of the M/A/G layer. The binding energies of these groups were fixed based on the binding energy values reported in Table 5.4 for G-Gold sample.

The O 1s signal was fitted with three components. Two of them were attributed to the preceding functionalization steps O-Si groups at 533.0 eV and C=$\underline{O}$ at 531.5 eV of the glutaraldehyde layer. This suggests that there might be some non-reacted glutaraldehyde. The presence of the carbonyl group also in the C 1s spectra confirms that not all the glutaraldehyde carbonylic groups underwent reaction with the PHMG.

As far for the N 1s signal, two intense components were found at 400.6 eV and 400.1 eV. These were assigned to the C-$\underline{N}$H and $C=NH_2^+$ of the PHMG respectively [42]. Additionally, two more small components were found at 402.5 eV and 399.8 eV suggesting the presence of $-NH_2$ and $-NH_3^+$ groups observed also in the A-gold samples [22].

The quantitative analysis results calculated considering all these contributes are reported in Table 5.5.

*Table 5.5 Binding energies values (eV), composition (at%) for P-Gold sample. Mean values over three different analysed areas of one sample are reported. The standard deviations are given in parentheses*

| | **Line** | **BE (eV)** | **Concentration (at%)** |
|---|---|---|---|
| **PHMG** | C 1s C-C PHMG | 285.0 (0.1) | 29 (3) |
| | C 1s C-N PHMG | 286.2 (0.1) | 15 (2) |
| | C 1s $\underline{C}=NH_2^+$ | 289.3 (0.1) | 8 (0.3) |
| | C 1s $\underline{C}$=N PHMG | 287.0 (0.1) | 3 (1) |
| | N 1s C-$\underline{N}$H | 400.6 | 15 (1) |

| | | | |
|---|---|---|---|
| **MPTMS**<br>**+**<br>**APTES**<br>**+**<br>**Glutaraldehyde**<br>**(M/A/G)** | | (0.1) | |
| | N 1s $C{=}\underline{N}H_2^+$ | 400.1 (0.1) | 5 (0.4) |
| | C 1s $\underline{C}{=}O$ | 288.1 (0.1) | 2 (1) |
| | C 1s C-Si/C-C M/A/G | 285.7 (0.1) | 4 (2) |
| | C 1s C-S, C-N M/A/G | 286.2 (0.1) | 1.5 (1) |
| | N 1s $NH_2$ | 399.1 (0.2) | 0.4 (0.2) |
| | N 1s $NH_3^+$ | 402.4 (0.2) | 1.4 (0.2) |
| | $C{=}\underline{O}$ | 531.6 (0.2) | 2.0 (0.4) |
| | O1s O-Si | 532.9 (0.2) | 4 (1) |
| | S2p | 164.2 (0.2) | 1.2 (0.4) |
| | Si2p | 103.2 (0.2) | 2.5 (0.4) |

#### 5.3.5.2 ARXPS results

The high-resolution spectra in ARXPS have been acquired also for the P-gold sample and are reported in Figure 5.18. While C 1s, O 1s and N1s are detected at all emission angles, the sulphur and silicon signals are barely visible at high emission angles (Figure 5.18d and e).

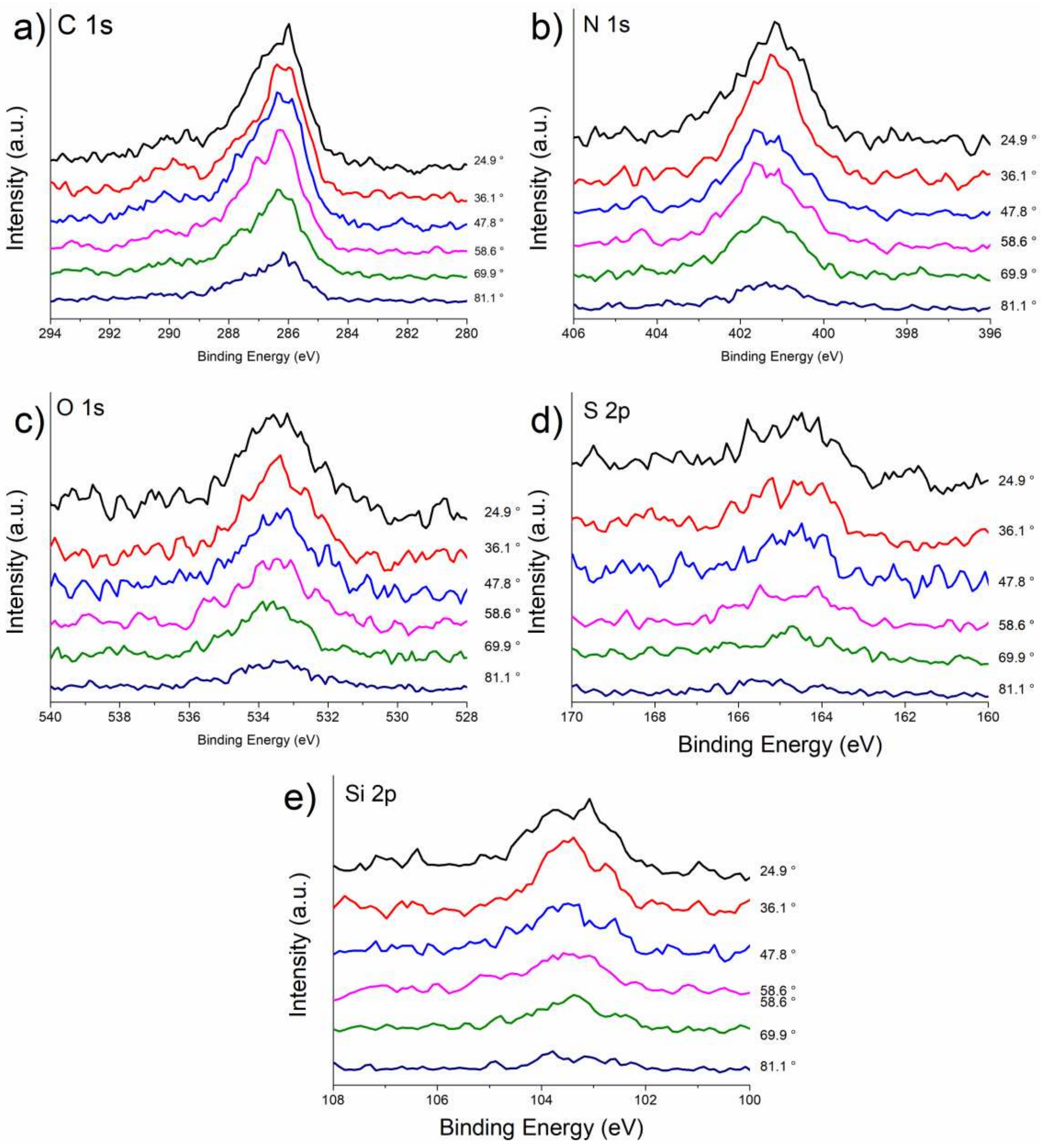

*Figure 5.18 High-resolution spectra of C 1s (a), N 1s (b), O 1s (c), S 2p (d), Si 2p (e) acquired in angle-resolved XPS for P-gold sample*

Figure 5.19a shows the apparent concentration of the elements of the P-gold sample at different emission angles. For P-gold, it can be observed that the C-C of PHMG concentration increases for angles greater than 24 degrees remaining constant between 28 and 58 degrees. The same trend is observed for the -NH-, $C=NH_2^+$. However, the C=O % functional group of the glutaraldehyde from the previous functionalization step decreases at high emission angles. The relative depth plot in figure 5.19b confirms the spatial structure of the functional groups.

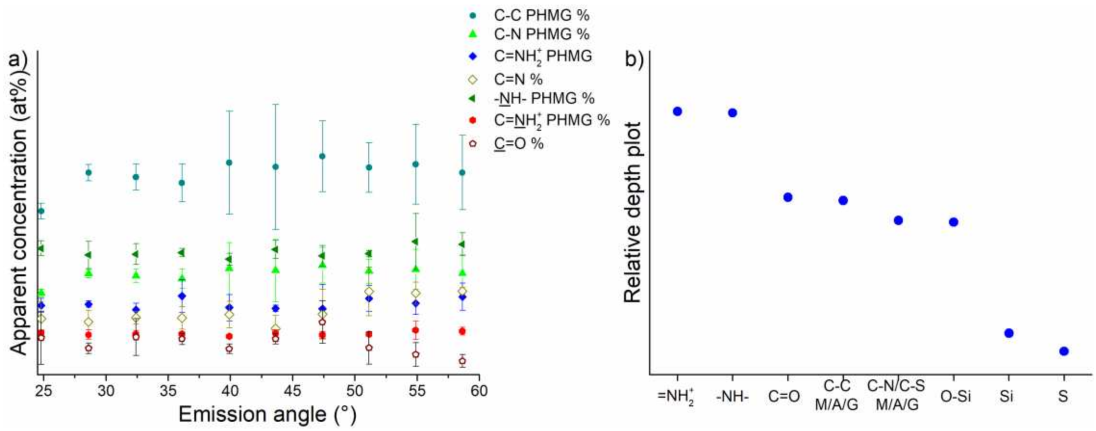

*Figure 5.19 Apparent concentration (%) versus emission angle calculated for C-C, C-N, C=NH$_2^+$, C=NH$_2^+$, -NH-, and C=O (a) and relative depth plot (b) for P-gold. Mean values and standard deviation are calculated over the results obtained on .three analysed areas of one sample.*

## 5.4 Thickness estimation

Different methodologies exploiting XPS and ARXPS have been reported in the literature for the estimation of the thickness of the functionalization layer [17,24,26]. Hill et alii proposed a method for measuring the thin film thickness on a substrate by applying the Hill's equation [43](Equation 1):

$$I_O = I_S\, e^{-\frac{t}{\lambda cos\theta}} \qquad 1)$$

Where 't' is the overlayer thickness, '$\theta$' is the emission angle and $\lambda$ is the attenuation length. The overlayer is assumed to be homogeneous, and the attenuation length is considered equal for both the bulk and the overlayer. Since in this work only angles below 60 degrees are taken into account in the thickness estimation, the elastic scattering is considered negligible and the IMFP has been used in the calculation instead of attenuation length [44]. Moreover, this approximation can be applied since the overlayer thickness is supposed to be lower than the IMFP. Since in the case of the system presented in this work, there are no element in common between the substrate and the organic overlayer, equation 1 cannot be used. For this reason, the thickness has been calculated applying a different equation based on the ARXPS results, considering the attenuation of the Au 4f signal intensity ($I_{Au}$) measured at two different emission angles, grazing (58.6 degrees) and near vertical (24.8 degrees). For this purpose, the following equation was used:

$$ln\left(\frac{I_{Au24°}}{I_{Au58°}}\right) = -\frac{t}{\lambda_{Au}}\left(\frac{1}{cos\,(58)} - \frac{1}{cos\,(24)}\right) \qquad 2)$$

$$t = \frac{ln\left(\frac{I_{Au24°}}{I_{Au58°}}\right)\cdot\lambda_{Au}}{cos(24)-cos(58)} \quad 3)$$

The same equation was applied to the S 2p and Si 2p intensities for M-gold, and N 1s for A-gold for calculating the respective thickness. IMFP was calculated according to Seah and Dench [32], since this model allows estimating IMFP value without considering the density. This approximation is necessary in this work, since the density of the MPTMS anchored on gold and of the APTES-MPTMS layer bound to gold are not known. The thickness values reported in Table 5.6 were calculated on three different analysed areas of three independent samples.

*Table 5.6 Total thickness of the overlayers calculated on M-gold and A-gold based on the attenuation of the elements Au, S, Si and N according to equation 3.*

| **Element** | **Au** | **S** | **Si** | **N** | **C=<u>O</u>** |
|---|---|---|---|---|---|
| **IMFP λ (nm)** | 2.02 | 3.16 | 3.24 | 3.06 | 2.68 |
| **Thickness M-Gold (nm)** | 1.9 (0.3) | 1.4 (0.3) | 1.1 (0.2) | - | - |
| **Thickness A-Gold (nm)** | 1.8 (0.3) | 1.2 (0.4) | 0.6 (0.2) | 0.3 (0.1) | - |

The total thickness of M-Gold was determined to be 1.9 (0.3) nm, considering the attenuation of the gold signal, and considering the MPTMS layer, the contamination layer ($l_c$), and the gold substrate. The calculated thickness, considering Si 2p electron attenuation, is 1.1 (0.2) nm, representing the sum of $l_c$ and O-CH3 groups. For A-Gold samples, the total thickness is 1.8 (0.3) nm, with the layer thickness determined by N 1s electron attenuation estimated at 0.3 (0.1) nm. These findings suggest a lower contamination layer thickness ($l_c$) on A-Gold compared to M-Gold samples with the MPTMS layer.

The preliminary results obtained on G-gold and P-Gold suggest the formation of a complex system and was not possible to estimate the layer thickness, additional measurements are required for understanding the functionalization mechanism.

## 5.5 Discussion

The investigation of functionalized surface layers on substrates like polymers or carbon-based materials with MPTMS and APTES can be challenging because of the overlapped components in the C 1s signals, from both the substrate and the different functionalized layers. To overcome this problem, the use of a model system as freshly cleaved gold, which is a carbon-free substrate with an ideally flat surface, can be crucial for determining curve-fitting parameters, especially for the C 1s spectrum, and avoiding interference from carbon atoms in substrates like PVC. By using the U 3 Tougaard background for background subtraction, XPS and ARXPS high-resolution spectra can be processed to simulate conditions for polymer surface characterization [29]. Parameters for curve fitting, including signal shape (G/L ratio), FWHM, and area ratios, were determined for C 1s, O 1s, Si 2p, S 2p, and N 1s spectra, enabling the identification of components ascribed to the functionalization layer. Through quantitative analysis, it was found that the mechanism of grafting MPTMS with APTES was a 2 MPTMS: 1 APTES reaction.

### 5.5.1 Spatial arrangement of the functional groups

*APTES:* In the scientific literature, the reaction between MPTMS and APTES has been documented [5]. Based on the expected stoichiometry using the model shown in Figure 5.1, a sulphur to nitrogen ratio of 1:1 is expected. However, quantitative analysis results presented in Table 5.3 revealed a sulphur to nitrogen ratio of 2:1, suggesting a possible different reaction mechanism. Various studies have explored the functionalization of $SiO_2$ substrates with APTES, and proposed different possible behaviours of this molecule during the functionalization process [13,22,45,46]. Figure 5.20 (a-d) provides a schematic representation of the various possible arrangements that APTES molecules might assume to produce A-Gold samples, with different reaction pathways corresponding to each arrangement.

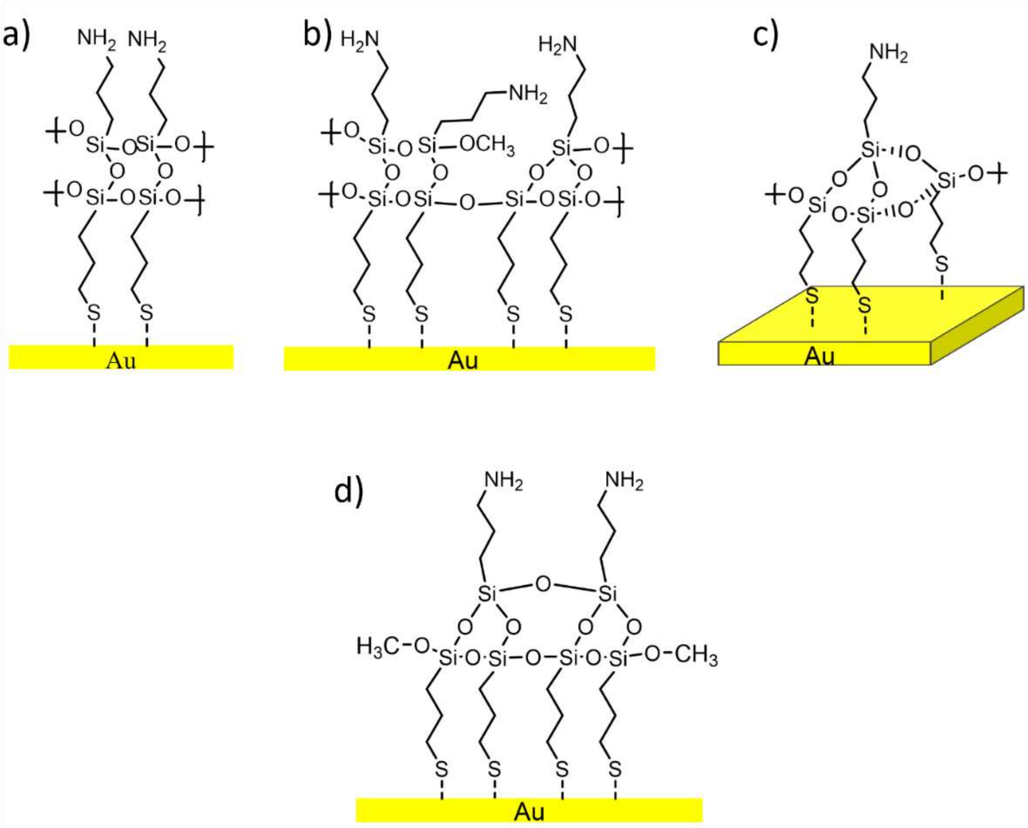

*Figure 5.20 Possible arrangement of APTES onto MPTMS functionalized gold surface (M-Gold) due to different APTES to MPTMS ratios: (a) APTES:MPTMS = 1:1; (b) APTES:MPTMS = 3:4; (c) APTES:MPTMS = 1:3; (d) APTES:MPTMS = 1:2.*

Figure 5.20a shows the expected result according to the literature [5], but the experimental results (Table 5.3) do not agree with the model stoichiometry. Additionally, Figure 5.20b and 20c can be excluded since the expected sulphur to nitrogen ratios for these reaction schemes are 4:3 and 3:1, respectively. The most likely arrangement of APTES in A-gold samples is shown in Figure 5.20d, where the sulphur to nitrogen ratio is 2:1, matching the experimental results.

*Glutaraldehyde:* The experimental results reported in Table 5.4 suggest that also the glutaraldehyde and APTES moieties do not react with a 1:1 ratio. This is because the N 1s spectra showed the presence of different components for the nitrogen on G-gold surfaces. If the concentration in at% is considered, a reaction ratio APTES : Glutaraldehyde equal to 5:3 can be proposed, leading to the formation of a functionalization layer that follows the scheme showed in figure 5.21. However, it is necessary to analyse more samples to prove the reproducibility.

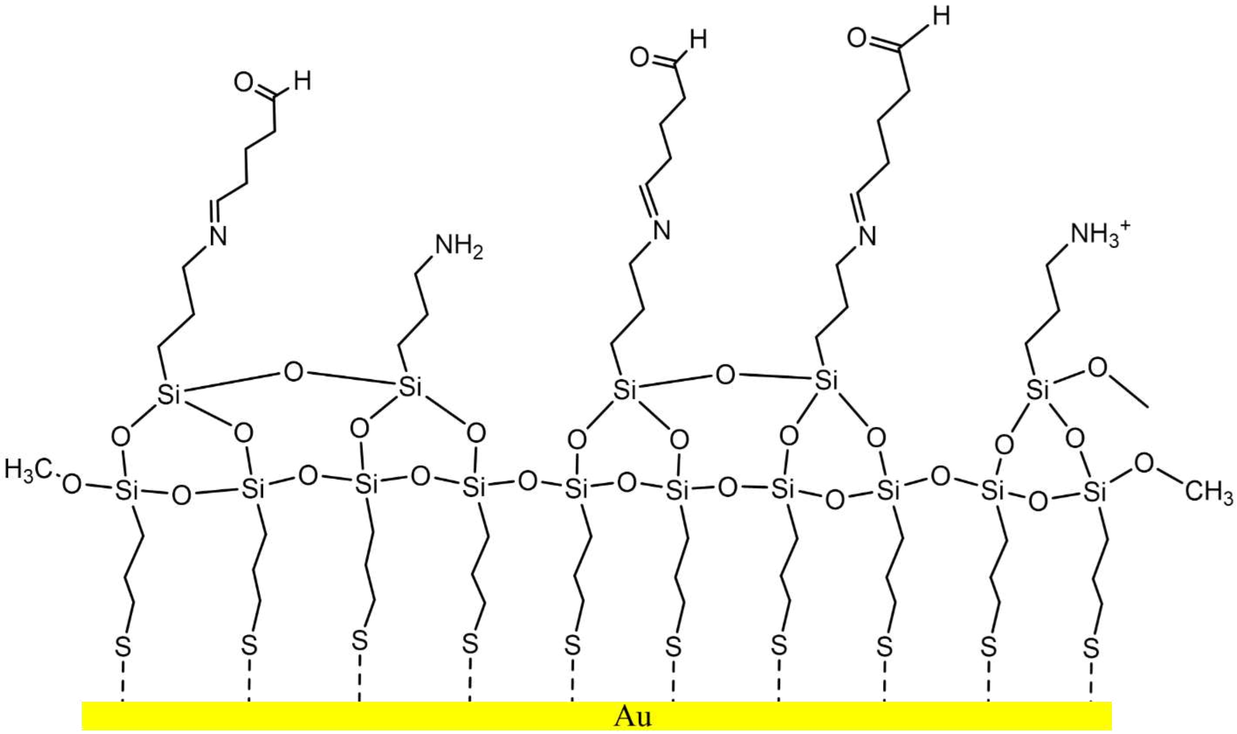

*Figure 5.21 Possible arrangement of glutaraldehyde onto A-gold surface*

*PHMG:* It is worth noting that the presence of the C=O component in both C1s and O1s spectra suggests that not all the glutaraldehyde reacts with the PHMG. According to Table 5.5, only 2% of C=O is present, indicating that the possible reaction ratio between glutaraldehyde and PHMG is 2:1. However, this ratio may vary as PHMG can react with other PHMG molecules, leading to the formation of a multilayer structure. Figure 5.22 shows a possible arrangement of the PHMG layer. More experiments are necessary to check the reproducibility of the synthesis and a more complex model should be developed for interpreting the data.

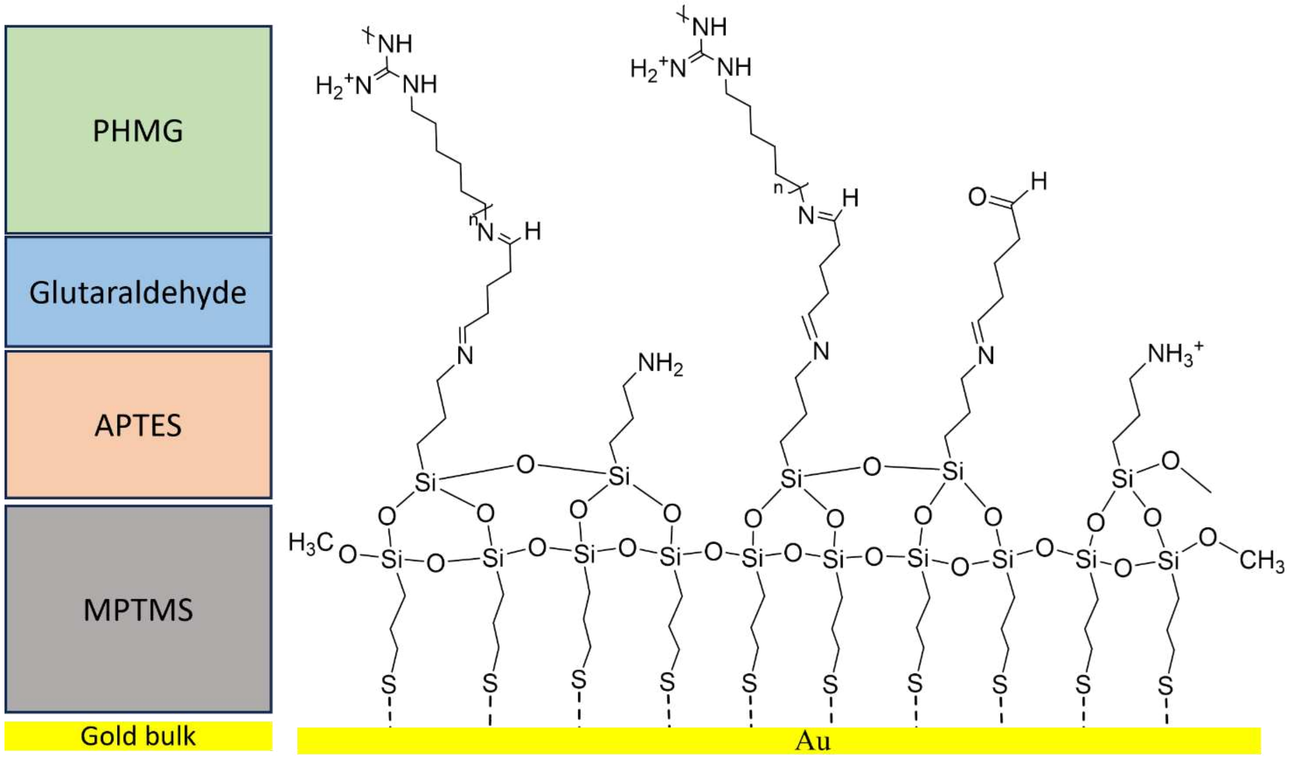

*Figure 5.22 Possible arrangement of PHMG onto G-gold surface*

### 5.5.2 Estimation of the layer thickness of the different functionalized steps

M-Gold: According to the ARXPS results, the total layer thickness calculated for M-Gold samples using equation (3) is 1.9 ± 0.3 nm (Table 5.6). This thickness comprises the contamination layer ($l_c$) and the functionalization layer of MPTMS (t), as illustrated in Figure 5.20. Utilizing equation (3) and considering the attenuation of the sulphur signal (Table 5.6), the total thickness is calculated to be 1.4 ± 0.3 nm, comprising both the MPTMS layer and the contamination layer. By employing the same equation and considering silicon, a thickness of 1.1 ± 0.2 nm is calculated, consisting of $l_c$ combined with the -OCH$_3$ groups situated at the outer part of the MPTMS layer. Avogadro software calculations estimate the bond length of -OCH$_3$ groups to be 0.2 nm, thus resulting in a contamination layer thickness ($l_c$) equal to 0.9 nm. As indicated in Table 5.6, the calculated thickness of the MPTMS layer t is estimated to be 0.5 nm (thickness calculated from the attenuation of the sulphur, 1.4 nm, minus the $l_c$ estimated to be 0.9 nm). The chain length of the MPTMS molecule is determined using Avogadro software, and the distance between sulphur and silicon is found to be 0.47 nm. These results, summarized in Table 5.7, are in good agreement with the experimental data reported in the case of the MPTMS layer formed onto PVC samples [47].

*Table 5.7 Summary of the thickness of the functionalized layer and the contamination layer on gold*

| Layer | Freshly cleaved gold | MPTMS on gold | MPTMS + APTES on gold |
|---|---|---|---|
| **Contamination $l_c$** | 0.4 nm | 0.9 nm | 0.3 nm |
| **Layer thickness t** | - | 0.5 nm | 0.9 nm |
| **Avogadro calculation** | - | 0.47 nm | 1.0 nm |

*<u>A-gold:</u>* The same considerations have been made for A-gold samples, the layer thickness calculated by applying equation (3) considering the attenuation of sulphur signal was estimated to be 1.2 ± 0.4 nm, thus including the two functionalization layers (MPTMS+APTES) and the contamination layer ($l_c$). By calculating the attenuation of nitrogen photoelectrons, a layer thickness of 0.3 ± 0.1 nm was calculated, the contamination layer can be estimated to be about 0.3 nm. Subtracting the contamination layer thickness from the thickness calculated considering the attenuation of sulphur photoelectrons (1.2 nm), an overlayer comprising MPTMS+APTES of 0.9 nm can be estimated. The distance between sulphur atoms of the MPTMS and nitrogen atoms of APTES calculated by an Avogadro simulation was 1 nm, thus resulting in a good agreement between the experimental results and the Avogadro simulation.

The contamination layer $l_c$ calculated for A-gold samples was lower with respect to the contamination layer thickness calculated on M-gold samples. This result can be attributed to the presence of the nitrogen atoms in the outer layer of the A-gold sample. Indeed, as observed in the 5.3.3.1 section (Table 5.2, Figure 5.9) nitrogen showed the presence of more than one components apart of the -$NH_2$ component (NHCOO carbamate and $NH_3^+$), the presence of these polar groups can hinders the formation of a thick contamination layer. Similar values of contamination layer have been suggested in the literature [22] where contamination layer thickness was estimated in the range between 0.1 and 0.5 nm for APTES monolayer on silicon substrates.

It is worth noting that the thickness calculated with Au, S and Si for A-gold samples is lower than the one calculated on the M-gold samples. Avogadro simulations suggest that the distance between Si and N atoms following the functionalization with APTES is 0.44 nm. Taking into account the contamination layer that is 0.3 nm (Table 5.7) and assuming the formation of a layer of APTES with no tilt angle, the total thickness of APTES layer (APTES + $l_c$) can be expected to be around 0.74 nm. Hence, the APTES layer thickness formed after the reaction with M-gold surfaces is lower than the contamination layer calculated for M-Gold samples (0.9 nm). Furthermore, the distance between sulphur and silicon atoms of the MPTMS measured on Avogadro after the addition of APTES slightly decreases form 0.47 nm to 0.41 nm.

Based on these results the models for M-gold and A-gold are proposed in Figure 5.23.

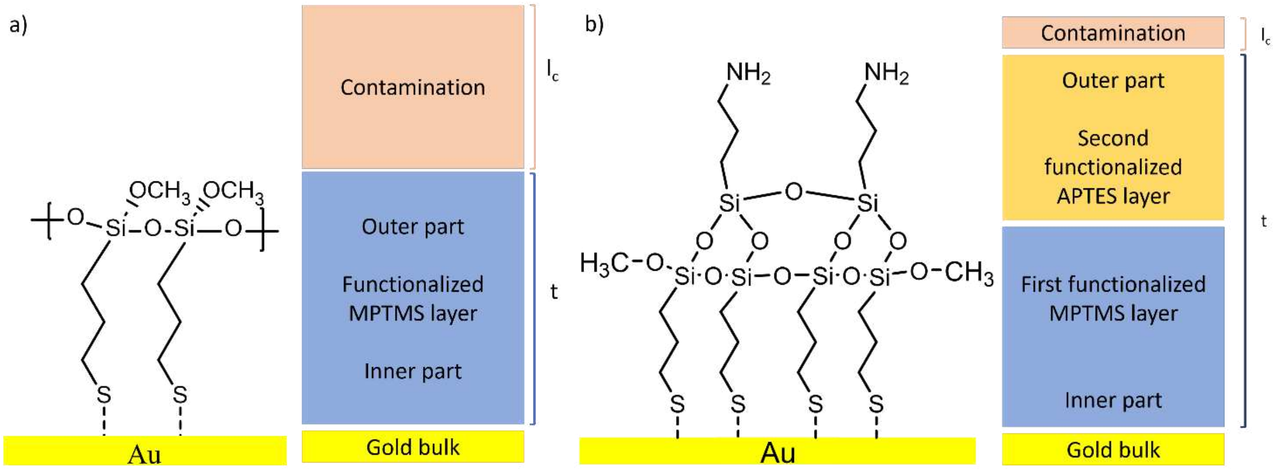

*Figure 5.23 Idealized model for MPTMS functionalization (M-gold, a) and MPTMS + ATPES functionalization (A-gold, b) based on XPS and ARXPS results*

The proposed model for the M-gold (Figure 5.23a) consists of three layers: gold substrate, MPTMS layer bonded via sulphur and a thick contamination layer. The A-gold model consists of four layers instead: the gold substrate, a MPTMS layer and a second layer of APTES following the functionalization procedure through polymerization of Si-O functional groups, and a thin contamination layer on top (Figure 5.23b).

It was not possible calculate the layer thickness on G-gold and P-gold, since the XPS since the XPS results suggests the formation of a more complex system and its characterization is challenging. Additional measurements on these samples are required to demonstrate the reproducibility of the experiment and to better understand the functionalization mechanism.

### 5.5.3 Chemical shift and estimation of the composition of the different functionalized layers

M-gold and A-gold: The expected stoichiometry was calculated based on the proposed model in Figure 5.20 for gold surface functionalized with MPTMS and MPTMS+APTES and are reported in

Table 5.8 for comparison with the experimental results determined by XPS. The experimental results are in good agreement with the theoretical stoichiometry, thus confirming the proposed models in Figure 5.20.

*Table 5.8 Experimental (mean value and standard deviation calculated over results obtained on three different areas of three independent samples) and calculated composition of the functionalized layer M-gold and A-gold*

| **Functional group** | **M-gold (at%)** | | **A-gold (at %)** | |
|---|---|---|---|---|
| | Experimental | Calculated | Experimental | Calculated |
| **C-Si, C-C** | 27 (2) | 24 | 27 (1) | 30 |
| **C-S** | 13 (1) | 12 | 13 (1) | 15 |
| **C Methoxide** | 4 (1) | 12 | 4 (1) | - |
| **O-C=O carbamate** | - | - | 1.3 (0.2) | - |
| **Si-O-Si** | 29 (2) | 29 | 23 (2) | 23 |
| **S** | 13 (2) | 12 | 10 (2) | 10 |
| **Si** | 13 (2) | 12 | 15 (1) | 15 |
| **-$NH_2$** | - | - | 3 (1) | 5 |
| **NHCOO** | - | - | 1.3 (0.4) | - |
| **-$NH_3^+$** | - | - | 0.5 (0.1) | - |

The concentration calculated for M-gold are in good agreement with the results reported in the literature by Villanueva [5] on medical-grade PVC. On the other hand A-gold samples shows differences with respect of the results reported in [5], in fact the Si:S ratio was found to be 1:1, while in this work the ratio was 3:2. This difference can be ascribed to a different reaction ratio between MPTMS:APTES as discussed in the previous paragraph and in [1], that can be related to the different exposure time of M-Gold to APTES adopted in this work that was one hour, while in [5] the MPTMS functionalized sample was incubated in APTES solution for 18 hours.

The S $2p_{3/2}$ binding energy in the M-gold samples was found to be 163.7 (0.1) eV (Table 5.2). The expected binding energy for the Au-S covalent bond typical of thiolate species is reported in the literature in the range between 162-163 eV [48]. The difference between experimental results and the literature may be related to the adopted functionalization condition especially to the short exposure time exploited for simulate the condition used in the functionalization process of the food-grade PVC.

Similar binding energies were reported in the literature for S $2p_{3/2}$, and were assigned to unbound thiolates [48] and/or disulphides [49]. In the literature those compounds were defined as physiosorbed molecules [49,50]. In those papers the author suggests that the high binding energy component should not be present in the S 2p spectra in the case of SAMs formation, and the physiosorbed molecules should be located at the SAM-ambient interface [50,51]. In this work the component at 162 eV typical of the thiolates was not revealed, but the ARXPS results showed in Figures 5.9 and 5.11 demonstrate that in depth-distribution of the functional groups agrees with the reaction schemes shown in Figure 5.1. More recently, in the literature was reported that for the SAM obtained by solution deposition, the gold-sulphur bond does not have a chemisorbed character and that the hydrogen in the -SH functional group is retained [52]. Furthermore, the presence of the electronegative O-Si-O functional group of MPTMS can also have a role in the observed chemical shift; similar binding energy values have been reported in the case of gold nanoparticles functionalized with MPTMS [53].

On the A-gold samples, as shown in table 5.3, the binding energy of C-Si, $CH_2$ as well as for the Si 2p and S 2p signal was shifted by +0.4 eV compared to the binding energy values reported for M-gold in Table 5.2. Also in this case, the chemical shift might be related to the cross-linking reaction between the Si-O groups of MPTMS and APTES; similar values have been reported for APTES monolayer on silicon oxide surfaces. Moreover, as discussed in the previous section, Avogadro simulation suggests that following the formation of APTES layer the distance between sulphur atoms and the Si-O-Si groups slightly decrease, passing from 0.47 nm to 0.41 nm, thus suggesting that the proximity of the electronegative Si-O-Si groups could affect the BE [54].

Table 5.4 shows the quantitative analysis performed on G-gold sample; the experimental composition is in good agreement with the expected stoichiometry calculated on the basis of the model proposed in figure 5.21. However, G-gold showed a concentration of nitrogen about three times higher than the concentration reported in the literature for a PVC sample functionalized following a similar procedure [5]. This difference can be ascribed also in this case to the different exposure time, but this aspect needs further studies since the concentration of G-gold samples were calculated on a single sample.

As observed in the A-gold samples, also in the case of G-gold, a chemical shift was observed, this effect can be explained taking into account the presence of numerous electronegative functional groups such as Si-O, C-N=C and C=O in a few nanometres thick layer, thus affecting the BE of the electrons of the different functional groups present.

The quantitative results obtained on P-gold sample showed that the concentration of nitrogen atoms is ten times higher than the results presented in the literature [5]. This difference may be related to the formation of a non-uniform layer of PHMG onto the gold surface; this can be confirmed by observing the SEM micrography that will be discussed in chapter 7. The formation of a multilayer onto the surface cannot be excluded, however additional data are necessary to understand the functionalization mechanism and to assess whether the formation of a multilayer is possible.

## 5.5 Conclusions

Based on the presented results the following conclusion can be drawn:

- Through detailed analysis of XPS high-resolution spectra, insights into the formation of MPTMS and MPTMS+APTES overlayers on freshly cleaved gold surfaces were obtained. Quantitative analysis indicated successful and laterally homogeneous functionalization of the gold surface with MPTMS, with an unexpected concentration of $CH_3O$ suggesting three-dimensional cross-linking of the Si-O-Si bond. Subsequent grafting of APTES onto the M-gold surface showed quantitative agreement with stoichiometry considering a 2:1 ratio of MPTMS:APTES.
- The quantitative analysis carried out on G-gold shows that also APTES and glutaraldehyde do not react according to a 1:1 ratio, but by the surface quantitative analysis an APTES : Glutaraldehyde ratio equal to 5:3 can be assumed. The theoretical concentration (at%) calculated on this model agrees with the experimental results.
- Angle-resolved XPS allowed understanding the distribution of functional groups within the overlayers after each step of functionalization. The layer thickness was calculated only after the first two functionalization steps, while on G-gold and P-gold the layer thickness

estimation resulted to be challenging. This approach here adopted was helpful for understanding the functionalization process.

- The analytical approach presented, utilizing XPS and ARXPS with gold as a carbon-free substrate, offers valuable insights into proper curve fitting of C 1s signals and layer thickness estimation, applicable to similar systems with carbon-based substrates such as polymers.

*References*

[1] "G. Casula, M. Fantauzzi, B. Elsener, A. Rossi, XPS and ARXPS for Characterizing Multilayers of Silanes on Gold Surfaces, Coatings 14 (2024) 327. https://doi.org/10.3390/coatings14030327.

[2] C. Vericat, M.E. Vela, G. Benitez, P. Carro, R.C. Salvarezza, Self-assembled monolayers of thiols and dithiols on gold: new challenges for a well-known system, Chem. Soc. Rev. 39 (2010) 1805–1834. https://doi.org/10.1039/B907301A.

[3] N.D. Spencer, Tailoring Surfaces: Modifying Surface Composition and Structure for Applications in Tribology, Biology and Catalysis, Co-Published with Indian Institute of Science (IISc), Bangalore, India, 2011. https://doi.org/10.1142/7506.

[4] Y. Xia, X.-M. Zhao, G.M. Whitesides, Pattern transfer: Self-assembled monolayers as ultrathin resists, Microelectronic Engineering 32 (1996) 255–268. https://doi.org/10.1016/0167-9317(95)00174-3.

[5] M.E. Villanueva, J.A. González, E. Rodríguez-Castellón, S. Teves, G.J. Copello, Antimicrobial surface functionalization of PVC by a guanidine based antimicrobial polymer, Materials Science and Engineering: C 67 (2016) 214–220. https://doi.org/10.1016/j.msec.2016.05.052.

[6] M.E. Villanueva, A. Salinas, J.A. González, S. Teves, G.J. Copello, Dual antibacterial effect of immobilized quaternary ammonium and aliphatic groups on PVC, New J. Chem. 39 (2015) 9200–9206. https://doi.org/10.1039/C5NJ01766A.

[7] J.C. Love, L.A. Estroff, J.K. Kriebel, R.G. Nuzzo, G.M. Whitesides, Self-Assembled Monolayers of Thiolates on Metals as a Form of Nanotechnology, Chem. Rev. 105 (2005) 1103–1170. https://doi.org/10.1021/cr0300789.

[8] S. Kumar, S. Soni, W. Danowski, C.L.F. van Beek, B.L. Feringa, P. Rudolf, R.C. Chiechi, Correlating the Influence of Disulfides in Monolayers across Photoelectron Spectroscopy Wettability and Tunneling Charge-Transport, J. Am. Chem. Soc. 142 (2020) 15075–15083. https://doi.org/10.1021/jacs.0c06508.

[9] S. Lee, R. Heeb, N.V. Venkataraman, N.D. Spencer, Macroscopic Tribological Testing of Alkanethiol Self-assembled Monolayers (SAMs): Pin-on-disk Tribometry with Elastomeric Sliding Contacts, Tribol Lett 28 (2007) 229–239. https://doi.org/10.1007/s11249-007-9266-1.

[10] W. Azzam, A. Bashir, P.U. Biedermann, M. Rohwerder, Formation of Highly Ordered and Orientated Gold Islands: Effect of Immersion Time on the Molecular Adlayer Structure of Pentafluorobenzenethiols (PFBT) SAMs on Au(111), Langmuir 28 (2012) 10192–10208. https://doi.org/10.1021/la301601c.

[11] E. Cortés, A.A. Rubert, G. Benitez, P. Carro, M.E. Vela, R.C. Salvarezza, Enhanced Stability of Thiolate Self-Assembled Monolayers (SAMs) on Nanostructured Gold Substrates, ACS Publications (2009). https://doi.org/10.1021/la804251a.

[12] P.K. Gothe, D. Gaur, V.G. Achanta, MPTMS self-assembled monolayer deposition for ultra-thin gold films for plasmonics, J. Phys. Commun. 2 (2018) 035005. https://doi.org/10.1088/2399-6528/aaaedd.

[13] I. Piwoński, J. Grobelny, M. Cichomski, G. Celichowski, J. Rogowski, Investigation of 3-mercaptopropyltrimethoxysilane self-assembled monolayers on Au(111) surface, Applied Surface Science 242 (2005) 147–153. https://doi.org/10.1016/j.apsusc.2004.08.009.

[14] Y. Yang, Y. Qing, X. Hao, C. Fang, P. Ouyang, H. Li, Z. Wang, Y. Liao, H. Fang, J. Du, APTES-Modified Remote Self-Assembled DNA-Based Electrochemical Biosensor for Human Papillomavirus DNA Detection, Biosensors 12 (2022) 449. https://doi.org/10.3390/bios12070449.

[15] D.N.G. Krishna, J. Philip, Review on surface-characterization applications of X-ray photoelectron spectroscopy (XPS): Recent developments and challenges, Applied Surface Science Advances 12 (2022) 100332. https://doi.org/10.1016/j.apsadv.2022.100332.

[16] J.F. Watts, J. Wolstenholme, An Introduction to Surface Analysis by XPS and AES, John Wiley & Sons, 2019.

[17] D. Briggs, Surface Analysis of Polymers by XPS and Static SIMS, Cambridge University Press, Cambridge, 1998. https://doi.org/10.1017/CBO9780511525261.

[18] H. Chen, C.K. Heng, P.D. Puiu, X.D. Zhou, A.C. Lee, T.M. Lim, S.N. Tan, Detection of Saccharomyces cerevisiae immobilized on self-assembled monolayer (SAM) of alkanethiolate using electrochemical impedance spectroscopy, Analytica Chimica Acta 554 (2005) 52–59. https://doi.org/10.1016/j.aca.2005.08.086.

[19] B.D. Gates, Q. Xu, M. Stewart, D. Ryan, C.G. Willson, G.M. Whitesides, New Approaches to Nanofabrication:  Molding, Printing, and Other Techniques, Chem. Rev. 105 (2005) 1171–1196. https://doi.org/10.1021/cr030076o.

[20] I. Piwoński, J. Grobelny, M. Cichomski, G. Celichowski, J. Rogowski, Investigation of 3-mercaptopropyltrimethoxysilane self-assembled monolayers on Au(111) surface, Applied Surface Science 242 (2005) 147–153. https://doi.org/10.1016/j.apsusc.2004.08.009.

[21] A. Penna, M. Careri, N.D. Spencer, A. Rossi, Effects of Tailored Surface Chemistry on Desorption Electrospray Ionization Mass Spectrometry: a Surface-Analytical Study by XPS and AFM, J. Am. Soc. Mass Spectrom. 26 (2015) 1311–1319. https://doi.org/10.1007/s13361-015-1135-9.

[22] N. Graf, E. Yegen, T. Gross, A. Lippitz, W. Weigel, S. Krakert, A. Terfort, W.E.S. Unger, XPS and NEXAFS studies of aliphatic and aromatic amine species on functionalized surfaces, Surface Science 603 (2009) 2849–2860. https://doi.org/10.1016/j.susc.2009.07.029.

[23] V.P. Afanas'ev, D.N. Selyakov, O.Y. Ridzel, M.A. Semenov-Shefov, A.N. Strukov, Investigation of monolayer and submonolayer films using X-ray photoelectron spectroscopy, J. Phys.: Conf. Ser. 1713 (2020) 012002. https://doi.org/10.1088/1742-6596/1713/1/012002.

[24] K.L. Parry, A.G. Shard, R.D. Short, R.G. White, J.D. Whittle, A. Wright, ARXPS characterisation of plasma polymerised surface chemical gradients, Surface and Interface Analysis 38 (2006) 1497–1504. https://doi.org/10.1002/sia.2400.

[25] D.M. Spori, N.V. Venkataraman, S.G.P. Tosatti, F. Durmaz, N.D. Spencer, S. Zürcher, Influence of Alkyl Chain Length on Phosphate Self-Assembled Monolayers, Langmuir 23 (2007) 8053–8060. https://doi.org/10.1021/la700474v.

[26] J. Walton, M.R. Alexander, N. Fairley, P. Roach, A.G. Shard, Film thickness measurement and contamination layer correction for quantitative XPS, Surface and Interface Analysis 48 (2016) 164–172. https://doi.org/10.1002/sia.5934.

[27] V.V. Naik, M. Crobu, N.V. Venkataraman, N.D. Spencer, Multiple Transmission-Reflection IR Spectroscopy Shows that Surface Hydroxyls Play Only a Minor Role in Alkylsilane Monolayer Formation on Silica, J. Phys. Chem. Lett. 4 (2013) 2745–2751. https://doi.org/10.1021/jz401440d.

[28] C. Passiu, A. Rossi, M. Weinert, W. Tysoe, N.D. Spencer, Probing the outermost layer of thin gold films by XPS and density functional theory, Applied Surface Science 507 (2020) 145084. https://doi.org/10.1016/j.apsusc.2019.145084.

[29] S. Tougaard, Practical guide to the use of backgrounds in quantitative XPS, Journal of Vacuum Science & Technology A 39 (2021) 011201. https://doi.org/10.1116/6.0000661.

[30] J.H. Scofield, Hartree-Slater subshell photoionization cross-sections at 1254 and 1487 eV, Journal of Electron Spectroscopy and Related Phenomena 8 (1976) 129–137. https://doi.org/10.1016/0368-2048(76)80015-1.

[31] L. Zommer, Determination of the spectrometer transmission function for XPS quantitative analysis, Vacuum 46 (1995) 617–620. https://doi.org/10.1016/0042-207X(94)00143-X.

[32] M.P. Seah, W.A. Dench, Quantitative electron spectroscopy of surfaces: A standard data base for electron inelastic mean free paths in solids, Surface and Interface Analysis 1 (1979) 2–11. https://doi.org/10.1002/sia.740010103.

[33] P.L.J. Gunter, O.L.J. Gijzeman, J.W. Niemantsverdriet, Surface roughness effects in quantitative XPS: magic angle for determining overlayer thickness, Applied Surface Science 115 (1997) 342–346. https://doi.org/10.1016/S0169-4332(97)00007-X.

[34] M.H. Engelhard, D.R. Baer, A. Herrera-Gomez, P.M.A. Sherwood, Introductory guide to backgrounds in XPS spectra and their impact on determining peak intensities, Journal of Vacuum Science & Technology A: Vacuum, Surfaces, and Films 38 (2020) 063203. https://doi.org/10.1116/6.0000359.

[35] N. Fairley, V. Fernandez, M. Richard-Plouet, C. Guillot-Deudon, J. Walton, E. Smith, D. Flahaut, M. Greiner, M. Biesinger, S. Tougaard, D. Morgan, J. Baltrusaitis, Systematic and collaborative approach to problem solving using X-ray photoelectron spectroscopy, Applied Surface Science Advances 5 (2021) 100112. https://doi.org/10.1016/j.apsadv.2021.100112.

[36] Y.-S. Li, W. Lu, Y. Wang, T. Tran, Studies of (3-mercaptopropyl)trimethoxylsilane and bis(trimethoxysilyl)ethane sol–gel coating on copper and aluminum, Spectrochimica Acta Part A: Molecular and Biomolecular Spectroscopy 73 (2009) 922–928. https://doi.org/10.1016/j.saa.2009.04.016.

[37] F.S. da Silva, H.G. de Melo, A.V. Benedetti, P.H. Suegama, Influence of Ce(IV) ions amount on the electrochemical behavior of organic-inorganic hybrid coatings in 0.1 mol L-1 NaCl solution, Eclética Química 44 (2019) 27–56.

[38] E.D. Eren, G. Guisong, L. Mingming, Z. Bingchun, Y. Ke, C. Shanshan, A novel chitosan and polydopamine interlinked bioactive coating for metallic biomaterials, J Mater Sci: Mater Med 33 (2022) 65. https://doi.org/10.1007/s10856-022-06688-x.

[39] X. Yan, T. Xu, G. Chen, S. Yang, H. Liu, Q. Xue, Preparation and characterization of electrochemically deposited carbon nitride films on silicon substrate, J. Phys. D: Appl. Phys. 37 (2004) 907. https://doi.org/10.1088/0022-3727/37/6/015.

[40] W. Cao, D. Wei, Y. Jiang, S. Ye, A. Zheng, Y. Guan, Surface chemical bonding with poly(hexamethylene guanidine) for non-leaching antimicrobial poly(ethylene terephthalate), J Mater Sci 54 (2019) 2699–2711. https://doi.org/10.1007/s10853-018-2966-0.

[41] A. R. Santos, R. K. Blundell, P. Licence, XPS of guanidinium ionic liquids: a comparison of charge distribution in nitrogenous cations, Physical Chemistry Chemical Physics 17 (2015) 11839–11847. https://doi.org/10.1039/C5CP01069A.

[42] T. He, Y. Jiang, S. Chang, X. Zhou, Y. Ji, X. Fang, Y. Zhang, Antibacterial and high-performance bioplastics derived from biodegradable PBST and lignin, Industrial Crops and Products 191 (2023) 115930. https://doi.org/10.1016/j.indcrop.2022.115930.

[43] J.M. Hill, D.G. Royce, C.S. Fadley, L.F. Wagner, F.J. Grunthaner, Properties of oxidized silicon as determined by angular-dependent X-ray photoelectron spectroscopy, Chemical Physics Letters 44 (1976) 225–231. https://doi.org/10.1016/0009-2614(76)80496-4.

[44] C.R. Brundle, G. Conti, P. Mack, XPS and angle resolved XPS, in the semiconductor industry: Characterization and metrology control of ultra-thin films, Journal of Electron Spectroscopy and Related Phenomena 178–179 (2010) 433–448. https://doi.org/10.1016/j.elspec.2010.03.008.

[45] W. Sui, W. Zhao, X. Zhang, S. Peng, Z. Zeng, Q. Xue, Comparative anti-corrosion properties of alkylthiols SAMs and mercapto functional silica sol–gel coatings on copper surface in sodium chloride solution, J Sol-Gel Sci Technol 80 (2016) 567–578. https://doi.org/10.1007/s10971-016-4108-y.

[46] M. Sypabekova, A. Hagemann, D. Rho, S. Kim, Review: 3-Aminopropyltriethoxysilane (APTES) Deposition Methods on Oxide Surfaces in Solution and Vapor Phases for Biosensing Applications, Biosensors 13 (2023) 36. https://doi.org/10.3390/bios13010036.

[47] G. Casula, M. Fantauzzi, B. Elsener, A. Rossi, Surface modification of food-grade PVC monitored by angle-resolved XPS, Vacuum (2024) 113010. https://doi.org/10.1016/j.vacuum.2024.113010.

[48] D.G. Castner, K. Hinds, D.W. Grainger, X-ray photoelectron spectroscopy sulfur 2p study of organic thiol and bisulfide binding interactions with gold surfaces, Langmuir 12 (1996) 5083–5086. https://doi.org/10.1021/la960465w.

[49] L.J. Cristina, G. Ruano, R. Salvarezza, J. Ferrón, Thermal Stability of Self-Assembled Monolayers of n-Hexanethiol on Au(111)-(1 × 1) and Au(001)-(1 × 1), J. Phys. Chem. C 121 (2017) 27894–27904. https://doi.org/10.1021/acs.jpcc.7b05883.

[50] S. Watcharinyanon, D. Nilsson, E. Moons, A. Shaporenko, M. Zharnikov, B. Albinsson, J. Mårtensson, L.S.O. Johansson, A spectroscopic study of self-assembled monolayer of porphyrin-functionalized oligo(phenyleneethynylene)s on gold: the influence of the anchor moiety, Phys. Chem. Chem. Phys. 10 (2008) 5264–5275. https://doi.org/10.1039/B802914H.

[51] J. Jia, A. Kara, L. Pasquali, A. Bendounan, F. Sirotti, V.A. Esaulov, On sulfur core level binding energies in thiol self-assembly and alternative adsorption sites: An experimental and theoretical study, J Chem Phys 143 (2015) 104702. https://doi.org/10.1063/1.4929350.

[52] M.S. Inkpen, Z.-F. Liu, H. Li, L.M. Campos, J.B. Neaton, L. Venkataraman, Non-chemisorbed gold–sulfur binding prevails in self-assembled monolayers, Nat. Chem. 11 (2019) 351–358. https://doi.org/10.1038/s41557-019-0216-y.

[53] P. Wu, B. Peng, Z. Yan, X. Zhao, Gold nanoparticles supported on mesoporous silica: Origin of high activity and role of Au NPs in selective oxidation of cyclohexane, Scientific Reports 6 (2016) 18817. https://doi.org/10.1038/srep18817."

[54] P.M. Dietrich, S. Glamsch, C. Ehlert, A. Lippitz, N. Kulak, W.E.S. Unger, Synchrotron-radiation XPS analysis of ultra-thin silane films: Specifying the organic silicon, Applied Surface Science 363 (2016) 406–411. https://doi.org/10.1016/j.apsusc.2015.12.052.

# Chapter 6 Surface functionalization of a food-grade PVC

In this chapter the characterization of food-grade PVC surface, functionalized as described in chapter 4 by exploiting the analytical strategy developed on gold samples will be described.

The results obtained in the case of food-grade PVC samples functionalized with MPTMS has been recently published [1].

## 5.1 Introduction

When exposed to a nucleophile, C-Cl groups of PVC can react allowing the grafting of molecules such as MPTMS onto its surface [2]. By modifying the food-grade PVC surface it is possible to anchor different organic molecules, such as PHMG to develop an active food packaging with antimicrobial properties [3,4]. XPS can be a useful tool for characterizing the surface of the modified polymer, but the presence of carbon atoms in both the polymer, plasticizers/stabilizers and functionalization layer represent a challenge for understanding the surface composition of the samples.

By applying an analytical strategy based on XPS and ARXPS developed on a carbon-less substrate, such as freshly cleaved gold [5], it is possible to identify the curve fitting parameters necessary to distinguish the different components of C 1s signal that can be assigned to the functionalization layer and to the bulk (PVC in this work). Moreover, ARXPS can provide information about the functionalization layer thickness and the spatial disposition of the functional groups onto the polymer surface, as well as it gives the possibility to understand whether a monolayer or a multilayer is formed.

In this chapter, the experimental results obtained on food-grade PVC samples functionalized following the procedure presented in Chapter 4 are presented.

## 6.2 Experimental

### 6.2.1 Surface functionalization of food-grade PVC

The surface functionalization of food-grade PVC consists in the reaction with a MPTMS solution in ethanol (M-PVC), followed by the grafting of APTES (A-PVC), glutaraldehyde (G-PVC) and finally the anchoring of PHMG (P-PVC). The details are given in Chapter 4. Samples were named using the same nomenclature proposed in the literature [3].

### 6.2.1 X-ray photoelectron spectroscopy (XPS) and Angle-resolved X-ray photoelectron spectroscopy (ARXPS)

The XPS spectra were acquired using the same conditions adopted for the acquisition of the freshly cleaved gold functionalized with the same procedure. In this case, since the polymer are not conductive samples charge compensation was carried out using low energy electrons and argon ions. The base pressure into the XPS analysis chamber was $2x10^{-9}$ mbar but since the charge neutralization system requires Argon gas to be ionized, the residual pressure during the analysis was at $2x10^{-7}$ mbar. No changes in the residual pressure were observed during spectra acquisition. Fresh-cut polyethylene terephthalate (PET) samples were used to test the charge compensation settings in both standard and angle resolved lens mode. This test was carried out before the spectra acquisition on the functionalized samples.

Since the use of adventitious carbon as reference is controversial in the literature [6], the binding energy scale was referred to the aliphatic carbon C 1s component ascribed to the long-chain of plasticizer/stabilized used in the formulation of commercial food-grade PVC. This component was taken at 285.0 eV as suggested in the literature for aliphatic carbon [7]. The PVC samples are degraded when exposed to an X-ray beam, for this reason the acquisition of the C 1s signal was repeated at the end of the experiment using the same experimental condition used at the beginning. Visual comparison between the first and the last C 1s scan was done for confirming that no degradation occurred.

To exclude the PVC degradation under ultra-high vacuum (UHV) conditions the spectra of PVC samples immersed in ethanol were acquired after they were inserted into the analysis chamber and after 72 h in UHV without exposing the samples to the X-rays. No difference was observed in the C 1s and Cl 2p line-shape, nor in the CH:C-Cl atomic ratio that was found to be 1:1.

In table 6.1 the curve fitting parameters adopted for processing the most intense XPS signals of both as received and functionalized PVC are reported.

*Table 6.1 Curve-fitting parameters used for processing the most intense signals of as received PVC, M-PVC and A-PVC, G-PVC and P-PVC.*

| | FWHM (eV) | Background | Line shape | Constrains |
|---|---|---|---|---|
| C 1s contamination | 1.6 (0.1) | U 3 Tougaard | GL(30) | FWHM C 1s Contamination = FWHM C 1s C-Si, C-C x 1 |
| C 1s C-Si, C-C | 1.6 (0.1) | | GL(30) | |
| C 1s C-S/C-N | 1.6 (0.1) | | GL(30) | FWHM C 1s C-S = FWHM C 1s C-Si, C-C x 1<br>Area C 1s C-S=Area C-Si, C-C x 0.5 |
| C 1s methoxide | 1.6 (0.1) | | GL(30) | FWHM C 1s methoxide = FWHM C 1s C-Si, C-C x 1 |
| C 1s COO plasticizer | 1.6 (0.1) | | GL(30) | FWHM C 1s of the NH(C*O)O group = FWHM C 1s of C-Si, and of C-C x 1 |
| O 1s Si-O-Si | 1.8 (0.1) | | GL(30) | |
| O 1s C-O | 1.8 (0.1) | | GL(30) | FWHM O 1s NH(CO)O* = FWHM O 1s Si-O-Si x 1 |
| O 1s C=O | 1.8 (0.1) | | GL(30) | Area O 1s NH(CO*)O = Area O 1s NH(CO)O* x 1<br>FWHM O 1s NH(CO)O* = FWHM O1s Si-O-Si x 1 |
| S 2p | 1.6 (0.1) | | GL(30) | Area S $2p_{1/2}$ = Area S $2p_{3/2}$ x 0.5<br>FWHM S $2p_{1/2}$ = FWHM S $2p_{3/2}$ x 1<br>BE $2p_{1/2}$ = BE $2p_{3/2}$ + 1.16 |
| Si 2p | 1.5 (0.1) | | GL(30) | Area Si $2p_{1/2}$ = Area Si $2p_{3/2}$ x 0.5 |

| | | | | |
|---|---|---|---|---|
| | | | | FWHM Si $2p_{1/2}$ = FWHM Si $2p_{3/2}$ x 1<br>BE $2p_{1/2}$ = BE $2p_{3/2}$ + 0.6 |
| N 1s $NH_2$ | 1.6 (0.1) | | GL(30) | FWHM N 1s $NH_2$ = FWHM N 1s $NH_3^+$ x 1 |
| N 1s $NH_3^+$ | 1.6 (0.1) | | GL(30) | |
| N 1s NHCOO | 1.6 (0.1) | | GL(30) | FWHM N 1s NHCOO = FWHM N 1s $NH_3^+$ x 1 |
| C 1s C-C PHMG | 1.6 (0.1) | | GL(30) | Area C 1s C-C PHMG = Area C 1s C-NH-C PHMG x 2 |
| C 1s C-NH-C PHMG | 1.6 (0.1) | | GL(30) | FWHM C 1s C-NH-C = FWHM C 1s C-C PHMG x 1 |
| C 1s $C=NH_2^+$ | 1.6 (0.1) | | GL(30) | FWHM C 1s $C=NH_2^+$ = FWHM C 1s C-C PHMG x 1 |
| N 1s C-NH-C/C=N | 1.6 (0.1) | | GL(30) | Area N 1s C-NH-C = Area N 1s $C=NH_2^+$ x 3 |
| N 1s $C=NH_2^+$ | 1.6 (0.1) | | GL(30) | FWHM N 1s $C=NH_2^+$ = FWHM N 1s C-NH-C x 1 |

## 6.3 Results

### 6.3.1 XPS results and ARXPS on food-grade PVC

XPS spectra acquired before and after immersion for 1 h in ethanol of the food-grade PVC sample are showed in figure 6.1. In the survey spectra of the as received samples the signal of Carbon (C 1s, C KLL) and chlorine (Cl 2p, Cl 2s) characteristic of the PVC are detected with those of the Zn 2p, Zn KLL and the O 1s ascribed to the presence of zinc-based stabilizer/plasticizer. Following the immersion in ethanol, no Zn 2p signal was detected on the sample survey.

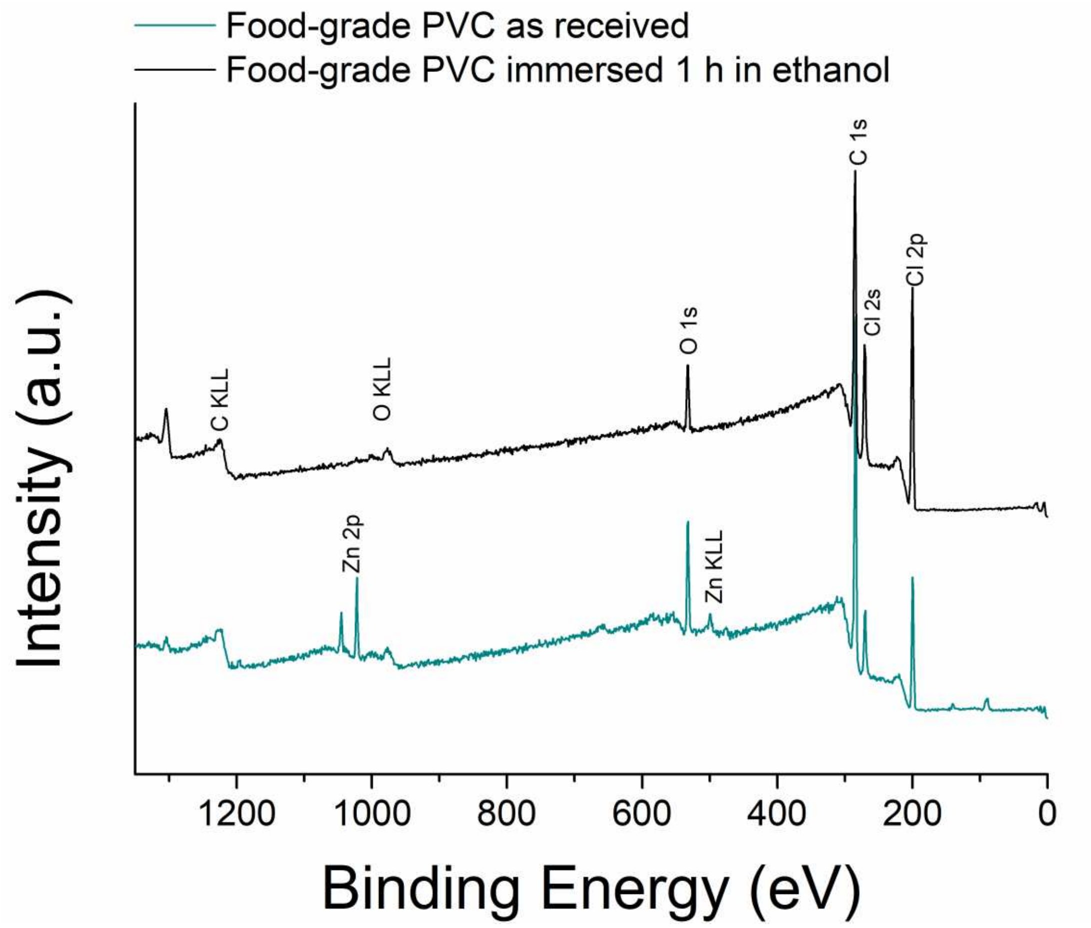

*Figure 6.1 Survey spectra of food-grade PVC as received (cyan curve) and after 1 h immersion in ethanol (black curve)*

In figure 6.2 the high-resolution spectra of the C 1s, Cl 2p, O 1s and Zn 2p signal are reported. The curve-fitting parameters for the Gaussian/Lorentzian curves were derived from the spectra of a reference sample such as PET, analysed with the same experimental settings. The C 1s signal was resolved using five components. The two components at 285.9 eV and 287 eV were attributed to the $CH_2$ and the C-Cl functional groups of the PVC [8] and the area ratio was constrained to be 1:1 as expected from the stoichiometry of the PVC. The component at 289.2 eV was attributed to the -COOH group of the plasticizer [9].

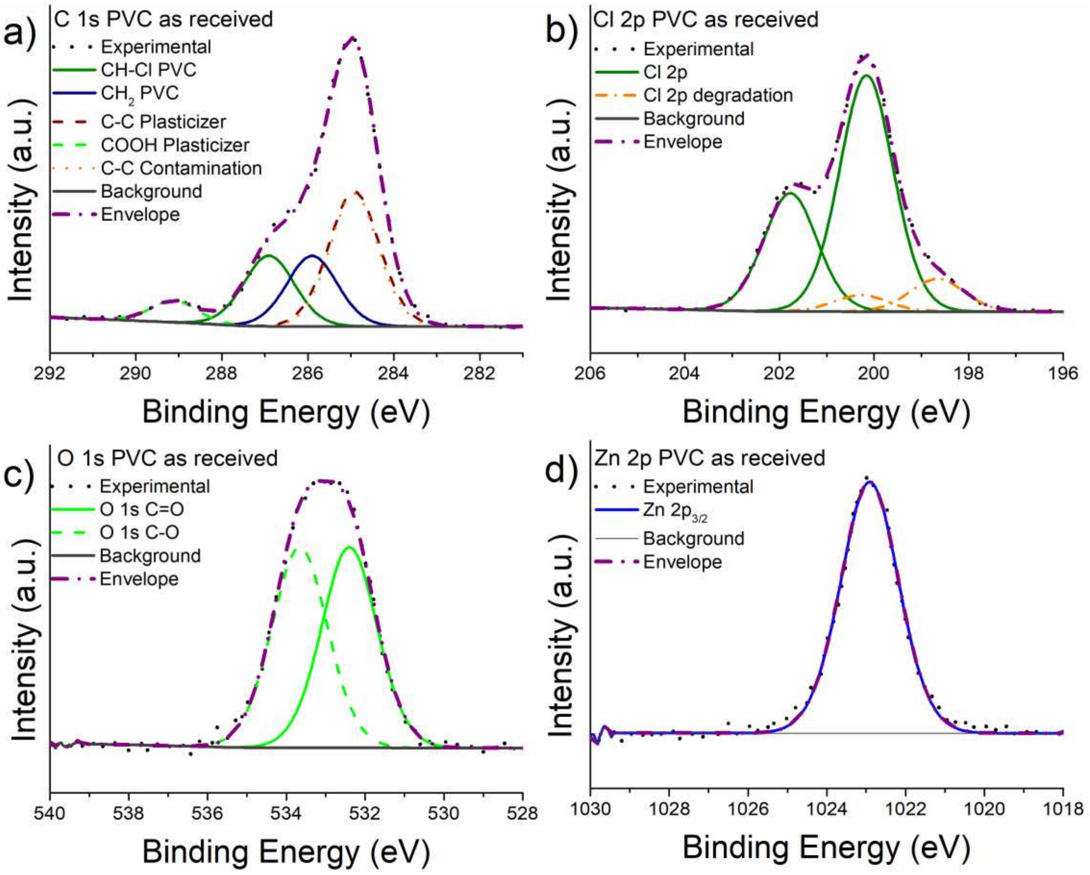

*Figure 6.29 High-resolution spectra of a) C 1s, b) Cl 2p, c) O 1s and d) Zn 2p for PVC as received*

The Cl 2p signals were fitted with two doublets due to the spin-orbit coupling, the area ratio between the Cl $2p_{3/2}$ and Cl $2p_{1/2}$ was constrained to be 2:1 with an energy separation of 1.6 eV. The Cl $2p_{3/2}$ component found at 200.2 eV was attributed to the chloride of the PVC, while the second component found at 198.5 eV was attributed to the sample degradation after 40 minutes of exposure to the X-ray beam.

The O 1s signal was fitted with two components assigned to the O-C=O* (532.2 eV) and to the O*-C=O (533.8 eV) of the carboxylic functional groups of the plasticizer/stabilizer. The Zn $2p_{3/2}$ signals were fitted with a single component found at 1023.4 eV.

After the immersion in ethanol for 1 hour no changes were observed in the spectra except for the Zn 2p that is not revealed.

The composition of the “as received” food grade PVC and of the PVC following the immersion in ethanol for 1 h, obtained by XPS data acquired in standard lens mode, is shown in table 6.2 and it is comparable for the two samples.

*Table 6.23 Quantitative results obtained from the spectra of as received PVC, food grade PVC after immersion in ethanol. The spectra were obtained in standard lens mode.*

| | as received PVC at% | washed PVC at % |
|---|---|---|
| C contamination | 26 (3) | 16 (4) |
| C 1s $CH_2$ PVC | 13 (2) | 15 (1) |
| C 1s CH-Cl PVC | 13 (2) | 15 (1) |
| Cl 2p | 13 (1) | 17 (2) |
| C 1s Carboxylate | 4.1 (0.3) | 4.1 (0.2) |
| O 1s C=O | 4.0 (0.2) | 4 (1) |
| O 1s C-O | 4.0 (0.2) | 4 (1) |
| C 1s plasticizer | 23 (3) | 26 (1) |
| Zn 2p | 1 (0.2) | - |

The ARXPS experiments were carried out on as received PVC and on ethanol-washed PVC and the high-resolution spectra are shown in figure 6.3 and 6.4, respectively. On the as received PVC the signals of carbon, chlorine, oxygen and zinc (Figure 6.3) were detected at all emission angles, while for PVC after immersion in ethanol, the Zn $2p_{3/2}$ signal was no more detected (Figure 6.4).

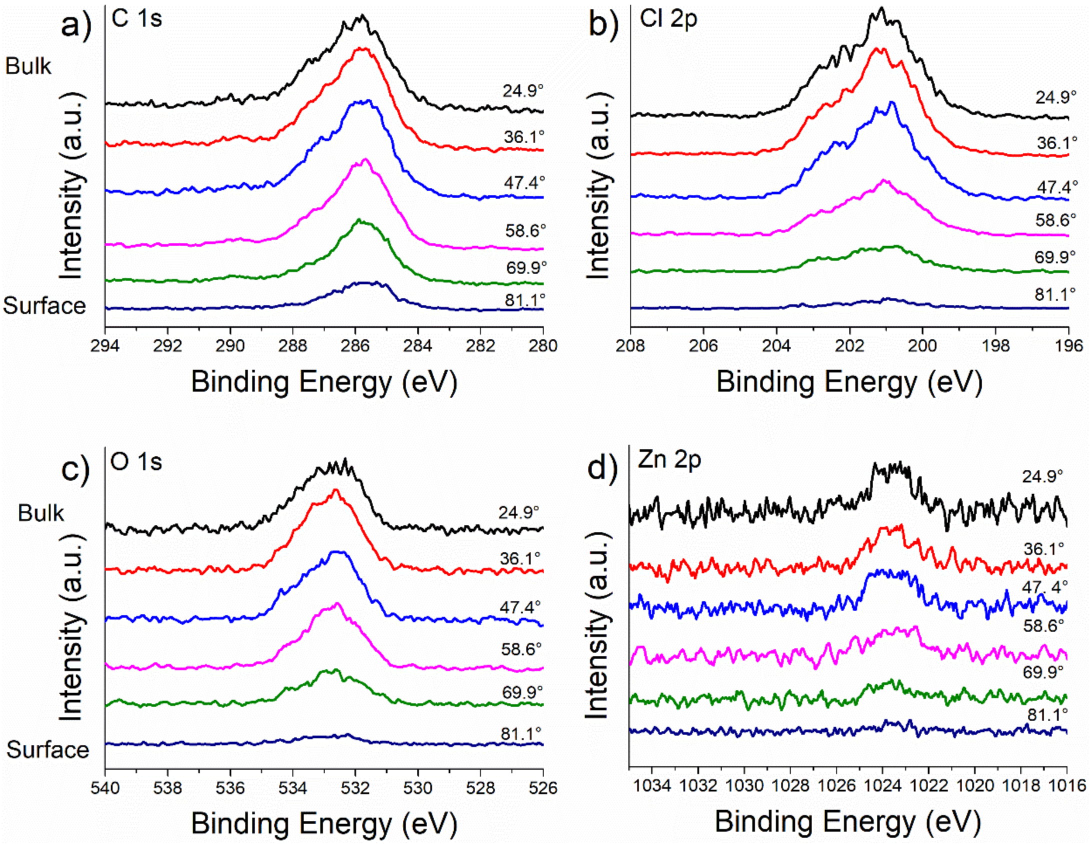

*Figure 6.3 Angle-resolved high-resolution C 1s, Cl 2p, O 1s and Zn 2p spectra of as received PVC acquired at different emission angles.*

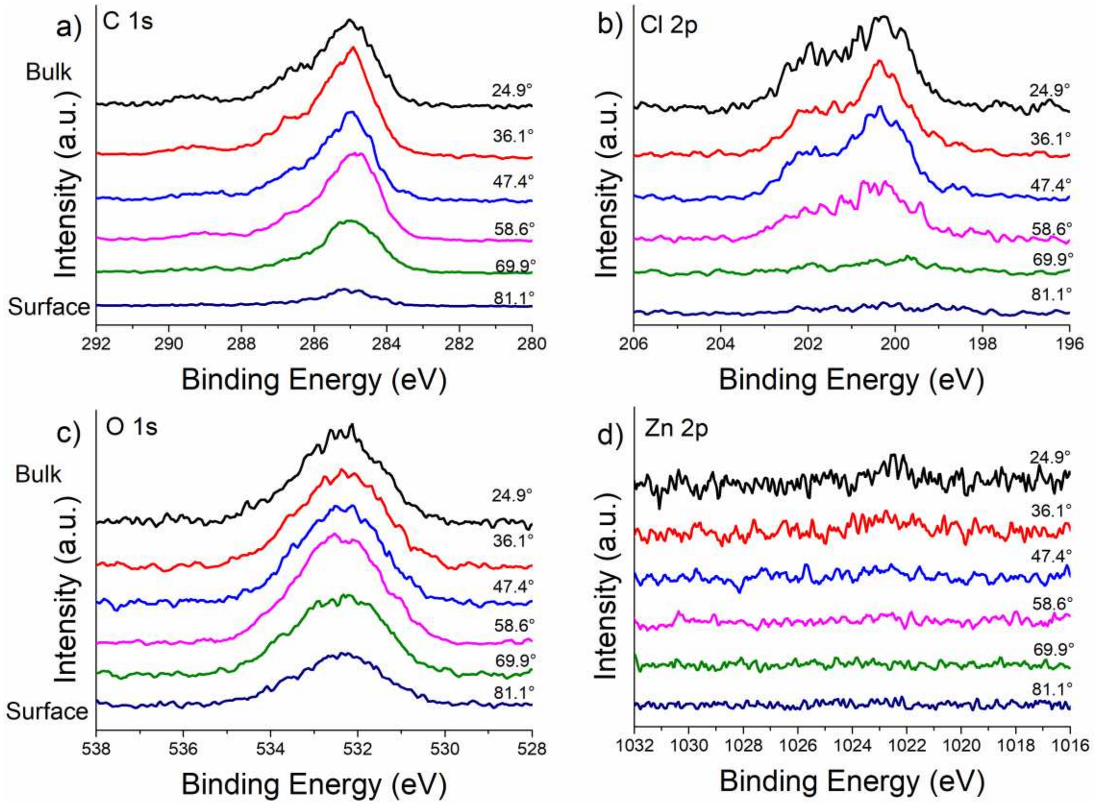

*Figure 6.4 Angle-resolved high-resolution C 1s, Cl 2p, O 1s and Zn 2p spectra of PVC after 1 h immersion in ethanol, acquired at different emission angles.*

By comparing the high-resolution spectra at two different emission angles (24 ° and 58 °) the intensity of component located at 285 eV labelled as “contamination” (orange dotted line in Fig. 6.5) increases, thus indicating its presence on the outermost layer of the sample (Figure 6.5).

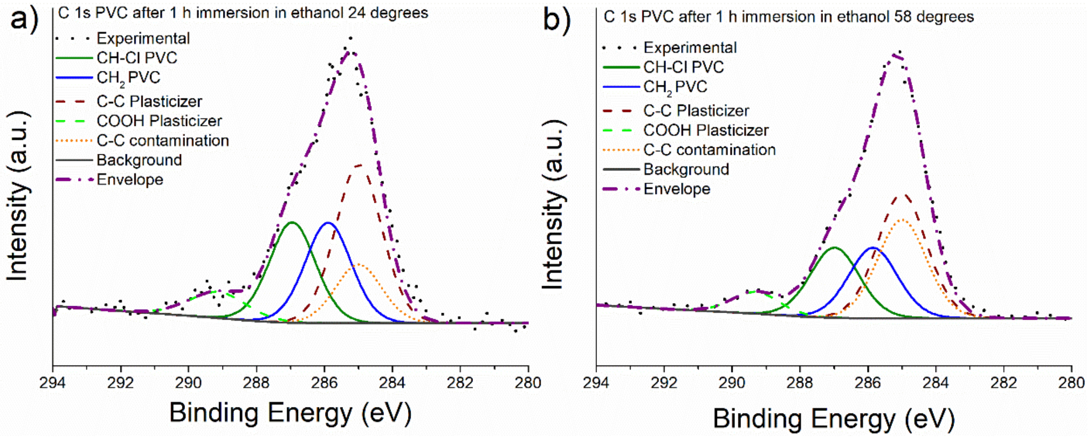

*Figure 6.5 High-resolution spectra of the C 1s signal acquired at two different angles 24 degrees (a) and 58 degrees (b)*

### 6.3.2 XPS and ARXPS results on PVC after functionalization.

#### 6.3.2.1 XPS results of M-PVC

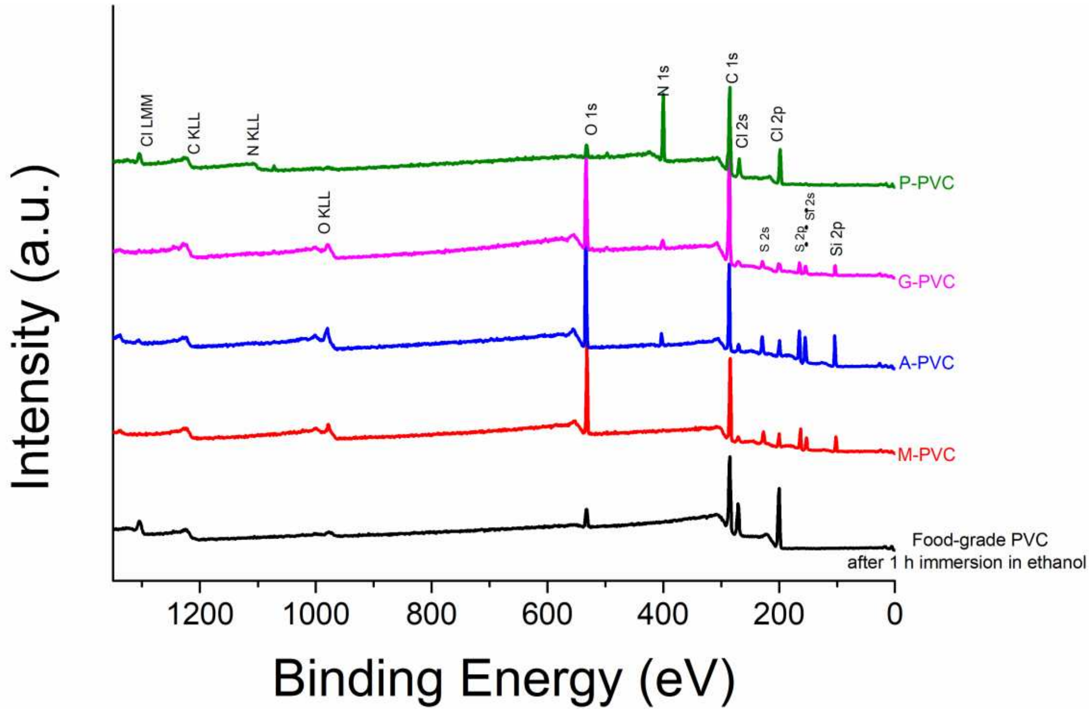

*Figure 6.6 Survey spectra of food-grade PVC after 1 h immersion in ethanol (black), M-PVC (red), A-PVC (blue), G-PVC (pink) and P-PVC (green)*

XPS spectra were acquired for the M-PVC samples obtained as described in chapter 4. The survey spectra (Figure 6.6) showed the presence of silicon and sulphur signals in addition to the C 1s and O 1s signals detected also in PVC; the Cl 2p signal of the PVC is still detected. High-resolution XPS spectra of C 1s, O 1s, S 2p and Si 2p signals, acquired in standard mode are showed in Figure 6.7.

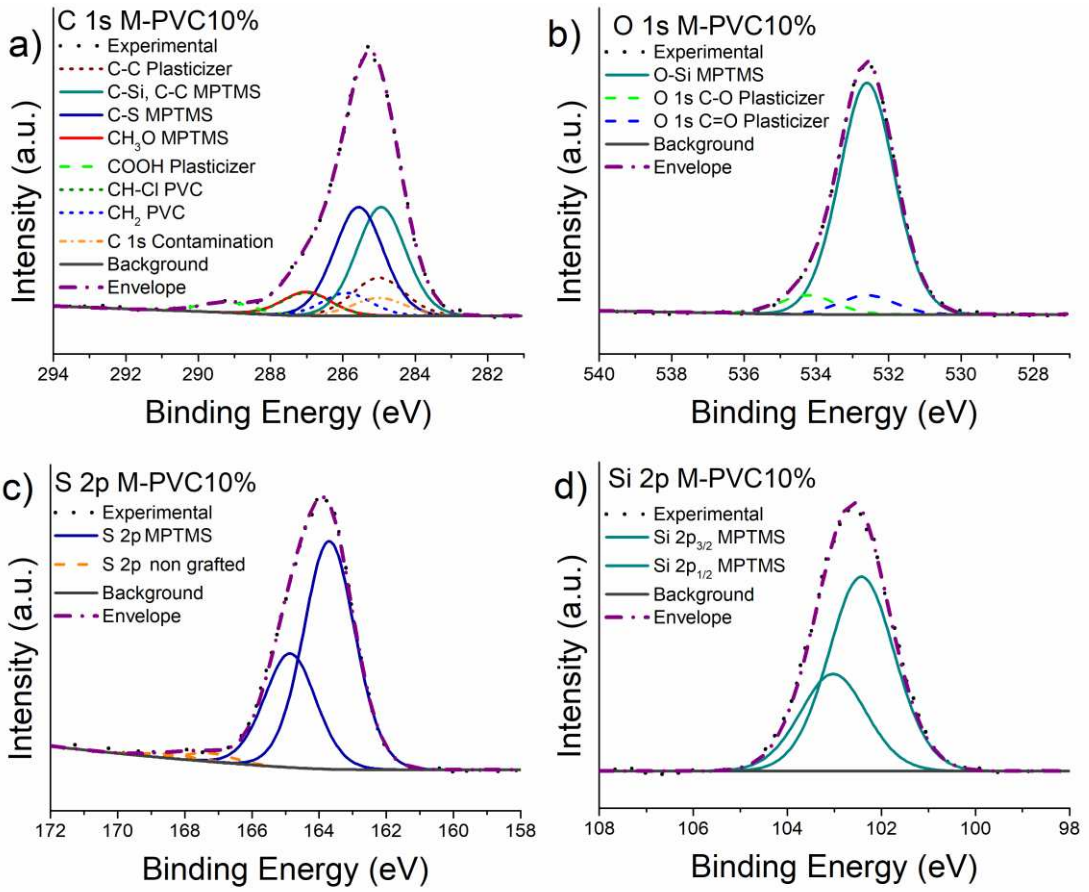

*Figure 6.7 High-resolution spectra of C 1s (a), O 1s (b), S 2p (c) and Si 2p (d) acquired on M-PVC samples*

Following the functionalization of the PVC with MPTMS three components that can be ascribed to the MPTMS layer are detected in C 1s signal (Figure 6.7 a): C-Si and C-C (284.9 eV), C-S (285.7 eV) and $CH_3O$ (287.0 eV). The contribution of the signal at 285 eV due to the plasticizer is overlapped with the contribution of the contamination layer, moreover small signals from the PVC substrate were detected.

O 1s signal (Figure 6.7 b) was fitted with three components, the most intense one at 532.4 eV was assigned to the O-Si functional groups, while the two smaller components at 532.3 eV and 534.2 eV were attributed to the -COOH group of the plasticizer (§ 6.3.1); an area ratio of 1:1 between these two components was imposed.

Figures 6.7 c and 6.7 d show the S 2p and Si 2p spectra of the M-PVC samples. The S 2p signals were fitted with two doublets due to the spin-orbit coupling with an energy separation of 1.16 eV and the area ratio constrained to be equal to 2:1. The binding energy of the most intense S $2p_{3/2}$ signal was found to be 163.7 eV; similar binding energy values were reported for thioethers in the literature [10]. The second components at 167.1 eV was ascribed to non-grafted sulphur atoms due to an oxidative reaction of sulphur of MPTMS [11]. The Si 2p peaks (Figure 6.7 d) consist of a doublet with an energy separation between the Si $2p_{3/2}$ and Si $2p_{3/2}$ of 0.6 eV and an area ratio of 2:1.

In table 6.3 the quantitative analysis results calculated for M-PVC samples are reported.

*Table 6.3 Quantitative analysis results obtained from the spectra of M-PVC acquired in standard lens mode. The theoretical concentrations are also calculated assuming 30% contribution of not functionalized substrate.*

| | | M-PVC (at %) | Theoretical stoichiometry (at %) |
|---|---|---|---|
| | | | calculated for PVC immersed in EtOH for 1 h |
| PVC (Bulk) | C contamination | 5 (3) | 5 |
| | C 1s $CH_2$ PVC | 4 (1) | 5 |
| | C 1s CH-Cl PVC | 4 (1) | 5 |
| | Cl 2p | 5 (2) | 5 |
| | C 1s Carboxylate | 2 (1) | 1 |
| | O 1s C=O | 2 (1) | 1 |
| | O 1s C-O | 2 (1) | 1 |
| | C 1s plasticizer | 8 (2) | 8 |
| | Zn 2p | - | - |
| | | | Overlayer composition at% |
| MPTMS (Overlayer) | C 1s C-Si, C-C | 15 (1) | 15 |
| | C 1s C-S | 15 (1) | 15 |
| | C 1s Methoxide | 4 (1) | 7 |
| | O 1s Si-O-Si | 17 (2) | 18 |
| | S 2p | 7 (1) | 7 |
| | S 2p non grafted | 1.0 (0.4) | - |
| | Si 2p | 10 (1) | 7 |

The presence of Cl 2p signals and the concentration of Si and S calculated for M-PVC samples suggested that not all chlorine have reacted. About the 12 % of silicon and sulphur would be expected for a complete reaction. The calculated composition reported in table 6.3 has been calculated assuming that 30% of the polymer surface analysed did not react.

### 6.3.2.2 ARXPS results on M-PVC

The high-resolution spectra acquired on M-PVC in ARXPS are reported in figure 6.8. The C 1s, O 1s, S 2p and Si 2p that are attributed to the MPTMS layer were detected at all angles, while the Cl 2p ascribed to the PVC is strongly attenuated at shallow angles.

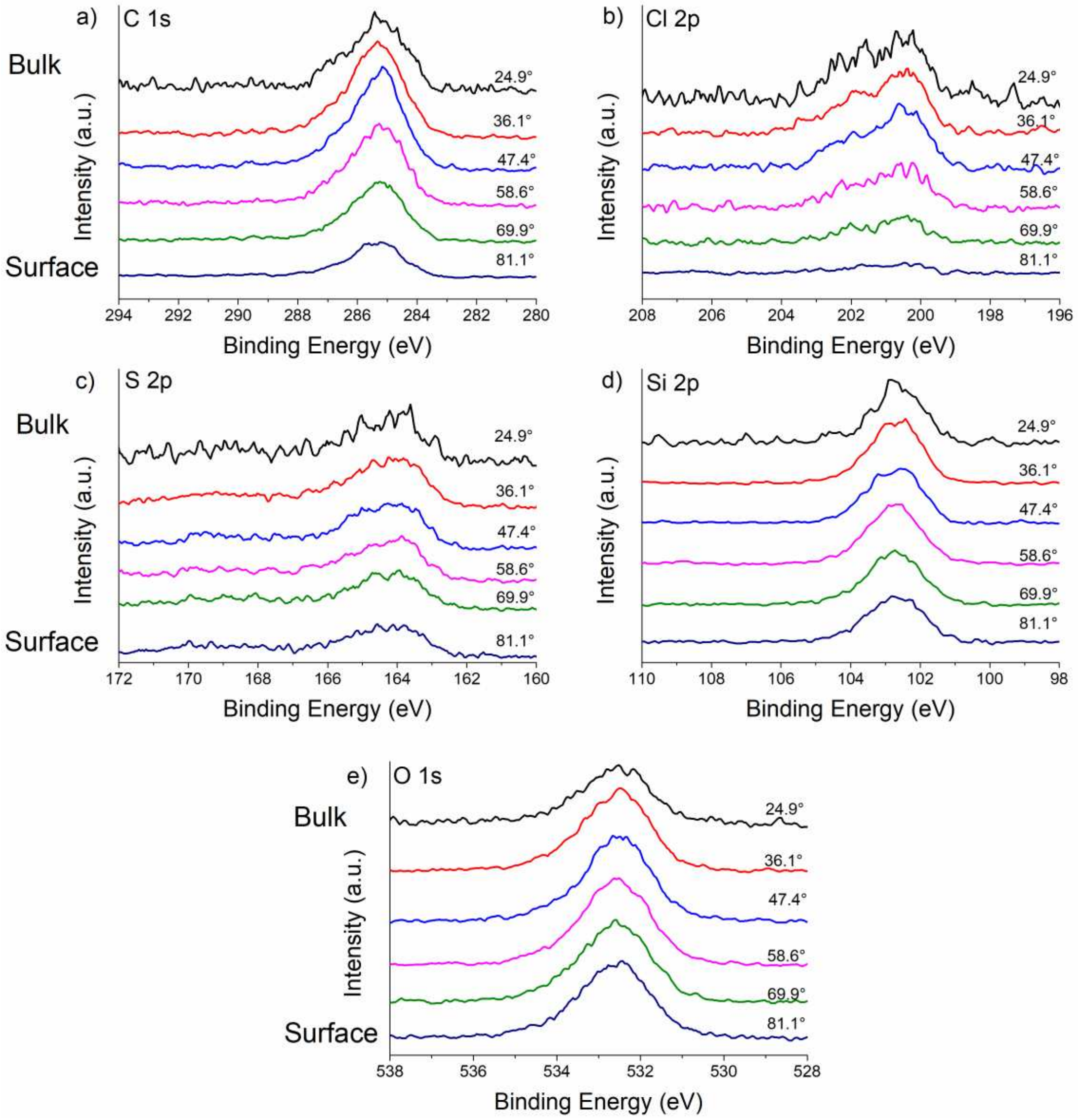

*Figure 6.8 High-resolution spectra of C 1s (a), Cl 2p (b), S 2p (c), Si 2p (d) and O 1s (e), acquired by ARXPS.*

The apparent concentration versus emission angle plot is reported in figure 6.9 a for M-PVC samples. The apparent concentration of Si 2p and the corresponding carbon atoms belonging to C–Si are nearly independent on the emission angle, indicating that these elements, that belong to the MPTMS molecule, are in the centre of the surface layer. The apparent concentration of sulphur S 2p, at the interface with the PVC, and the chlorine Cl 2p, that belongs to the PVC, decreases at high emission angles while the apparent concentration of the oxygen and the $CH_3O$- groups increases with the emission angle.

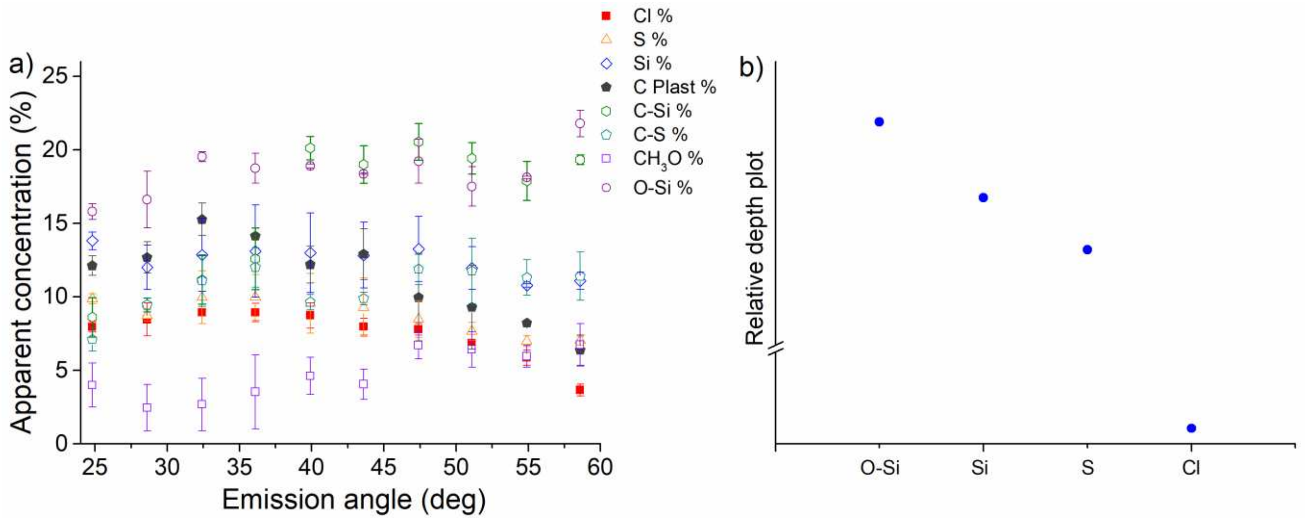

*Figure 6.9 Apparent concentration versus emission angles (a) and relative depth plot (b)*

The relative depth plot reported in Figure 6.9 b was calculated by using Avantage software v 5.932 (Thermo Fisher) based on the results showed in figure 6.9 a: oxygen and silicon are located at the outermost part of the layer while the sulphur at the interface and the chloride of the PVC at the greatest depth.

### 6.3.2.3 XPS results on A-PVC

In A-PVC survey spectrum (figure 6.6), in addition to the signals of C 1s, O 1s, S 2p and Si 2p revealed in the M-PVC samples, N 1s signal was also detected, thus indicating the presence of APTES molecules on the sample surface.

Figure 6.10 shows the high-resolution spectra acquired on A-PVC samples with the same conditions used of M-PVC sample.

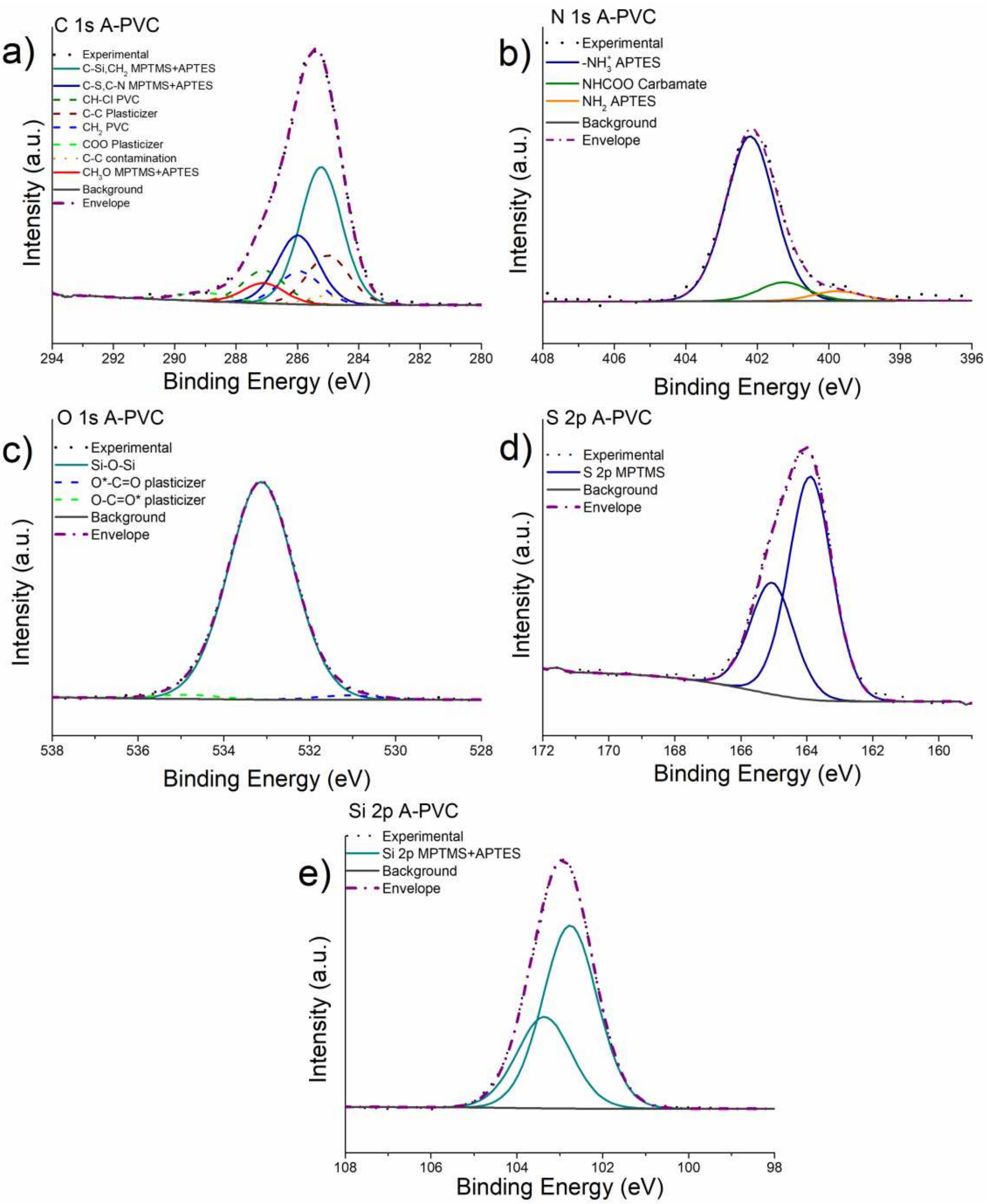

*Figure 6.10 High-resolution spectra of the most intense signals of A-PVC: C 1s (a), N 1s (b), O 1s (c), S 2p (d) and Si 2p (e)*

The Cl 2p signal was still detected and no differences were observed in the peak shape and binding energy. The signals reported in figure 6.10 were fitted by using the curve fitting parameters adopted for the A-gold sample (Chapter 5). The C 1s signal (Figure 6.10 a) was fitted considering three components at 285.2 eV, 286.1 eV and 287 eV assigned to the C-Si/CH$_2$, C-S/C-N and CH$_3$O of the MPTMS+APTES layer, respectively. Moreover, the presence of the components ascribed to the PVC from the bulk was considered, as reported also in the M-PVC samples.

The experimental line shape of the N 1s signal (Figure 6.10 b) suggested the presence of three components attributed to NH$_2$ groups (399.8 eV), NHCOO carbamate groups (401.1 eV) and to the

$NH_3^+$ groups (402.7 eV). As discussed in the case of the A-gold samples, the three components can be ascribed to the amino groups of the APTES molecules that, due to the experimental conditions, react with the $CO_2$ forming carbamates [12]; the $NH_3^+$ component may be due to the weak hydrogen bonding interaction between the other APTES chain, or its presence can be promoted by the presence of water in the solvent [12,13].

The O 1s signal (Figure 6.10 c) was fitted with three components: the O-Si groups component found at 532.9 eV, and two components ascribed to the $\underline{O}$-C=O and O-C=$\underline{O}$ components due to the presence of the carbamate species. The area ratio of these two components was constricted to be 1:1.

S 2p (Figure 6.10 d) and Si 2p (Figure 6.10 e) signals were fitted as shown in the case of MPVC samples as well as in the functionalized gold samples (Chapter 5).

In table 6.4 shows the experimental concentration (at %) calculated based on the XPS results. The theoretical concentration of A-PVC was calculated considering 30% contribute from the PVC as discussed in the case of M-PVC samples.

*Table 6.4 Quantitative analysis results obtained from the spectra of A-PVC acquired in standard lens mode. The theoretical concentrations are also calculated assuming 30% contribution of not functionalized substrate.*

| | | A-PVC (at %) | Theoretical stoichiometry (at %) calculated for PVC immersed in EtOH for 1 h |
|---|---|---|---|
| PVC (Bulk) | C contamination | 2 (1) | 4 |
| | C 1s $CH_2$ PVC | 3 (1) | 5 |
| | C 1s CH-Cl PVC | 3 (1) | 5 |
| | Cl 2p | 4 (2) | 5 |
| | C 1s plasticizer | 5 (1) | 8 |
| | Zn 2p | - | - |
| | | | Overlayer composition at% |
| MPTMS (Overlayer) | C 1s C-Si, C-C | 20 (1) | 22 |
| | C 1s C-S | 10 (1) | 11 |

| | | |
|---|---|---|
| C 1s Methoxide | 2 (1) | - |
| C 1s Carbamate | 1.0 (0.3) | - |
| O 1s Si-O-Si | 20 (1) | 18 |
| N 1s $-NH_2$ | 4 (1) | 4 |
| N 1s -NHCOO | 1 (0.5) | |
| N 1s $NH_3^+$ | 0.3 (0.1) | |
| O 1s C=O Carbamate | 1.0 (0.2) | - |
| O 1s C-O Carbamate | 1.0 (0.2) | - |
| S 2p | 8 (3) | 7 |
| Si 2p | 15 (1) | 11 |

#### 6.3.2.4 ARXPS results on A-PVC

A-PVC samples were also analysed by ARXPS spectroscopy, and the high-resolution spectra of the most intense signals acquired at different emission angles are reported in Figure 6.11.

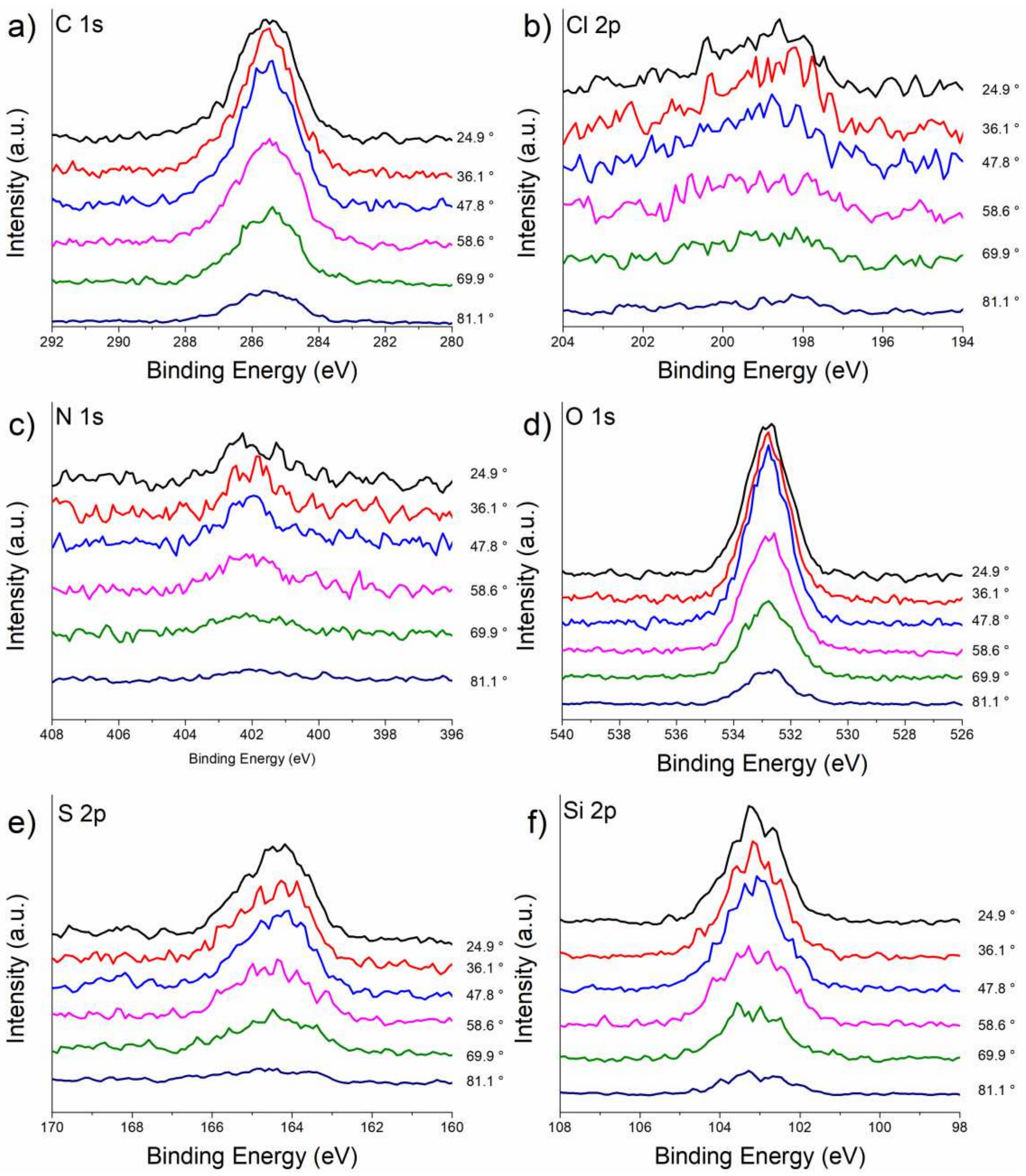

*Figure 6.11 High-resolution spectra of the C 1s (a), Cl 2p (b), N 1s (c), O 1s (d), S 2p (e) and Si 2p (f) signals, acquired at different emission angles*

Figure 6.12a shows the apparent concentration (at%) of the functionalization layer functional groups and of the chloride signal ascribed to the bulk, versus the emission angle. The apparent concentration of C-Si, $CH_2$ groups and C-N groups increases with the emission angle, while it can be noticed that silicon and sulphur concentration slightly decrease, thus suggesting that sulphur and silicon atoms are not in the outer part of the functionalization layer. The nitrogen apparent concentration slightly increases from 3 % (24.9 °) to 4 % (58.6 °) with the emission angle.

The results observed in Figure 6.12 a are substantiated by the relative depth plot reported in figure 6.12 b, in which nitrogen atoms are found to be in the outer layer, silicon and oxygen in the middle part of the functionalization layer and sulphur and chloride at the greatest depth.

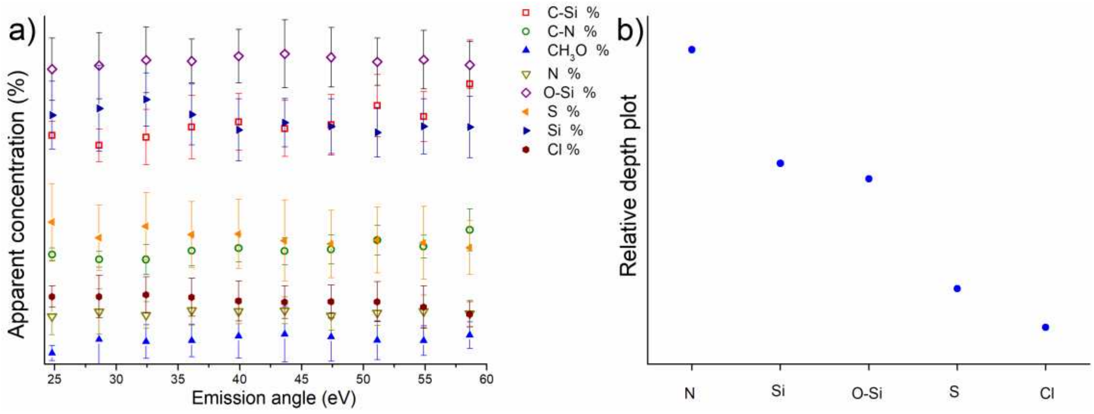

*Figure 6.12 Apparent concentration of C-Si, C-N, CH$_3$O, N, O-Si, S, Si and Cl % (a) and relative depth plot (b)*

#### 6.3.2.5 XPS results on G-PVC

The results presented below were obtained from three independent samples of G-PVC.

Following the grafting of glutaraldehyde as described in chapter 4, the G-PVC samples were analysed by means of XPS. Figure 6.13 shows the high-resolution spectra acquired on the G-PVC samples of the most intense signals observed in the survey spectrum (Figure 6.6).

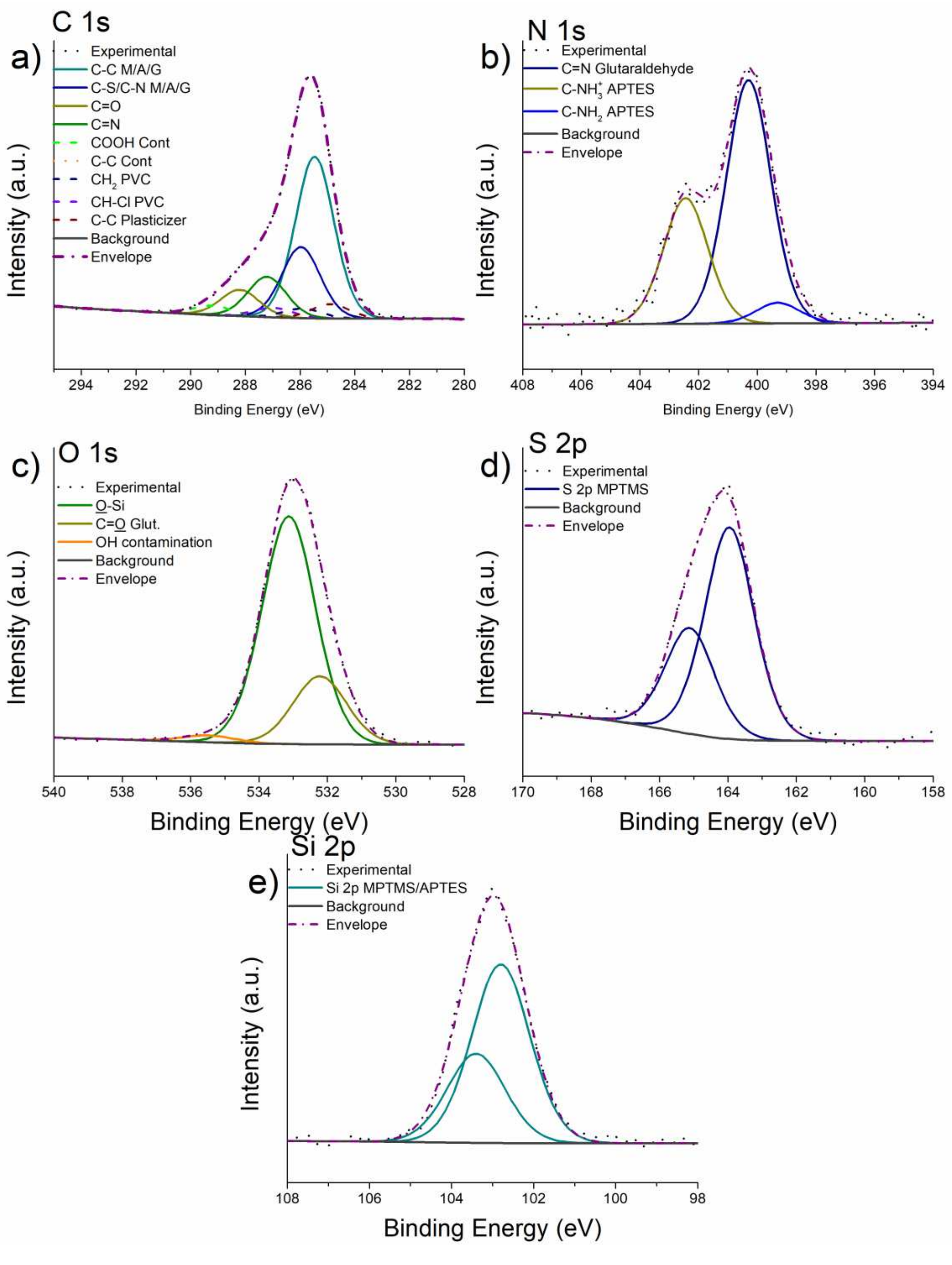

*Figure 6.13 High-resolution spectra of the most intense signals of G-PVC: C 1s (a), N 1s (b), O 1s (c), S 2p (d) and Si 2p (e)*

The C 1s signal (Figure 6.13 a) of G-PVC sample was fitted using the parameters found on G-gold sample (§5.3.4), hence, using four components ascribed to the functionalization layer composed by MPTMS+APTES+Glutaraldehyde (M/A/G) found at 285.5 eV, 286.2 eV, 286.6 eV and 288.3 eV assigned to the C-C bonds of the M/A/G layer, C-S and C-N bond, C=N bond and C=O of the glutaraldehyde layer, respectively [12,14,15]. Moreover, the contribution of the components ascribed to the PVC from the bulk were considered since the Cl 2p was still detected as showed in Figure 6.6.

Th N 1s was fitted with three components found at 399.3 eV, 400.5 eV and 402.3 eV. The components at 399.3 and 402.3 eV were assigned to the $NH_2$ and the $NH_3^+$ groups of the non-reacted APTES, while the component at 400.5 eV can be ascribed to the C=N bond formed by reaction between amino groups of the APTES with the glutaraldehyde carbonyl groups.

The O 1s signal showed the most intense component at 533.2 eV assigned to the O-Si-O groups of the previous functionalization steps. The other two components at 531.7 and 534.5 eV were assigned to the $C=\underline{O}$ group of the glutaraldehyde and to contamination layer due the presence of water, respectively [14].

The S 2p and Si 2p signals were found at 164.1 and 102.8 eV respectively and were fitted as shown in paragraph 6.3.2.1.

These results are in agreement with the results observed in the gold samples functionalized with the same procedure. Table 6.5 shows the quantitative analysis results obtained on G-PVC samples. The composition of the sample surface is the calculated considering the results obtained on three different analysed areas on three independent samples. The standard deviations are provided in parentheses.

*Table 6.5 Quantitative analysis results obtained from the spectra of G-PVC acquired in standard lens mode. The theoretical concentrations are also calculated assuming 30% contribution of not functionalized substrate.*

| | | G-PVC (at %) | Theoretical stoichiometry (at %) calculated for PVC immersed in EtOH for 1 h |
|---|---|---|---|
| PVC (Bulk) | C contamination | 3 (1) | 3 |
| | C 1s $CH_2$ PVC | 1 (0.4) | 2 |
| | C 1s CH-Cl PVC | 1 (0.4) | 2 |
| | Cl 2p | 1 (0.3) | 2 |
| | C 1s plasticizer | 3 (1) | 3 |

| | | | |
|---|---|---|---|
| | C 1s COO contamination | 1 (0.8) | - |
| | Zn 2p | - | - |
| | | | Overlayer composition at%* |
| MPTMS (Overlayer) | C 1s C-Si, C-C | 28 (2) | 28 |
| | C 1s C-S | 12 (1) | 12 |
| | C 1s C=O | 6 (1) | 3 |
| | C 1s C=N | 8 (2) | 3 |
| | O 1s Si-O-Si | 16 (1) | 16 |
| | O 1s C=O Glut. | 4 (1) | 3 |
| | O 1s OH contamination | 0.5 (0.1) | - |
| | N 1s $-NH_2$ | 0.6 (0.2) | 1 |
| | N 1s $C=\underline{N}$ | 2.0 (0.5) | 3 |
| | N 1s $NH_3^+$ | 0.6 (0.2) | 1 |
| | S 2p | 5 (1) | 7 |
| | Si 2p | 7 (1) | 11 |

The XPS results obtained on G-PVC were in good agreement with the one obtained on G-gold. The atomic ratio between the N 1s component assigned to the C=N bond and to the one assigned to the free amino groups of the APTES is 1.7:1, suggesting that the reaction between the APTES and Glutaraldehyde is 5:3, similar results were observed on G-gold samples.

### 6.3.2.6 ARXPS results on G-PVC

Figure 6.14 shows the high-resolution spectra of the most intense signals of G-PVC samples acquired at different emission angles by means of ARXPS.

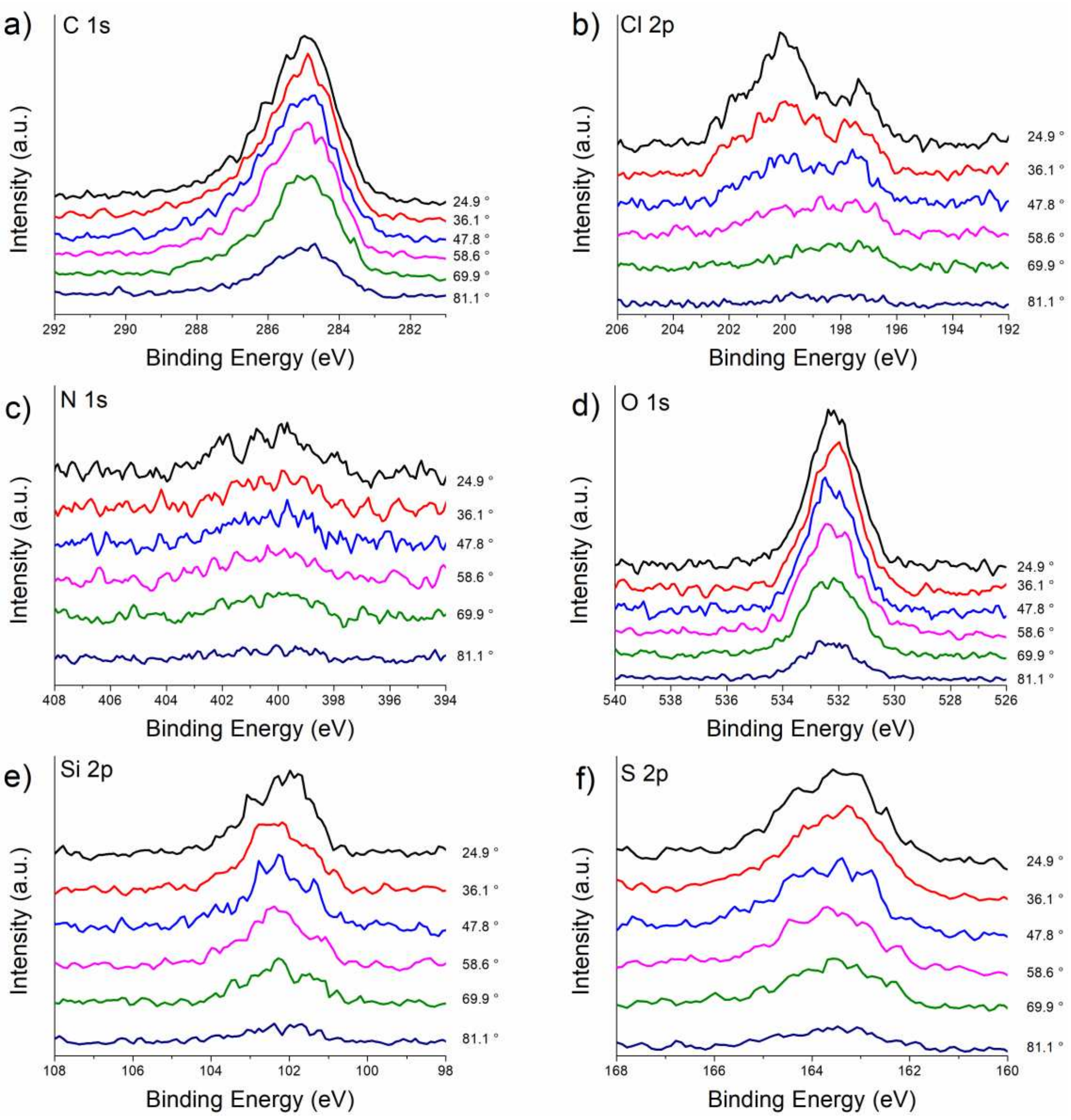

*Figure 6.14 High-resolution spectra of C 1s (a), Cl 2p (b), N 1s (c), O 1s (d), Si 2p (e) and S 2p (f) of G-PVC samples*

The apparent concentration versus emission angle plot of the characteristic functional groups of the functionalization layer is reported in figure 6.15 a. It can be noticed that the concentration (at%) of the C-Si/C-C groups slightly increases with the emission angle, while the concentration of chlorine decreases. The concentration of the C-S/C-N and the C=O groups increases by the 1% with the emission angles. Overall, the concentration of the other signals remains constant.

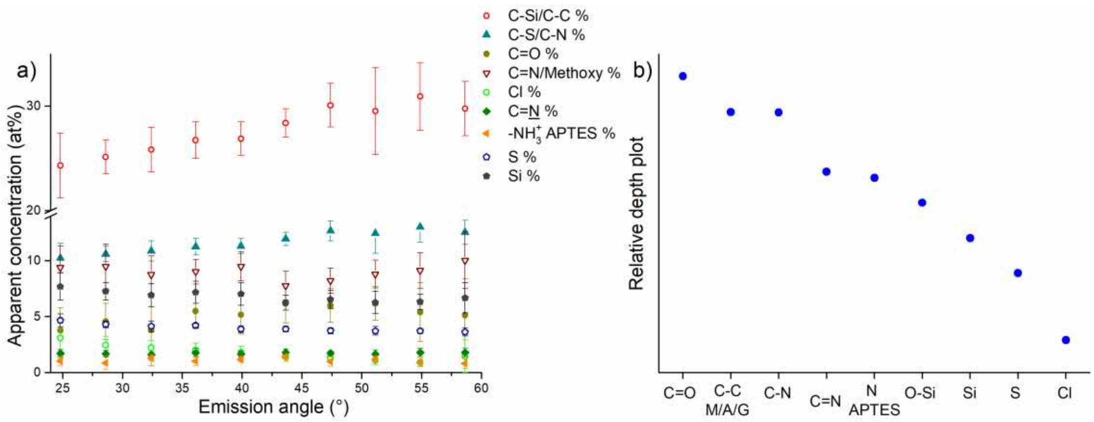

*Figure 6.15 Apparent concentration (%) versus emission angle calculated for Cl, Si, S, C-Si/C-C, C=N, C=O and N (a) and relative depth plot (b) for G-PVC. Mean values and standard deviation are calculated for three independent samples.*

From the relative depth plot (Figure 6.15 b) the spatial disposition of the functional groups was confirmed, being the carbonyl groups on top and the sulphur and chlorine at the greatest depth. The results obtained for G-PVC samples are in good agreement with the results reported for G-gold samples (§5.3.4.2).

### 6.3.2.7 XPS results on P-PVC

The following results obtained on P-PVC were obtained by analysing three independent samples.

XPS measures were also performed on P-PVC samples. The survey spectrum (Figure 6.6) shows that the C 1s and the N 1s are the most intense signals, O 1s, Cl 2p, Si 2p and S 2p signals were also detected. Cl 2p signal as discussed in 5.3.5 is present since a PHMG chloride salt was used for the last functionalization step (§ 4.2.1.3). The sulphur and silicon signals are still detected but strongly attenuated by the functionalization layer.

Figure 6.16 shows the high-resolution spectra acquired on P-PVC samples.

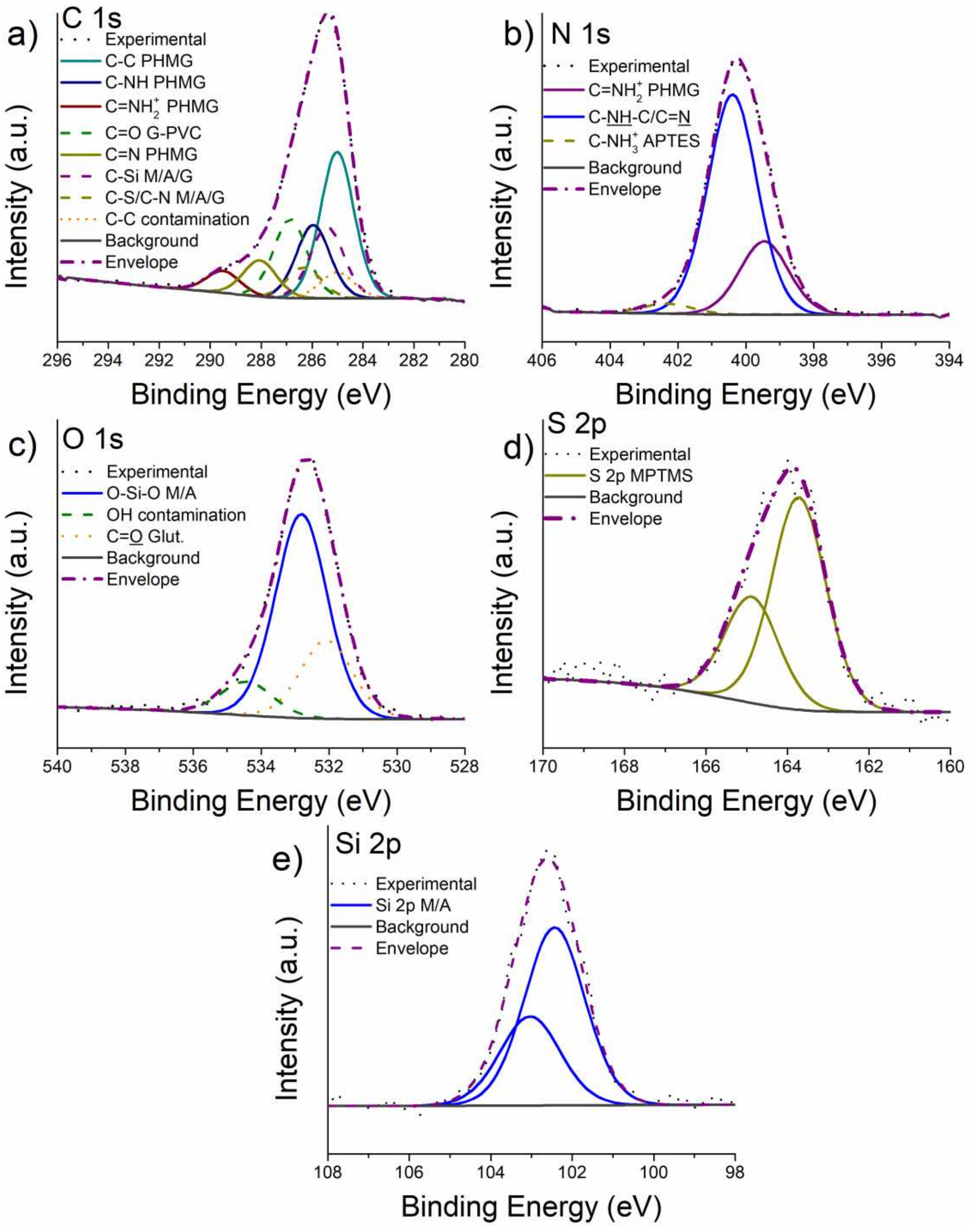

*Figure 6.16 High-resolution spectra of C 1s (a), N 1s (b), O 1s (c), S 2p (d) and Si 2p (e) acquired on P-PVC sample*

Four components ascribed to the PHMG was used for resolving the C 1s signal (Figure 6.16 a) and they were assigned to the following functional groups: aliphatic C-C of the PHMG (285.0 eV), secondary amine C-NH- groups of the PHMG (286.2 eV), C=N groups as a result of the reaction between glutaraldehyde and PHMG (287.0 eV) and finally the $C=NH_2^+$ iminium groups of the PHMG (289.3 eV). Moreover, as observed in P-gold sample (§ 5.3.5.1), since silicon and sulphur signals were detected, the contribution of the components assigned to the previous functionalization layer was considered. Since the aliphatic carbon component due to the plasticizers/stabilizers was not revealed, C-C PHMG component was considered as a reference at 285.0 eV as expected from the literature[16]. The BE value of the components ascribed to the functional groups from the previous steps was fixed to be the same as the one observed in G-PVC samples, and same area ratio between these components was imposed.

The N 1s signal (Figure 6.16 b) was fitted with three components; the most intense one was found at 400.7 eV and it was assigned to the secondary amine group of the PHMG and the C=N groups formed as a result of the reaction between the amino group of the PHMG and the carbonyl groups of the glutaraldehyde. The component at 399.8 eV was attributed to the iminium groups of the PHMG; an area ratio equal to 3:1 was fixed between this component and the component at 400.7 eV, as expected by the stoichiometry of the PHMG. The third component was found at 402.5 eV and it was assigned to the $-NH_3^+$ of the free amino groups of the APTES.

The O 1s signal (Figure 6.16 c) was fitted with three components, as in the case of P-gold samples (§ 5.3.5.1): the C=O of the non-reacted carbonyl group of the glutaraldehyde component at 531.6 eV, the O-Si groups attributed to the previous functionalization steps found at 532.9 eV and finally the third component ascribed to absorbed water since water was used as solvent during this last functionalization step, found at 534.8 eV. The area of all these components was let free to vary.

The surface composition is reported in table 6.6; the concentrations here reported, and the standard deviations are referred to three different analysed areas on three independent samples.

*Table 6.6 Quantitative analysis results obtained from the spectra of P-PVC acquired in standard lens mode. Means value and standard deviation are calculated for three analysed area for three independent samples*

| | | P-PVC at % |
|---|---|---|
| MPTMS+APTES+Glutaraldehyde | C 1s C-Si/C-C | 5 (2) |
| | C 1s C-S/C-N | 2 (1) |
| | C 1s C=O | 4 (2) |
| | N 1s $-NH_3^+$ | 0.8 (0.2) |
| | O 1s O-Si | 7 (3) |

| | | |
|---|---|---|
| | O 1s C=O | 3 (2) |
| | S 2p | 1 (0.3) |
| | Si 2p | 3 (1) |
| | | |
| PHMG (Overlayer) | C 1s C-C Cont. | 8 (3) |
| | C 1s C-C | 27 (2) |
| | C 1s C-NH- | 13 (1) |
| | C 1s C=N | 8 (3) |
| | C 1s $C=NH_2^+$ | 5 (2) |
| | O 1s $H_2O$ | 0.5 (0.1) |
| | N 1s C-NH-C/C=N | 10 (2) |
| | N 1s $C=\underline{N}H_2^+$ | 4 (1) |

The presence of the components ascribed to the C=O groups of the glutaraldehyde in the C 1s and O 1s signals suggests that not all the carbonyl group present in the G-PVC sample reacted with the PHMG.

### 6.3.2.8 ARXPS results on P-PVC

Figure 6.17 shows the high-resolution spectra of the most intense signals of P-PVC sample acquired at different emission angles by means of ARXPS. It is worth noting that sulphur signal is not detected at all the considered emission angles while silicon was barely visible at the lowest emission angles, and it is not detected at grazing angles. This can be attributed to the layer thickness of the PHMG, that can influence the detection of the electrons associated to the atoms located in the inner layer such as silicon and sulphur. The O 1s signal was strongly attenuated but still detected at all angles.

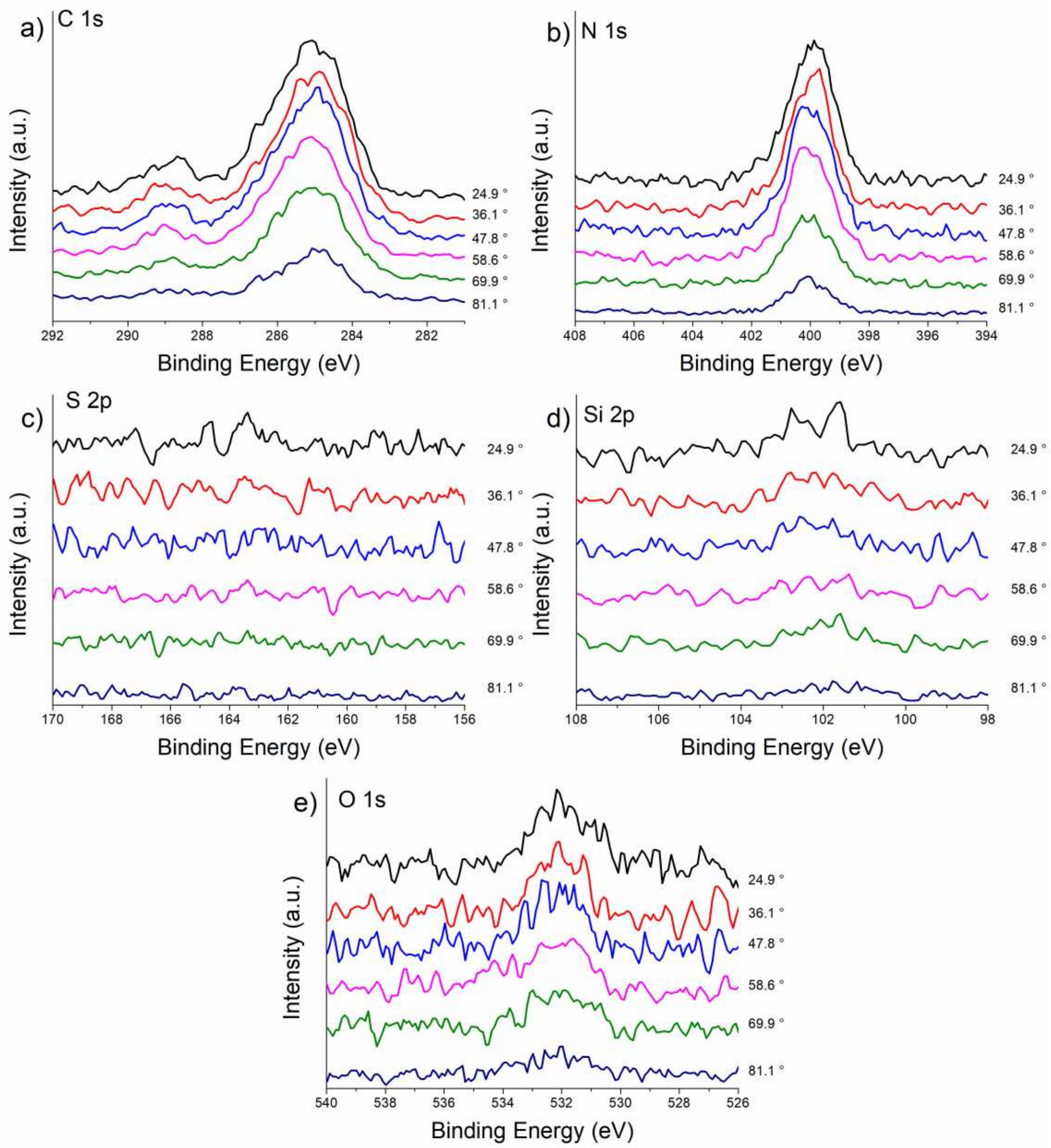

*Figure 6.17 High-resolution spectra of C 1s (a), N 1s (b), S 2p (c), Si 2p (d) and O 1s (e) acquired in angle-resolved XPS for P-PVC sample*

Figure 6.18a show the apparent concentration of the characteristic functional groups of P-PVC sample versus the emission angle. The concentration of the groups assigned to the functional groups of PHMG remain constant at all angles, as well as the C=<u>O</u> group of the glutaraldehyde. The relative depth plot reported in Figure 6.18 b shows the spatial disposition of the functional groups revealed on P-PVC sample, confirming that C=O groups are located in the inner part of the functionalization layer, while the functional groups of the PHMG such as C-C, C-NH-C and C=N are found at the same height, thus suggesting that the PHMG might be not perpendicularly bonded.

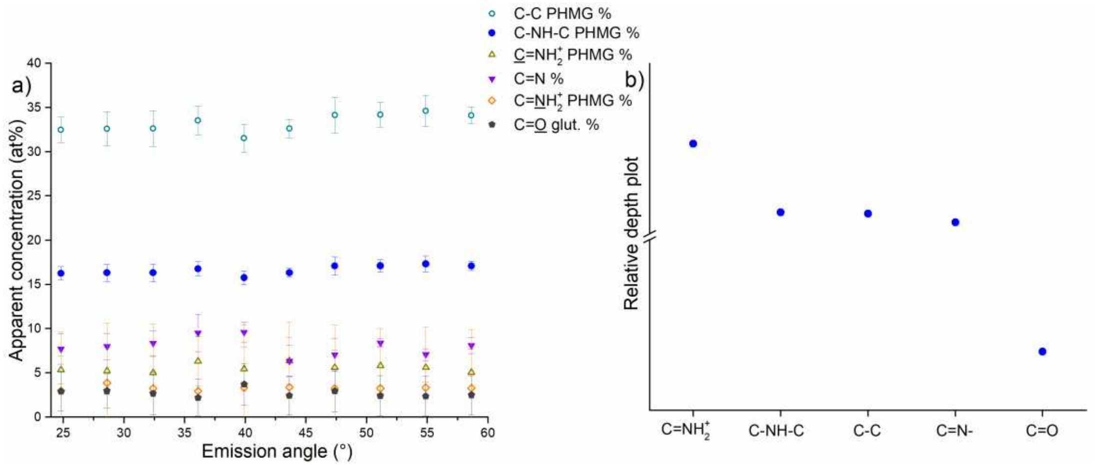

*Figure 6.18 Apparent concentration (%) versus emission angle calculated for Cl, Si, S, C-Si/C-C, C=N, C=O and N (a) and relative depth plot (b) for G-PVC. The apparent concentration and the standard deviation are calculated on three analysed areas for one P-PVC sample.*

### 6.3.3 Thickness estimation

The thickness layer was calculated by using the same approach exploited in gold samples. Since in the PVC samples the only signal attributed to the bulk was the Cl 2p, the total thickness that comprises the functionalization layer and the contamination layer was estimated considering the attenuation of the chlorine signal. For this reason, the equation 5.2 was applied based on the ARXPS results, considering the Cl 2p signal intensity ($I_{Cl}$) measured at two different emission angles, grazing (58.6 degrees) and near vertical (24.8 degrees). For this purpose, the following equations were used:

$$ln\left(\frac{I_{Cl24°}}{I_{Cl58°}}\right) = -\frac{t}{\lambda_{Cl}}\left(\frac{1}{cos\,(58)} - \frac{1}{cos\,(24)}\right) \quad \textit{eq. 6.4}$$

$$t = \frac{ln\left(\frac{I_{Cl24°}}{I_{Cl58°}}\right) \cdot \lambda_{Cl}}{cos(24) - cos(58)} \quad \textit{eq. 6.5}$$

Equation 6.2 was applied also to the S 2p and Si 2p intensities in the case of M-PVC, A-PVC and G-PVC. IMFP was calculated according to Seah and Dench [17], since this model allows estimating IMFP value without considering the density. This approximation is necessary in this work, since the density of the functionalization layer anchored on PVC is not known. The thickness values reported in Table 6.7 were calculated on three different analysed areas of three independent samples.

Table 6.7 *Total thickness of the overlayers calculated on M-PVC, A-gold, G-PVC and P-PVC based on the attenuation of the elements Cl, S, Si, N and O according to equation 6.2.*

| **Element** | **Cl** | **S** | **Si** | **N** | **C=O** |
|---|---|---|---|---|---|
| **IMFP $\lambda$ (nm)** | 3.12 | 3.16 | 3.24 | 3.06 | 2.68 |
| **Thickness M-PVC (nm)** | 2.2 (0.4) | 1.6 (0.4) | 1.3 (0.4) | - | - |
| **Thickness A-PVC (nm)** | 2.1 (0.4) | 1.4 (0.4) | 1.0 (0.3) | 0.4 (0.1) | - |

The total thickness of M-PVC was determined to be 2.2 (0.4) nm, considering the attenuation of the chlorine signal, and considering the MPTMS layer, the contamination layer ($l_c$), and the gold substrate. The calculated thickness, considering Si 2p electron attenuation, is 1.3 (0.4) nm, representing the sum of $l_c$ and O-$CH_3$ groups. For A-PVC samples, the total thickness is 2.1 (0.4) nm, with the contamination layer thickness determined by N 1s electron attenuation estimated at 0.4 (0.1) nm. These findings suggest a lower contamination layer thickness ($l_c$) on A-Gold compared to M-Gold samples with the MPTMS layer.

The formation of a complex system in G-gold and P-gold samples was confirmed also on the PVC; moreover, on PVC, the system complexity is enhanced by the contributes from the substrate that makes challenging the estimation of the layers thickness as well as the composition.

## 6.4 Discussion

The characterization of the carbon-based substrate such as polymers, functionalized with organic molecules is challenging due to the presence of overlapped components from both substrate and functionalization layer, in the C 1s signals. The analytical strategy developed on gold surfaces and presented in Chapter 5 was exploited for characterizing the PVC samples modified as presented in Chapter 4. By applying this analytical approach and using the same curve-fitting parameters exploited on gold samples, such as line-shape, FWHM, area ratios determined for C 1s, S 2p, Si 2p, O 1s and N 1s spectra, the component ascribed to the bulk (PVC and plasticizers) and the component ascribed to the functional groups of the functionalization layer can be distinguished. Moreover, the quantitative analysis results obtained on functionalized PVC samples were in good agreement with the results obtained on the gold samples. The same reaction ratio between the MPTMS:APTES and APTES:Glutaradehyde found in the gold samples were confirmed in the case of A-PVC and G-PVC.

### 6.4.1 Spatial disposition of the functionalization layer

Following the functionalization of the PVC with MPTMS and APTES (A-PVC), according to the expected stoichiometry showed in Figure 4.2 the sulphur to nitrogen ratio is expected to be 1:1, as also discussed in paragraph 5.4.1. The quantitative analysis results reported in table 6.4 revealed a sulphur to nitrogen ratio of 2:1, indicating a possible different reaction ratio. As discussed in the previous chapter (§5.4.1) APTES can differently arrange during the functionalization process, as discussed also in the literature [12,18–20]. The S : N atomic ratio found on A-PVC samples (Table 6.4) was also found on A-gold samples, thus confirming that the MPTMS:APTES ratio is 2:1 also in the A-PVC samples, leading to the arrangement showed in Figure 6.19.

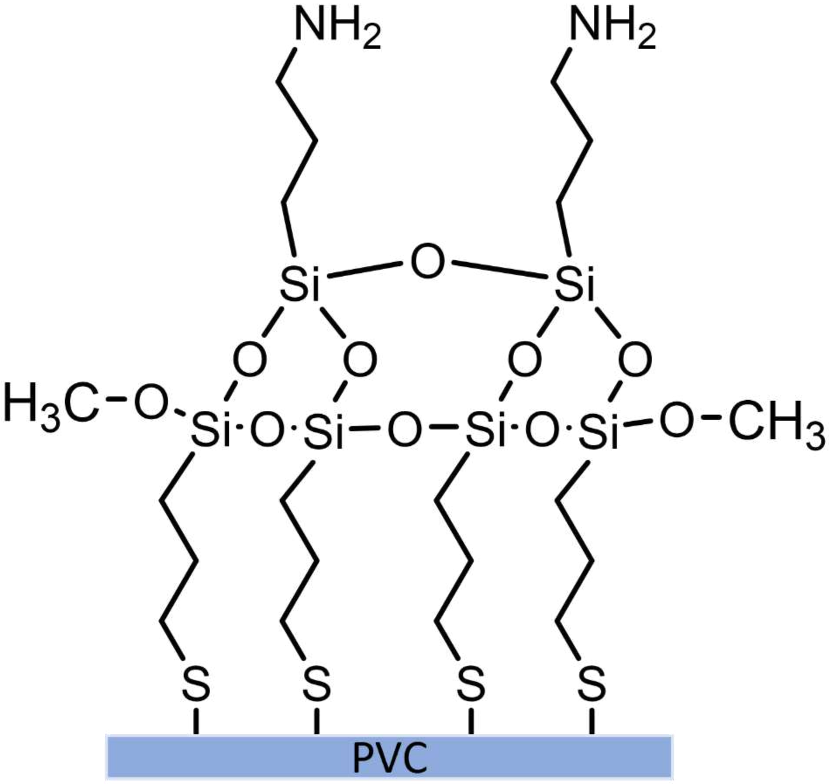

*Figure 6.19 A-PVC model considering an MPTMS:APTES ratio of 2:1*

The quantitative analysis of the G-PVC reported in Table 6.5, suggests that also the reaction between glutaraldehyde and APTES is not 1:1, since the N 1s spectra suggests the presence of non-reacted amino groups of the APTES moieties. The experimental atomic ratio calculated between the component ascribed to the C=N formed by the reaction of the carbonyl groups of glutaraldehyde and the amino groups of the APTES, and the component ascribed to the free amino groups was found to be 1.7:1. Similar results were observed in G-gold sample, for this reason the same model reported for G-gold sample (Figure 5.21) can be proposed (Figure 6.20) also for the G-PVC: according to this model reaction ratio between APTES and glutaraldehyde is equal to 5:3.

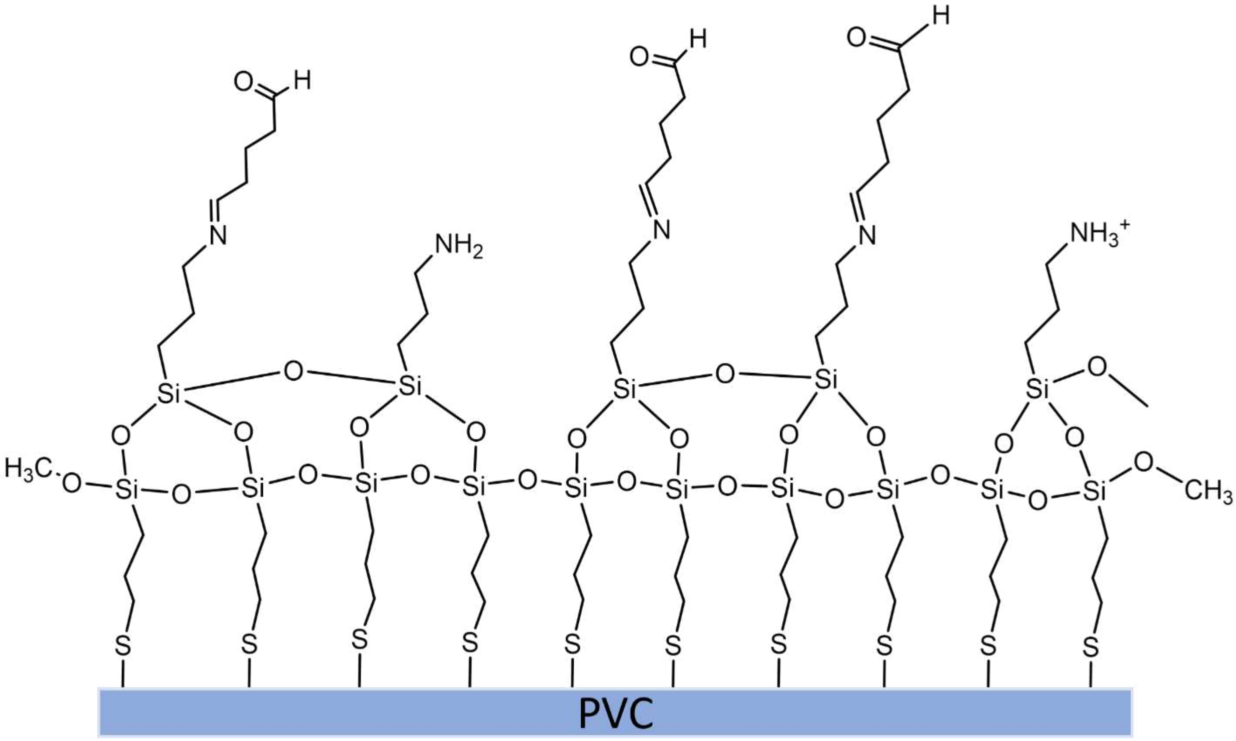

*Figure 6.20 G-PVC model proposed on the base of the experimental results*

A similar consideration can be done regarding the P-PVC; the presence of the C=O component in both C 1s and O 1s spectra suggests that not all the glutaraldehyde react with the PHMG. The presence of 4% of C=O (Table 6.6) suggests that the possible reaction ratio between glutaraldehyde and PHMG is 2:1. In figure 6.21 the possible arrangement of the PHMG layer is shown. However, the quantitative results suggest a high grade of complexity for both G-PVC and P-PVC, and more in-depth analyses are needed to fully understand the interactions between the glutaraldehyde and the PHMG. Further theoretical investigations will be essential to clarify the spatial disposition of the overlayer in the case of G-PVC and P-PVC.

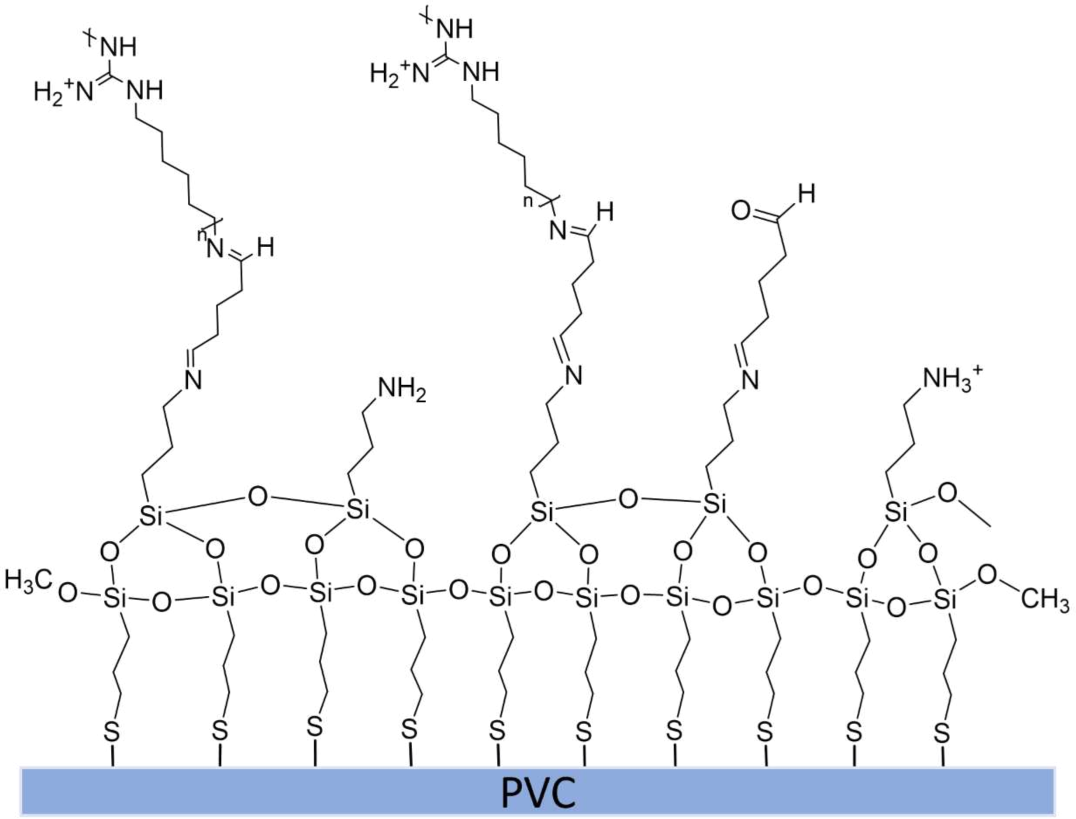

*Figure 6.21 P-PVC model proposed based on the experimental results*

### 6.4.2 Layer thickness

According to the ARXPS results, the total layer thickness calculated on M-PVC samples (§ 6.3.4) was estimated to be 2.2 ± 0.4 nm (Table 6.7). This thickness comprises the contamination layer ($l_c$) and the functionalization layer of MPTMS (t). Using the same equation and considering the attenuation of the sulphur signal (Table 6.7) the total thickness calculated was 1.6 ± 0.4 nm, comprising the MPTMS layer and the contamination. By employing the same equation considering the silicon signal a thickness of 1.3 ± 0.4 nm was calculated, consisting of $l_c$ and the -$OCH_3$ groups facing the outer part of the MPTMS layer. By Avogadro software it was possible to estimate that the bond length -$OCH_3$ groups to be 0.2 nm, thus suggesting a $l_c$ of 1.1 nm. A layer thickness of the MPTMS layer (t) of 0.5 nm can be calculated from the attenuation of the sulphur, 1.6 nm, minus the $l_c$ (1.1 nm). The chain length of the MPTMS can be estimated by measuring the distance between sulphur and silicon atoms using Avogadro software and it was found to be 0.7 nm (Table 6.8). By using the same approach on the A-PVC samples, the $l_c$ can be estimated to be 0.4 nm, considering the attenuation of the nitrogen signal in the case of A-PVC. Moreover, calculating the difference between the thickness estimated considering the attenuation of the sulphur and the $l_c$ in both samples, the layer thickness t resulted to be 1.0 nm in the case of A-PVC. Both results agree with the estimation obtained by Avogadro.

In the case of G-PVC and P-PVC the total layer thickness was not calculated given the high complexity of the overlayer in both cases. Moreover, in P-PVC samples sulphur and silicon signals were strongly attenuated in ARXPS.

*Table 6.8 Summary of the thickness of the functionalized layer and the contamination layer on gold*

| **Layer** | **M-PVC** | **A-PVC** |
|---|---|---|
| **Contamination $l_c$** | 1.1 nm | 0.4 nm |
| **Layer thickness t** | 0.5 nm | 1.0 nm |
| **Avogadro calculation** | 0.7 nm | 1.2 nm |

The results obtained on functionalized PVC samples were comparable with those obtained on gold samples, as well as to the values calculated on Avogadro software, even if in the case of gold, a better agreement between the thickness values determined by ARXPS and calculated by Avogadro was observed, especially for M-gold and A-gold (Table 5.7 in paragraph 5.4.2). Further studies are required to calculate the total thickness in the case of G-PVC and P-PVC.

### 6.4.3 Composition of the functionalized layers

In the previous paragraphs the experimental concentration (at%) calculated for M-PVC, A-PVC and G-PVC and the theoretical stoichiometry and calculated based on the models presented in paragraph 6.4.2 were reported. For all the analysed samples a good agreement between the theoretical and the experimental concentrations was obtained, considering a 30% contribution from the non-functionalized bulk, that was estimated by the experimental results on M-PVC samples (Table 6.3). However, the experimental concentrations calculated on these samples showed differences with respect to the results presented by Villanueva et alii [3] in the case of A-PVC and G-PVC. In fact, the Si : S ratio reported in the literature for A-PVC was found to be equal to 1:1, while in this work a 2:1 ratio was found. This difference can be ascribed to the different immersion time exploited in this work, in fact in the literature 18h of immersion time was proposed.

G-PVC samples showed a similar silicon to sulphur ratio with respect to the results reported in [3] and was found 2:1 as discussed in previous paragraph (§6.4.3), however G-PVC sample showed an higher concentration of nitrogen (3 %) with respect to the concentration reported in [3] where a 1% nitrogen concentration. These differences may be attributed to the different solvent and the immersion time exploited in this work. Moreover, the chloride concentration in this samples was higher than the one reported in the literature, this discrepancy may be related to the fact that acetone was replaced with ethanol as a solvent in the functionalization step with MPTMS due to the fact that acetone can damage the PVC [21].

In the case of P-PVC the experimental concentrations were not in agreement with the literature results [3]. The nitrogen concentration in P-PVC was calculated to be equal to 24 %, which is ten times higher than the concentration reported in the literature. This difference may suggest the formation of a non-uniform multilayer of PHMG as suggested by SEM results that will be shown in Chapter 7.

For both G-PVC and P-PVC samples additional measurements are necessary to prove the reproducibility of the experiments, and for obtaining more information about the functionalization process.

## Conclusions

Based on the presented results the following conclusions can be drawn:

- The analytical strategy developed on freshly cleaved gold samples and presented in Chapter 5, was successfully applied to a more complex system such as the food-grade PVC. This strategy allowed distinguishing the contributes due to the carbon atoms present in both the PVC and the functionalization layer present in the C 1s spectra.
- Through the detailed analysis of XPS high-resolution spectra, insights into the formation of MPTMS and MPTMS+APTES overlayers on food-grade PVC surfaces were obtained. Quantitative analysis indicated successful and laterally homogeneous functionalization of the gold surface with MPTMS, with an unexpected concentration of $CH_3O$ suggesting three-dimensional cross-linking of the Si-O-Si bond. Moreover, the experimental concentration calculated on A-PVC and G-PVC showed that the reaction between MPTMS and APTES was in a 2:1 ratio in the case of A-PVC samples, and that the reaction between APTES and

glutaraldehyde was 5:3 in the case of G-PVC. The experimental results showed differences with respect to the literature, thus can be related to the different experimental setup such as immersion time and exploited solvents.

- P-PVC and G-PVC experimental concentration obtained by XPS quantitative analysis, suggested the formation of a complex system that requires additional in experimental and theoretical studies to understand the architecture of the overlayer as well as for estimating the layer thickness.
- Angle-resolved XPS allowed understanding the distribution of functional groups within the overlayers after the first two functionalization steps and allow estimating with a good agreement with the theoretical values the layer thickness.

*References*

[1] "G. Casula, M. Fantauzzi, B. Elsener, A. Rossi, Surface modification of food-grade PVC monitored by angle-resolved XPS, Vacuum (2024) 113010. https://doi.org/10.1016/j.vacuum.2024.113010.

[2] T. Kameda, M. Ono, G. Grause, T. Mizoguchi, T. Yoshioka, Antibacterial effect of thiocyanate substituted poly(vinyl chloride), J Polym Res 18 (2011) 945–947. https://doi.org/10.1007/s10965-010-9492-3.

[3] M.E. Villanueva, J.A. González, E. Rodríguez-Castellón, S. Teves, G.J. Copello, Antimicrobial surface functionalization of PVC by a guanidine based antimicrobial polymer, Materials Science and Engineering: C 67 (2016) 214–220. https://doi.org/10.1016/j.msec.2016.05.052.

[4] M.E. Villanueva, A. Salinas, J.A. González, S. Teves, G.J. Copello, Dual antibacterial effect of immobilized quaternary ammonium and aliphatic groups on PVC, New J. Chem. 39 (2015) 9200–9206. https://doi.org/10.1039/C5NJ01766A.

[5] G. Casula, M. Fantauzzi, B. Elsener, A. Rossi, XPS and ARXPS for Characterizing Multilayers of Silanes on Gold Surfaces, Coatings 14 (2024) 327. https://doi.org/10.3390/coatings14030327.

[6] D.R. Baer, K. Artyushkova, H. Cohen, C.D. Easton, M. Engelhard, T.R. Gengenbach, G. Greczynski, P. Mack, D.J. Morgan, A. Roberts, XPS guide: Charge neutralization and binding energy referencing for insulating samples, J. Vac. Sci. Technol. A 38 (2020). https://doi.org/10.1116/6.0000057.

[7] C.D. Easton, C. Kinnear, S.L. McArthur, T.R. Gengenbach, Practical guides for x-ray photoelectron spectroscopy: Analysis of polymers, J. Vac. Sci. Technol. A 38 (2020). https://doi.org/10.1116/1.5140587.

[8] E.D. Giglio, N. Ditaranto, L. Sabbatini, 2 Polymer surface chemistry: characterization by XPS, in: 2 Polymer Surface Chemistry: Characterization by XPS, De Gruyter, 2022: pp. 45–88. https://doi.org/10.1515/9783110701098-002.

[9] H. Hantsche, High resolution XPS of organic polymers, the scienta ESCA300 database. By G. Beamson and D. Briggs, Wiley, Chichester 1992, 295 pp., hardcover, £ 65.00, ISBN 0-471-93592-1, Advanced Materials 5 (1993) 778–778. https://doi.org/10.1002/adma.19930051035.

[10] H.J. Jang, C.-S. Park, E.Y. Jung, G.T. Bae, B.J. Shin, H.-S. Tae, Synthesis and Properties of Thiophene and Aniline Copolymer Using Atmospheric Pressure Plasma Jets Copolymerization Technique, Polymers 12 (2020) 2225. https://doi.org/10.3390/polym12102225.

[11] A. Penna, M. Careri, N.D. Spencer, A. Rossi, Effects of Tailored Surface Chemistry on Desorption Electrospray Ionization Mass Spectrometry: a Surface-Analytical Study by XPS and AFM, J. Am. Soc. Mass Spectrom. 26 (2015) 1311–1319. https://doi.org/10.1007/s13361-015-1135-9.

[12] N. Graf, E. Yegen, T. Gross, A. Lippitz, W. Weigel, S. Krakert, A. Terfort, W.E.S. Unger, XPS and NEXAFS studies of aliphatic and aromatic amine species on functionalized surfaces, Surface Science 603 (2009) 2849–2860. https://doi.org/10.1016/j.susc.2009.07.029.

[13] A. Miranda, L. Martínez, P.A.A. De Beule, Facile synthesis of an aminopropylsilane layer on Si/SiO2 substrates using ethanol as APTES solvent, MethodsX 7 (2020) 100931. https://doi.org/10.1016/j.mex.2020.100931.

[14] E.D. Eren, G. Guisong, L. Mingming, Z. Bingchun, Y. Ke, C. Shanshan, A novel chitosan and polydopamine interlinked bioactive coating for metallic biomaterials, J Mater Sci: Mater Med 33 (2022) 65. https://doi.org/10.1007/s10856-022-06688-x.

[15] X. Yan, T. Xu, G. Chen, S. Yang, H. Liu, Q. Xue, Preparation and characterization of electrochemically deposited carbon nitride films on silicon substrate, J. Phys. D: Appl. Phys. 37 (2004) 907. https://doi.org/10.1088/0022-3727/37/6/015.

[16] W. Cao, D. Wei, Y. Jiang, S. Ye, A. Zheng, Y. Guan, Surface chemical bonding with poly(hexamethylene guanidine) for non-leaching antimicrobial poly(ethylene terephthalate), J Mater Sci 54 (2019) 2699–2711. https://doi.org/10.1007/s10853-018-2966-0.

[17] M.P. Seah, W.A. Dench, Quantitative electron spectroscopy of surfaces: A standard data base for electron inelastic mean free paths in solids, Surface and Interface Analysis 1 (1979) 2–11. https://doi.org/10.1002/sia.740010103.

[18] I. Piwoński, J. Grobelny, M. Cichomski, G. Celichowski, J. Rogowski, Investigation of 3-mercaptopropyltrimethoxysilane self-assembled monolayers on Au(111) surface, Applied Surface Science 242 (2005) 147–153. https://doi.org/10.1016/j.apsusc.2004.08.009.

[19] W. Sui, W. Zhao, X. Zhang, S. Peng, Z. Zeng, Q. Xue, Comparative anti-corrosion properties of alkylthiols SAMs and mercapto functional silica sol–gel coatings on copper surface in sodium chloride solution, J Sol-Gel Sci Technol 80 (2016) 567–578. https://doi.org/10.1007/s10971-016-4108-y.

[20] M. Sypabekova, A. Hagemann, D. Rho, S. Kim, Review: 3-Aminopropyltriethoxysilane (APTES) Deposition Methods on Oxide Surfaces in Solution and Vapor Phases for Biosensing Applications, Biosensors 13 (2023) 36. https://doi.org/10.3390/bios13010036.

[21] W.A. Woishnis, S. Ebnesajjad, eds., 32 - Polyvinyl Chlorides (PVC), in: Chemical Resistance of Thermoplastics, William Andrew Publishing, Oxford, 2012: pp. 3177–3300. https://doi.org/10.1016/B978-1-4557-7896-6.00032-7."

# Chapter 7 Characterization of modified PVC samples by means of ATR-FTIR, AFM, SEM and contact angle.

In this chapter the characterization of food-grade PVC functionalized as described in Chapter 4 by exploiting different surface sensitive techniques will be discussed. By using ATR-FTIR spectroscopy was possible to optimize the functionalization protocol for the surface functionalization of the PVC, as well as validate the XPS results. Using Atomic Force Microscopy (AFM) and Scanning Electron Microscopy (SEM) it was possible to obtain information about the topographical properties and morphology of the PVC after each functionalization step and AFM allowed also estimating the surface roughness of the sample. Scanning Electron Microscopy (SEM) was exploited to study the morphology of the functionalized polymers. Contact angle measurements allowed determining changes in the hydrophobicity of the samples following the functionalization.

I assisted Ms. Federica Zara, an undergraduate student at Università degli Studi di Cagliari, during the characterization of functionalized PVC by ATR-FT IR and FTIR spectroscopy and they are reported in her Bachelor thesis [1].

The synthesis of TPPA and the surface functionalization of food-grade PVC with TPPA were carried out in D-CHAB at the ETH of Zürich under the supervision of Professor Yamakoshi and Dr. Çelik.

## 7.1 Introduction

As discussed in the previous chapters, X-ray photoelectron spectroscopy is a powerful tool for characterizing the sample surface and obtaining information about the chemical composition and the thickness of the functionalization layer. On the other hand, XPS requires ultra-high vacuum conditions, and it requires long acquisition time.

ATR-FTIR allows studying the chemical composition of a surface since it permits distinguishing the different functional groups that are present on the surface taking advantage of the lower acquisition time required for the experiment. Using ATR-FTIR spectroscopy it is possible to validate the results obtained in XPS by comparing the functional groups identified by XPS investigation with those detected by the analysis of the vibrational bands that are found in ATR-FTIR spectra.

SEM and AFM are other two techniques that can be used in combination with XPS and ATR-FTIR, for characterizing the surface morphology of the samples, moreover by AFM the surface roughness can be estimated. The knowledge of the samples' roughness is particularly important since it affects both the quantitative analysis results and the layer thickness estimation obtained by XPS and ARXPS analyses, especially if the XPS spectra are acquired at emission angles higher than 45 °[2].

Contact angle measurements gives information about the hydrophobicity of the surface, which is important in the case of antimicrobial materials since the formation of biofilm of specific bacteria strain is dependent on contact angle.

By integrating the information from these techniques a comprehensive understanding of the functionalization process can be obtained, thus assessing the impact of multilayer formation on surface properties, discerning whether cluster formation or uniform coverage predominates.

## 7.2 experimental

### *7.2.1 ATR-FTIR spectroscopy*

The ATR-FTIR spectrometer used in this work is the Jasco ATR pro 4X model PSK-D1 for characterization of polymeric samples, and for selecting the best conditions for the functionalization process in the modification protocol of the food-grade PVC. The spectrometer was equipped with a diamond crystal. The spectra were acquired in the range from 4000 $cm^{-1}$ to 500 $cm^{-1}$ with a resolution of 4 $cm^{-1}$ and 32 scans. The polymer samples were prepared following the procedure discussed in Chapter 4 and were analysed in air at room temperature. The samples were analysed after drying and they were placed on top of the crystal. Background subtraction was performed before the acquisition of each sample. Vibrational band attribution was performed by peak peaking function of the most intense band and experimental wavenumbers were compared with the literature.

The sampling depth of the ATR is dependent from the wavelength, and it is estimated to be comprised between 0.1 and 1 $\mu$m as reported in [3,4].

### *7.2.2 Atomic force microscopy*

AFM topographical imaging was performed in tapping mode in air using a Dimension Icon AFM (Bruker, UK). A silicon nitride cantilever (DNP-10 , Bruker, UK) was used with a resonance frequency of 56 kHz and a spring constant of 0.24 N $m^{-1}$, at a scan rate of 0.9 Hz. The roughness $R_a$ was measured on 5$\mu$m x 5 $\mu$m areas. Images were processed with Gwyddion software version 2.65. To obtain a good quality image a second-grade polynomial function was applied to background subtraction and flatten the image, followed by the application of damage correction data to correct the image artefacts. Roughness was calculated by Gwyddion software by applying equation.

$$R_a = \frac{1}{N}\sum_{n=1}^{N}(|z_n - \bar{z}|)^i \quad 7.1$$

Where $R_a$ is the average roughness, N is the number of analysed points, $z_n$ is the height value of the n point and $\bar{z}$ is the average height value.

The software calculates as well as the root means square roughness $R_q$ by applying the following equation:

$$R_q = \sqrt{\frac{1}{N}\sum_{n=1}^{N}(|z_n - \bar{z}|)^2} \quad 7.2$$

### 7.2.3 Scanning electron microscopy

SEM was exploited to obtain morphological information of the food-grade PVC in the as received state and following the surface functionalization. The Phenom™ XL G2 Desktop SEM (Thermo Fisher) scanning electron microscope operating at 20 kV was used and secondary electrons images were acquired. Since the analysed samples were non-conductive a thin layer of gold was applied onto the surface samples; to guarantee an optimal resolution of the non-conductive samples the pressure in the proximity of the sample surface was 0.1 Pa.

### 7.2.4 Contact angle measurements

Water contact angle measurement have been carried out using a Krüss Drop-Shape Analysis DSA 100 (Krüss GmbH, Hamburg, Germany) instrument that was equipped with an optical system that acquire images of the liquid droplet located on the sample surface, and a goniometer that measures the contact angle on both sides of the droplet. The water volume (9 µL) was controlled by the instrument software, and it was placed on the sample surface by a syringe.

## 7.3 Results

### 7.3.1 ATR-FTIR results

ATR-FTIR spectra were acquired after each functionalization step. Figure 7.1 shows the spectra obtained for food-grade PVC, M-PVC, A-PVC, G-PVC, and P-PVC.

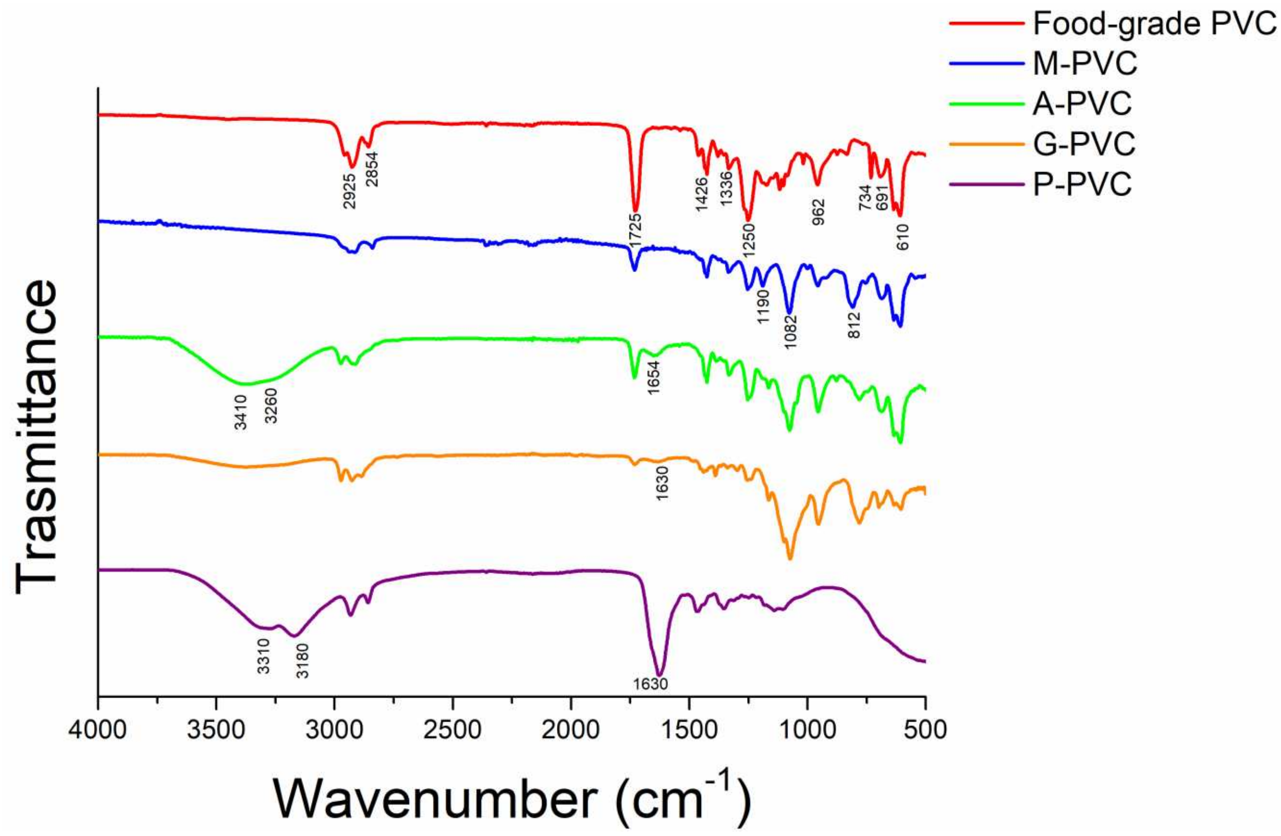

*Figure 7.10 ATR-FTIR spectra of food-grade PVC, M-PVC, A-PVC, G-PVC and P-PVC*

In Figure 7.1 are also reported the wavenumber associated with the principal bands that are characteristic for each functionalization step. The wavenumber of the most intense band of the food-grade PVC are reported in Table 7.1.

*Table 7.4 Wavenumber (cm$^{-1}$) of the most intense band detected in the as received food grade PVC and related functional groups according to literature data [4,6]*

| **Wavenumber (cm$^{-1}$)** | **Attribution** | **Functional groups** | **Reference** |
|---|---|---|---|
| **2925** | Asymmetric stretching C-H | $CH_2$ | [5,6] |
| **2854** | Symmetric stretching C-H | $CH_2$ | [5,6] |
| **1725** | Stretching C=O | C=O plasticizers | [5,6] |
| **1426** | Bending C-H | C̲H-Cl PVC | [5,6] |
| **1336** | Bending C-H | $CH_2$ | [5,6] |
| **1250** | Rocking C-H | $CH_2$ | [5,6] |
| **962** | Wagging C-H | $CH_2$ | [5,6] |
| **734** | Stretching C-H | C̲H-Cl PVC or aromatic compounds | [5,6] |
| **691** | Stretching C-Cl | C̲H-Cl PVC | [5,6] |
| **610** | Wagging C-H | $CH_2$ | [5,6] |

The band found at 734 $cm^{-1}$ can be ascribed to the stretching of the C-H bond of aromatic compounds that might be present in the polymer as a plasticizer. As it can be observed in figure 7.1, most of the signals reported in table 7.1 are detected also in all the functionalization steps but strongly attenuated by the presence of new bands, such as the band relative to the stretching of the Si-O-Si groups found at 1082 $cm^{-1}$ [7] in M-PVC, A-PVC and G-PVC.

In the M-PVC spectra, together with the stretching band of the silanes groups mentioned above, and with the band observed in the PVC samples, the presence of the band at 1190 $cm^{-1}$ and 812 $cm^{-1}$ is observed. These two bands can be ascribed to the C-O and Si-C bond stretching and to O-Si-O symmetric stretching bond stretching respectively [7–9].

Following the grafting of APTES (A-PVC), two broad bands between 3500 and 3250 $cm^{-1}$ are detected and they were assigned to the free amino groups stretching as expected from the literature [10,11]. The band at 1650 $cm^{-1}$ further substantiates this attribution since it can be assigned to the bending of the amino groups [10,11].

In the G-PVC samples the attenuation of the band between 3500 $cm^{-1}$ and 3250 $cm^{-1}$ ascribed to the amino groups in A-PVC, and the presence of the band at 1630 $cm^{-1}$ (stretching C=N) [12,13] might suggest the grafting of the glutaraldehyde onto the PVC surface. Finally, the P-PVC spectrum showed a major difference with respect to the previous ones. In fact, the bands at 1082 $cm^{-1}$, 1190 $cm^{-1}$ and 812 $cm^{-1}$ assigned to the stretching of O-Si-O and of C-Si groups are not detected in P-PVC samples. On the other hand the intensity of the band at 1630 $cm^{-1}$ that has been ascribed to the C=N bond stretching increases [13], thus suggesting the formation of a PHMG multilayer. The wavenumber values of all these bands are summarized in Table 7.2 for all the functionalized sample.

*Table 7.5 Wavenumber ($cm^{-1}$) of the most intense bands detected in the functionalized food grade PVC and related functional groups according to literature data [4, 7-13]*

| | **Wavenumber ($cm^{-1}$)** | **Attribution** | **Functional groups** | **Reference** |
|---|---|---|---|---|
| **M-PVC** | 1082 | O-Si-O asymmetric stretching | Si-O | [7–9] |
| | 1190 | C-O and Si-$CH_2$ symmetric stretching | Si-$OCH_3$ and Si-$CH_2$ | [7–9] |
| | 812 | O-Si-O symmetric | Si-O | [7–9] |

| | | | | |
|---|---|---|---|---|
| | | stretching | | |
| **A-PVC** | 3410 | $NH_2$ asymmetric stretching | $NH_2$ | [10,11] |
| | 3260 | $NH_2$ symmetric stretching | $NH_2$ | [10,11] |
| | 1654 | $N-H_2$ bending | $NH_2$ | [10,11] |
| **G-PVC** | 1630 | C=N | C-N=C | [12] |
| **P-PVC** | 3310 | -NH- asymmetric stretching | C-NH-C | [5,13] |
| | 3180 | -NH- symmetric stretching | C-NH-C | [5,13] |
| | 1630 | C=N stretching | $C=NH_2^+$ | [5,13] |
| | 1468 | $CH_2$ bending | $CH_2$ | [5,13] |

ATR-FTIR spectra were also acquired for TPPA-PVC samples (§4.3.2). The spectra were acquired to confirm the surface functionalization of G-PVC with TPPA. The functionalization was carried out as described in paragraph 4.3.2 and the ATR spectra were acquired following different immersion times, i.e. 1, 3 and 12 hours (Figure 7.2)

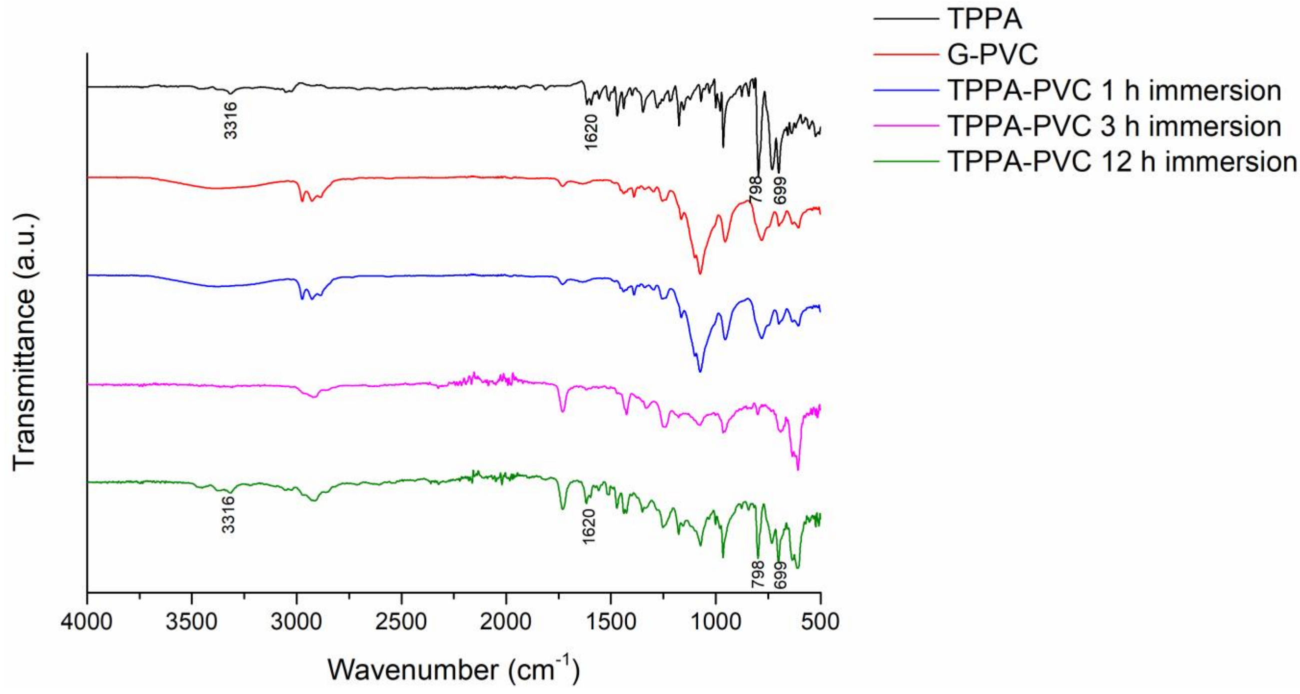

*Figure 7.11 ATR-FTIR spectra of TPPA (black), G-PVC (red), TPPA-PVC 1 h immersion (blue), TPPA-PVC 3 h immersion (pink) and TPPA-PVC 12 h immersion (green)*

The ATR-FTIR spectrum of TPPA shows (black line in Figure 7.2) the presence of four characteristic bands ascribed to the NH stretching of the pyrrolic ring (3316 $cm^{-1}$), C=N stretching (1620 $cm^{-1}$), bending of the C-C-C bonds of the porphyrin ring (798 $cm^{-1}$) and NH out of plane bending vibration (699 $cm^{-1}$) are detected. [14] Following the immersion of G-PVC in TPPA (TPPA-PVC 1h: blu line in figure 7.2) for one hour the spectrum is almost identical to the spectrum of G-PVC (G-PVC: red line in figure 7.2). Only after 12 hours of immersion the characteristic bands of TPPA are clearly detected in the TPPA-PVC sample (TPPA-PVC 12h: green line in Figure 7.2), thus suggesting that prolonged immersion time is required to functionalize the G-PVC.

### *7.3.2 AFM results*

AFM images of as received food-grade PVC, after immersion in ethanol for 1h and following each functionalization step, as described in paragraph 7.2.2 are shown in this paragraph. Figure 7.3 shows the images of food-grade PVC and PVC after 1 hour immersion in ethanol. No difference can be observed in the AFM images after immersion of the PVC in ethanol.

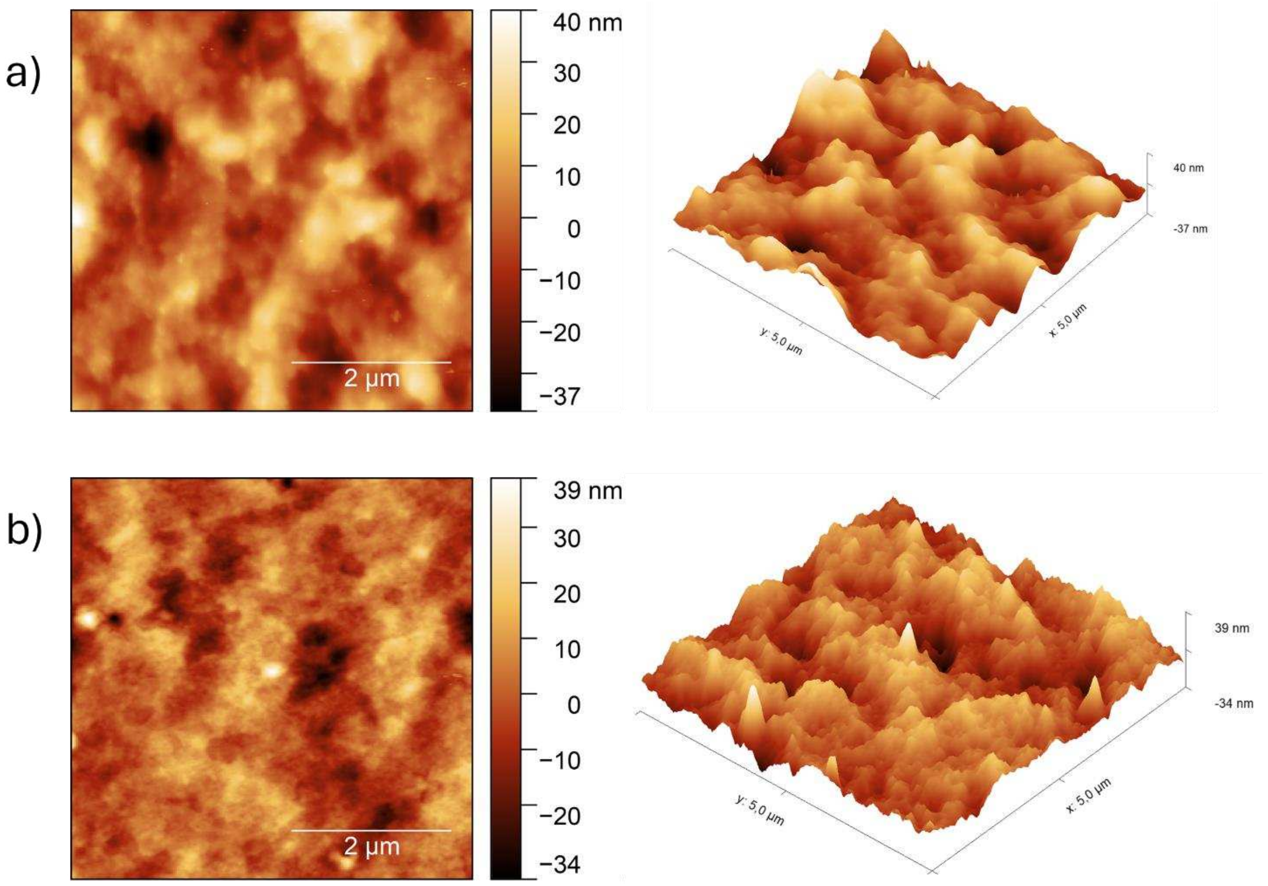

*Figure 7.12 AFM images acquired for food-grade PVC (a) and PVC after 1 h immersion in ethanol (b) in 2D and in 3D*

The surface roughness $R_a$ of the food-grade PVC was estimated to be 8 ± 1 nm for both samples. Root mean square roughness ($R_q$) was estimated to be 10 ± 1 nm; Rq is more sensitive to the presence of high peaks and deep valleys, thus it is more suitable to provided surface roughness measurement at the microscopic level [15]. These values agree with the roughness calculated for other PVC films that have been reported in the literature and suggest that the surface of the PVC is not uniform [16–18].

Figure 7.3 shows the images acquired for M-PVC, A-PVC and G-PVC. The average surface roughness $R_a$ of M-PVC does not change and was estimated to be 8 ± 1 nm, while a $R_q$ value equal to 12 ± 1 nm was found to be slightly higher than the 10 ± 1 nm found for the food -grade PVC. This may be due to the presence of the peaks that are visible in Figure 7.4 a probably related to the formation of MPTMS clusters.

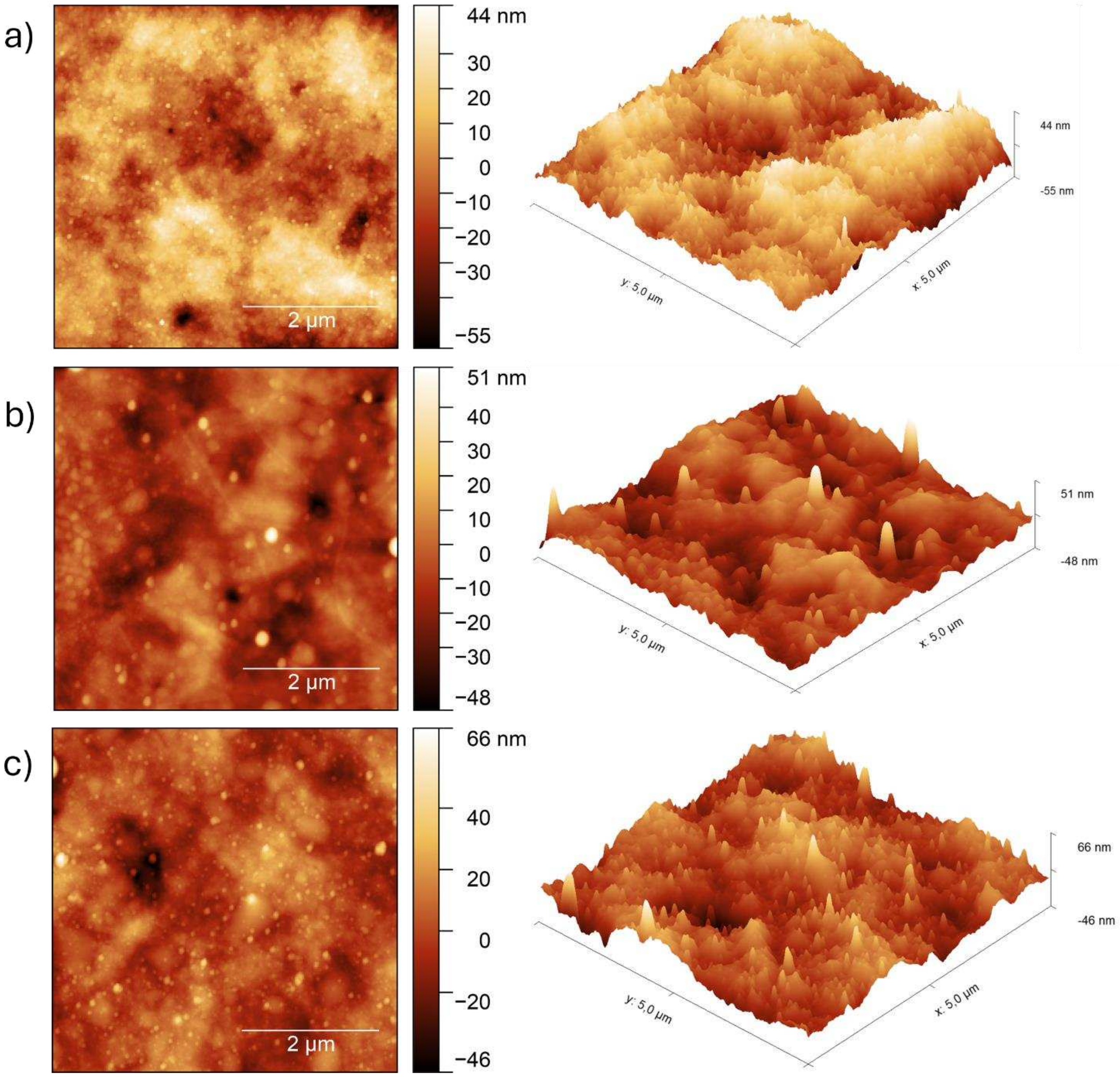

*Figure 7.13 AFM images acquired M-PVC (a), A-PVC (b) and G-PVC (c) in 2D (left) and in 3D (right)*

In A-PVC and G-PVC the formation of clusters is observed, and higher spikes are observed (Figure 7.4b and 7.4c). The $R_q$ values for these two samples were estimated to be 13 ± 2 nm for both samples.

Finally Figure 7.5 shows the AFM image acquired for P-PVC samples. The P-PVC surface show the presence of numerous clusters that cover uniformly the surface of the sample. The $R_q$ values measured for P-PVC samples are 15 ± 3 nm.

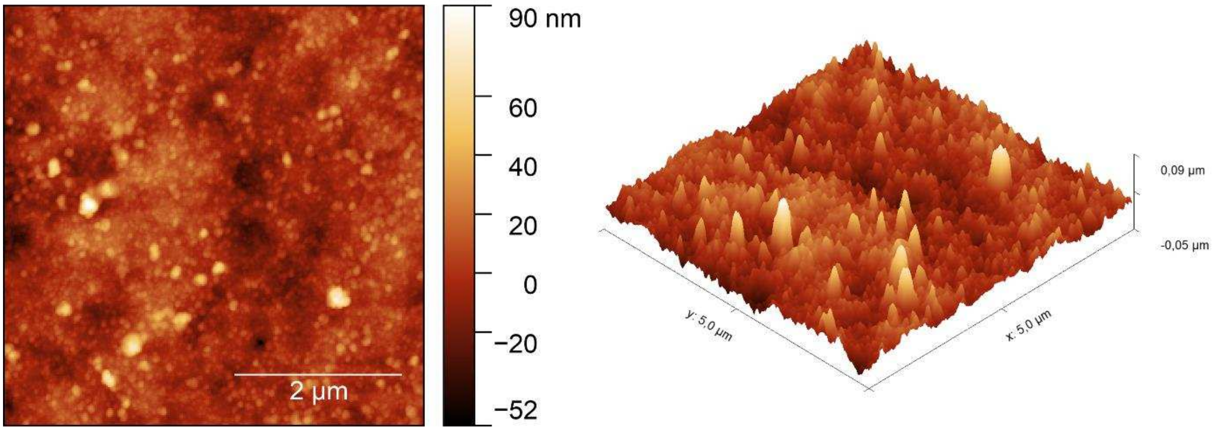

*Figure 7.14 AFM images acquired for P- PVC in 2D (left) and in 3D (right)*

The values of average roughness ($R_a$) and the root mean square roughness ($R_q$) calculated on all the PVC samples are summarized in Table 5.3.

*Table 5.6 Average roughness values ($R_a$) and root mean square roughness values ($R_q$) calculated for food-grade PVC as received, food-grade PVC after immersion in ethanol, M-PVC, A-PVC, G-PVC and P-PVC. Mean values and standard deviation are calculated on the analysed area on three independent samples*

| | **Food-grade PVC a.r.** | **Food-grade PVC after immersion in ethanol** | **M-PVC** | **A-PVC** | **G-PVC** | **P-PVC** |
|---|---|---|---|---|---|---|
| **$R_a$ (nm)** | 8 ± 1 nm | 8 ± 1 nm | 8 ± 1 nm | 9 ± 1 nm | 9 ± 1 nm | 11 ± 2 nm |
| **$R_q$ (nm)** | 10 ± 1 nm | 10 ± 1 nm | 12 ± 1 nm | 13 ± 2 nm | 13 ± 2 nm | 15 ± 3 nm |

### *7.3.3 SEM results*

SEM micrographs of as received and functionalized PVC are presented in this paragraph. Figure 7.6 shows the micrography acquired of food-grade PVC at two different magnifications (1400x – Figure 7.6a and 10500x Figure 7.6b), to observe the morphological features of the sample. The figure acquired at higher magnification (Fig. 7.6b) shows that the sample surface is not totally flat and not uniform.

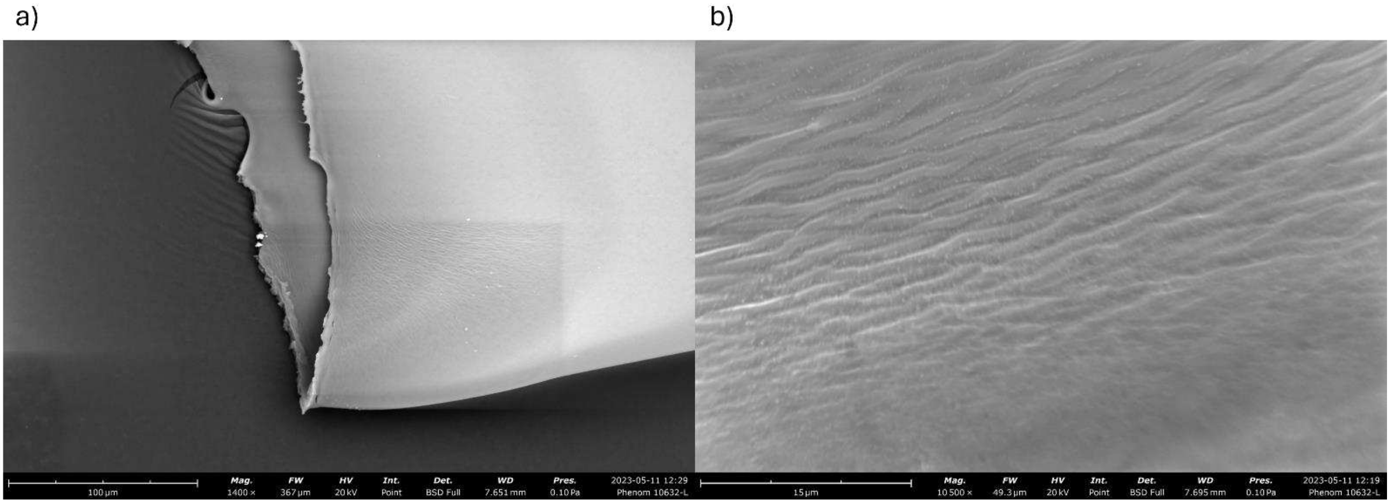

*Figure 7.15 SEM micrographs of as received food-grade PVC acquired at 1400x (a) and 10500x (b)*

After the functionalization with MPTMS, the surface of the polymer shows different regions in which the formation of MPTMS clusters is likely (Figure 7.7).

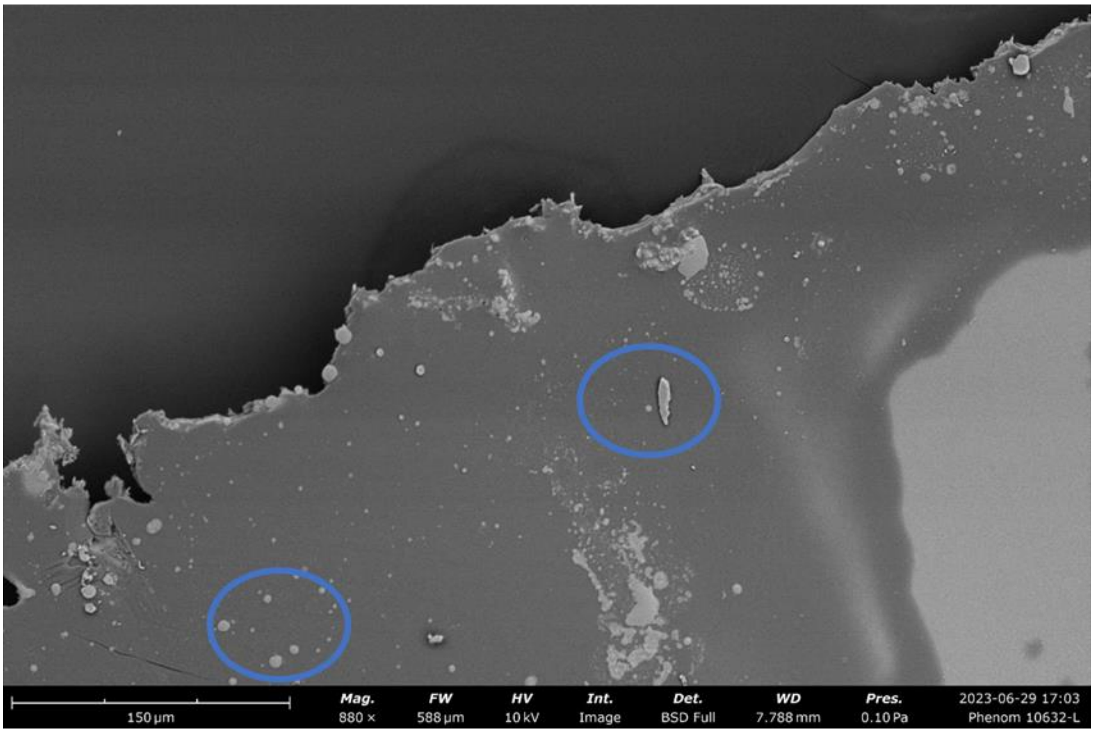

*Figure 7.16 SEM micrography of M-PVC sample*

Following the grafting of APTES (A-PVC) the formation of small particles on the sample surface can be observed (Figure 7.8). These particles can be attributed to the *"island-structure"* mentioned in paragraph 5.3.4, typical of silanes [19].

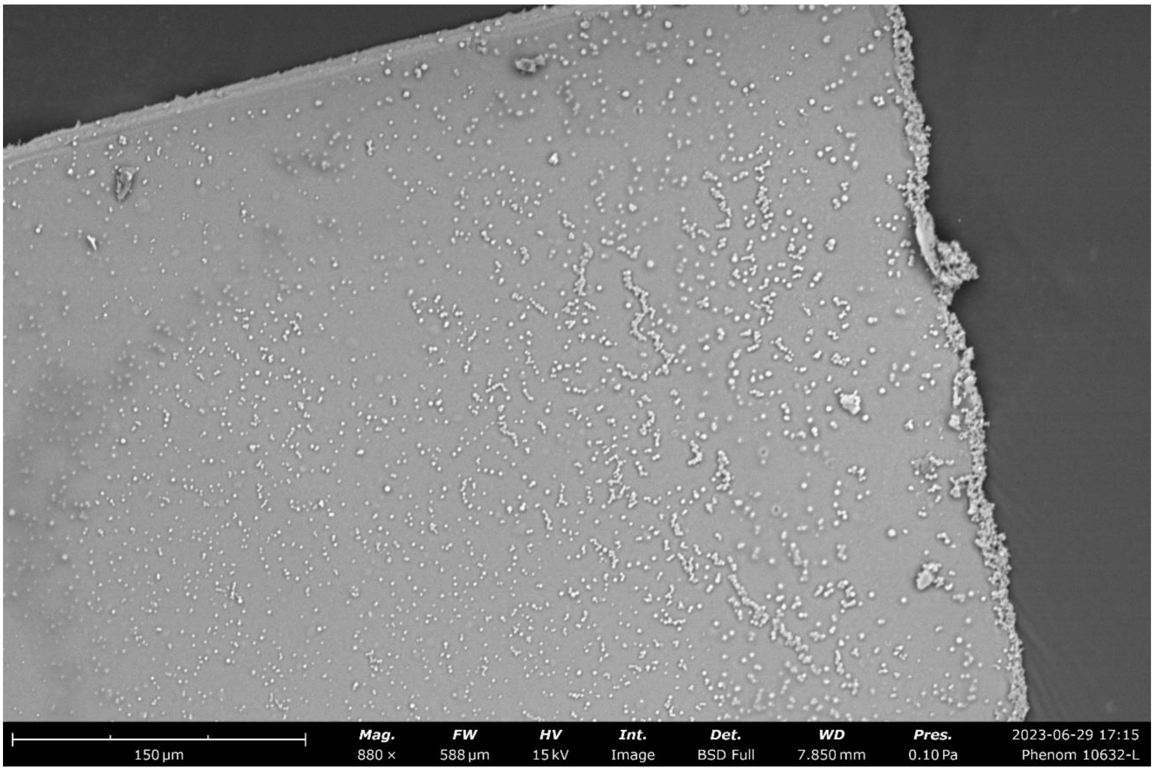

*Figure 7.17 SEM micrography of A-PVC sample*

The micrography acquired on G-PVC (Figure 7.9) shows similar results but in this case the formation of bigger clusters can be observed.

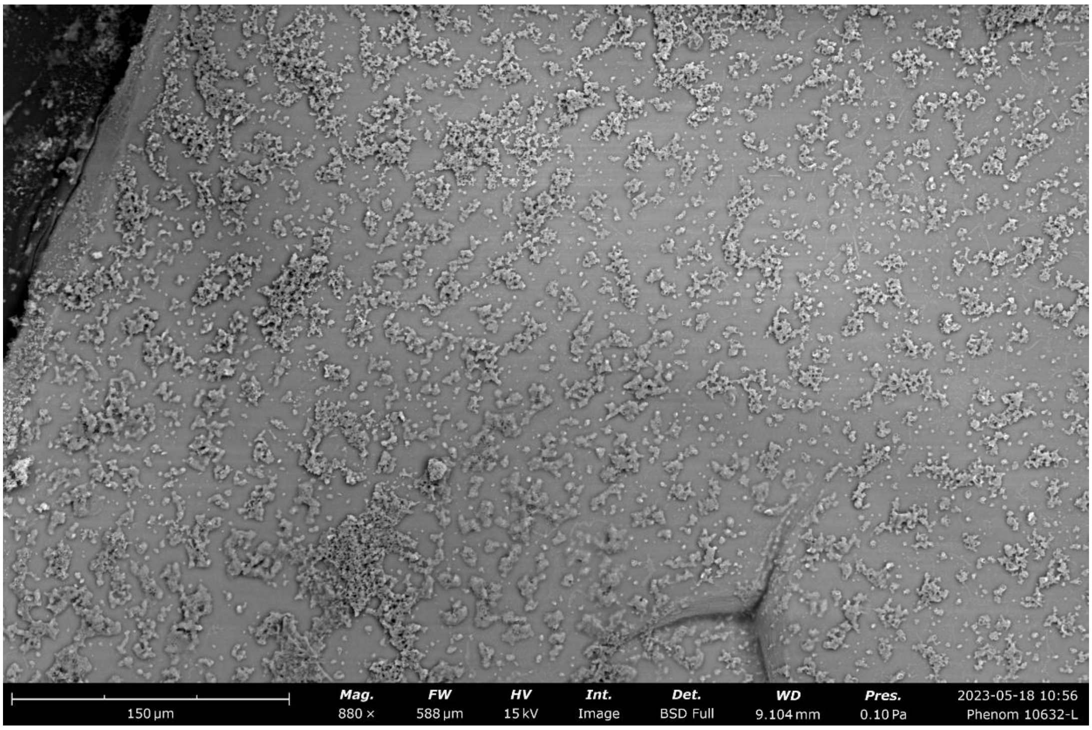

*Figure 7.18 SEM micrography of G-PVC sample*

Figure 7.10 shows the SEM image obtained for P-PVC sample. As mentioned in Chapter 5 and 6, PHMG molecules can polymerize forming multilayers, this reaction can lead to the formation polymeric film composed by PHMG. Figure 7.10 may substantiate this hypothesis since large areas covered by a polymer-like layer are observed.

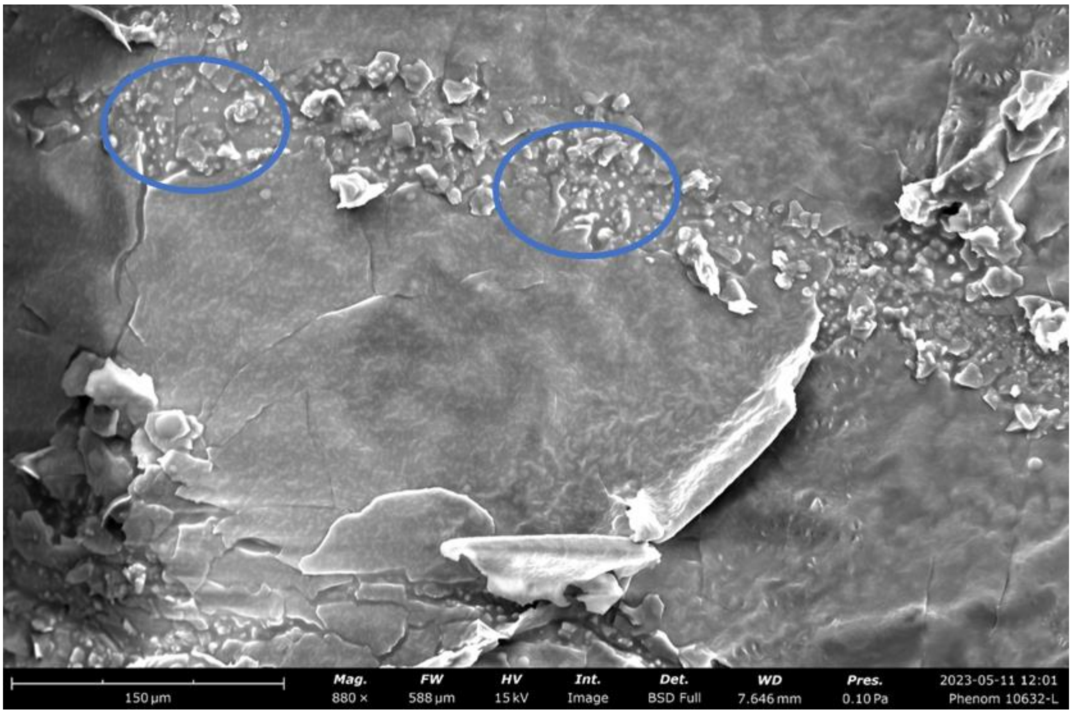

*Figure 7.19 SEM micrography of P-PVC sample*

It is worth noting that on the surface of the P-PVC samples the presence of small crystals (indicated by the blue circles) can be observed, this can be attributed to the presence of salt in the solution in which the functionalization step is carried out.

### 7.3.4 contact angle measurements results

The as received and functionalized PVC samples were studied by means of contact angle measurements for understanding how each functionalization step affects the hydrophobicity of the sample surface. The results collected with the contact angle measurements are reported in figure 7.11.

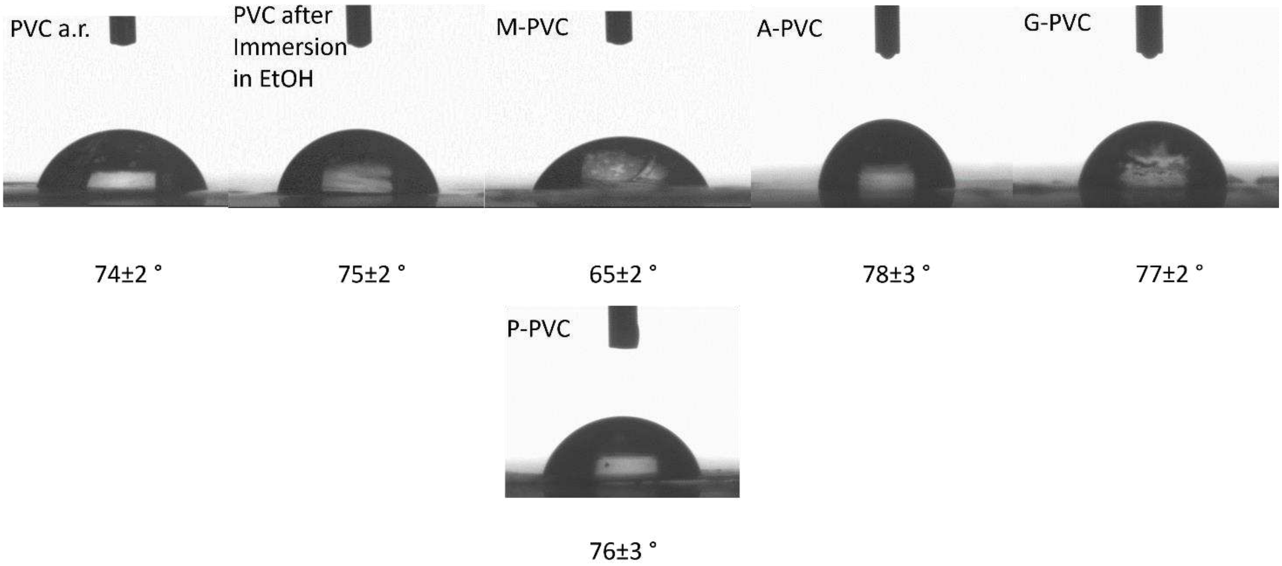

*Figure 7.20 Contact angle measurements conducted on food-grade PVC as received, PVC after immersion in ethanol, M-PVC, A-PVC, G-PVC and P-PVC, with the respective contact angle values*

In Figure 7.11 it can be noticed that the food-grade PVC sample present a high contact angle value (74 ± 2 °) indicating a hydrophilic surface, as also indicated by literature where an hydrophobic surface is defined as a surface that can repel water and has a contact angle greater than 90 °[20]. However for PVC sheets samples higher contact angles were reported [16], this difference may be attributed to the presence of plasticizers/stabilizers that can affect the contact angle values [21]. A 65 ± 2 ° were measured on M-PVC samples indicating that M-PVC surface is more hydrophilic if compared to the food-grade PVC, this can be related to the presence of Si-O groups on the surface. Following the grafting of APTES molecules on the polymer surface, the contact angle increases again with respect of the M-PVC due the presence of amino groups on the surface. Contact angle measured on G-PVC and P-PVC indicate an increased hydrophobicity of these samples.

## 7.4 Discussion

### *7.4.1 ATR-FTIR as a rapid technique for confirming the functionalization of PVC*

The sampling depth in ATR-FTIR is dependent on the radiation frequency and is typically higher than XPS. However, it represents a useful tool to verify the presence of the functional groups identified by XPS analyses and discussed in Chapter 6 for the functionalized PVC.

The ATR spectra presented in figure 7.1 showed that the PVC characteristic vibrational band (Table 7.1) such as the CH-Cl stretching at 691 cm$^{-1}$ and the carbonyl group due to the plasticizer/stabilizers at 1725 cm$^{-1}$ are detected also in M-PVC, A-PVC, and G-PVC. These results confirmed those obtained by XPS: at the surface of the as received PVC the presence of carboxylate and of zinc ascribed to the plasticizer/stabilizer was detected together with the signals that was assigned to PVC.

In M-PVC samples the ATR-FTIR results showed the presence of the bands ascribed to Si-O-Si at 1082 cm$^{-1}$ and 812 cm$^{-1}$ confirming the successful grafting on MPTMS on the PVC surface. Free thiol groups can be excluded since the SH stretching band is expected to be at 2560 cm$^{-1}$ [22]. Also this result is in agreement with XPS data: S 2p in M-PVC revealed the presence of a component at 163.7 eV that was assigned to thioethers and a component due to oxidized sulfur at about 167 eV, while no peaks that could be ascribed to thiol, at about 162 eV were found (§ 6.3.2). In A-PVC the presence of the characteristic band of the amino groups were detected at 3410, 3620 and 1654 cm$^{-1}$ [10,11], confirming the presence of the free amino groups of the APTES that were also revealed in N 1s XP-spectra (§ 6.3.2.2). These bands were attenuated but still detected in G-PVC thus indicating that free amino groups may be still present at on the sample surface. Similar results were obtained in XPS (§6.3.2.5), in fact the presence of the $NH_2$ and $NH_3^+$ components were detected on G-PVC samples indicating that not all the APTES moieties react with the glutaraldehyde carbonyl groups. Furthermore, the shift of the band at 1654 cm$^{-1}$ detected on A-PVC and at 1630 cm$^{-1}$ in G-PVC may suggest the formation of a C=N bond [12] thus confirming the assignment of the component at 286.6 eV in C 1s spectrum and the component at 400.5 eV in N1s spectrum to C=N of the G-PVC sample ((§ 6.3.2.7).

P-PVC spectra (Figure 7.1) showed the presence of the vibrational bands attributable to the PHMG (Table 7.2) and the absorption bands of the bulk PVC are not revealed, while the bands assigned to the O-Si-O are strongly attenuated and barely visible. The CH-Cl vibration band of the PVC should be also detected in P-PVC samples considering the sampling depth of FTIR-ATR and the thickness of the functionalizing layer, but the effect of the presence of $Cl^-$ from the last functionalizing step leads to the formation of the broad band at low wavenumber between 800 and 500 $cm^{-1}$ masking the presence of the CH-Cl and other signal in the same region.

The ATR-FTIR spectra allowed confirming the functionalization of G-PVC with TPPA as proposed in Chapter 3. By acquiring the TPPA spectrum it was possible to ascertain the presence of the vibrational bands of the functional groups of the tested porphyrin. The results suggested that the functionalization with TPPA occurred only after 12 hours of immersion since the band of pyrrolic NH stretching (3316 $cm^{-1}$), C=N stretching (1620 $cm^{-1}$), bending of the C-C-C bonds of the porphyrin ring (798 $cm^{-1}$) and NH out of plane bending vibration (699 $cm^{-1}$) were detected only after this immersion time. In fact, the ATR spectra of the polymers immersed for 1 and 3 hours does shows minor differences such as the attenuation of the Si-O-Si stretching band with respect to the G-PVC samples spectra, but no bands ascribed to the TPPA were detected. However it is possible that also after these immersion time grafting of TPPA occurs but since the functional groups such as Si-O-Si groups and CH-Cl have a stronger dipole moment and the vibrational band of the TPPA may be masked by more intense bands due to this groups[23,24].

### *7.4.2 Topographical properties of PVC and functionalized PVC*

SEM and AFM allowed studying the topographical properties of the functionalized PVC. As shown in figure 7.4, the formation of clusters of the functionalization layer that was hypothesized by the results obtained by AFM was confirmed by the SEM micrography showed in Figure 7.7, 7.8 and 7.9. The clusters are clearly visible in the A-PVC samples and are uniformly distributed onto the sample surface. The Presence of these aggregates can be related to the spikes observed in figure 7.4b for A-PVC analysed with AFM, moreover they can affect the sample roughness.

These clusters have spherical shape and can be attributed to the polymerization of Si-O groups of APTES. This hypothesis is confirmed by Figure 7.14 in which the micrography of A-PVC prepared with longer immersion time (6 h) is reported. It is worth noting that increasing the immersion time a multilayer of APTES is formed.

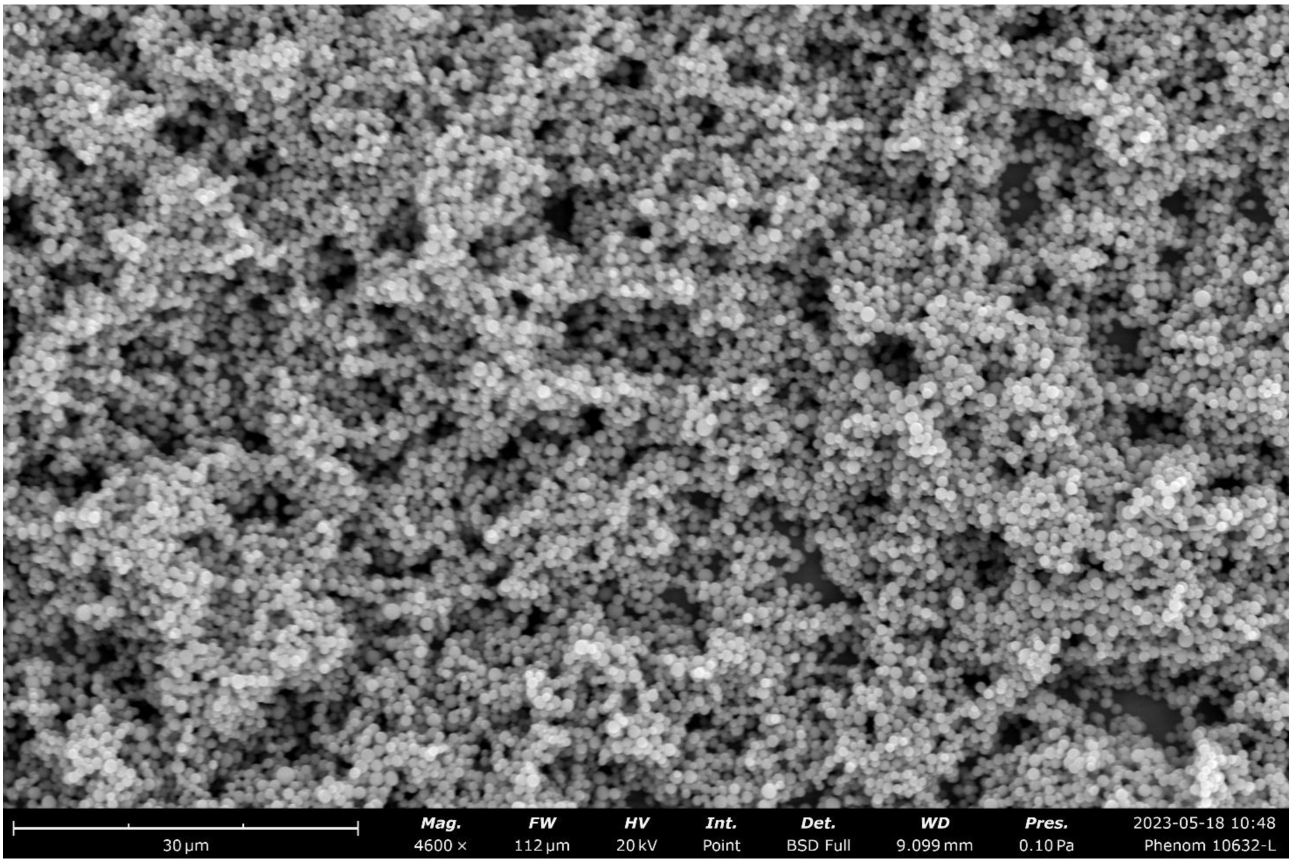

*Figure 7.21 SEM micrography of A-PVC prepared by 6 h immersion time*

XPS measurements may not be strongly affected by the formation of the aggregates since the analysed area in XPS is about 0.5 $mm^2$ in the experimental conditions used, thus suggesting that the analysed area can be considered uniformly covered by the "*islands*" of the functionalization layer. The typical "*islands*" formation can also justify the high contact angles values reported in section 7.3.4 [25].

Contact angle measurements showed no significant differences between as received PVC and P-PVC. Since the contact angle is below 90 °, P-PVC surface can be considered as hydrophilic [20]. Since microbiological tests showed that P-PVC effectively inhibit the growth of *S. aureus* compared to the as received PVC (Chapter 8), it seems that this effect is not related to changes in the hydrophobicity but on the bactericidal activity of PHMG against S. Aureus [28].

### *7.4.3 Guanidine density groups on P-PVC surface*

Preliminary results on guanidine density calculation, obtained by UV-Visible measurements following the procedure reported in [29], provided a value of 5.7 ± 0.2 $\mu mol/cm^2$; this value is higher than the one reported by Villanueva et alii [5] for PHMG grafted on medical grade PVC; in that paper a density value equal to 2.67 $\mu mol/cm^2$ was obtained.

The high guanidine density may be related to the polymerization of the PHMG on the surface of the polymer as clearly observed in Figure 7.10, where the probable formation of a multilayer of PHMG can be observed. This possibility was also discussed in Chapter 5 (5.3.5.1) for P-gold samples, and in Chapter 6 (6.3.2.4) for P-PVC samples analysed by means of XPS. The difference between the guanidine density values obtained in this work and those reported in the literature can be attributed to the different solvents exploited in this work, since ethanol was used instead of acetone that can damage the polymer surface [30].

The results obtained by applying this method should be considered a preliminary result. The development of an analytical method for the quantification of the guanidine groups it is necessary.

## 7.5 Conclusion

Based on the results discussed in this chapter the following conclusions can be drawn:

- ATR-FTIR represents a useful tool for optimizing the surface functionalization protocol, by taking advantage of the lower analysis time with respect to the X-ray photoelectron spectroscopy. This technique confirmed the successful functionalization of food-grade PVC by attributing the characteristic vibrational band of the exploited molecules such as MPTMS, APTES, glutaraldehyde and PHMG, and was also useful for verifying the interpretation of the results obtained by XPS spectroscopy.
- AFM and SEM were used to study the topography of the sample surface, and to understand the effects of each functionalization steps. AFM and SEM images suggest the formation of aggregates of the molecules exploited for the functionalization process of the food-grade PVC and showed that the surface roughness was slightly affected by the functionalization process, since the $R_q$ values increased from 10 ± 1 nm (PVC) to 15 ± 3 nm (PHMG).
- The preliminary estimation of the guanidine density on P-PVC samples suggested that the during the last functionalization step a multilayer of PHMG is formed, confirming the hypothesis proposed in the previous chapters.

[1] "F. Zara, Impiego della poliesametilenguanidina come agente antimicrobico per pellicole per alimenti, Bachelor thesis, Università degli Studi di Cagliari, 2023.

[2] P.L.J. Gunter, O.L.J. Gijzeman, J.W. Niemantsverdriet, Surface roughness effects in quantitative XPS: magic angle for determining overlayer thickness, Applied Surface Science 115 (1997) 342–346. https://doi.org/10.1016/S0169-4332(97)00007-X.

[3] N.J. Harrick, K.H. Beckmann, Internal Reflection Spectroscopy, in: P.F. Kane, G.B. Larrabee (Eds.), Characterization of Solid Surfaces, Springer US, Boston, MA, 1974: pp. 215–245. https://doi.org/10.1007/978-1-4613-4490-2_11.

[4] F. Mangolini, A. Rossi, 5 Advances in attenuated total reflection (ATR) infrared spectroscopy: a powerful tool for investigating polymer surfaces and interfaces, in: 5 Advances in Attenuated Total Reflection (ATR) Infrared Spectroscopy: A Powerful Tool for Investigating Polymer Surfaces and Interfaces, De Gruyter, 2022: pp. 173–216. https://doi.org/10.1515/9783110701098-005.

[5] M.E. Villanueva, J.A. González, E. Rodríguez-Castellón, S. Teves, G.J. Copello, Antimicrobial surface functionalization of PVC by a guanidine based antimicrobial polymer, Materials Science and Engineering: C 67 (2016) 214–220. https://doi.org/10.1016/j.msec.2016.05.052.

[6] N.S. Alghunaim, Spectroscopic analysis of PMMA/PVC blends containing CoCl2, Results in Physics 5 (2015) 331–336. https://doi.org/10.1016/j.rinp.2015.11.003.

[7] J. Wu, L. Ling, J. Xie, G. Ma, B. Wang, Surface modification of nanosilica with 3-mercaptopropyl trimethoxysilane: Experimental and theoretical study on the surface interaction, Chemical Physics Letters 591 (2014) 227–232. https://doi.org/10.1016/j.cplett.2013.11.043.

[8] N. Nematidil, M. Sadeghi, S. Nezami, H. Sadeghi, Synthesis and characterization of Schiff-base based chitosan-g-glutaraldehyde/NaMMTNPs-APTES for removal Pb2+ and Hg2+ ions, Carbohydrate Polymers 222 (2019) 114971. https://doi.org/10.1016/j.carbpol.2019.114971.

[9] M. Hezarjaribi, G. Bakeri, M. Sillanpää, M.J. Chaichi, S. Akbari, A. Rahimpour, New strategy to enhance heavy metal ions removal from synthetic wastewater by mercapto-functionalized hydrous manganese oxide via adsorption and membrane separation, Environ Sci Pollut Res 28 (2021) 51808–51825. https://doi.org/10.1007/s11356-021-14326-2.

[10] A. Boldeiu, K. Mihaela, A. Radoi, M. Danila, M. Simion, F. Craciunoiu, R. Pascu, I. Mihalache, T. Ignat, Microstructures and growth characteristics of polyelectrolytes on silicon using layer-by-layer assembly, Central European Journal of Chemistry 11 (2012) 205–214. https://doi.org/10.2478/s11532-012-0152-9.

[11] E. Lecoq, D. Duday, S. Bulou, G. Frache, F. Hilt, R. Maurau, P. Choquet, Plasma Polymerization of APTES to Elaborate Nitrogen Containing Organosilicon Thin Films: Influence of Process Parameters and Discussion About the Growing Mechanisms, Plasma Processes and Polymers 10 (2013) 250–261. https://doi.org/10.1002/ppap.201200108.

[12] T. Sreethawong, K.W. Shah, S.-Y. Zhang, E. Ye, S.H. Lim, U. Maheswaran, W.Y. Mao, M.-Y. Han, Optimized production of copper nanostructures with high yields for efficient use as thermal conductivity-enhancing PCM dopant, J. Mater. Chem. A 2 (2014) 3417–3423. https://doi.org/10.1039/C3TA14550F.

[13] T.M. Kamenieva, O.P. Tarasyuk, K.Y. Derevianko, O.A. Aksenovska, O.V. Shybyryn, L.O. Metelytsia, S.P. Rogalsky, Antioxidant activity of polymeric biocide polyhexamethylene guanidine hydrochloride, Catalysis and Petrochemistry (2020) 73–82. https://doi.org/10.15407/kataliz2020.30.073.

[14] J.A. Obaleye, A.C. Tella, G.K. Obiyenwa, N. Simon, M.D. Olawale, Zinc(II) Complex of Meso-Tetraphenylporphyrin With 4-Methoxyaniline: Crystal Structure and Antimicrobial Activities of 4-Methoxyaniline-5, 10, 15, 20-Tetraphenyl-Porphyrinatozinc (II), Synthesis and Reactivity in

Inorganic, Metal-Organic, and Nano-Metal Chemistry 46 (2016) 589–595. https://doi.org/10.1080/15533174.2014.988813.

[15] F. Marinello, A. La Storia, G. Mauriello, D. Passeri, Atomic Force microscopy techniques to investigate activated food packaging materials, Trends in Food Science & Technology 87 (2019) 84–93. https://doi.org/10.1016/j.tifs.2018.05.028.

[16] W. DeFlorio, A. Zaza, Y. Arcot, Y. Min, A. Castillo, M. Taylor, L. Cisneros-Zevallos, M.E.S. Akbulut, Bioinspired Superhydrophobic Nanocoating Based on Polydopamine and Nanodiamonds to Mitigate Bacterial Attachment to Polyvinyl Chloride Surfaces in Food Industry Environments, Ind. Eng. Chem. Res. (2024). https://doi.org/10.1021/acs.iecr.3c04230.

[17] A. Suganya, G. Shanmugavelayutham, C.S. Rodríguez, Study on structural, morphological and thermal properties of surface modified polyvinylchloride (PVC) film under air, argon and oxygen discharge plasma, Mater. Res. Express 3 (2016) 095302. https://doi.org/10.1088/2053-1591/3/9/095302.

[18] N. Demirci, M. Demirel, N. Dilsiz, Surface Modification of PVC Film with Allylamine Plasma Polymers, Advances in Polymer Technology 33 (2014). https://doi.org/10.1002/adv.21435.

[19] R. Helmy, A.Y. Fadeev, Self-Assembled Monolayers Supported on TiO2: Comparison of C18H37SiX3 (X = H, Cl, OCH3), C18H37Si(CH3)2Cl, and C18H37PO(OH)2, Langmuir 18 (2002) 8924–8928. https://doi.org/10.1021/la0262506.

[20] B.W. Chieng, N.A. Ibrahim, N. Ahmad Daud, Z.A. Talib, Chapter 8 - Functionalization of Graphene Oxide via Gamma-Ray Irradiation for Hydrophobic Materials, in: S.A. Rashid, R.N.I. Raja Othman, M.Z. Hussein (Eds.), Synthesis, Technology and Applications of Carbon Nanomaterials, Elsevier, 2019: pp. 177–203. https://doi.org/10.1016/B978-0-12-815757-2.00008-5.

[21] J. Määttä, H.-K. Koponen, R. Kuisma, H.-R. Kymäläinen, E. Pesonen-Leinonen, A. Uusi-Rauva, K.-R. Hurme, A.-M. Sjöberg, M. Suvanto, T.A. Pakkanen, Effect of plasticizer and surface topography on the cleanability of plasticized PVC materials, Applied Surface Science 253 (2007) 5003–5010. https://doi.org/10.1016/j.apsusc.2006.11.017.

[22] O.A. Dudarko, S. Barany, Synthesis and characterization of sulfur-containing hybrid materials based on sodium silicate, RSC Adv. 8 (2018) 37441–37450. https://doi.org/10.1039/C8RA07119E.

[23] E.G. Cowley, Dipole Moments of Aliphatic and Aromatic Amines, Nature 168 (1951) 705–706. https://doi.org/10.1038/168705b0.

[24] Y. Kikuchi, A. Wada, T. Kurotori, M. Sakamoto, T. Nozawa, S. Samukawa, Non-porous ultra-low-k SiOCH (k = 2.3) for damage-free integration and Cu diffusion barrier, Journal of Physics D: Applied Physics 46 (2013) 395203. https://doi.org/10.1088/0022-3727/46/39/395203.

[25] T.T. Chau, W.J. Bruckard, P.T.L. Koh, A.V. Nguyen, A review of factors that affect contact angle and implications for flotation practice, Advances in Colloid and Interface Science 150 (2009) 106–115. https://doi.org/10.1016/j.cis.2009.07.003.

[26] J. Chandra, J.D. Patel, J. Li, G. Zhou, P.K. Mukherjee, T.S. McCormick, J.M. Anderson, M.A. Ghannoum, Modification of Surface Properties of Biomaterials Influences the Ability of Candida albicans To Form Biofilms, Appl Environ Microbiol 71 (2005) 8795–8801. https://doi.org/10.1128/AEM.71.12.8795-8801.2005.

[27] A. Yousefi Rad, H. Ayhan, Ü. Kisa, E. Pişkin, Adhesion of different bacterial strains to low-temperature plasma treated biomedical PVC catheter surfaces, Journal of Biomaterials Science, Polymer Edition 9 (1998) 915–929. https://doi.org/10.1163/156856298X00244.

[28] Z. Zhou, D. Wei, Y. Lu, Polyhexamethylene guanidine hydrochloride shows bactericidal advantages over chlorhexidine digluconate against ESKAPE bacteria, Biotechnology and Applied Biochemistry 62 (2015) 268–274. https://doi.org/10.1002/bab.1255.

[29] M.F. Chaplin, The use of ninhydrin as a reagent for the reversible modification of arginine residues in proteins., Biochem J 155 (1976) 457–459.

[30] W.A. Woishnis, S. Ebnesajjad, eds., 32 - Polyvinyl Chlorides (PVC), in: Chemical Resistance of Thermoplastics, William Andrew Publishing, Oxford, 2012: pp. 3177–3300. https://doi.org/10.1016/B978-1-4557-7896-6.00032-7."

# Chapter 8 Anti-microbial property tests of functionalized PVC

This chapter presents an overview of the antimicrobial tests performed on food-grade PVC samples functionalized with PHMG as an antimicrobial active agent. Moreover, the potential application as food packaging of the P-PVC will be discussed.

The antimicrobial tests, a pivotal part of the present research, were performed at the Laboratorio Chimico Nuorese, our project partner, under the supervision of Dr. Laura Brundu and Dr. Claudio Mura.

Dr. Giovanni Loi has played a decisive role in supervising the microbiological experiments.

## 8.1 General introduction

The antimicrobial activity is defined by ISO20743:2021 as the "*activity of an antibacterial finish used to prevent or mitigate the growth of bacteria, to reduce the number of bacteria or to kill bacteria*" where an antimicrobial finish is a *"treatment designed to prevent or mitigate the growth of bacteria, to reduce the number of bacteria or to kill bacteria"*.[1]

ISO20743:2021 reports also different methods for the investigation of the antimicrobial activity of antimicrobial textiles. In this paragraph the main methods for the measurement of the antimicrobial activity that can be applied to polymers will be presented.

Mainly the antimicrobial tests are divided into different categories [2]:

- Agar-based methods
- Broth-based methods
- In vitro microbiological tests

*Agar-based methods* are the most used in the literature for the evaluation of antimicrobial potential. Disk-diffusion, well diffusion and disk volatilization methods have been extensively explored in antimicrobial evaluation. The application of these methods depends on whether the antimicrobial activity is investigated on films or solutions. The disk-diffusion method, also known as Kirby-Bauer disk-diffusion method is used for evaluating a potential antimicrobial active agent: a disk saturated with the active agent under evaluation is placed in an agar medium inoculated with the tested bacterial strain following the specific procedure provided for the microbial strain (e.g. *S. aureus* 24 h incubation time) [3]. Following the incubation in the agar medium with the target bacteria a region around the disk in which the growth is inhibit will be observed in the case of antimicrobial activity. In the traditional Kirby-Bauer method for testing the antimicrobial activity of textiles, the inhibition of bacterial growth is typically associated to the release of the antimicrobial agent. A modified Kirby-Bauer method has been proposed in the literature for testing antimicrobial activity of polymers for food-packaging applications [4]. In the case of antimicrobial polymers prepared by surface immobilization of the active agent, instead of preparing disks saturated with the active agent, a 1 $cm^2$ square of the polymer under study is placed on the agar medium; the functionalized face will be placed in direct contact with the inoculated agar medium. Disk-diffusion methods give qualitative information about the antimicrobial activity. By quantifying the area of the inhibition zone it could be possible to obtain a semi quantitative information, although in the literature there are not clear criteria for the quantification of the antimicrobial activity [5].

*Broth-based methods* are typically exploited in the studies of antimicrobial performance of films, especially for films with different shapes/size in order to understand the interaction between the antimicrobial active agents and the bacteria cells. This method allows studying the interaction with the microbial cells, and the lethality of the antimicrobial agents over a defined time [6]. Moreover, it is used to investigate the antimicrobial activity of the films under dynamic contact conditions [7]. Broth-based method consists in the immersion of the studied film into a flask containing the culture medium and standardized bacteria (typically *S. aureus*) or fungi (*C. albicans* and *Aspergillus*). The flask is subsequently incubated under continuous shaking for a specific contact time (usually up to 48 h for microorganisms and yeast and between 4 and 7 days for mould. The colony count is performed at defined time intervals [8].

*In vitro microbiological tests* comprises two different methods for evaluating the antimicrobial properties of the films: direct inoculation method [9] and dry droplet method [2]. The direct inoculation consists in the inoculation of bacterial suspension onto the sample surface that is subsequently covered with a plastic film and placed in a Petri dish and incubated for 24 h. The sample is transferred to a stomacher bag containing an appropriate dilution solution. The solution is then sampled with a swab and transferred in an agar medium to perform the colony count.

The *dry droplet method* is similar to the inoculation method and consists of an inoculum drop (usually 15 μL) placed on the film under testing and incubated. The incubation conditions can be changed based on the storage conditions of the target food. Following the incubation time, the tested film is transferred to a peptone water buffer and shacked by a vortex mixer for few minutes before proceeding with the colony count [10].

In this chapter, the antimicrobial activity tests performed on P-PVC samples will be presented. The antimicrobial activity was tested by exploiting two methods: the disk-diffusion method and the dry droplet method for the evaluation of the antimicrobial activity towards *S. aureus* and *E. coli*. Moreover, the antimicrobial activity of the polymer was investigated also on food samples such as culurgiones and pane carasau.

## 8.1 Antimicrobial tests of P-PVC

### 8.1.1 Materials

Petri dishes with a 90 mm diameter were used for preparing the agar medium for the microbial colony count. *Staphylococcus aureus* (Sigma Aldrich) with a certified value of $8.9 \times 10^4$ colony forming unit (CFU) per disc and *Escherichia coli* (Sigma Aldrich) with a certified value of $9.9 \times 10^4$ colony forming unit (CFU) per disc were used as tested bacterial strain. The bacterial disks were solubilized in a peptone water saline solution (100 mL), subsequently 1 mL of this solution was diluted in 5 mL of peptone water saline and refrigerated for 24 hours. Baid-Parker Agar medium was exploited for the Petri dishes in which the *S. aureus* have been inoculated, while Rapid *E. coli* medium was used for *E. coli* cultures; the media and methods exploited are accredited according to the ISO20743:2021 by the Laboratorio Chimico Nuorese. The bacterial solutions were standardized following the ISO20743:2021. Carasau bread and culurgiones samples were supplied by craft pasta factories in the inland areas of Sardinia.

### 8.1.2 Experimental

### 8.1.2.1 Dry droplet method

To evaluate the antimicrobial activity of the P-PVC samples towards bacteria strains such as *S. aureus* and *E. coli*, the dry droplet method was exploited. 15 mL of the two types of bacteria solution were placed onto the surface of food-grade PVC and P-PVC samples and kept in contact with the polymers for 1 h, 6 h and 24 h. Following the contact time, the solution was transferred in a peptone water saline solution (10 mL) and shaked for 5 minutes. Finally, 1 mL of the S. aureus solution was inoculated in a Baid-Parker agar medium and incubated for 24 hours at 37 °C, thus allowing the bacterial growing in the agar medium. The same procedure was applied to *E. coli* bacterial strain using a PCA (plate count agar) medium. The PCA medium, that is supplied as a powder, is immersed in a boiling water-bath for liquefying. Once PCA medium is liquid, it is cooled down at room temperature. 1 mL of *E. coli* solution is placed in a Petri dish in which PCA is poured down. The two solutions are homogenized by stirring for few minutes and left at room temperature until the medium becomes solid.

Blank samples were made up by diluting 15 mL of the bacterial starting solution in 10 mL peptone water saline and then inoculated in a Baid-Parker Agar and PCA medium for *S. aureus* and *E. coli* respectively.

### 8.1.2.2 Disk-diffusion method

For evaluating the direct contact antimicrobial activity of P-PVC, the modified disk-diffusion method that is typically exploited for polymer [4,11] was used. According to this method, 1 $cm^2$ of PVC and P-PVC samples were put in contact with the agar medium inoculated with *S. aureus* and *E. coli*. The culture media were made up by placing 1 mL of the *S. aureus* (§ 8.1.1) in a Baid-Parker Agar medium while for *E. coli,* the medium used was PCA.

The 1 $cm^2$ samples of the as received and functionalized polymer are placed on top of the two Petri dishes and incubated at 37 °C for 24 hours allowing the bacterial growth.

### 8.1.2.3 Antimicrobial activity tests on food samples

Antimicrobial activity of P-PVC was also tested on typical Sardinian food samples, such as culurgiones and Carasau bread. Culurgiones samples were cut into two pieces (10 g) with a sterilized knife and then transferred to a Petri dish. The food samples were inoculated with a 1 mL solution of *S. aureus* and *E. coli*, and one sample was stored in the fridge completely covered by food-grade PVC film and one with P-PVC for 3h, 6h and 24 hours.

After storage, the culurgiones samples were transferred in a stomacher in which 10 mL of peptone water solution was added, and then the samples are homogenized in the stomacher. The obtained solution is then inoculated (1 mL) in a Baid-Parker Agar medium for the samples exposed to *S. Aureus*, and Rapid *E. coli* medium for the *E. Coli*. The incubation of Petri dishes was carried out for 24 hours at 37 °C.

The antimicrobial tests on culurgiones with both *S. aureus* and *E. coli* were carried out on three independent samples consisting of three different P-PVC samples wrapping three different culurgiones.

In the case of Carasau bread, the homogenization process in the stomacher was not possible. For this reason, the food samples were stored in food-grade PVC and P-PVC at room temperature to evaluate the effectiveness of the P-PVC in increasing the shelf-life of the Carasau bread.

### 8.1.2.4 ATR-FTIR spectroscopy

ATR-FTIR analyses were carried out on P-PVC samples before and after the disk diffusion method experiments and after the antimicrobial activity tests on food samples. A Cary 630 FTIR Spectrometer (Agilent, Santa Clara, USA) was used for acquiring ATR-FTIR spectra; the spectrophotometer operated under computer control (Micro Lab FTIR Software). The spectrometer uses a Golbar source (silicon carbide (SiC) rods) in the range of 7000 $cm^{-1}$ and 400 $cm^{-1}$. The measurements were conducted in air with a resolution of 4 $cm^{-1}$, and the acquisition range was between 4000 $cm^{-1}$ and 650 $cm^{-1}$. The background acquisition was performed before the measurement of each sample. The spectra were acquired in Total Attenuated Reflectance mode and plotted as transmittance % *vs* wavenumber ($cm^{-1}$). In the case of the tests after contact with the food samples, the polymer samples were analysed in the area in contact with the dough of the culurgiones.

### 8.1.2.5 Scanning Electron Microscopy

SEM was used to obtain morphological information of P-PVC after being exploited as envelope for storing culurgiones samples contaminated with bacteria solution. The Phenom™ XL G2 Desktop SEM (Thermo Fisher) scanning electron microscope operating at 20 kV was used and secondary electrons images were acquired. Since the analysed samples were non-conductive a thin layer of gold was applied onto the surface of the samples; to guarantee an optimal resolution of the non-conductive samples the pressure in the proximity of the sample surface was 0.1 Pa.

## 8.2 Results

### 8.2.1 Dry droplet method results

Figure 8.1 shows the colonies formed after the contact between the droplet of *S. aureus* solution in absence (Figure 8.1a) and at the presence of the food-grade PVC sample (Figures 1 b-d), exploiting the dry droplet method described in 8.1.2.1.

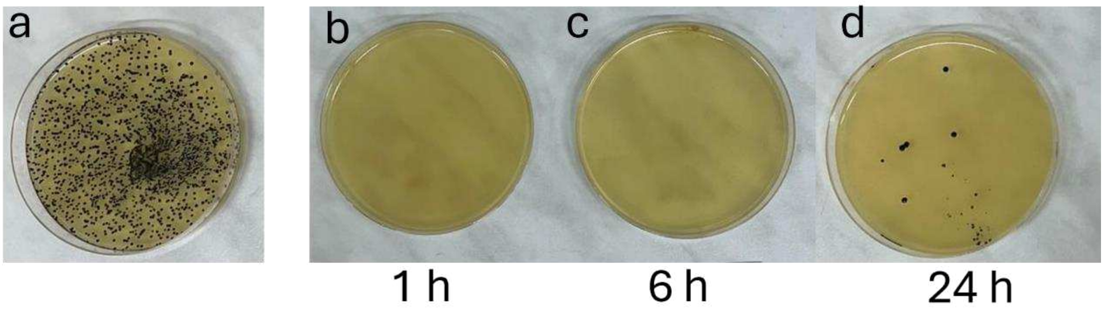

*Figure 8.1. S. aureus colonies formed with dry droplet method without the contact with food-grade PVC (a) and in contact with food-grade PVC for 1 h (b), 6 h (c) and 24 h (d).*

As Figure 8.1d shows, *S. aureus* colonies are observed on the agar medium only after 24 h. Moreover, the number of colonies formed after 24 h of contact time is lower compared with the number of CFU observed in the Petri dish without PVC (Figure 8.1a). For the *S. aureus* in contact with P-PVC, the Petri dishes prepared with the procedure described above are shown in Figure 8.2.

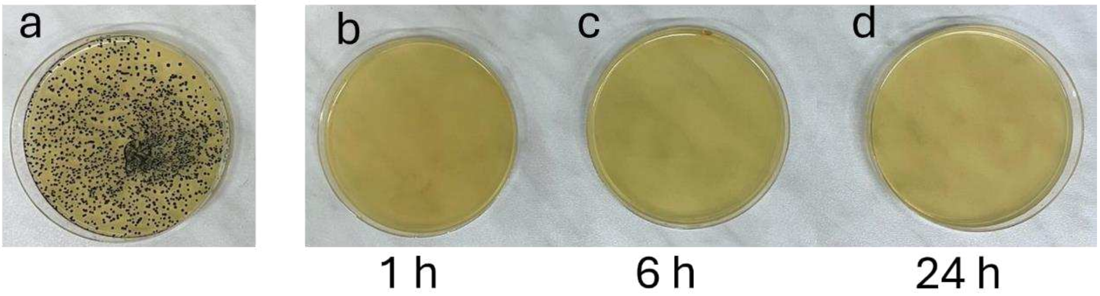

*Figure 8.2. S. aureus colonies formed with dry droplet method without P-PVC and in contact with P-PVC for 1 h (b), 6 h (c) and 24 h (d).*

No colonies were observed in Petri dishes inoculated with *S. aureus* solutions in contact with the P-PVC surface, (Figure 8.2 b-d) suggesting the functionalized polymer’s antimicrobial activity.

### 8.2.2 Disk-diffusion method

The direct contact antimicrobial effect of the P-PVC was evaluated using the disk-diffusion method. Figure 8.3 shows the results obtained in the case of as received food-grade PVC and P-PVC in contact with the Baid-Parker Agar medium inoculated with 1 mL of *S. aureus*.

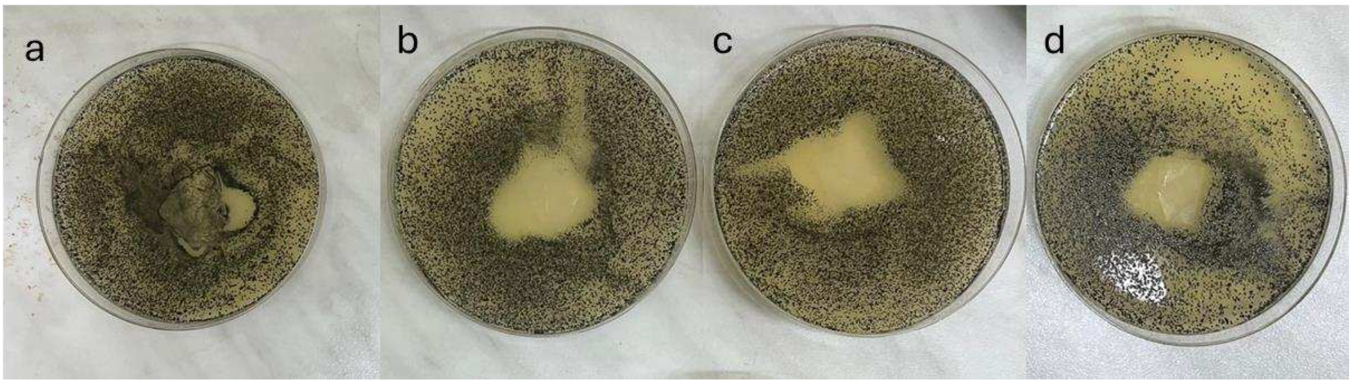

*Figure 8.3. Food-grade PVC in contact with the Baid-Parker Agar medium inoculated with S. aureus (a) P-PVC in contact with the Baid-Parker Agar medium inoculated with S. aureus (b,c and d)*

The results reported in Figure 8.3b show the presence of a clear area around the P-PVC samples, where the *S. aureus* colonies growth is inhibited, thus suggesting an antimicrobial activity due to the polyhexamethylene guanidine (PHMG). In the case of the as received PVC samples, the bacterial growth is not inhibited (Figure 8.3a). Moreover, the growth of the *S. aureus* is observed in the area below the PVC.

Figure 8.4 shows the disk diffusion method results obtained on food-grade PVC and P-PVC in contact with a PCA medium inoculated with *E. coli.*

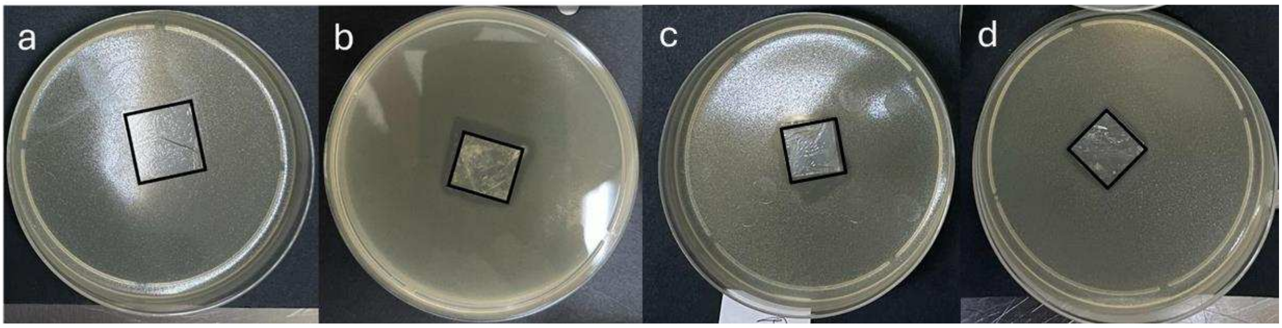

*Figure 8.4 Food-grade PVC in contact with the PCA medium inoculated with E. coli (a)and P-PVC in contact with the PCA inoculated with E. coli (b,c,d)*

Figure 8.4 (b,c,d) shows that P-PVC can also inhibit *E. Coli*. The presence of clear area around the polymer in which no colonies growth is observed substantiates this finding. In this case, the inhibition zone is smaller with respect to the results obtained for *S. Aureus.*

### 8.2.3 Antimicrobial activity tests on food samples

Following the promising results obtained on the *in vitro* methods presented in the precedent paragraphs, the antimicrobial activity of P-PVC samples was also tested on food to evaluate the antimicrobial activity under conditions similar to a real-use of the polymer. Firstly, the bacterial growth was investigated on culurgiones samples stored without any envelope after inoculation of 100 ml solution *S. aureus* (Figure 8.5).

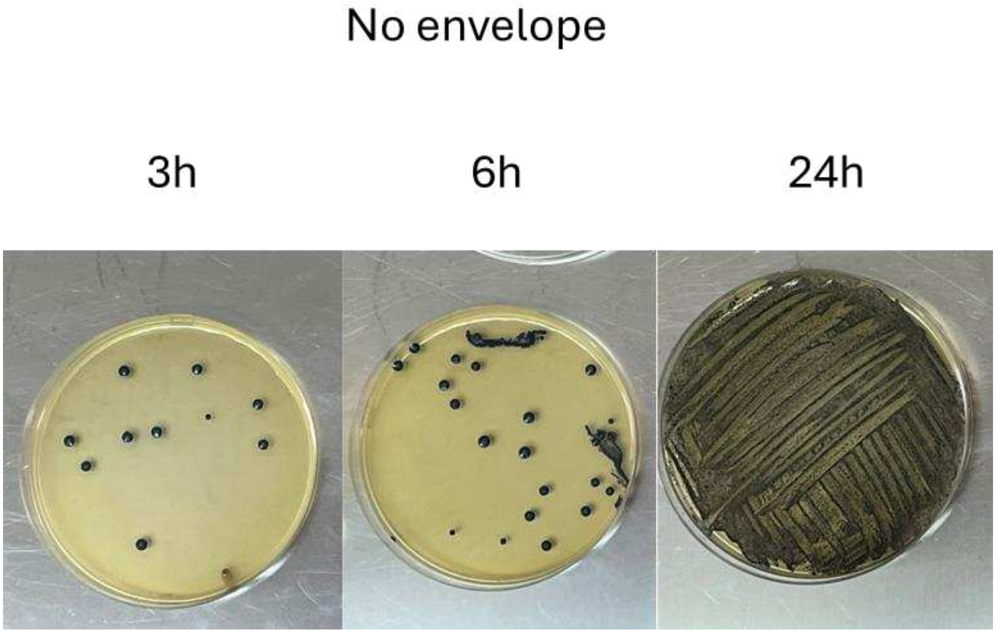

*Figure 8.5 S. aureus colonies formed after 3, 6 and 24 h contact with the culurgiones samples stored without any envelope*

If no envelope was used to wrap culurgiones, 10 CFU of *S. aureus* were formed after 3 h of storage of the culurgiones samples (Figure 8.5). Following the 6 h of storage time the number of colonies increased reaching a number higher than 50 CFU. Finally, after 24 hours of storage time, the petri dish was entirely covered by *S. aureus* colonies (Figure 8.5). Figure 8.6 shows *S. aureus* colonies formed after storing culurgiones samples in PVC.

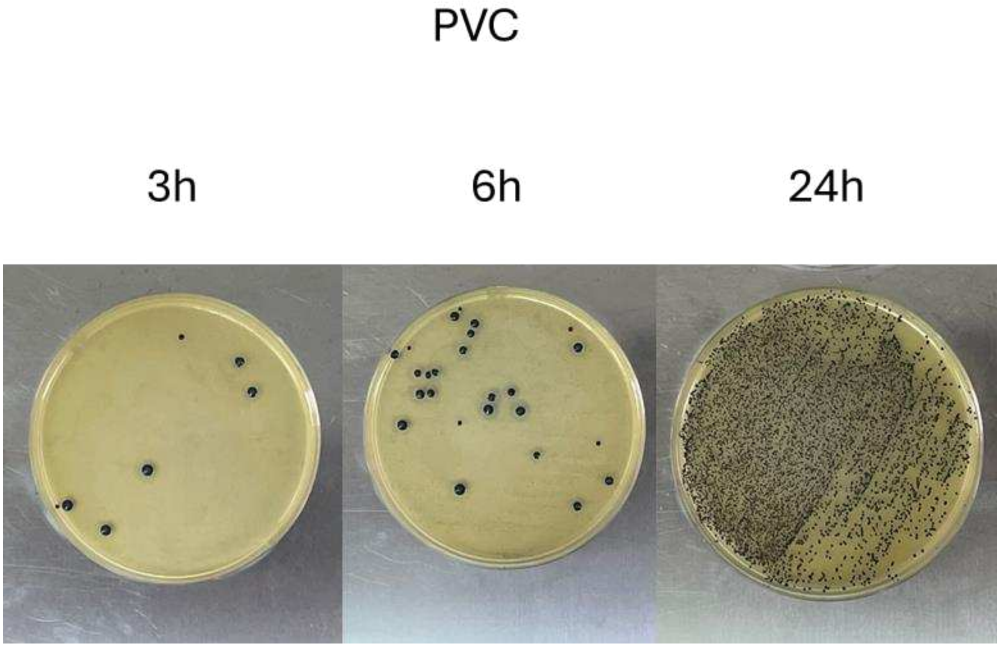

*Figure 8.6. S. aureus colonies formed after storing the culurgiones samples in food-grade PVC for 3, 6 and 24 h*

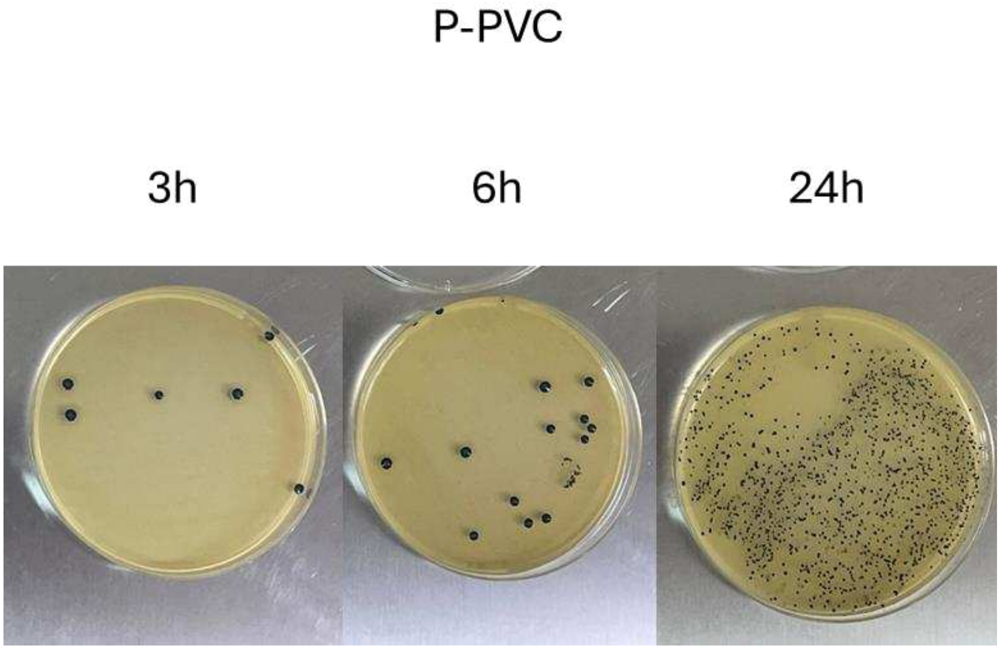

*Figure 8.7 S. aureus colonies formed after storing the culurgiones samples in P- PVC for 3, 6 and 24 h*

Culurgiones stored in P-PVC (Figure 8.7) show a reduced bacteria growth during the selected storage time. After 24 hours, the P-PVC samples show the formation of numerous colonies, but a higher number of colonies is observed in the case of PVC (Figure 8.6), suggesting that even though the formation of *S. aureus* is observed in the case of P-PVC, its antimicrobial activity partially inhibits the bacterial growth.

The same procedure was exploited to evaluate the antimicrobial activity in culurgiones samples inoculated with *E. coli*. In Figure 8.8 shows the E. coli colonies formed after 3, 6 and 24 h of storage time without any food packaging.

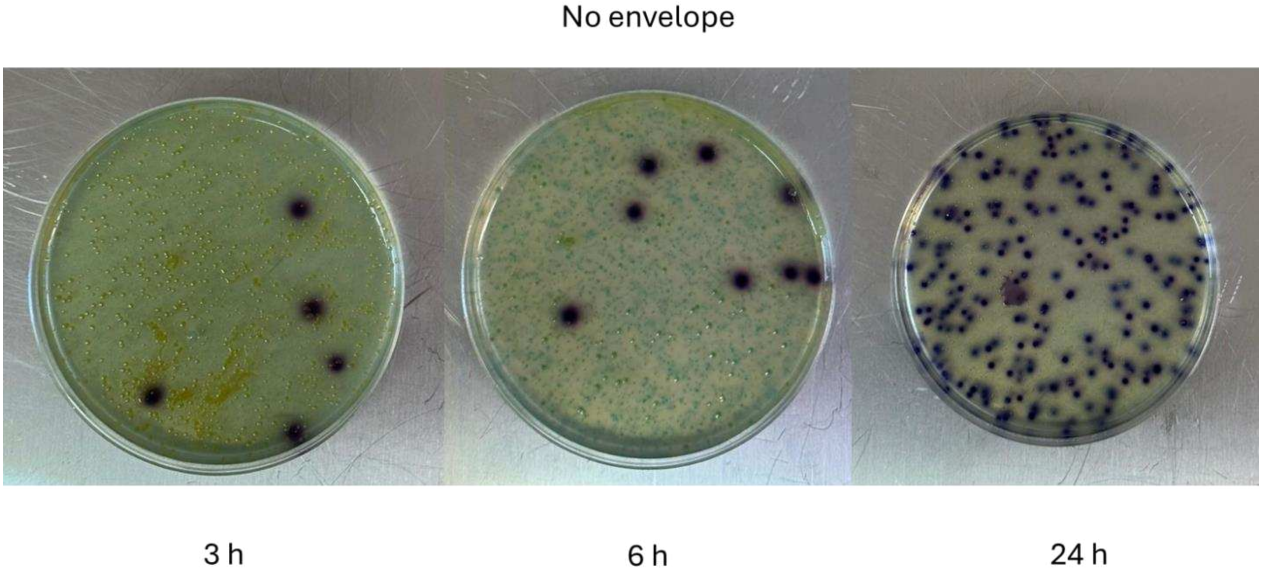

*Figure 8.8. E. coli colonies formed after 3 h contact with the culurgiones samples stored with no envelope for 3, 6 and 24 h*

Figure 8.9 shows the bacterial growth observed in samples stored for 3, 6, and 24 hours in PVC and P-PVC.

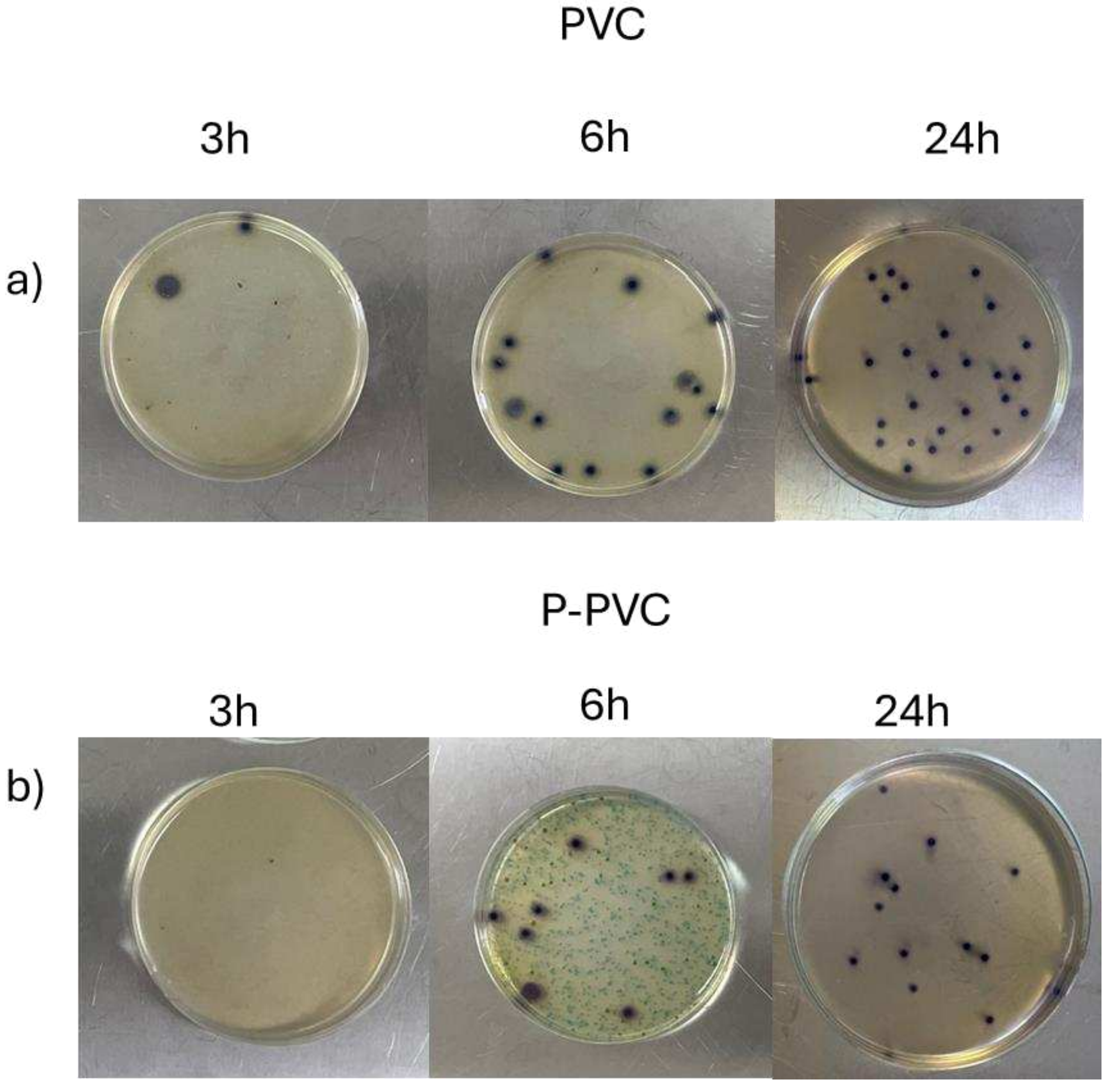

*Figure 8.9 E. coli colonies formed after storing the culurgiones samples in food-grade PVC (a) and P-PVC (b) for 3, 6 and 24 h*

The dark dots observed on the petri dish are attributed to the *E. coli* colonies. The green colonies observed in Figures 8.8 and 8.9 represent the coliforms bacteria present in the culurgiones samples. By comparing the results shown in Figures 8.8 and 8.9, it can be noted that a smaller number of colonies is formed in the P-PVC with respect of the sample stored in PVC. After the 24 h of storage time the inhibition effect of the P-PVC sample is evident, since in the case of PVC sample around 30 CFU were observed (Figure 8.9a) while only 9 CFU were observed in the case of P-PVC samples (Figure 8.9b), thus suggesting an antimicrobial activity. Also, it is worth to notice that the culurgiones stored in PVC presented less colonies with respect of the samples stored with no envelope, thus suggesting that also food-grade PVC can reduce the bacterial growth; this inhibition effect may be attributed to the presence of $Zn^{2+}$ in the polymer due to the plasticizer. [12]

The homogenization process using a stomacher was not suitable for the Carasau bread samples. Therefore, storage tests were conducted to check the shelf-life extension of Carasau bread kept in food-grade PVC and P-PVC at room temperature for 15 days. (Figure 8.10)

*Figure 8.10 Carasau bread stored in food-grade PVC (left) and P-PVC sample (right) after 15 days of storage time.*

After fifteen days of storage, mold formation was observed on the samples stored in PVC as received (Figure 8.10 left). However, the Carasau bread stored in P-PVC did not show any mold formation on its surface Figure 8.10 right).

### 8.2.4 ATR-FTIR spectroscopy results

ATR-FTIR spectra of P-PVC samples were collected before and after exposure to bacteria strains using the disk-diffusion method. Additionally, experiments were performed on the P-PVC before and after contact with the culurgiones samples, to determine whether exposure to bacteria altered the functionalization of the P-PVC layer. Figure 8.11 displays the spectra obtained using the experimental setup reported in section 8.1.2.4 following the disk-diffusion method experiments.

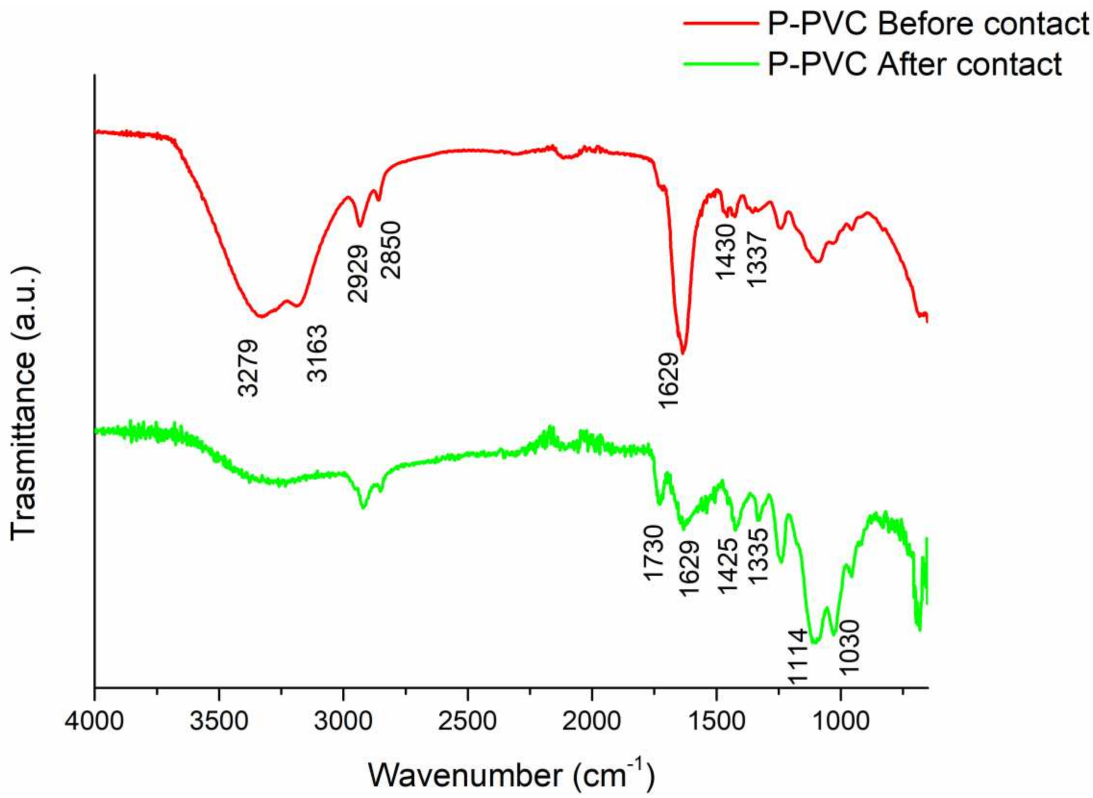

*Figure 8.11 ATR-FTIR spectra acquired before and after performing the disk-diffusion method experiment with S. aureus*

Table 8.1 reports the attribution of the characteristic vibrational band of the P-PVC.

*Table 8.1 Attribution of the vibrational band detected on P-PVC samples after disk-diffusion experiment*

| Wavenumber ($cm^{-1}$) | Attribution | Functional groups | |
|---|---|---|---|
| **3279** | Asymmetric N-H stretching ($n_{as}$) | $NH_2$ | [13,14] |
| **3163** | Symmetric N-H stretching ($n_s$) | $NH_2$ | [13,14] |
| **2929** | Asymmetric C-H stretching ($n_{as}$) | $CH_2$ | [13,14] |
| **2850** | Symmetric C-H stretching ($n_s$) | $CH_2$ | [13,14] |
| **1629** | Stretching C=N | $C=NH_2^+$ | [13,14] |
| **1430-1337** | Bending C-H | $CH_2$ | [13,14] |

After being exposed to the agar medium, the ATR-FTIR spectra showed a significant reduction in the intensity of the band at 1629 $cm^{-1}$, which corresponds to the iminium group of PHMG. This group is responsible for the antimicrobial activity of PHMG. The literature explains the mechanism of action of PHMG on bacterial membranes [15]. Jiang at al. [16] suggest that the positive charge in the PHMG due to the iminium group may absorb in the bacteria membrane that is typically negatively charged, favouring the formation of complexes with the phospholipids of the lipidic bilayer, thus destabilizing the osmotic equilibrium and leading to cell lysis. The decreased intensity of the C=N band might be due to the formation of complexes with the bacteria membrane. The antimicrobial mechanism described here represents a hypothesis since the bacterial membrane may be protected by the capsule (e.g. *E. coli*) affecting the antimicrobial effect of the PHMG. Other factors, such as hydrophobicity and roughness, may affect the bacterial adhesion, as discussed in Chapter 7.

Figure 8.12 shows the ATR-FTIR spectra acquired on P-PVC before and after the contact with culurgiones inoculated with *S. aureus* and following the selected storage time for evaluating the antimicrobial activity. The P-PVC after its application as packaging for contaminated culurgiones, shows the comparison of new bands with respect of the P-PVC precontact. These bands may be related to both the presence of residual of the killed bacteria on the polymer surface and to residual of culurgiones.

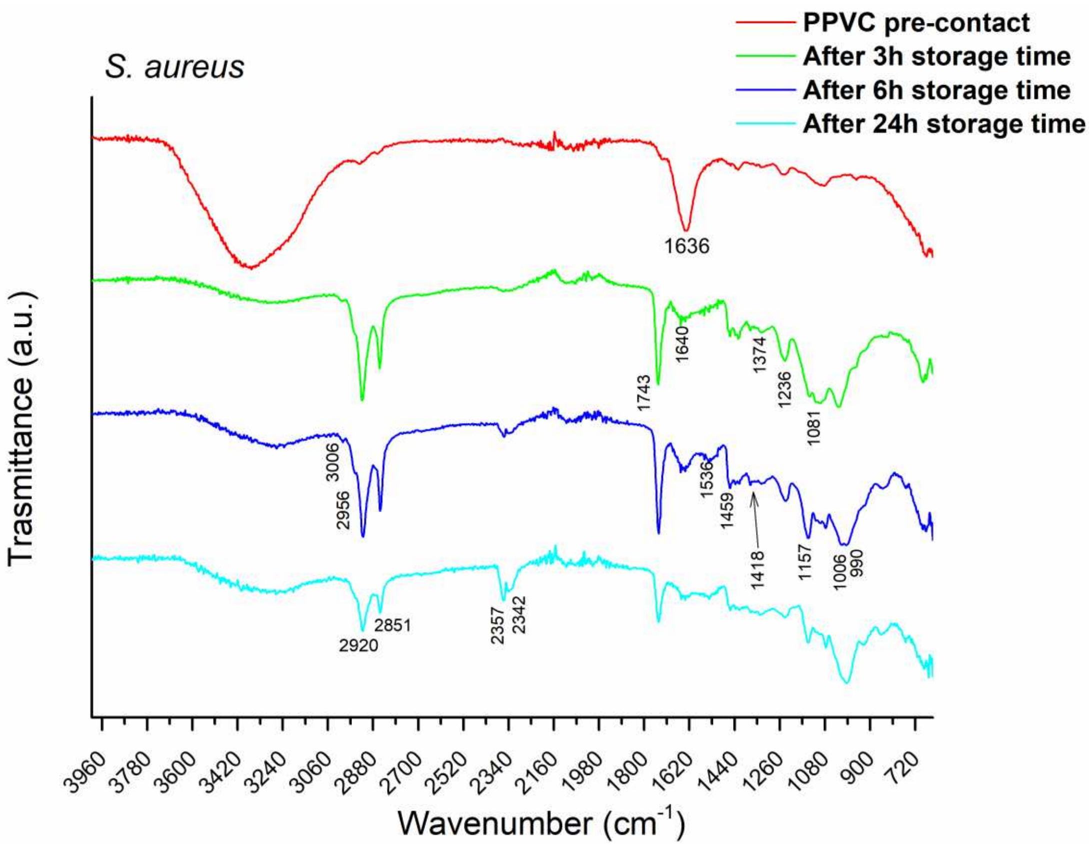

*Figure 8.12 ATR-FTIR spectra acquired before and after wrapping culurgiones inoculated with S. aureus at different storage time*

The spectra shown in figure 8.12 can be divided in four regions. These regions reveal the presence of numerous organic compounds that can be found in both the culurgiones and the bacteria. These compounds include fatty acids (3100-2800 cm$^{-1}$), proteins and peptides (1800-1500 cm$^{-1}$), carbohydrates (1200-900 cm$^{-1}$) and the fingerprint region (900-600 cm$^{-1}$).

The wavenumbers and their attribution are reported in Table 8.2.

*Table 8.2 Attribution of the vibrational band detected on P-PVC samples after its application as food-packaging for culurgiones*

| Wavenumber ($cm^{-1}$) | Attribution | Functional groups | Ref. |
|---|---|---|---|
| **3200-3100** | N-H stretching | NH amides | [17,18] |
| **3100-2800** | Aliphatic C-H stretching vibration | $CH_3$, $CH_2$ , CH stretching of fatty acid chains | [17,19] |
| **3006** | CH=CH stretching | CH=CH ascribed to fatty acids | [17] |
| **2956** | -CH asymmetric stretching | $-CH_3$ in fatty acids | [17,19] |
| **2920** | -CH asymmetric stretching | $-CH_2$ in fatty acids | [17,19] |
| **2851** | -CH symmetric stretching | $-CH_2$ in fatty acids | [17,19] |
| **1236** | $PO^{2-}$ asymmetric stretching | $PO^{2-}$ groups of phosphodiester in phospholipides | [17,19] |
| **1743** | C=O stretching | C=O carbonyl group | [20] |
| **1640** | C=N stretching | $C=NH_2^+$ or C=N due to PHMG or contribution from proteins | [15] |
| **1536** | N-H bending | NH amides | [17,21] |
| **1459** | C-H bending (scissoring) | $-CH_2$ and $-CH_3$ in fatty acids | [20] |
| **1418** | =C-H bending (rocking) | =C-H bonds of cis-disubstituted olefins | [20] |
| **1150** | C-O ring stretching | C-O-C stretching ascribed to carbohydrates | [22,23] |
| **1115** | C-O stretching | C-O stretching ascribed to carbohydrates<br>or $PO_3^{2-}$ of phosphoryl groups | [22,23] |
| **1081** | C-C ring stretching | C-C stretching ascribed to carbohydrates | [22,23] |
| **997** | C-OH bending | C-OH stretching ascribed to carbohydrates | [22,23] |

Figure 8.13 shows the ATR- FTIR of P-PVC before and after the contact with culurgiones inoculated with *E. coli* and following the selected storage time for evaluating the antimicrobial activity.

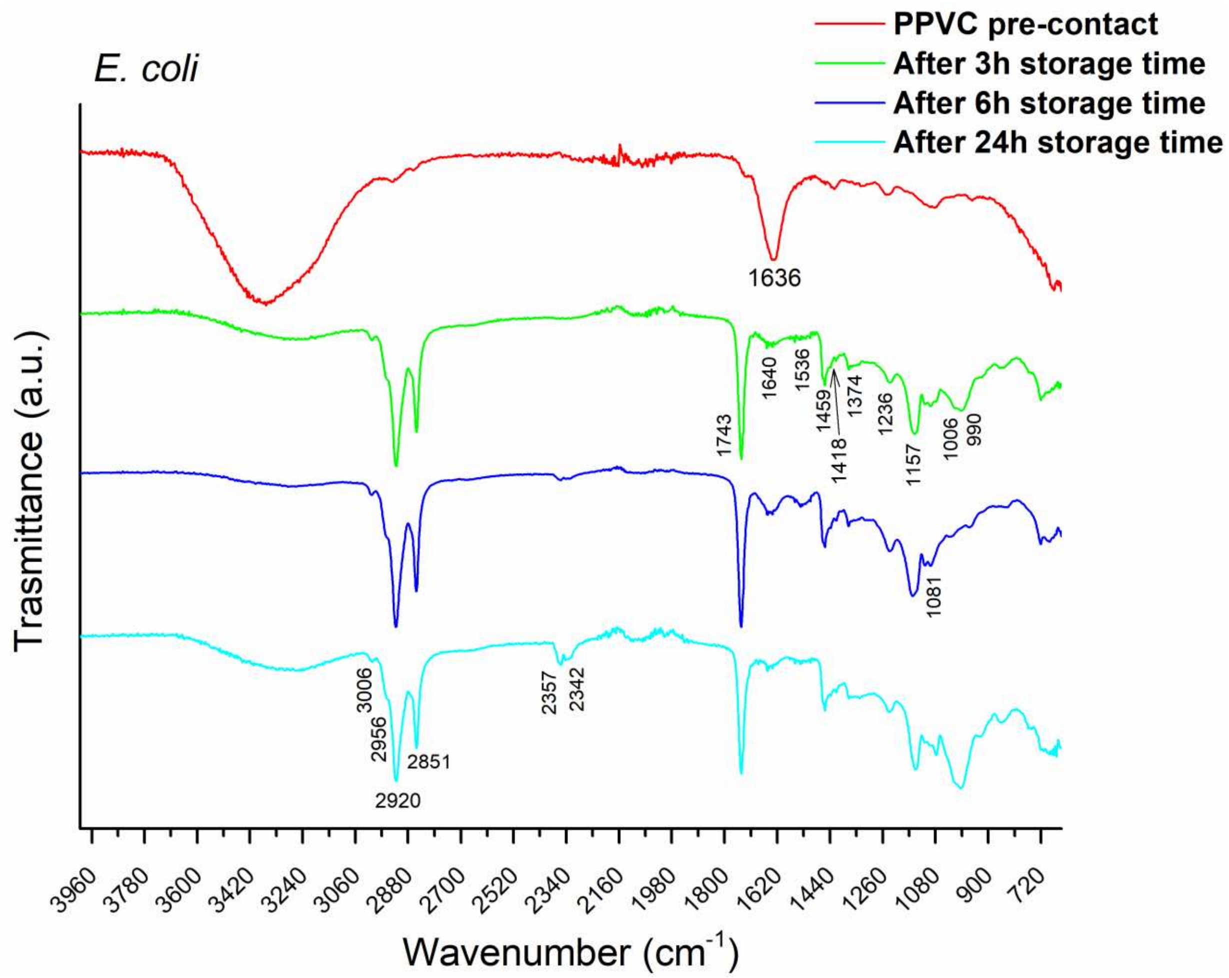

*Figure 8.13 ATR-FTIR spectra acquired before and after wrapping culurgiones inoculated with E. coli at different storage time*

ATR spectra were also acquired after exposing both food-grade PVC and P-PVC to as received culurgiones samples, with no inoculum, in order to compare the vibrational bands observed in Figure 8.12 and 8.13 for P-PVC. Figure 8.14 shows the ATR-FTIR spectra for food-grade PVC (Figure 8.14a) and for P-PVC (Figure 8.14b) after a storage time of 6 hours.

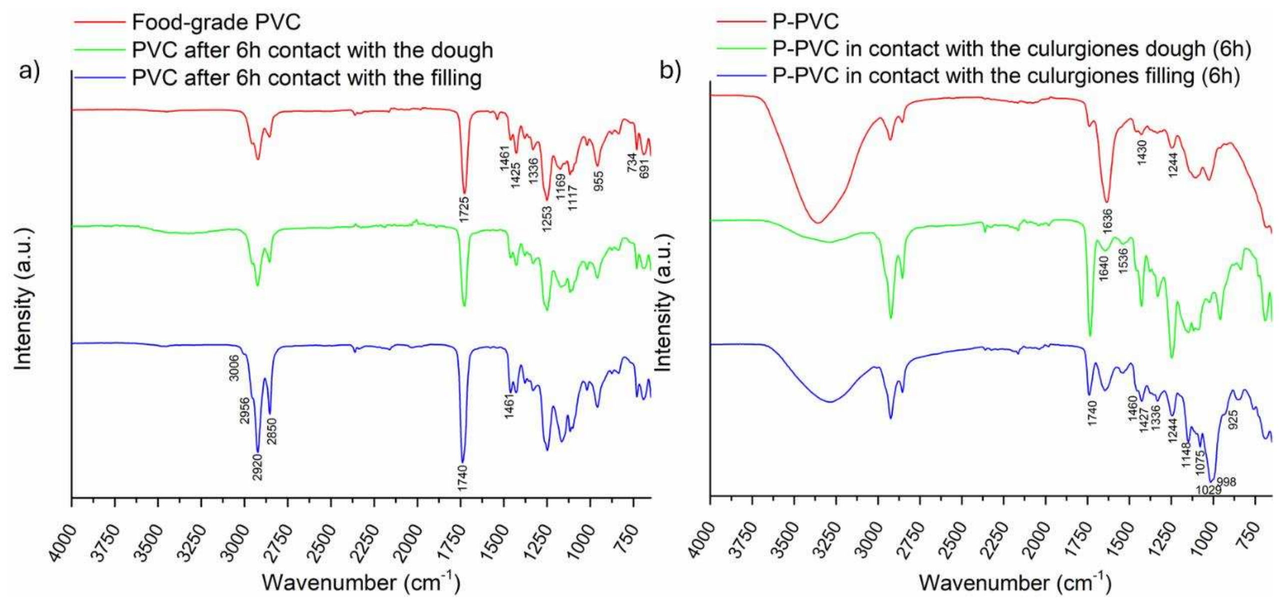

*Figure 8.14 ATR-FTIR spectra of food-grade PVC (a) and P-PVC (b) used for storing culurgiones samples*

For both samples, the spectra were acquired in the area in direct contact with the culurgiones dough and in the area in direct contact with the filling.

## 8.2.5 SEM results

SEM micrography were acquired as described in sections 7.3.3 and 8.1.2.5. Figure 8.15 shows one example of micrography acquired on P-PVC samples used to store a culurgione sample contaminated with 1 mL of *S. aureus* for 6 h.

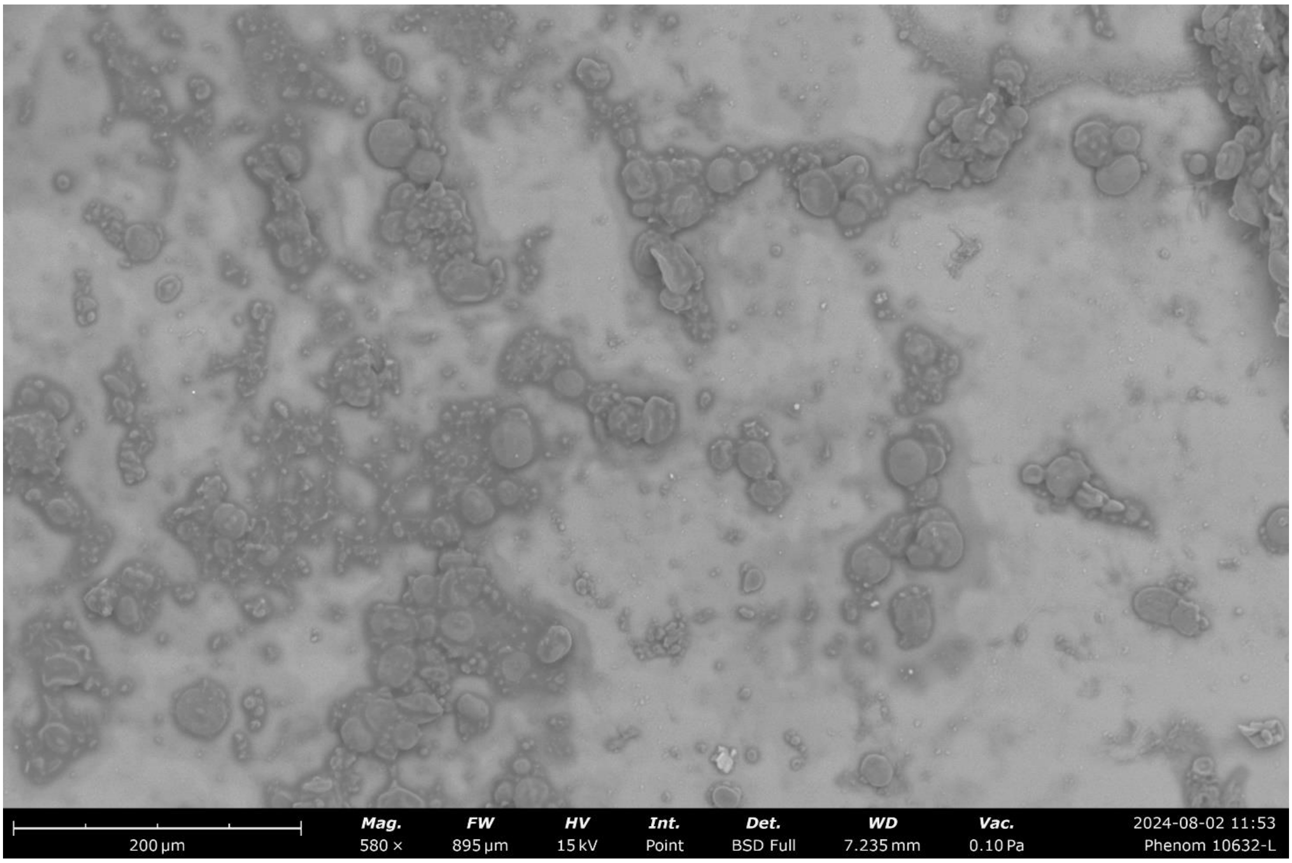

*Figure 8.15 SEM micrography of P-PVC used as envelope for storing culurgiones samples inoculated with S. aureus*

In figure 8.15 it is worth noting the presence of circular shaped objects onto the P-PVC samples that can be ascribed to the presence of residuals from the culurgiones or due the presence of *S. aureus* colonies. *S. aureus* are gram-positive bacteria with a diameter of 0.5-1 mm, while the colonies are formed by clusters of *cocci* and the diameter range from 1 to 5 mm [24].

The circular shape object has a diameter around the 26 mm thus excluding that are *S. aureus* colonies. It is possible that these objects represent residuals of the colonies that were damaged by the antimicrobial action of PHMG during the storage time. In fact similar results were reported in the literature for *S. aureus* after their exposure to gold nanoparticles[25]. The clear area can be ascribed to the P-PVC surface free of these residuals.

## 8.3 Discussion

### 8.3.1 Antimicrobial activity against *S. aureus* by dry droplet methods

The results from the dry droplet tests (§ 8.2.1) on as received PVC (Figure 8.1) showed that the bacterial growth of *S. aureus* was not observed during the first 6 hours of contact with the polymer surface. However, after 24 hours, *S. aureus* colonies were detected on the agar medium. This suggests that the as received

PVC samples may reduce the bacterial vitality during short time exposure. Plasticizers and additives, commonly used in food-grade packaging, can have weak antimicrobial activity. Food-grade polymers can also have intrinsic features, such as hydrophobicity, oxygen, and vapor barriers, that can affect bacterial vitality. The hydrophobicity of the surface also plays a role in inhibiting bacterial growth, with high hydrophobic surfaces preventing the formation of a biofilm on the surface and inhibiting bacterial growth. The food-grade PVC surface used in this work is hydrophobic (contact angle around 74 degrees) and this hydrophobicity may explain the inhibition of bacterial growth for a short contact time. Furthermore, XPS spectra of as received PVC showed the presence of Zn, and it is known from literature that Zn (II) might act as a biocidal against both *S. aureus* and *E. coli* [12].

Similar results were observed for the first three hours and after six hours of exposure in the case of P-PVC (Figure 8.2). However, after 24 hours of contact between the bacteria solution and the P-PVC surface, the growth of *S. aureus* was inhibited, suggesting a stronger antimicrobial activity due to the presence of polyhexamethylene guanidine on the surface. In tests carried out for prolonged exposure time (48 hours) the solution evaporated. Immersion of the polymer in peptone water saline solution indicates no bacterial growth.

### 8.3.2 Antimicrobial activity towards S. aureus and E. coli by disk diffusion method

Disk-diffusion method provides qualitative information about the antimicrobial activity of the samples tested. The results shown in Figure 8.3b demonstrate the antimicrobial activity of P-PVC against *S. aureus* by contact. The as received PVC samples show the formation of colonies also in the area in which the polymer was in direct contact with the agar-inoculated medium. This finding seems to exclude the intrinsic antimicrobial properties of the as received polymer tested and it might seem to contradict what was observed in the case of the dry droplet method. But the difference of the concentration of the bacteria has to be considered. In the disk diffusion method, the concentration of the inoculum was about 1000 times higher than the concentration in the dry droplet one.

The inhibition area around the sample is not symmetric. This can be attributed to possible movements of the polymer during the incubation process. It is possible to estimate the area of the inhibited zone by measuring its height and width. By adding up the area of the samples (1 $cm^2$) where no bacterial colonies were found, the total area of the inhibited zone is approximately 2.0 $cm^2$.

The antimicrobial activity against the *E. Coli* evaluated by disk diffusion method shown in Figure 8.4, demonstrates that the P-PVC exploits an antimicrobial activity also against *E. coli.* However, the inhibition zone observed in this case is smaller than the one with *S. aureus* samples, thus suggesting a weaker activity. It was estimated that the inhibition zone had a total area of approximately 1.5 $cm^2$.

The ATR-FTIR results showed a significant decreased intensity of the C=N stretching band (1630 cm$^{-1}$), suggesting that the inhibition of the bacterial growth might be due to a complex formation of PHMG's iminium group with phospholipids of the double layer membrane (Figure 8.11), while two more bands at 1114 cm$^{-1}$ and 1030 cm$^{-1}$ can be detected on the P-PVC after the disk diffusion method experiment. In order to clarify if these two bands are due to the release of PHMG the ATR-FTIR spectra of G-PVC and P-PVC after the disk diffusion method experiment are compared. In the case of G-PVC the presence of the bands ascribed to silanols are found at 1078 cm$^{-1}$ [26,27] (Figure 8.16). In the case of P-PVC after the disk diffusion test, the shape of the spectra and the bands found at 1114 and 1030 cm$^{-1}$ suggest that different species have formed on the surface of the polymer samples probably due to the interaction with both bacteria membranes and amino acid species contained in the agar medium; similar bands are reported for the asymmetric stretching of CO-O-C groups and for the symmetric stretching of phosphate groups attributed to the phospholipids of the bacteria membrane [28,29], or to the stretching and bending of the functional group of carbohydrates [29]. The vibrational bands ascribed to the bending of $CH_2$ groups of the PHMG are still present (1430-1337 cm$^{-1}$).

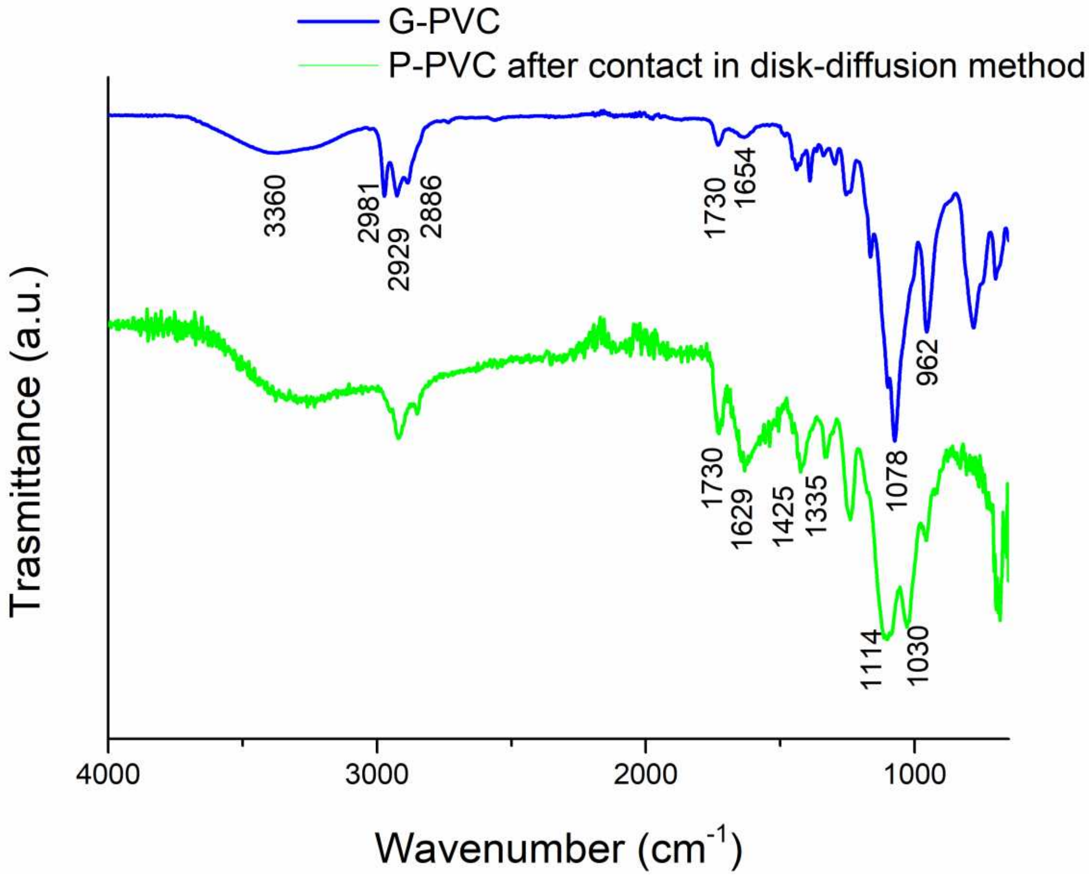

*Figure 8.16 ATR-FTIR spectra of G-PVC (blue curve) and P-PVC acquired before and after performing the disk-diffusion method experiment on S. aureus (green curve)*

The presence of the inhibition zone around the P-PVC samples in the disk diffusion method tests might suggest that the PHMG is released from the sample surface to the Agar medium, thus indicating that the antimicrobial molecule is not strongly attached to the surface. However, the absence of the bands ascribed to silanols and the presence of the $C=NH_2^+$ indicates that PHMG is not completely released. This hypothesis needs to be further studied in order to fully understand the antimicrobial mechanism.

### 8.3.3 Antimicrobial activity of P-PVC in preserving food samples

As discussed in paragraph 8.2.3, P-PVC was used as a food envelope for samples contaminated with *S. aureus* and *E. coli*. The results obtained showed excellent antimicrobial activity against *S. aureus*. Figure 8.6 indicates that after 1 and 6 hours of storage time in P-PVC, a reduced number of CFU (colony forming units) of the examined bacteria has grown in comparison to the samples stored for the same time in no-functionalised PVC. The samples stored in PVC had 30 colonies, while the culurgiones (fresh pasta) stored without any envelope had about 100 colonies (Figure 8.5). The reduced number of colonies grown on the fresh pasta observed in this sample may be due to the reduced microbial activity exerted also by no-functionalized PVC (§ 8.3.1). However, the samples wrapped in P-PVC for 3 hours showed the formation of a single colony of *S. aureus* (Figure 8.7).

After being stored for 24 hours, a significantly high number of colonies were formed in both PVC and P-PVC samples. However, when compared to PVC samples, the P-PVC samples showed a visible lower number of colonies. This suggests a weak antimicrobial activity in P-PVC samples after 24 hours.

By considering the number of colonies observed in Figures 5 and 6, and the dilution factor that takes into account all the dilution steps of the starting bacterial disk, it is possible to calculate the initial bacterial concentration expressed in CFU/mL and to plot it as a function of the storage time (Figure 8.17).

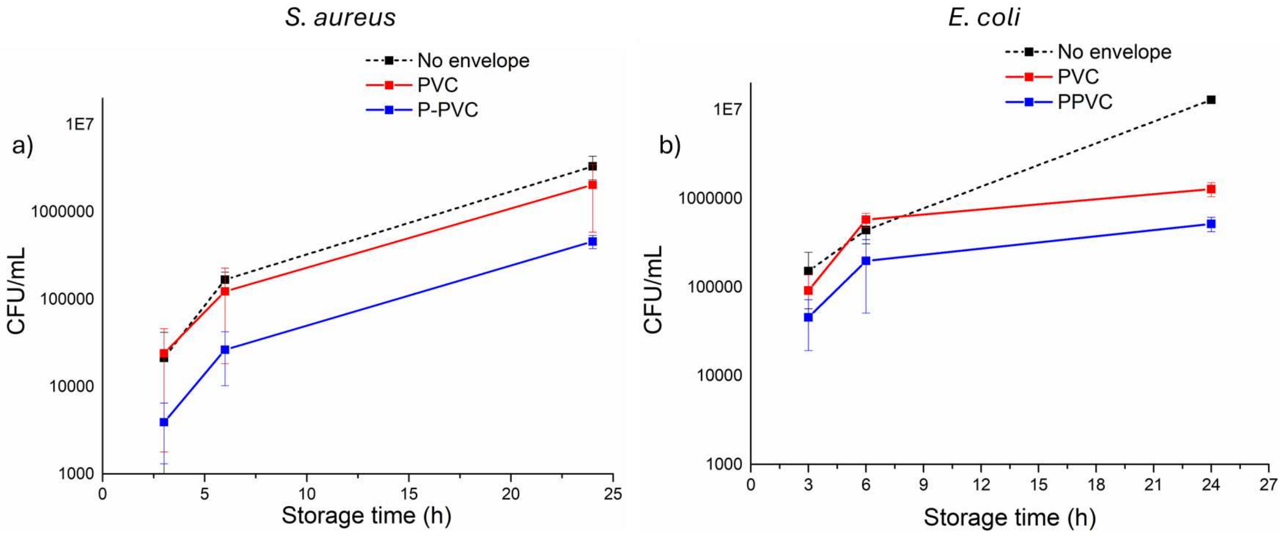

*Figure 8.17 Colony forming unit variation vs storage time of culurgiones samples without envelope (black curve), and wrapped in food-grade PVC (red curve) and in P-PVC (blue curve), inoculated with S. aureus (a) and E. coli (b). The standard deviation reported in the graph is calculated on three replicas of the experiments discussed in the results section*

Figure 8.17 a shows that despite the increasing concentration over time of *S. aureus,* there is a significant difference between the samples stored in P-PVC in terms of CFU/mL and in PVC; in the case of P-PVC the CFU/mL is about one order of magnitude lower with respect to PVC. In the case of *S. aureus*, no significant difference in terms CFU/mL is observed between the culurgiones stored in PVC and the sample stored with no envelope.

On the contrary, a very pronounced decrease of the number of colonies formed after 24 hours is observed in the case of culurgiones inoculated with *E. coli* stored with PVC (Figure 8.17b) compared to the unwrapped ones, due to the inhibition effect of $Zn^{2+}$ that is present the polymer due to the plasticizer [12]. Furthermore, the decrease of CFU/mL observed for P-PVC compared to PVC is less pronounced.

The ATR-FTIR spectra shown in Figures 8.11 and 8.12 indicate that the band related to the C=N stretching at 1630 $cm^{-1}$, which is responsible for the antimicrobial activity of P-PVC, can still be detected after 24 hours of contact with the contaminated food-samples, even though it is strongly attenuated. The ATR-FTIR spectra showed the presence of signals that can be ascribed to organic residual due to the presence of both dead colonies of the studied bacteria and to food sample residuals. Similar bands have been reported in the literature by numerous studies on bacteria which were exposed to antimicrobial agents [17–19,21–23,30]. The bands detected after exploiting P-PVC as envelope for storing culurgiones inoculated with *S. aureus* and *E.coli* can be ascribed to the presence of fatty acids, carbohydrates and peptides on the polymer surface. However, these compounds can be present in both the culurgiones and in the bacteria strains. In the region comprised between 1695 and 1550 $cm^{-1}$ the bands relative to the amide groups of the protein should be visible [17], but in both figure 8.12 and 8.13 these bands are not clearly detected, possibly due to overlap with stronger bands ascribed to carbohydrates. It is important to notice that the C=O stretching band at 1725 $cm^{-1}$ was detected also for PVC samples and was ascribed to the presence of carboxylic compounds used as plasticizer. After the contact with the filling of the culurgiones (Figure 8.14a) that band was shifted to 1740 $cm^{-1}$ and this shift can be ascribed to the ester functional group of triglycerides[20]. That band can be exclusively assigned to culurgiones residuals since its presence in bacteria can be observed only following an oxidative stress of the nucleic acids when treated with nanoparticles [17].

The presence of the band at 1236 $cm^{-1}$ ascribed to the phosphodiester groups of the phospholipids (Figures 8.12-8.14 and Table 8.2) can substantiate the antimicrobial effect of PHMG as described in section 8.2.4, since they can indicate the presence of plasmatic membrane residuals; this assignment can be substantiated by the presence of the band at about 1115 $cm^{-1}$ ascribed to the phosphoryl groups as suggested in [17]. On the other hand, the band at 1115 $cm^{-1}$ can be also ascribed to the C-O stretching of carbohydrates and the presence of phospholipids from the culurgiones filling cannot be ruled out. Moreover, it is worth noting that a band at about 2360 $cm^{-1}$ was detected after 6 and 24 hours of storage of culurgiones in P-PVC inoculated with *S. aureus* and *E. coli* (Figures 8.12 and 8.13) and it is ascribed to the

$CO_2$ stretching. The band intensity increases upon the storage time, probably due to fermentative and degradative processes of the organic compounds such as carbohydrates that have been found on the P-PVC surface. Similar results were reported in the literature for different types of food samples [31], due to the activity of fermentative bacteria. The ATR-FTIR results obtained with both the bacteria studied were comparable, in fact no significant difference were observed between the spectra obtained in the case of *S. aureus* and *E. coli*.

The comparison of the spectra shown in figure 8.12 and 8.13 with those reported in figure 8.14 allows observing that the P-PVC used for storing culurgiones with and without inoculum showed similar bands. Figure 8.18 shows a comparison between P-PVC in contact with culurgiones not contaminated and exposed to *E. coli* for 6 hours.

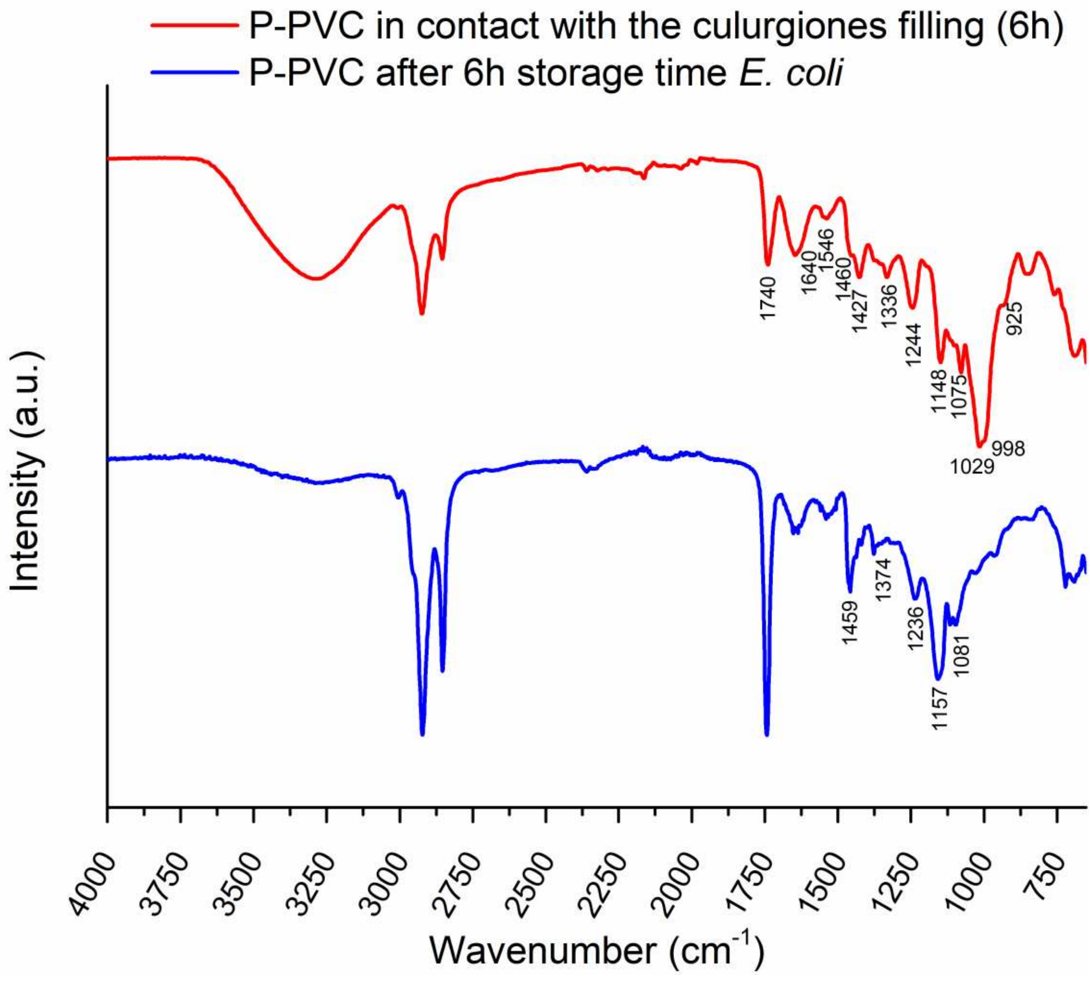

*Figure 8.18* ATR-FTIR spectra of PPVC in contact with the culurgiones filling (red curve) and P-PVC after 6h storage time of the culurgiones inoculated with E. coli

The main difference between the two spectra is the presence of two intense band at 1029 and 998 $cm^{-1}$ that can be ascribed to the formation of a complex between the bacterial membrane as discussed in section 8.2.4 or eventually to the C-O-C ring stretching of the carbohydrates of the culurgiones. The ATR-FTIR spectra showed in this work are comparable to the one reported in the literature on typical Italian dishes that contains similar ingredients to the culurgiones samples (e.g. fresh Pasta, cheese)[32].

The P-PVC micrography showed in Figure 8.15 shows the presence of circular features that are similar to the shapes of dead colonies reported in the literature [25] thus suggesting that the residual observed on the P-PVC can be attributed to *S. aureus* after their interaction with PHMG. However, also in this case it is not possible to rule out that these features are related to food sample residuals.

Qualitative results were obtained by wrapping Carasau bread samples with PVC and P-PVC for 15 days at room temperature. Figure 8.10 shows that the Carasau bread samples stored with PVC developed molds on their surface during the storage time, which is common occurrence for bread stored at room temperature. On the other hand, the samples stored in P-PVC did not develop any mold.  This suggests that the functionalized polymer may have antifungal properties, but more replicas and statistical analysis is required to confirm the reproducibility of this preliminary result.

## 8.5 Conclusions

The results presented and discussed in this chapter demonstrate an overall good antimicrobial activity of the P-PVC against *S. aureus* and *E. coli* microorganisms. Moreover, its antimicrobial activity has been demonstrated on typical Sardinian food samples such as culurgiones (fresh pasta) and Carasau bread.

In this investigation, chemical analysis by ATR-FTIR spectroscopy was exploited to try to clarify the mechanism of the interaction between the microorganisms and the functional groups present on the surface of the P-PVC samples. The attenuation of the C=N stretching band at 1629 cm$^{-1}$ might suggest the formation of complexes between the PHMG and the membranes of the microorganisms. Despite the significant differences observed between the G-PVC and the P-PVC after exposure to the inoculated agar medium a partial release of PHMG from the P-PVC sample cannot be ruled out. This hypothesis is substantiated by the inhibition growth area observed in the disk diffusion method experiments. Moreover, ATR-FTIR results demonstrate the presence of the characteristic bands due to the organic compounds (such as fatty acids, carbohydrates) that are characteristic for both bacteria and food residual. The comparison between the spectra does not allow ascertaining whether the bands can be ascribed to the culurgiones residuals or to the bacteria.

The results obtained on Carasau bread are promising and indicates that PHMG can inhibits the growth of molds. On the other hand, these represents preliminary results, and it is necessary to repeat the experiment on Carasau samples.

Based on the promising achievements in the in-vitro and food samples studies, P-PVC could potentially serve as an antimicrobial packaging material for food. However, further investigation is required.

*References*

[1] "ISO 20743:2021(en), Textiles — Determination of antibacterial activity of textile products, (n.d.). https://www.iso.org/obp/ui/#iso:std:iso:20743:ed-3:v1:en (accessed March 11, 2024).

[2] M. Moradi, S.A. Kousheh, R. Razavi, Y. Rasouli, M. Ghorbani, E. Divsalar, H. Tajik, J.T. Guimarães, S.A. Ibrahim, Review of microbiological methods for testing protein and carbohydrate-based antimicrobial food packaging, Trends in Food Science & Technology 111 (2021) 595–609. https://doi.org/10.1016/j.tifs.2021.03.007.

[3] F.C. Tenover, Antibiotic Susceptibility Testing, in: M. Schaechter (Ed.), Encyclopedia of Microbiology (Third Edition), Academic Press, Oxford, 2009: pp. 67–77. https://doi.org/10.1016/B978-012373944-5.00239-X.

[4] P. Appendini, J.H. Hotchkiss, Review of antimicrobial food packaging, Innovative Food Science & Emerging Technologies 3 (2002) 113–126. https://doi.org/10.1016/S1466-8564(02)00012-7.

[5] B. Hilgenberg, A. Prange, L. Vossebein, 2 - Testing and regulation of antimicrobial textiles, in: G. Sun (Ed.), Antimicrobial Textiles, Woodhead Publishing, 2016: pp. 7–18. https://doi.org/10.1016/B978-0-08-100576-7.00002-X.

[6] M. Balouiri, M. Sadiki, S.K. Ibnsouda, Methods for in vitro evaluating antimicrobial activity: A review, J Pharm Anal 6 (2016) 71–79. https://doi.org/10.1016/j.jpha.2015.11.005.

[7] Faculty of Food Industry and Agriculture, Department of Food Science & Technology, Standard Research Institute (SRI), Karaj P. O. Box 31745-139, Iran, S. Belgheisi, R. Soltani, R. Massoud, Effect of Whey Protein Based Edible Coating on the Quality of Fresh Mutton, IJCEA 7 (2016) 62–65. https://doi.org/10.7763/IJCEA.2016.V7.543.

[8] R. Niazmand, B.M. Razavizadeh, F. Sabbagh, Low-Density Polyethylene Films Carrying *ferula asafoetida* Extract for Active Food Packaging: Thermal, Mechanical, Optical, Barrier, and Antifungal Properties, Advances in Polymer Technology 2020 (2020) e4098472. https://doi.org/10.1155/2020/4098472.

[9] ISO 22196:2011(en), Measurement of antibacterial activity on plastics and other non-porous surfaces, (n.d.). https://www.iso.org/obp/ui/en/#iso:std:iso:22196:ed-2:v1:en (accessed March 11, 2024).

[10] M.D. Campos, P.C. Zucchi, A. Phung, S.N. Leonard, E.B. Hirsch, The Activity of Antimicrobial Surfaces Varies by Testing Protocol Utilized, PLOS ONE 11 (2016) e0160728. https://doi.org/10.1371/journal.pone.0160728.

[11] H. Dogan, M. Koral, T.Y. İnan, Ag/Zn Zeolite Containing Antibacterial Coating for Food-Packaging Substrates, Journal of Plastic Film & Sheeting 25 (2009) 207–220. https://doi.org/10.1177/8756087909354479.

[12] G. Yao, J. Lei, W. Zhang, C. Yu, Z. Sun, S. Zheng, S. Komarneni, Antimicrobial activity of X zeolite exchanged with Cu2+ and Zn2+ on Escherichia coli and Staphylococcus aureus, Environ Sci Pollut Res Int 26 (2019) 2782–2793. https://doi.org/10.1007/s11356-018-3750-z.

[13] M.E. Villanueva, J.A. González, E. Rodríguez-Castellón, S. Teves, G.J. Copello, Antimicrobial surface functionalization of PVC by a guanidine based antimicrobial polymer, Materials Science and Engineering: C 67 (2016) 214–220. https://doi.org/10.1016/j.msec.2016.05.052.

[14] T.M. Kamenieva, O.P. Tarasyuk, K.Y. Derevianko, O.A. Aksenovska, O.V. Shybyryn, L.O. Metelytsia, S.P. Rogalsky, Antioxidant activity of polymeric biocide polyhexamethylene guanidine hydrochloride, Catalysis and Petrochemistry (2020) 73–82. https://doi.org/10.15407/kataliz2020.30.073.

[15] M.S. Brzezinska, M. Walczak, U. Jankiewicz, M. Pejchalová, Antimicrobial Activity of Polyhexamethylene Guanidine Derivatives Introduced into Polycaprolactone, J Polym Environ 26 (2018) 589–595. https://doi.org/10.1007/s10924-017-0974-9.

[16] Y. Jiang, A. Zheng, Y. Guan, D. Wei, X. Xu, W. Gong, Gene reconstruction spandex with intrinsic antimicrobial activity, Chemical Engineering Journal 404 (2021) 125152. https://doi.org/10.1016/j.cej.2020.125152.

[17] F. Faghihzadeh, N.M. Anaya, L.A. Schifman, V. Oyanedel-Craver, Fourier transform infrared spectroscopy to assess molecular-level changes in microorganisms exposed to nanoparticles, Nanotechnol. Environ. Eng. 1 (2016) 1. https://doi.org/10.1007/s41204-016-0001-8.

[18] J.C. Feo, M.A. Castro, L.C. Robles, A.J. Aller, Fourier-transform infrared spectroscopic study of the interactions of selenium species with living bacterial cells, Anal Bioanal Chem 378 (2004) 1601–1607. https://doi.org/10.1007/s00216-004-2494-4.

[19] D. Naumann, D. Helm, H. Labischinski, Microbiological characterizations by FT-IR spectroscopy, Nature 351 (1991) 81–82. https://doi.org/10.1038/351081a0.

[20] M. Lucarini, A. Durazzo, J. Sánchez del Pulgar, P. Gabrielli, G. Lombardi-Boccia, Determination of fatty acid content in meat and meat products: The FTIR-ATR approach, Food Chemistry 267 (2018) 223–230. https://doi.org/10.1016/j.foodchem.2017.11.042.

[21] M. Beekes, P. Lasch, D. Naumann, Analytical applications of Fourier transform-infrared (FT-IR) spectroscopy in microbiology and prion research, Veterinary Microbiology 123 (2007) 305–319. https://doi.org/10.1016/j.vetmic.2007.04.010.

[22] M. Kačuráková, M. Mathlouthi, FTIR and laser-Raman spectra of oligosaccharides in water: characterization of the glycosidic bond, Carbohydrate Research 284 (1996) 145–157. https://doi.org/10.1016/0008-6215(95)00412-2.

[23] Gué Michaël, V. Dupont, A. Dufour, O. Sire, Bacterial Swarming: A Biochemical Time-Resolved FTIR−ATR Study of Proteus mirabilis Swarm-Cell Differentiation, Biochemistry 40 (2001) 11938–11945. https://doi.org/10.1021/bi010434m.

[24] T. Foster, Staphylococcus, in: S. Baron (Ed.), Medical Microbiology, 4th ed., University of Texas Medical Branch at Galveston, Galveston (TX), 1996. http://www.ncbi.nlm.nih.gov/books/NBK8448/ (accessed August 30, 2024).

[25] S. Yougbaré, C. Mutalik, D.I. Krisnawati, H. Kristanto, A. Jazidie, M. Nuh, T.-M. Cheng, T.-R. Kuo, Nanomaterials for the Photothermal Killing of Bacteria, Nanomaterials 10 (2020) 1123. https://doi.org/10.3390/nano10061123.

[26] S.G. Coombs, S. Khodjaniyazova, F.V. Bright, Exploiting the 3-Aminopropyltriethoxysilane (APTES) autocatalytic nature to create bioconjugated microarrays on hydrogen-passivated porous silicon, Talanta 177 (2018) 26–33. https://doi.org/10.1016/j.talanta.2017.09.038.

[27] N. Nematidil, M. Sadeghi, S. Nezami, H. Sadeghi, Synthesis and characterization of Schiff-base based chitosan-g-glutaraldehyde/NaMMTNPs-APTES for removal Pb2+ and Hg2+ ions, Carbohydrate Polymers 222 (2019) 114971. https://doi.org/10.1016/j.carbpol.2019.114971.

[28] S. Garip, F. Bozoglu, F. Severcan, Differentiation of Mesophilic and Thermophilic Bacteria with Fourier Transform Infrared Spectroscopy, Appl Spectrosc 61 (2007) 186–192. https://doi.org/10.1366/000370207779947486.

[29] J. Kiwi, V. Nadtochenko, Evidence for the Mechanism of Photocatalytic Degradation of the Bacterial Wall Membrane at the TiO2 Interface by ATR-FTIR and Laser Kinetic Spectroscopy, Langmuir 21 (2005) 4631–4641. https://doi.org/10.1021/la046983l.

[30] L. Beney, Y. Mille, P. Gervais, Death ofEscherichia coli during rapid and severe dehydration is related to lipid phase transition, Appl Microbiol Biotechnol 65 (2004) 457–464. https://doi.org/10.1007/s00253-004-1574-x.

[31] C.H. Threlkeld, Detection of Microbial Contamination Utilizing an Infrared CO2 Analyzer, Journal of Food Science 47 (1982) 1222–1225. https://doi.org/10.1111/j.1365-2621.1982.tb07652.x.

[32] A. Durazzo, J. Kiefer, M. Lucarini, E. Camilli, S. Marconi, P. Gabrielli, A. Aguzzi, L. Gambelli, S. Lisciani, L. Marletta, Qualitative Analysis of Traditional Italian Dishes: FTIR Approach, Sustainability 10 (2018) 4112. https://doi.org/10.3390/su10114112."

# Chapter 9 Conclusions and outlooks

This thesis presents an investigation on the surface functionalization of food-grade PVC, with the aim of developing a potential antimicrobial food packaging for extending the food shelf-life especially of bread and fresh pasta, which are typical Sardinian products. The resulting complex layered systems of functionalized polymers were characterized using different surface-sensitive techniques such as XPS, ATR-FTIR, AFM and SEM. Based on the results presented and discussed, the following conclusions can be drawn:

- A procedure for the surface functionalization of food-grade PVC with polyhexamethylene guanidine (PHMG) as antimicrobial active agent was studied.
- The grafting of a new potential antimicrobial molecule such as 4-(10,15,20triphenylporphyrin-5-yl) aniline (TPPA) was also studied.
- XPS and ARXPS were performed on ideally flat gold samples functionalized using the same procedure as PVC. This allowed finding the curve fitting parameters that were successfully applied to the carbon-based substrate (PVC) to distinguish the contribution on C 1s spectra due to the polymer substrate and to the functionalization layer. The quantitative composition of the functionalized PVC obtained by standard-mode XPS spectra and the thickness of the functionalization layer, determined starting by ARXPS experiments, were comparable with the results obtained on gold. The thickness estimation was also in agreement with the simulation obtained by Avogadro.
- Considering the stoichiometry determined by XPS the following functionalization mechanism, under the adopted conditions, can be hypothesized: in the first step of functionalization, (3-mercaptopropyl) trimethoxysilane (MPTMS) was attached to a food grade PVC by a nucleophilic substitution reaction (M-PVC) that involved 70% of the chlorine present on the surface of the substrate, therefore leaving 30% of the substrate's surface unreacted.

  In the following step, 3-(aminopropyl)-triethoxysilane (APTES) was anchored to MPTMS via a reaction involving the silanol groups (A-PVC) with a MPTMS : APTES ratio equal to 2:. In the third step of functionalization the reaction between the free amino groups of the anchored APTES with glutaraldehyde (G-PVC), is exploited and the APTES : glutaraldehyde ratio was found to be 5:3. Preliminary results regarding the last step involved the anchoring of the bioactive molecule, PHMG, to the free aldehydic group of glutaraldehyde (P-PVC); in this case the ratio between glutaraldehyde and PHMG was found to be 2:1 but XPS results appear to suggest the polymerization of PHMG.

- The presence of the functional groups hypothesized during the curve fitting of XPS signals, especially for the components of C 1s peak, was checked by ATR-FTIR spectroscopy, that was also exploited to select the best conditions to achieve the surface modification of the polymer.
- AFM showed an increase of the PVC roughness upon functionalization and SEM provided the evidence of the change in the morphology of the food grade PVC following the four steps of functionalization, leading to the formation of a thick layer of PHMG after the last functionalization step, due to the polymerization reaction that can occur between PHMG molecules.
- The antimicrobial potential of the P-PVC samples against *S. Aureus* and *E. Coli* was tested by different methods. P-PVC samples showed a strong antimicrobial activity against the *S.Aureus*; since no significant changes in hydrophobicity between the as-received food grade PVC and the P-PVC were observed by contact angle measurments, the bacterial growth inhibition seems to only be related to the antimicrobial activity of polyhexamethylene guanidine. A weaker antimicrobial activity was observed toward *E. Coli*. Furthermore, P-PVC was also tested on typical Sardinian food samples showing promising results concerning the shelf-life extension of these sample.

### *Outlooks*

The surface functionalization of a carbon-based substrate (PVC) with organic compounds was studied with a variety of surface analytical methods. The results presented in this thesis may be useful for future research on surface functionalization of other carbon-based substrates such as polylactic acid (PLA), polyvinyl alcohol (PVA) following similar procedures to develop new anti-microbial packaging. Moreover, the same strategy can be used for characterizing the PVC functionalized with TPPA.

TPPA-PVC samples analysed in this work showed an intrinsic fluorescence when irradiated by a 366 nm wavelength after 1 hour of immersion time. This may suggest that even if the TPPA band are not observed on the ATR-FTIR spectrum the functionalization occurred. Studying the fluorescence properties of the functionalized polymer with a fluorimeter for solids may be useful to understand the potential applications of the PVC as an active fluorescent food-packaging. Thus it might be interesting not only to test the antimicrobial activity of TPPA-PVC but also to investigate if the antimicrobial effect can modify the fluorescence properties of the material.

Furthermore, the preliminary results obtained by applying UV-Vis spectroscopy for the quantification of guanidine group density were promising and suggested the formation of PHMG multilayer. For this reason, it would be interesting to develop a more accurate analytical method for the quantification of guanidine groups.

This work has shown the antimicrobial potential of P-PVC against *S.Aureus* and *E.Coli,* and its potential as antimicrobial food-packaging. For this reason, another aspect that could be studied is the activity against other bacteria strains and against molds and yeasts. ATR-FTIR spectra acquired on P-PVC samples after the contact with food samples showed that the band at 1630 cm$^{-1}$, attributed to the iminium group associated with the antimicrobial activity of P-PVC, is still detected but attenuated. This is probable due to the formation of complexes with the bacteria membranes. XPS could be used to characterize the surfaces after the contact with the contaminated samples to ascertain whether PHMG is or not released from the surface and to confirm the presence of the complexes formed between PHMG and the bacteria membrane.

# Acknowledgements

I would like to express my deepest gratitude to all those who supported me throughout my doctoral journey. First and foremost, I would like to thank my supervisor, Prof. Antonella Rossi, for her guidance, encouragement, and unwavering support. Her expertise and insight have greatly contributed to the completion of this work.

I am deeply grateful to Prof. Marzia Fantauzzi, who has been an essential part of my academic and personal growth. Her support over the years has fostered many meaningful professional and personal discussions that have enriched my journey.

My sincere thanks go to Prof. Bernhard Elsener for his valuable guidance and for fostering numerous stimulating and insightful conversations throughout the course of this dissertation.

I would also like to thank Dott. Giovanni Loi for his invaluable assistance in interpreting the microbiological results and for providing many insightful suggestions that improved the quality of the presented findings.

I am profoundly grateful to Prof. Yoko Yamakoshi for giving me the opportunity to work in her research group at the Department of Chemistry and Applied Biosciences at ETH Zurich. My thanks extend to Dr. Çetin Çelik for his help with the synthesis of the porphyrins used in this work. I would also like to thank Andrin Aot for welcoming me into the group and offering continuous support. Additionally, I am thankful to Dr. Shivaprakash N. Ramakrishna for introducing me to Atomic Force Microscopy, and to Prof. Lucio Isa for allowing me to use the optical tensiometer for contact angle measurements, as well as for the opportunity to attend his fascinating lessons on Surface and Interface Chemistry.

I am sincerely grateful to Dr. Lino Brundu and Dr. Laura Brundu for hosting me at the Laboratorio Chimico Nuorese, giving me access to their instruments, and assisting with the microbiological experiments. I also extend my thanks to all the collaborators at the laboratory for their support during my time in Nuoro, for welcoming me as part of their team, and for helping me enhance my knowledge in the biological field.

To my family, I am forever thankful for your constant support and belief in me during these past three years, even through the most difficult moments.

Finally, to my “second family” – those who have been part of my life for the past ten years – thank you for being my number one supporters. Even though I sometimes missed your birthdays and was far away during important moments, your encouragement has been invaluable. To all of you, I am eternally grateful.

UNIONE EUROPEA
Fondo Sociale Europeo
Fondo Europeo di Sviluppo Regionale

Ministero dell'Università
e della Ricerca

FSC
Fondo per lo Sviluppo
e la Coesione

La borsa di dottorato è stata cofinanziata con risorse del
Piano Stralcio «Ricerca e Innovazione» 2015-2017 Asse "Capitale Umano", del Fondo per lo
Sviluppo e la Coesione, "Dottorati A Tema Vincolato – Aree Interne/Aree Marginalizzate"